Freie Universität Berlin (FU)
Fachbereich Geowissenschaften
Malteserstr. 74-100, 12249 Berlin

GeoForschungsZentrum (GFZ)
Helmholtz-Zentrum Potsdam
Telegrafenberg, 14473 Potsdam

Lithospheric structure and seismotectonic setting of the Hindu Kush, the Tajik-Afghan basin and the western Pamir from analysis of local- and teleseismic data

Dissertation zur Erlangung des Doktorgrades
im Fachbereich Geowissenschaften der
Freien Universität Berlin

vorgelegt von

Sofia-Katerina Kufner

eingereicht: 04.05.2016
verteidigt: 24.06.2016

Prüfungskommission: Prof. Dr. Onno Oncken (Vorsitz), Prof. Dr. Frederik Tilmann, Prof. Dr. Lothar Ratschbacher, Prof. Dr. Mark Handy, Dr. Bernd Schurr

Erstgutachter:
Prof. Dr. Frederik Tilmann
GeoForschungsZentrum

Zweitgutachter:
Prof. Dr. Lothar Ratschbacher
TU Bergakademie Freiberg

Instead of looking at the sky -
you picked me up and showed me how to fly.

Katie Melua, Half Way Up The Hindu Kush

Abstract

The Pamir-Hindu Kush mountains at the northwestern margin of the India-Asia collision zone form a geodynamic peculiarity, both in the context of this collision and globally, as they host one of the most intense nests of intermediate depth seismicity not associated to oceanic subduction worldwide. Neither the deep lithospheric structure of Pamir-Hindu Kush, nor the physical processes causing this extraordinary seismicity are clear yet. Here, I use seismic data, mainly from the TIPTIMON network, which recorded during 2012 to 2014 in Tajikistan and Afghanistan, but also from other temporarily deployed, permanent and global seismic stations, aiming to untangle this seismotectonic puzzle.

From a combined analysis of teleseismic tomography, local seismicity and earthquake source mechanisms, I suggest that intermediate depth seismicity beneath Pamir-Hindu Kush is associated to two different lithospheric slabs of Asian and Indian origin, respectively. As the whole mountain range, the Pamir slab is northward offset relative to the Hindu Kush and the earthquakes' stress regime indicates vertical tearing in its center. The Hindu Kush slab is in the process of breaking-off, testified by the down-dip extensional stress regime of the earthquakes and the thinning of the subducted mantle lithosphere at ∼200 km depth, where seismicity is most intense. This contrasting behavior can be understood when considering the different properties of the three types of lithosphere involved: while the northward advancing cratonic Indian indenter forces delamination and rollback of the Asian lithosphere beneath the Pamir, India's thinned western continental margin subducts beneath the Hindu Kush. The tearing of these two Indian lithospheric domains can also be traced into the Asian crust on top, marked by a seismically active zone of distributed shear at the transition between Pamir and Hindu Kush.
Including results from a local earthquake tomography (LET), the relocated largest events over the last 30 years and a strain rate analysis, I suggest that the Hindu Kush break-off propagates along a localized shear-zone, splitting the seismogenic part of the slab in a region involving crustal subduction (∼60-160 km) and a deeper domain (∼180-270 km), where seismicity occurs along this shear-zone and which hosts the largest and most frequent earthquakes. Whereas seismicity in the shallower domain might be enabled by different processes related to metamorphic reactions in the subducted crust, shear-instabilities on the intra-lithospheric detachment interface might trigger brittle-like failure in the deeper domain.

The Tajik basin's lithosphere acts as hanging wall for the Hindu Kush subduction but subducts itself eastward beneath the Pamir at the same time. LET resolved a thick, high-velocity mantle lithosphere beneath the basin, which however includes a heterogeneous low velocity layer at ∼120-140 km. I interpret this zone as midlithospheric discontinuity, which was recently discovered to be a widespread feature of cratonic lithosphere. As deep earthquakes are usually absent in such an environment, it is resolved here for the first time with LET. At crustal levels, deformation in the basin and its sedimentary cover is partitioned between seismically active strike-slip faults at the basin's northern and eastern rim and its interior, where earthquakes occur mainly along a horizontal sliding interface at ∼10-12 km depth. Pressure axes and slip vectors of these events are parallel to the west-east oriented GPS-velocity vector field, suggesting that seismogenic deformation is controlled by the westward oriented gravitational collapse of the Pamir.

Zusammenfassung

Die tektonische Struktur von Pamir und Hindukusch ist einzigartig; nicht nur relativ zum Rest des indisch-asiatischen Kollisionssystems, dem der Pamir und Hindukusch zugeordnet werden, sondern auch weltweit. Nirgends sonst treten so häufig mitteltiefe Erdbeben auf, die nicht in Verbindung mit einer ozeanischen Subduktionszone gebracht werden können. Dabei ist weder die Geometrie der Lithosphärenplatten unter diesen beiden Gebirgen noch der eigentliche Grund für das Auftreten dieser Beben vollends geklärt. In der folgenden Arbeit versuche ich mithilfe seismologischer Methoden Teile dieses tektonischen Puzzles zu lösen. Für meine Analyse verwende ich vor allem Daten des seismischen Netzwerkes TIPTIMON, welches zwischen 2012 und 2014 in Tadschikistan und Afghanistan installiert war.

Basierend auf den Ergebnissen von teleseismischer Tomografie, Lokalisierung von Erdbeben und Bestimmung der jeweiligen Bruchmechanismen leite ich her, dass die Seismizität unter dem Pamir und dem Hindukusch zwei unterschiedlichen, gerade abtauchenden Lithosphärenplatten zugeordnet werden kann: der Indischen unter dem Hindukusch und der Asiatischen unter dem Pamir. Genau wie das Pamirgebirge ist auch die unterliegende Lithosphärenplatten nach Norden verschoben. Die Spannungsachsen der Erdbeben, die in dieser subduzierenden Lithosphärenplatte liegen, deuten ein vertikales Aufreißen der Platte an. Unter dem Hindukusch hingegen befindet sich die abtauchende Lithosphärenplatte im Stadium der finalen Ablösung. Dies drückt sich zum einen durch das vertikal nach unten orientierte Spannungsregime der Erdbeben Bruchmechanismen und zum anderen durch die Verdünnung der abtauchenden Platte in ∼200 km Tiefe aus. Die seismische Aktivität ist genau an der Stelle dieser Verdünnung am ausgeprägtesten. Dieses unterschiedliche Verhalten des Mantels unter dem Pamir und Hindukusch lässt sich durch die Struktur der einzelnen Lithosphärenteile erklären, die in den Kollisionsprozess involviert sind: Während die indische kratonische Lithosphäre die Delamination und das Zurück-rollen der asiatischen Lithosphäre unter dem Pamir erzwingt, taucht westlich davon gleichzeitig Indiens ausgedünnter Kontinentalrand unter dem Hindukusch ab. Das damit einhergehende Aufreißen der indischen Lithosphäre im subkrustalen Bereich lässt sich auch an der Oberfläche in der stark deformierten Region zwischen Pamir und Hindukusch erkennen.
Das Abreißen der Hindukusch-Platte kann mithilfe von Lokalbeben-Tomografie, der Reokalisierung der größten Hindukusch-Beben der letzten 30 Jahre und einer Spannungsfeldanalyse genauer beobachtet werden: Basierend auf Resultaten dieser Studien schlage ich vor, dass sich während des Abtrennens eine klar definierte Scherzone durch die Lithosphärenplatte ausbildet. Diese Scherzone trennt den oberen Teil der Mantelseismizität im Hindukusch (∼60-160 km Tiefe) vom tieferen Teil (∼180-270 km Tiefe). Während der obere Teil der Seismizität räumlich mit der mitgerissenen, ebenfalls abtauchenden kontinentalen Kruste zusammenfällt, tritt die tiefere Seismizität, mit mehr und größere Beben als im flachen Bereich, entlang der Scherzone auf. Die flachere Seismizität könnte im Zusammenhang mit metamorphischen Reaktionen, die in der abtauchenden Kruste ablaufen, stehen. Im tieferen Teil dagegen könnten Instabilitäten entlang der Scherzone sprödbruchähnliche Deformation herbeiführen.

Die Lithosphäre des tadschikischen Beckens fungiert als Puffer für die Hindukusch Subduktion und taucht gleichzeitig unter dem Pamir ab. Mit Hilfe von Lokalbeben-Tomografie

zeige ich, dass sich die Lithosphäre durch hohe seismische Geschwindigkeiten auszeichnet und dass sie relativ dick ist. Sie wird jedoch in ca. 120-140 km Tiefe von einer heterogenen Niedergeschwindigkeitszone durchzogen, welche ich als *Mittel-Lithosphärische Diskontinuität (MLD)* interpretiere, wie sie vermehrt in alter kratonischer Lithosphäre beobachtet wird. Da tiefe Erdbeben in Kratonen normalerweise eher unüblich sind, wurde die MLD bis jetzt noch nie mit Lokalbeben-Tomografie sichtbar gemacht.
Die Deformation der Kruste des tadschikischen Beckens ist aufgeteilt zwischen seismisch aktiven Verwerfungen am nördlichen und östlichen Rand des Beckens und dem Becken selber. Im Inneren des Beckens häufen sich die Beben entlang einer Sedimentschicht in ca. 10-12 km Tiefe. Die Spannungsachsen und die Orientierung der Bruchflächen dieser Beben sind, genau wie das GPS-Vektorfeld, West-Ost orientiert, was durch den gravitatinsbedingten Kollaps des Pamirs in das tadschikische Becken erklären werden kann.

Contents

1 Motivation and Introduction

"Subduction of lithosphere at island arc structures occurs along relatively narrow zones, apparently in a simple manner, but because of the buoyancy of the continental lithosphere, subduction of one continent beneath another is often assumed to be impossible (McKenzie, 1969; Isacks et al., 1968)"
Molnar and Tapponnier (1975)

"[..] findings of crustal xenoliths of clearly Eurasian provenance in the south-east Pamir testified that the crustal rocks have resided at least at 90 km depth in this region (Hacker et al., 2005). Together with our observation of the south-dipping LVZ (low velocity zone, resolved by receiver functions - e.d. note) this provides strong evidence for the ongoing subduction of Eurasian continental crust beneath the Pamir."
Schneider et al. (2013)

During the plate tectonic Wilson cycle, which describes the opening and closure of oceans, and represents thus the fundamental concept of plate tectonics, each plate passes through the stage of continental collision. Collision manifests itself by shortening in the lithosphere accompanied by a gradual slowdown in relative motion between the two plates and eventually the detachment of the earlier subducted oceanic slab (Moores and Twiss, 1995; Cox and Hart, 2009). However, how, where and in which time-frame these processes occur is by far not understood yet, especially because most direct markers in the geological record are destroyed or overprinted in the course of the collisional event (Molnar and Tapponnier, 1975). Subduction of lithosphere, the most prominent mechanism to accommodate convergence during the preceding oceanic subduction phase, has long been considered as impossible or negligible for continents because continental crust is much more buoyant than oceanic crust (see the Molnar and Tapponnier, 1975, quote at the beginning of this chapter). Thus, fully developed continental crust (i.e. 35 km thickness) should resist subduction (Isacks et al., 1968; McKenzie, 1969; Molnar and Gray, 1979). Over the last decades, the discovery of ultra-high pressure (UHP) terrains has challenged this concept (Chopin, 1984; Smith, 1984; Sobolev and Shatsky, 1990), as the UHP rocks were interpreted to have formed in crustal material after the transition from oceanic subduction to continental collision (Guillot et al., 2003; Rosenbaum and Lister, 2005). Nowadays, after several dozen regions hosting these UHP rocks have been described, the possibility of subduction of continental crust is generally well established (Tsujimori et al., 2006; Schertl and O'Brien, 2013). However, these exhumed UHP rocks represent probably only a small portion of the subducted material, as can be deduced from rare geophysical observations. Schneider et al. (2013), for instance, interpreted a south-dipping zone of low seismic velocity beneath the Pamir in Central Asia to represent ongoing subduction of Asian continental crust (see the second quote at the beginning of this chapter). Thus, once crustal material has reached mantle depths, it is not necessarily exhumed but could

be dragged to greater depths, physically attached to the descending mantle lithosphere and possibly undergoing metamorphic reactions that increase its density (Krystopowicz and Currie, 2013). Alternatively, buoyant crustal material might detach but pond in the upper mantle, or ascend and relaminate to the lower crust (Hacker et al., 2011).
Numerical modeling provides a powerful tool to explore how continental collision might evolve subsequent to oceanic subduction (e.g. Gerya et al., 2004; Burov and Yamato, 2008; van Hunen and Allen, 2011; Duretz and Gerya, 2013). In such numerical models, the continental subduction is generally driven by an earlier subducted oceanic plate, which after its consumption pulls continental material to depth. At the point where the competing forces of buoyant crust and descending cold (oceanic) lithosphere level-off, the subduction is stalled and the earlier subducted oceanic lithosphere detaches. Depending on the imposed slab-pull and the rheology, the continental crust might partially subduct or exhume again. Apart from these slab-detachment models, alternative ideas to explain the removal of lithosphere during collision include the drop-like downwelling of overthickened lithosphere into the mantle (Houseman et al., 1981; Koulakov, 2011) or a delamination process, where only parts of the lithosphere are removed (Bird, 1979).

Whereas such geodynamic models highly depend on the initial parametrization, the investigation of UHP rocks only provides constraints on past tectonic events. In contrast, geophysical measurements enable to observe active tectonic processes during continental collision. In this context, nests of intermediate depth seismicity (i.e. seismicity between ∼60-300 km depth; Frohlich, 2006; Faccenda et al., 2012), far away from an active oceanic subduction zone have been interpreted to originate from processes associated with lithospheric removal during continental collision. However, at the same time, the physical processes causing these earthquakes are enigmatic (Thielmann et al., 2015). The intense seismicity testifies that brittle or brittle-like failure seems to be frequently possible under pressure-temperature (PT) conditions when deformation is expected to occur in a ductile manner (Raleigh and Paterson, 1965; Green and Houston, 1995; Kirby et al., 1996). Dehydration embrittlement due to phase transformations of hydrous minerals (Kirby et al., 1996; Yamasaki and Seno, 2003; Hacker et al., 2003), which is a common explanation for intermediate depth seismicity in active oceanic subduction zones, can only partly be applied to a continental environment due to the more felsic lithology of the latter (Rudnick and Gao, 2003). Another possible mechanism is thermal runaway, where localized viscous creep is suggested to result in a temperature increase, subsequent weakening and finally slip on a narrow shear-zone (Kelemen and Hirth, 2007; Braeck and Podladchikov, 2007; John et al., 2009). Both these processes depend strongly on rheology and PT-conditions. Thus, to understand the origin of intra-continental intermediate depth seismicity as well as its role during continental subduction and collision, the detailed understanding of the regional tectonic setting is an inevitable requirement.
Worldwide, only two nests of intra-continental intermediate depth seismicity were clearly recognized: the Pamir-Hindu Kush in Central Asia (Billington et al., 1977; Pegler and Das, 1998; Sippl et al., 2013b; Bai and Zhang, 2015) and Vrancea in Romania (Oncescu et al., 1999; Ismail-Zadeh et al., 2012; Vacareanu et al., 2015). Among these two, the Pamir and Hindu Kush will be the focus region of this study, aiming to understand its peculiar seismotectonic characteristics.

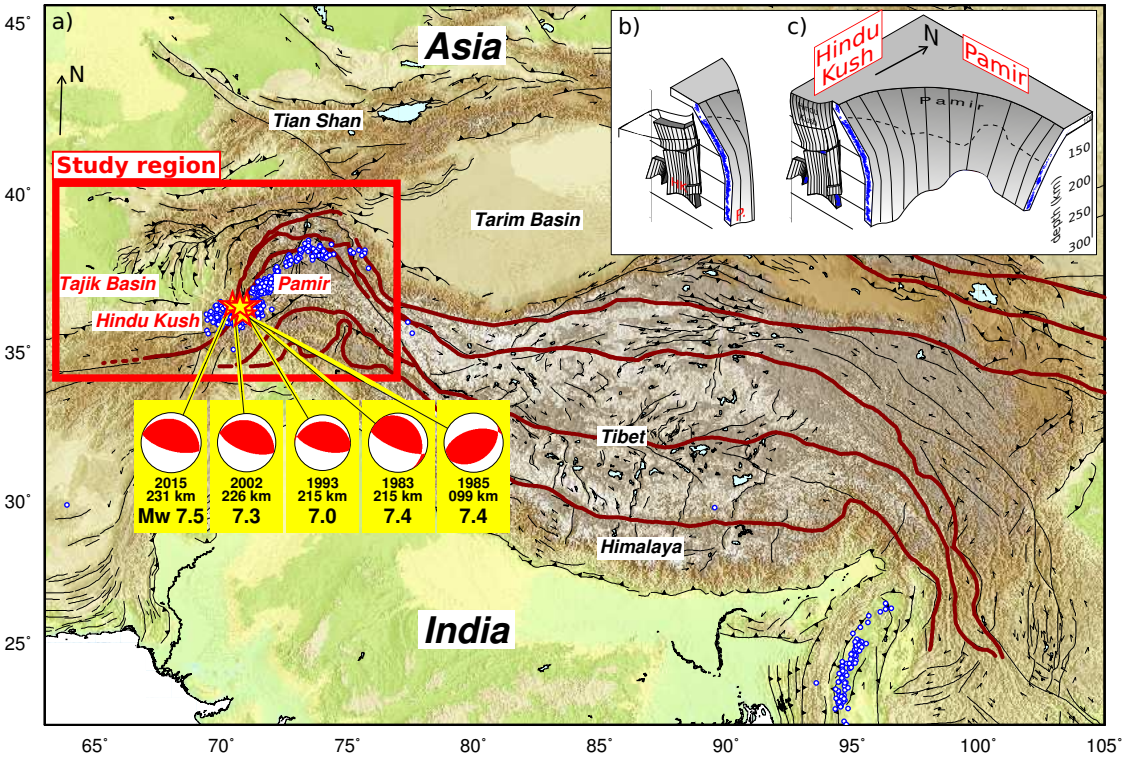

Figure 1.1: a) The Pamir-Hindu Kush region, part of the India-Asia collision zone. Seismicity deeper than 100 km (blue) from the EHB catalog (Engdahl et al., 1998). The largest intermediate depth earthquakes since the 1980s are highlighted as stars and their focal mechanisms are plotted as beach balls. The associated labels refer to the event years, depths and moment magnitudes (USGS, 2016). Sutures (dark red) from Schwab et al. (2004), Yin and Harrison (2000) and L. Ratschbacher (pers. comm.). Faults (black) from Styron et al. (2010) and Schurr et al. (2014). **b/c)** Schematic sketch from Sippl et al. (2013b) illustrating the geometry outlined by the Pamir-Hindu Kush intermediate depth seismicity, located using the TIPAGE seismic network (see Fig. 1.2 for the station and event locations). Whereas the analysis of Sippl et al. (2013b) resolved an arcuate seismogenic structure, dipping from the Asian side beneath the Pamir, the dip direction of the Hindu Kush seismogenic structure could not be resolved due to unfavorable event-station geometry. Thus, two possible scenarios were suggested.

The Pamir and Hindu Kush mountains, located north of the western syntaxis of the India-Asia collision system and east of Tibet and Himalaya (Fig. 1.1), have long been recognized as outstanding compared to the rest of the collision zone as only this region features intense intermediate depth seismicity. But despite these currently differing seismic characteristics, the Pamir-Hindu Kush and the Tibet-Himalaya systems share a common early formation history: India collided against Asia around ∼55-50 Ma (Patriat and Achache, 1984; van Hinsbergen et al., 2011a; Guillot et al., 2003), but subsequently advanced several hundreds of kilometers further northward to reach its present position. Different processes have been postulated how this convergence could be accommodated, including lithospheric scale underthrusting or continental subduction, deformation inside India and Asia as well as crustal scale escape (Molnar and Tapponnier, 1975; Molnar and Gray, 1979; Avouac and Tappon-

nier, 1993; Van der Voo et al., 1999; Chemenda et al., 2000; Replumaz and Tapponnier, 2003; Guillot et al., 2003; Li et al., 2008; Molnar and Stock, 2009; Yin, 2010). However, both the timing as well as the relevance of these different mechanisms is debated.
Whereas the Indian continent currently underthrusts under Tibet over a longitudinal range of several hundred kilometers (Li et al., 2008; Kind and Yuan, 2010), tectonic processes at the western syntaxis of the collision system vary over smaller scales (Seno and Rehman, 2011): On the one hand, global earthquake tomography resolved a localized, near vertically dipping high velocity structure in the mantle only below the Hindu Kush, which has been interpreted as an isolated lithospheric slab of narrow width (Bijwaard et al., 1998; Villaseñor et al., 2003; Van der Voo et al., 1999). On the other hand, only the Pamir was offset to the north, relative to the Hindu Kush and Tibet, as testified e.g. by the current offset of suture zones (Burtman and Molnar, 1993, marked as bold red lines in Figure 1.1a). Further, as noted above, only the Pamir-Hindu Kush features a zone of intense intermediate depth seismicity, the geometric shape of which, however, differs below the two mountain ranges, forming an arcuate structure beneath the Pamir and a west-east striking zone further to the southwest beneath the Hindu Kush (Billington et al., 1977; Pegler and Das, 1998; Sippl et al., 2013b). The largest intermediate depth earthquakes locate below the Hindu Kush mountains (red stars in Fig. 1.1a).
Recent temporary seismic experiments (mainly TIPAGE, see the next paragraph) brought new insights regarding these earthquakes and the underlying processes: high precision earthquake hypocenters, local tomography and receiver function analysis showed that the Pamir seismicity is hosted in a narrow layer of subducted continental crust, descending from the Asian side beneath the Pamir (Schneider et al., 2013; Sippl et al., 2013a). The dip-direction of the Hindu Kush earthquakes is still debated (see the schematic sketch from Sippl et al., 2013b, in Figs. 1.1b, c), although an Indian-sided origin is more widely accepted (Burtman and Molnar, 1993; Pegler and Das, 1998; Koulakov and Sobolev, 2006; Bai and Zhang, 2015). Together with the Asian-sided subduction beneath the Pamir, this would yield a situation of two continental subduction zones of different polarity in direct vicinity to each other. How and if such a scenario could develop, as well as the role of the Tajik basin, which is bounded at two sides by the Pamir-Hindu Kush mountains, is still unclear. Given that continental subduction was mainly postulated based on geological records and numerical simulation studies, but is only rarely observable today, the Pamir-Hindu Kush region is a treasure, showcasing geodynamically highly relevant processes.

This thesis will examine the seismotectonics of the Pamir-Hindu Kush region, concentrating on two main questions: Initially, I aim to decrypt the present constellation of the subducting slabs beneath Pamir and Hindu Kush in order to clarify their tectonic affinity and history. Then, I will use the Hindu Kush as a case example to study continental subduction and the processes driving intermediate depth seismicity.
The results presented here are mainly gained from the analysis of seismological data recorded by recent passive seismic experiments, deployed in Tajikistan, Kyrgyzstan and Afghanistan during two periods between 2008 to 2010 and 2012 to 2014. The earlier of these networks (TIPAGE) focused on the Pamir, the later on the Tajik basin, western Pamir and Hindu Kush (TIPTIMON; see Fig. 1.2 for the station locations). Work based on TIPAGE data yielded several international publications (Mechie et al., 2012; Sippl et al., 2013b,a; Schneider et al., 2013; Sippl et al., 2014; Schurr et al., 2014), and two dis-

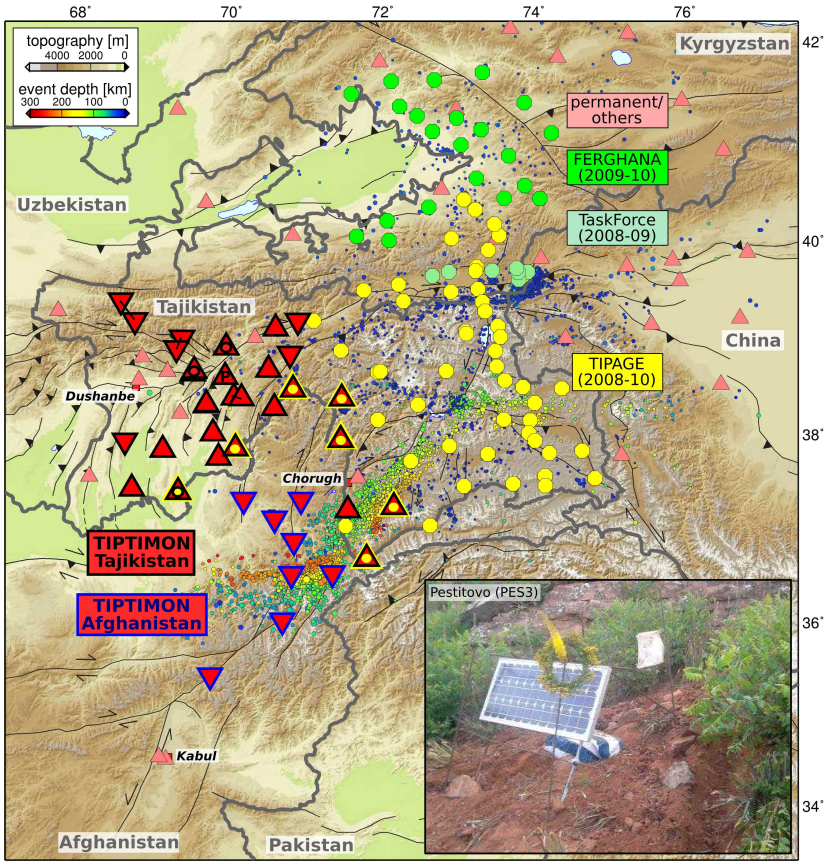

Figure 1.2: Map showing the seismic stations used in this study and political boundaries (gray) together with the seismicity from Sippl et al. (2013b) and local tectonic features (black) from Schurr et al. (2014). TIPTIMON stations (red triangles) were deployed between 2012-14 and 2013-14 in Tajikistan and Afghanistan, respectively. Triangles represent Guralp CMG-3ESP seismometers, inverted triangles Nanometrics Trillium-120 and MARK L-4C-3D seismometers on the Tajik and Afghan side, respectively. Stations marked with a yellow dot are redeployed TIPAGE sites. The three stations with a black circle temporarily lost their GPS antenna. Stations connected with a black line were moved during the deployment accordingly. The label *P* marks the Pestitovo station, which is shown in the map inset as an example for our setup. The other labeled networks were deployed prior to TIPTIMON, but also used in this study (see Sippl, 2013, for a detailed description of these stations). Most of the other/permanent stations (light red), which I included in my work operated during both deployment periods (see Supplementary Section A.1 for more detailed information regarding the TIPTIMON network and the permanent stations).

sertations (Sippl, 2013; Schneider, 2014). The later network was installed and maintained during the course of this thesis in the framework of the TIPTIMON (Tien Shan - Pamir Monitoring Program) project, a research program funded by the German Federal Ministry of Education and Research (BMBF). The analysis of these data forms the core of my thesis. Whereas TIPAGE publications in general concentrated on the crustal and upper mantle structure of the Pamir in its seismogenic portion (i.e. down to depths of ∼300 km), I could here use the combined data from TIPAGE and TIPTIMON and other Central

Asian networks (see Fig. 1.2) to apply geophysical methods whose success depends on network size (e.g. for teleseismic tomography, where penetration depth scales with network dimension). Thus, my work focused initially on the upper mantle structure beneath both orogens, later on the characteristics of the Hindu Kush and Tajik basin. I also included the contributions from different networks in the local analysis if it was reasonable, e.g. to improve resolution at the external domains of the TIPTIMON network.
Aiming to understand the seismotectonic processes in the Pamir-Hindu Kush region as a whole, the following thesis is not arranged according to the used methods, but rather according to the problems being addressed: Chapter 4 uses a combination of teleseismic tomography and local seismicity analysis to constrain the regional framework in which tectonic processes take place. The subsequent chapters then deal with different sub-aspects in this framework: Chapter 5 describes the lithospheric structure of the Tajik basin and its interaction with the two subduction zones to its sides, using local earthquake tomography. Chapter 6 is concerned with different aspects of the crustal seismicity. In Chapter 7, the characteristics of the earlier proposed slab break-off beneath the Hindu Kush are discussed in detail, based on a local seismicity analysis, tomography and source mechanisms. Here, an investigation of the most recent magnitude seven earthquake that struck the Hindu Kush in autumn 2015, is also included. This work is based on global seismic records in combination with the local data from the temporarily deployed seismic stations. Chapter 4 is published in *Earth and Planetary Science Letters* (Kufner et al., 2016), the other chapters are written as paper drafts. Thus, a specific geology and methods part is included at the beginning of each of these chapters. Additionally, a broader overview regarding tectonic context and methods can be found in the Chapters 2 and 3, respectively. Chapter 8 summarizes the results of the whole thesis comprehensively. Detailed information on the TIPTIMON stations can be found in the appendix A.1. Appendix A.2 contains technical details regarding timing corrections I applied to recordings of three TIPTIMON stations that temporarily lost their GPS antenna. Supplementary material, which is associated to the results presented in the Chapters 4-7, is included in the Appendices B-E.

The focal mechanisms and the local earthquake catalog of the TIPAGE time period, which were further processed in this study, were initially created by C. Sippl (Sippl et al., 2013a,b; Sippl, 2013). E. Brzoska and B. Schurr derived parts of the phase picks of the local TIPTIMON data. The GEOFON picks at the global stations used in Chapter 7 were reviewed by J. Saul. The finite fault model also shown in Chapter 7 was calculated by Y. Zhang and R. Wang. All other data analysis presented here was undertaken by myself.

2 Tectonic context

The Pamir-Hindu Kush mountains form the westernmost part of the Cenozoic India-Asia collision system, according to van Hinsbergen et al. (2011a), the largest deformed region in the world, as it includes the Himalaya and Tibet east of my study region as well as the Tian Shan and even Mongolia and southern Siberia further to the north. The following chapter will outline the tectonic context in which this giant collision takes place. The first part focuses on the tectonic history of Central Asia as a whole (Section 2.1) while the subsequent Section 2.2 discusses the regional tectonics. In Section 2.3, different concepts to explain the peculiar seismotectonic characteristics of Pamir and Hindu Kush are introduced.

2.1 The big picture - Central Asia

2.1.1 Paleozoic and Mesozoic history

Today's Central Asia is part of a multi-segmented collisional system, which marks the southern edge of the Asian continent, from western Europe to southeast Asia. The deforming units comprise a collage of crustal terranes and island arcs, whose accretion can be attributed to three main orogenic events (Fig. 2.1):

1. The Tian Shan and the units further north comprise fragments of Precambrian to Paleozoic micro-continents and arc complexes that were amalgamated with Asia during the closure of different basins of the Paleo-Asian Ocean (Şengör et al., 1993; Windley et al., 2007; Xiao et al., 2010). The relatively rigid Tarim and Tajik blocks south of the Tian Shan, which amalgamated to Asia in the late Paleozoic (Han et al., 2011), can also be attributed to these Variscan realms (Yang and Liu, 2002; Siehl, 2015).

2. Tibet, Pamir and Hindu Kush are built of Gondwana derived terranes, which collided in the Paleozoic to Mesozoic against Asia (Cimmerian units in Fig. 2.1; Chang and Zheng, 1973; Allegre et al., 1984; Şengör and Natal'in, 1996; Yin and Nie, 1996; Yin and Harrison, 2000).

3. The units further south are elements of the Himalayan belt, which formed as part of the India-Asia collision.

The formation history of today's Cimmerian and Himalayan realms dates back to the Devonian when the Paleo-Tethys ocean opened and separated the blocks which form today's North and South China, Tarim and Indochina, thus the currently more stable part of Central Asia, from Gondwana (Garzanti et al., 1999; Metcalfe, 2002; Xu et al., 2015). The later opening of the Neo-Tethys ocean in the early Permian then separated Northern Gondwana, which included today's India, from the continental blocks of today's Iran,

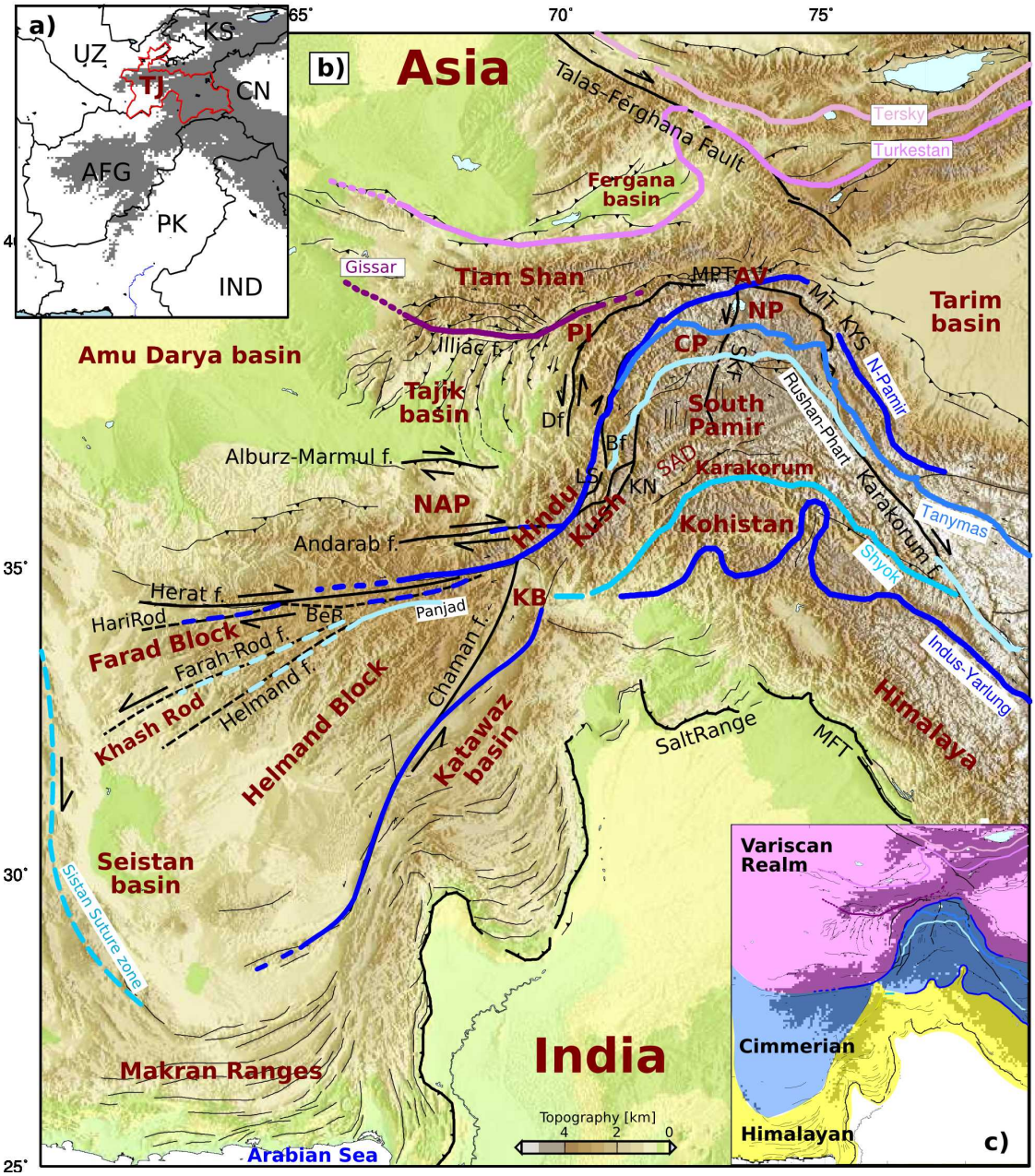

Figure 2.1: Regional setting of the Pamir-Hindu Kush region. See Figure caption on the subsequent page.

Afghanistan, South Tibet, Myanmar and Thailand (Fig. 2.2). Classification of the geological formations of Central Asia today in major tectonic units (Fig. 2.1c) is mainly based on the closure of these oceanic basins: the older Cimmerides formed during the closure of the Paleo-Tethys and the younger Himalayan units formed during the closure of the Neo-Tethys ocean (Şengör et al., 1988; Karagianni et al., 2015).

Figure 2.1: a) Political boundaries: UZ - Uzbekistan; KS - Kyrgyzstan; TJ - Tajikistan (highlighted in red - the central country of this study); CN - China; AFG - Afghanistan; PK - Pakistan; IND - India. Topography higher than 2000 m in gray. **b)** Topographic map, tectonic features and suture zones. Faults in black: Bf - Badakhshan Fault; BeB - Bad-e-Bayan Fault; Df - Darvaz Fault; IF - Illiac Fault; KN - Kapisa-Nuristan Fault; KYS - Kashgar-Yecheng Fault System; LS - Lake-Shiwa Fault; MFT - Main Frontal Thrust; MT - Muji-Tashkorgan Graben System; SAD - Shakhdara-Alichur domes; SKF - Sarez-Karakul Graben System. Other tectonic features: AV - Alai valley; CP - Central Pamir; KB - Kabul block; NP - North Pamir; NAP - North Afghan Platform; PI - Peter I. range. Sutures as bold lines, associated names in white boxes. The northern dark blue suture is the Paleozoic, the southern the Himalayan suture. The lighter blue sutures in between are Cimmerian sutures (lightest blue is the Mesozoic). Pink sutures in the Tian Shan are Paleozoic. Structures in the Pamir, Tian Shan and Tajik basin after Schurr et al. (2014), Schwab et al. (2004) and L. Ratschbacher (pers. comm.). Faults and sutures in Afghanistan after Tapponnier et al. (1981); Boulin (1988); Klootwijk et al. (1992); Burtman and Molnar (1993); Treloar and Izatt (1993); Faryad et al. (2013); Mistiaen et al. (2015); Siehl (2015) and references therein. Faults and sutures are dotted if the outline was taken from a low-resolution map or if differing scenarios were stated by the authors cited above. Thin black faults from Styron et al. (2010). **c)** Simplified overview of tectonic units after Siehl (2015).

These subsequently accreted Central Asian terranes are currently separated by narrow suture zones, where ophiolite complexes outcrop at the surface. Deformation of these tectonic units and reactivation of the old plate boundaries forms the base for Cenozoic tectonics in Central Asia. However, due to the strong deformation and the large displacements recorded on some of the geologic units, there is ongoing discussion how to correlate the different Cimmerian blocks of Tibet, Pamir and Hindu Kush. The Himalayan (Cenozoic) suture to their south can be traced along the entire length of the Indian collision system, from the Makran subduction zone in Pakistan to the Indus-Yarlung suture in India (Figs. 2.1). In the following, I will shortly introduce the geometry and the proposed correlation scenarios of the different fragments north of the Cenozoic suture.

Suture zones south of the Tarim block and north of India, at the longitudinal range of Tibet, are roughly west-east oriented (see Fig. 2.3a). The terranes separated by these sutures are, from north to south: the Kunlun and the Songpan-Ganzi Terrane (separated by the Kunlun Suture), the Qiangtang terrain (with the Jingsha Suture to its north and the Bangong-Nujiang Suture to its south) and the Lhasa Terrane (with the Indus-Yarlung suture to its south) (Yin and Harrison, 2000; Zhang et al., 2011). With the exception of the Songpan-Ganzi terrane, which is a flysch complex, all these terranes have a Gondwana origin and collided against Asia between the Permian and the Jurassic. At the transition from Tibet to the Pamir, these suture zones are bent and displaced northward. As in Tibet, the accreted units in the Pamir become younger towards the south. They form the North Pamir block (bounded by the Main Pamir Thrust and the North Pamir suture in the north and the Tanymas suture in the south), the Central Pamir (with the Rushan Pshart zone to its south), the Southern Pamir (with the Shyok Suture to its south) and the Kohistan-Ladakh arc (with the Indus-Yarlung Suture to its south) (Burtman and Molnar, 1993).

Due to structural similarities, it has been inferred that terranes of Tibet and Pamir formed a continuity before being displaced and deformed during India-Asia collision (Molnar and Tapponnier, 1975). However, the correlation of the individual terranes is not straight forward, resulting in competing schools of thought on how to correlate the Pamir to the Tibetan sutures. In one model, the north Pamir correlates to the Songpan-Ganzi terrane (Fig. 2.3a; Schwab et al., 2004; Lacassin et al., 2004), in another to the Kunlun terrane (Fig. 2.3b; Burtman and Molnar, 1993; Searle, 1996; Yin and Harrison, 2000). In the first scenario the Kohistan-Ladakh arc would not correlate to any unit in Tibet. Instead, it was proposed to form a magmatic arc complex of limited longitudinal extent (Petterson, 2010). Robinson et al. (2012) suggested a third correlation scenario in which the Central Pamir remains without counterpart in Tibet and therefore agrees with the first model for the two northernmost terranes but with the second model for the two southernmost terranes (Fig. 2.3c). Thus, although the correlation of the different unit in Tibet and Pamir is debated, all scenarios imply a northward offset of the Pamir relative to Tibet. Burtman and Molnar (1993), for instance, suggested ∼300 km.
In Afghanistan, at the westernmost section of the Himalayan orogenic belt, the suture zones bend back to the south. As in the Pamir-Tibet segment, the correlation of suture zones between the Pamir and Afghanistan is unclear. In fact, even the exact location of the sutures is uncertain. The west-east striking Paleozoic suture (the continuation of the North Pamir suture) crops out in the vicinity of the Herat Fault (see Fig. 2.1b for different outlines suggested by Tapponnier et al., 1981; Boulin, 1981; Burtman and Molnar, 1993; Faryad et al., 2013; Mistiaen et al., 2015; Siehl, 2015). The Cimmerian units in central Afghanistan again include a complex framework of blocks, mainly attributed to two collisional events. During a first pre-Early-Cretaceous collisional event, the Farad block collided against the Tajik block. In a second event, the Helmand block collided against the Farad block, forming the pre-Mid-Cretaceous Panjad suture (Krumsiek, 1976;

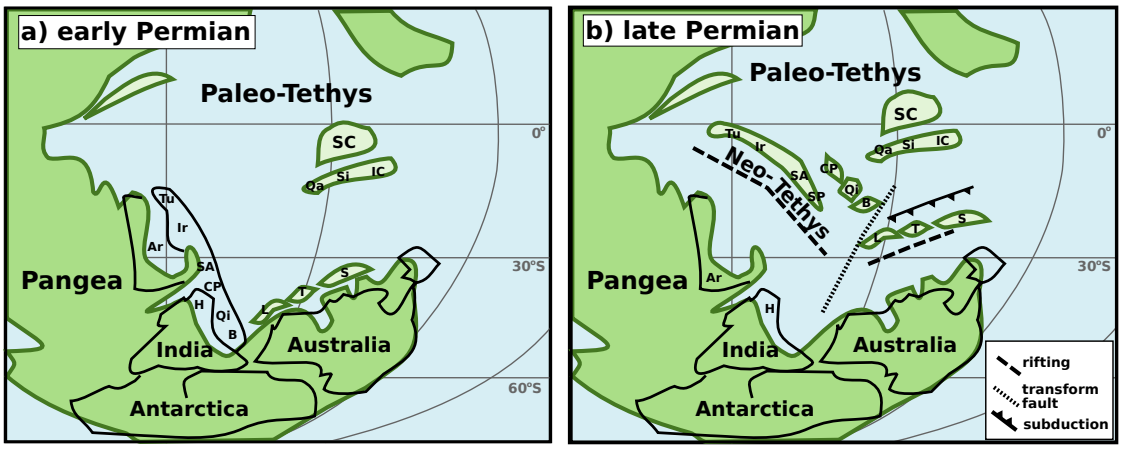

Figure 2.2: Schematic paleogeographic reconstruction of northern Peri-Gondwana (green) and Paleo-Tethys, focusing on the crustal blocks in Tibet (simplified after Metcalfe, 2002; Xu et al., 2015). **a)** Samarian **b)** Changhsingian. Tectonic blocks: Ar - Arabia; B - Baoshan; CP - Central Pamir; IC - Indochina; Ir - Iran; H - Himalaya; L - Lhasa; Qa - Qamdo; Qi - Qiangtang; SB - Sibumasu; SC - South China; Si - Simao; SP - South Pamir; T - Tengchong; Tu - Turkey.

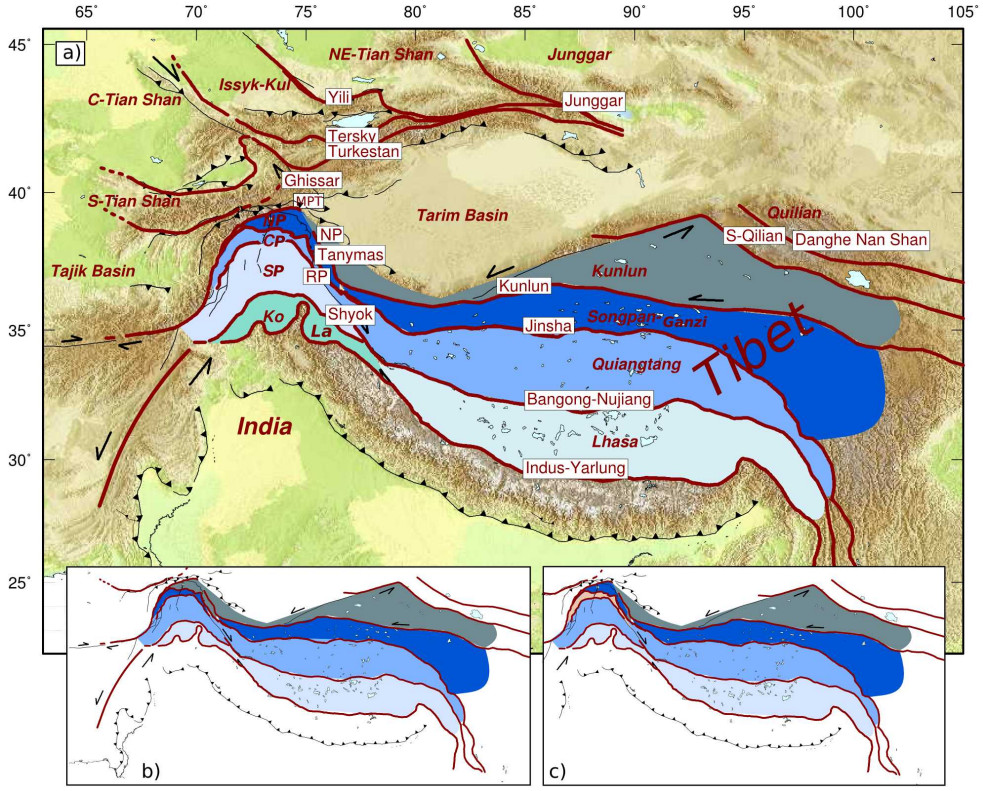

Figure 2.3: Suture zones and terrane names of Tibet, the Pamir and Tian Shan together with three suggested correlations. **a)** Correlation after Schwab et al. (2004); Lacassin et al. (2004). SP - South Pamir block; Ko - Kohistan arc; La - Ladakh arc; RP - Rushan-Pshart suture. Faults and Sutures in Tibet simplified after Styron et al. (2010). All other features and abbreviations as in Fig. 2.1. **b)** After Burtman and Molnar (1993); Searle (1996); Yin and Harrison (2000); **c)** After Robinson et al. (2012).

Şengör, 1984; Boulin, 1991). The Farad block in the north might roughly correspond to the North Pamir (Burtman and Molnar, 1993). The Panjad suture might represent the Mesozoic suture zone, corresponding to the Rushan-Pshart zone in the Pamir (Burtman and Molnar, 1993; Treloar and Izatt, 1993). It is, however, unclear if the Panjad suture follows the outline of the Farah Rod or the Helmand faults in central Afghanistan (Faryad et al., 2013; Burtman and Molnar, 1993).

2.1.2 (Greater) India and onset of collision

During the Paleozoic, India together with Madagascar, East Antarctica and Australia formed the East Gondwana Subcontinent (Fig. 2.2) and drifted northward after its break-off ∼125 Ma ago (Gaina et al., 2007). The velocity of the northward migration varied with time and reached its maximum speed of 18-20 cm/yr in the late Mesozoic (Kumar et al., 2007; Copley et al., 2010). Hypotheses aiming to explain this acceleration suggest that India's lithospheric root might have been removed during its movement on top of the Deccan plume (Müller, 2007; van Hinsbergen et al., 2011b). Such a scenario is supported by India's currently relatively thin mantle lithosphere of 100 km in combination with geo-

logical units which suggest the existence of a thick lithosphere before Gondwana break-off (Kumar et al., 2007).

The collision of India with Asia (the continental fragments are described in the above paragraph 2.1.1) marked a major reorganization in the tectonics of Central Asia. Nevertheless, the onset of this collision is still debated. Estimates range from 34 Ma (Aitchison et al., 2007) to 65 Ma (Cai et al., 2011). The variable dates might partly be attributed to the fact that different authors assign to the term *collision* various meanings. For example, several estimates are deduced from findings in geological records, such as the exhumation of ultra-high pressure rocks, the onset of continent derived sedimentation or the termination of the deposition of marine facies (Leech et al., 2005; Aitchison et al., 2007). Other estimates are based on paleontological constraints (Jaeger et al., 1989). Further, India probably collided first against Asia at the longitudinal range of the Kohistan-Ladakh arc. Regarding the Kohistan-Ladakh arc itself, there is ongoing debate whether it accreted to Asia only shortly before India-Asia collision (Klootwijk et al., 1992; Petterson, 2010) or if it collided first with India (Khan et al., 2009).
One strong indicator for the onset of collision is the decrease of Indian convergence velocity relative to Asia from roughly 11-12 cm/yr before the collision to 3.4 cm/yr at today's western and 4.4 cm/yr at today's eastern Indian syntaxes (Molnar and Stock, 2009; DeMets et al., 2010). The slowdown might mark the point where all Neo-Tethyan oceanic crust had been consumed and the entrainment of more buoyant continental material hindered the ongoing subduction process. However, other interpretations for the decrease of convergence velocity suggest a weak intra-oceanic arc collision prior to a subsequent hard collision between India and Asia (Aitchison et al., 2007; van Hinsbergen et al., 2012).

Despite the different concepts, estimates for the onset of India-Asia collision converge to ∼50-55 Ma (van Hinsbergen et al., 2011a). However, this collision age bears another problem: plate circuits show that the northern edge of India was still much further south than its present position at 55-50 Ma (Patriat and Achache, 1984; Molnar and Tapponnier, 1975; Molnar and Stock, 2009; van Hinsbergen et al., 2011b). Consequently, a large amount of shortening must have taken place since the closure of the Neo-Tethys ocean (e.g. approx. 2400 km convergence for western and 3200 km for eastern Tibet as suggested in van Hinsbergen et al., 2011a). Geologic reconstructions yield not enough shortening in the Himalaya, Tibet and the Central Asian units further north, suggesting that convergence could not be accommodated by purely internal shortening and crustal thickening. A possibility to explain the discrepancy between estimated shortening and the paleo-position of India at the onset of collision was the concept of *Greater India*, which had been first brought forward by Argand (1924), even before the theory of plate tectonics had been established. In today's understanding, Greater India is the landmass of the Indian subcontinent prior to its collision with Asia, which presumably extended further north than the currently visible part of India. The northern part of Greater India might have been composed of thinned continental material, which would have allowed subduction without significant accretion of the upper crust. Whereas this Greater India concept is generally well established, estimates for the size of the Greater Indian landmass differ (see Ali and Aitchison, 2005, and references therein). While Ali and Aitchison (2005), for example, conclude that Greater India must have been relatively small to fit between its neighboring

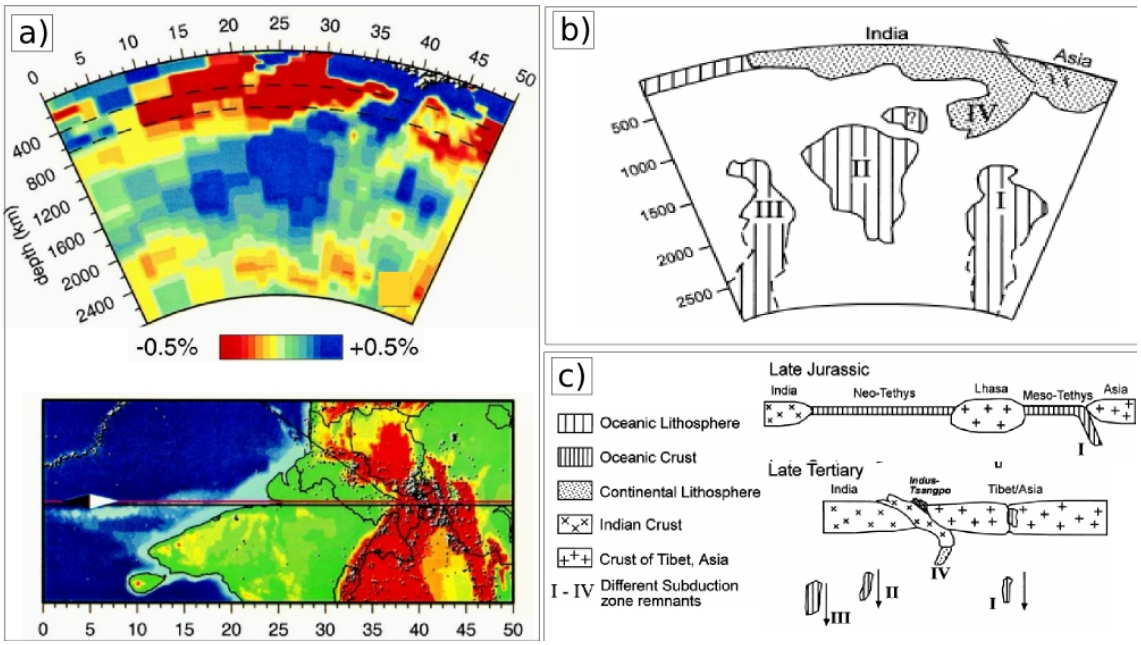

Figure 2.4: Tomographic results and simplified cartoons depicting the accretion of blocks in Tibet/Pamir (Van der Voo et al., 1999). **a)** P-wave velocity anomaly relative to ak135 (Kennett et al., 1995). **b/c)** Interpretation of the resolved high velocity anomalies (I-IV, also from other cross sections) and suggested evolution of Tethyan subduction zones.

Gondwana blocks before rifting apart, van Hinsbergen et al. (2012) postulate an intra-Indian rifting event after Gondwana break-off to overcome this problem.

2.1.3 India-Asia collision and Cenozoic deformation

Convergence since the onset of the collision had been accommodated by different mechanisms causing near- and far-field deformation in Central Asia, such as crustal thickening and associated intra-continental thrusting (Gansser, 1964; Yin et al., 1994; Hodges, 2000; DeCelles et al., 2002; Guillot et al., 2003). Strike-slip dominated mountain belts were created as far north as Mongolia and southern Siberia (Molnar and Tapponnier, 1975; Cunningham, 2005; Yin and Harrison, 2000; Arzhannikova et al., 2011). Prominent strike-slip faults also developed at the syntaxes of the collision system and promoted the lateral escape of the accreted units to the east (Yin et al., 1994; Yin and Harrison, 2000; Yin, 2010) and to the west (Molnar and Tapponnier, 1975; Tapponnier et al., 1982; Replumaz and Tapponnier, 2003). The formation of the Himalayan fold-and-thrust belt, which is composed of rocks, scraped-off from the Indian plate, was directly associated with the lithospheric scale underthrusting of India under Asia. This underthrust plate can currently be imaged with geophysical methods, reaching up to 400 km further north than the current plate boundary at the surface (Li et al., 2008; Kind and Yuan, 2010).
Due to high velocity anomalies (HVAs), which were imaged by global tomography in the mantle beneath India, south of the current Himalaya, and beneath Asia (Van der Hilst et al., 1997; Bijwaard et al., 1998; Villaseñor et al., 2003; Van der Voo et al., 1999) in com-

bination with distinct magmatic events in Tibet (Guillot et al., 2003; Kohn and Parkinson, 2002), multiple occurrences of slab break-off have been proposed. The tomographically imaged high velocity anomalies were interpreted as cold (thus high velocity in tomography; Sobolev et al., 1997), detached slabs. The timing of detachment was reconstructed from their current position in the mantle in combination with the past plate motion of India (Van der Voo et al., 1999) as well as by the Himalayan/Tibetan geological record. These break-off events controlled the type and extent of active deformation in the region. Replumaz et al. (2014), for instance, proposed that Indian slab break-offs generated localized stress pulses in the Asian continent, which, in turn, triggered the activity of prominent strike-slip faults.

Figure 2.4 shows the often cited sequence of break-off events according to Van der Voo et al. (1999), who imaged four prominent high velocity anomalies in the mantle (Fig. 2.4a). Based on this and subsequent work, a tectonic scenario since India-Asia collision could have developed as follows (Fig. 2.4b, c): A first break-off event happened presumably in the early stage of the collision (e.g. Negredo et al., 2007, suggest 45-35 Ma based on modeling and reconstructions) which removed the oceanic slab and the early subducted continental unit. The first break-off event seems to have occurred along the entire Indian margin, which was inferred from a continuous west-east striking HVA, underlying India along its complete longitudinal range (Replumaz et al., 2004), but also from magmatism and metamorphic events, recorded in the Pamir's and Tibet's crust (Kohn and Parkinson, 2002; Stearns et al., 2013; Smit et al., 2014; Stearns et al., 2015). Smit et al. (2014), for instance, related Cenozoic metamorphic rocks from the Pamir to metamorphism having followed this first break-off event. The break-off age of 45-35 Ma is also in good agreement with K-rich magmatism observed in southeastern Tibet in the Late Eocene (Kohn and Parkinson, 2002).
Based on little recorded subsidence in India's foreland basin, which can be explained by a small relief at this time, Guillot et al. (2003) suggested that the first break-off might have been followed by a period of low angle subduction. A second break-off could have happened at ∼23-25 Ma as documented by a pulse of volcanism around this time, e.g. mantle derived magmatic rocks in the Karakorum (Mahéo et al., 2009). Further, this age coincides with the onset of exhumation of the Pamir gneiss domes (Schmidt et al., 2011; Stübner et al., 2013b). This second break-off event was associated with a major change of the deformation pattern in the collision system. The deformation before the break-off was mostly focused in Tibet and in the Pamir, but subsequently moved to the north of the Tarim and Tajik basins (Hendrix et al., 1994; Yin, 2010; van Hinsbergen et al., 2011a). Further, Tibet underwent a counterclockwise rotation as testified in the paleomagnetic records (Klootwijk et al., 1992) and the cusp-like geometry of the HVA associated to this break-off (Van der Voo et al., 1999). The second break-off might not have been complete. Instead, a pinpointing of the whole mountain range at the longitudinal range of the Hindu Kush was proposed (Van der Voo, 2005; Van der Voo et al., 1999).

In addition to the underthrusting of India, underthrusting or subduction of the Asian lithosphere beneath Tibet has been proposed as a further mechanism to accommodate India's convergence (Tapponnier et al., 2001; Kind and Yuan, 2010; Replumaz et al., 2014). Lastly, deformation in Central Asia might have been affected by the Asia-Arabia collision

around 25 Ma (Yin, 2010; Hatzfeld and Molnar, 2010). A possible indicator for this influence are the northwest-striking right-slip transpressional fault zones, present within the entire Central Asian region (e.g. the Talas-Fergana Fault; Fig. 2.1).

2.2 Zooming into Tajikistan and its surroundings

On a close up map centered around Tajikistan (Fig. 2.1), the Pamir-Hindu Kush, the Tajik-Tarim basins and the Tian Shan to their north form a complex, highly deformed but well-interwoven unit. Each of these bodies records different Cenozoic deformation. In the following, I will describe their tectonic and geological context.

2.2.1 Pamir and surrounding

The Pamir forms a convex orogen on the Asian side of the India-Asia collision system (see Fig. 2.1 for the tectonic features described in the following). Compared to the Tibetan plateau further to the east, the Pamir accommodated much more Cenozoic crustal shortening within a smaller north-south distance (Schmidt et al., 2011; van Hinsbergen et al., 2011a). Pamir's geometry is asymmetric at its sides. It is bounded by the dextral Karakorum Fault and the dextral Kashgar-Yecheng Fault System to the east, the Main Pamir Thrust to the north and the sinistral Darvaz Fault to the west. Pamir's interior can be subdivided along the Sarez-Karakul Graben System into the western part, characterized by deep valleys and high mountains and the plateau like eastern part.

Lithology: Pamir's lithology is primarily controlled by the north-south juvenating sequence of accreted Gondwana blocks (see Section 2.1): south of the Paleozoic North Pamir suture, the **North Pamir** mainly consists of Carboniferous igneous and sedimentary rocks, deposited in an oceanic environment (Pashkov and Budanov, 1988; Leven, 1981). The marine sequence is overlain by upper Carboniferous conglomerates and limestones (Pospelov, 1987) and was interpreted to result from an active continental margin with a southward-dipping subduction zone. Andesitic rocks in the southern part of the North Pamir formed an island arc or an intra-continental rift. The **Central Pamir** mainly consists of shallow marine sediments, i.e. carbonate sediments deposited in shallow water in late Paleozoic to Jurassic time. No evidence for volcanic rocks could be found. Thus, it is believed to be a former continental margin or platform, which collided in the Jurassic against Asia (Burtman and Molnar, 1993). The **Rushan-Pshart** zone features regions where ophiolite and limestone crop out, which were associated to the closure of a small ocean basin in the late Jurassic or early Cretaceous (Shvolman, 1978). This marine sequence was then covered by Cretaceous redbeds. South of the Rushan-Pshart zone, the **South Pamir** is lithologically divided into its western and eastern parts. Carboniferous to Permian sand- and siltstones dominate in the west (Pashkov and Budanov, 1990), whereas the eastern part of the South Pamir consists mainly of Precambrian metamorphites. The South Pamir is separated by the Shyok suture from the **Kohistan-Ladakh** arc, which features a basement consisting of strongly sheared volcanic rocks, very different to average continental crust (Klootwijk et al., 1992).

Northward offset of the Pamir: Due to similarities in the basement rocks of the western and southwestern Tian Shan and the eastern Tian Shan and Tarim basin, it was inferred that the current Tajik and western Tarim basins formed one unit during the Paleozoic and Mesozoic (the Tajik-Yarkand basin). Prior to the onset of India-Asia collision, this Tajik-Yarkand basin occupied the current location of the Pamir (Burtman and Molnar, 1993). During India-Asia collision, the Pamir then penetrated northward into the Asian plate, overriding the Tajik-Yarkand basin and scraping off its Late Cretaceous and Paleogene marine sedimentary cover (Burtman and Molnar, 1993; Sobel et al., 2013). At present, the Pamir orogen has penetrated several hundreds of kilometers into the Asian interior (e.g. Burtman and Molnar, 1993, infer 300 km), which was postulated from the offset of the corresponding suture zones, the sedimentary record in the Tajik basin and paleomagnetic measurements (Bazhenov and Burtman, 1990; Burtman and Molnar, 1993). Today, the Alai valley represents the only remnant of the Tajik-Yarkand basin north of the Pamir. The onset of the northward offset of the Pamir, however, is debated. Deformation along the North Pamir Main thrust system initiated at ∼25-16 Ma (Sobel and Dumitru, 1997; Coutand et al., 2002) but intensified later as indicated by the activity of the strike-slip faults and transfer systems surrounding the Pamir (e.g. between ∼12-5 Ma; Cao et al., 2013; Sobel et al., 2011; Thompson et al., 2015), the sedimentary record of the Tajik basin (e.g. the onset of inversion at $\leq$13 Ma) and the onset of the reactivation of the southwestern Tian Shan (Avouac et al., 1993; Käßner et al., 2016).
The northward penetration of the Pamir was accompanied by thickening of the Pamir's crust, resulting in a current average thickness of ∼65-75 km with a maximum of more than 85 km in the southwestern Pamir (Chen and Molnar, 1981; Holt and Wallace, 1990; Schneider, 2014). At mantle depths, the northward indentation is further supposed to be accompanied by the delamination of Asian lithosphere beneath the Pamir (Burtman and Molnar, 1993; Schneider et al., 2013; Sippl et al., 2013a). The ∼300 km of Pamir offset could correlate with the ∼300 km deep reaching earthquake zone (Billington et al., 1977; Pegler and Das, 1998; Sippl et al., 2013b; Bai and Zhang, 2015).

Cenozoic and active deformation: Currently, deformation at the edges of the Pamir is accommodated asymmetrically between its western and eastern flank. Whereas GPS vectors bend westward, towards the Tajik basin, at the Pamir's western flank, vectors in the east diverge between Pamir and Tarim basin. Thus, the whole Pamir block undergoes an overall anticlockwise rotation. Extension in the east was accommodated by normal faulting along the Karakul Rift and dextral strike-slip along the eastern bounding faults, which are the Karakorum Fault and the Kashgar-Yecheng Fault System. Whereas the **Kashgar-Yecheng Fault System** connects to the northern Pamir, the **Karakorum Fault** transfers right-lateral slip into the South and Central Pamir, where it is distributed in different splay systems (Strecker et al., 1995; Searle, 1996; Cowgill, 2010; Schurr et al., 2014). The Karakorum Fault terminates in the Muji-Tashkorgan Graben System where active normal faulting accommodates east-west extension. Thus, not necessarily the Karakorum Fault but the Kashgar-Yecheng System must have accommodated a large amount of the northward offset of the Pamir. Currently, there is negligible northward movement of the Pamir relative to Tarim as measured by GPS, suggesting that the Kashgar-Yecheng Fault System is inactive (Zubovich et al., 2010; Sobel et al., 2011), which could be explained by the migration of the north-south deformation into the Tian Shan

at ∼10-12 Ma (Sobel et al., 2011; Abdrakhmatov et al., 1996). The current slip rate on the Karakorum Fault further to the south is debated. Robinson et al. (2015) claim it to be inactive based on field observations and geochronologic data.
The sinistral transpressive **Darvaz Fault** separates the Pamir from the Tajik basin. It bends around the Pamir in the north, approaches the Peter I. range in the triangle between Pamir, Tajik basin and Tian Shan and ultimately connects into the Pamir thrust system on the Alai valley. Its termination to the south is unclear. The Darvaz Fault must accommodate the northward offset of the Pamir, but displacement rates along the fault are relatively badly constrained. GPS measurements show a gradual anticlockwise rotation of velocity vectors from a NW-SE orientation in the western Pamir to a west-east orientation in the Tajik basin. The shear between Pamir and basin measured by GPS is on the order of ∼10 mm/yr (Ischuk et al., 2013), but due to the large distance of the GPS points, it is not possible to deduce where exactly deformation locates. Older publications estimated a left-lateral slip of ∼10-15 mm/yr for the Darvaz Fault from offset features (Kuchai and Trifonov, 1977; Trifonov, 1978). Additionally to shear displacement, the Darvaz Fault might also feature a component of thrusting (Thomas et al., 1994). To the Pamir's north, GPS-velocity vectors decrease at the **Main Pamir Thrust** by as much as 10-15 mm/yr (Reigber et al., 2001; Mohadjer et al., 2010; Zubovich et al., 2010).
In Pamir's interior, one of the most striking features are the prominent **Cenozoic crystalline domes**, which occupy almost a third of the Pamir's surface exposure (Stübner et al., 2013b). This widespread exhumation stands in contrast to Tibet, and must arise from the India-Asia convergence being absorbed over a narrower north-south distance than in Tibet (Schmidt et al., 2011). Whereas a discontinuous band of domes follows the convex outline of the Central Pamir, the Alichur and Shakhdara domes in Pamir's southwest are clearly the largest features. Exhumation of the latter occurred from ∼30-40 km depth between 20-2 Ma (Schmidt et al., 2011; Stübner et al., 2013b). It was suggested to occur in response to the rollback of the Asian lithosphere beneath the Pamir (Stearns et al., 2015). Interestingly, Shakhdara and Alichur domes exhibited north-south extension rates of up to 1 cm/yr, while the Pamir itself underwent bulk north-south shortening (Schmidt et al., 2011).

Crustal deformation in the Pamir and surroundings is accompanied by intense seismicity. Seismicity seems to be most frequent at the Pamir's northern rim, especially along the Alai valley (Schurr et al., 2014; Sippl et al., 2014) and in the Peter I. range, where Pamir, Tajik basin and Tian Shan collide (Hamburger et al., 1992; Lukk et al., 1995). The Peter I. range, for instance, featured the M_w 7.6 Khait earthquake in 1949 (Kulikova, 2016), one of the biggest instrumentally recorded crustal earthquakes in the Pamir region (see Chapter 6 for more detail). The Pamir's interior is seismically divided along the Sarez-Karakul Graben System into the western, seismically active and eastern seismically relatively quiet part. The central Pamir also features large earthquakes, like the M_w 7.3 Lake Sarez earthquake in 1911 (Kulikova et al., 2016) or the most recent M_w 7.2 earthquake in December 2015 (GEOFON, 2016). Based on these seismotectonic characteristics, Schurr et al. (2014) suggest that deformation in the Pamir is partitioned between its eastern and western part. Northward movement of India along the Chaman Fault might connect with the intra-Pamir sinistral Sarez-Karakul Graben System.

2.2.2 Hindu Kush and Afghanistan

The Hindu Kush is located southwest of the Pamir orogen, south of the Tajik-Afghan basin and north of the Kabul block. It contains the Paleozoic suture zone in its center, but extends only along the northeastern part of Afghanistan's Cimmerian belt (see Fig. 2.1). The Afghan assembly, in turn, is restricted in the west by the Sistan suture zone and in the east by the Chaman Fault. As the Pamir, Afghanistan's crustal blocks were displaced by Cenozoic faults (Şengör, 1984; Boulin, 1988, 1991; Treloar and Izatt, 1993). In contrast to the Pamir, most of the thickening and metamorphism in Afghanistan happened in the Jurassic to early Cretaceous (Hildebrand et al., 2001, 2000). Thus, the Hindu Kush existed as a subduction-type orogen already before the India-Asia collision (Tapponnier et al., 1981; Boulin, 1988; Treloar and Izatt, 1993).

Lithology and Geology: Afghanistan can be separated into three main units based on the three major orogenic events in its tectonic history (Fig. 2.1c). Figure 2.5 shows a simplified geologic cross section from Tapponnier et al. (1981), cross-cutting these units:

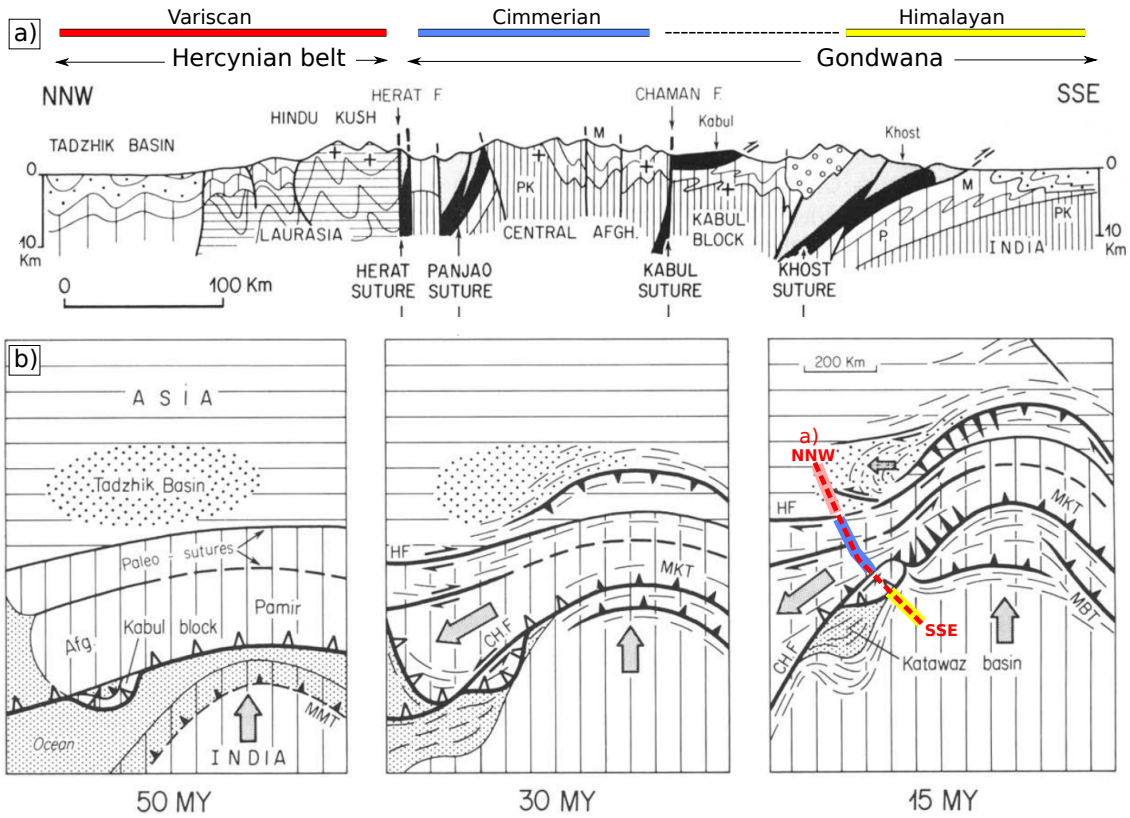

Figure 2.5: Afghanistan's geology and formation history from Tapponnier et al. (1981). **a)** Simplified cross section of eastern Afghanistan (approximate position is indicated in the 15 Ma map of Sub-figure b. **b)** Indentation of Cenozoic Asia by the Pamir wedge. Thin lines indicate the strike of folds. Open triangles correspond to subduction of ocean floor; solid triangles to intra-continental over-thrusts.

The **North Afghan Platform** occupies the domain north of the Paleozoic suture (in Tapponnier et al., 1981, the Herat Fault) and south of the dextral-reverse Alburz-Marmul Fault. The North Afghan Platform is part of the Tajik block and formed the active southern margin of the Asian plate during the Cimmerian orogeny, resulting in the intrusion of Triassic granitoids into the platform's basement. After closure of the Tethys, the North Afghan Platform experienced only little deformation during the Tertiary. A Jurassic clastic sequence was deposited which passes upwards to Cretaceous carbonate platform sediments (Shareq, 1981; Boulin, 1988; Brookfield and Hashmat, 2001). The various **Gondwana fragments** (Cimmerian units in Fig. 2.1) in central Afghanistan form several paleogeographic and structural domains, separated by complex fault systems. Subsequent to the Cimmerian orogeny, the accreted units were overlain by an extensive sedimentary sequence. This package of Cimmeride basement and Mesozoic and younger sediments was then deformed during India-Asia collision (Tapponnier et al., 1981; Şengör, 1984; Girardeau et al., 1989). The region east of the Chaman Fault consists of **Indian affinity rocks**. Here, several tectonic units have over-thrust south of the margin of the Indian shield. In particular, two major ophiolite complexes can be separated: (1) The Kabul and Khost ophiolites to the northeast surround the Kabul block, which, in turn, probably originated as an isolated continental fragment. (2) The Katawaz Basin to the southeast formed at the western margin of the Indian plate. It was suggested to have formed either at the transition between thinned continental crust and oceanic crust (Treloar and Izatt, 1993) or as a transitional basin (Robinson et al., 2000). An up to eight kilometers thick sequence of silicic clastic sediments was later deposited and is exposed now in the strongly subsiding basin (Siehl, 2015).

Cenozoic and active deformation: In contrast to the Pamir, where Indian indentation caused the northward offset of the entire orogen, Cenozoic tectonics in Afghanistan were affected by the obliquity of deformation. India-Asia collision resulted in the formation of strike-slip faults, as the Afghan Cimmerian units were not restricted by a landmass to their west (Tapponnier et al., 1981; Burtman and Molnar, 1993, see schematic sketch in Fig. 2.5b). Strike-slip displacement in Afghanistan was proposed to have migrated north from the **Herat** to the **Andarab Fault** at ∼23 Ma together with a counterclockwise rotation of the whole Afghan block (Treloar and Izatt, 1993), possibly as a response to the initiating northward displacement of the Pamir (Şengör, 1984; Boulin, 1988; Treloar and Izatt, 1993). Currently, the Herat Fault is inactive as derived from geological constraints (Tapponnier et al., 1981) and GPS measurements (Mohadjer et al., 2010). Movement on the strike-slip faults was probably stopped due to the collision of the Afghan blocks with the Lut block along the Sistan suture (not prior to ∼30 Ma; Tapponnier et al., 1981).
The formation scenario in Figure 2.5 requires a large amount of slip on the left-lateral **Chaman Fault**, which they estimated to 500-1000 km. This value is in general agreement with values derived from plate reconstructions (DeMets et al., 2010) and GPS measurements (Mohadjer et al., 2010), although the latter might be biased due to sparse sampling. Other authors, however, estimate less total displacement on the Chaman Fault from geological constraints (e.g. 300-500 km; De Lapparent, 1972; Auden, 1974; Prévost, 1980). Lateral escape of the Afghan units, rather than internal deformation is also likely as nearly no post-collisional magmatism occurred in the Hindu Kush. This makes the Hindu Kush significantly different to the Karakorum to the east, which is dominated by post-

collisional metamorphism, melting and deformation (Searle, 1991; Hildebrand et al., 2000).

Currently, the northward push of India and the displacement along the Chaman Fault might be translated via transfer systems into the central Pamir (Schurr et al., 2014). Schurr et al. (2014) suggested that the left-lateral **Lake-Shiwa** and **Kapisa-Nuristan Fault** systems at the transition between Hindu Kush and Pamir could translate into the Chaman Fault, which then separates the Hindu Kush and the rest of Afghanistan from India. Crustal seismicity in Afghanistan is clearly focused in the northeastern part and along the Chaman Fault whereas central Afghanistan is a relatively stable (Boyd et al., 2007; Ambraseys and Bilham, 2003).

2.2.3 Tajik basin and Tian Shan

The Tajik basin is characterized by a thick sedimentary cover, reaching up to ∼10 km thickness in its southern part. The sediment sequence consists of clastic sedimentary rocks and limestones at its base, separated by a layer of Jurassic evaporites from a sequence of dominantly marine Late Triassic to Oligocene pre-orogenic epicontinental sediments, which in turn is overlain by syn- and post-orogenic Neogene to Quaternary continental clastics. Marine units were deposited in the Tajik basin from the Jurassic to the late Eocene, when the basin was part of a branch of the Paratethyan sea (Nikolaev, 2002; Carrapa et al., 2015). The timing of the post-Jurassic sedimentation was primarily controlled by the orogenic event in the Pamir. The first conglomerate deposits shed from the Pamir appear in the Upper Oligocene-Lower Miocene strata of the northwestern Tajik basin. Reduced sediment supply followed, before massive deposition resumed with significant erosion of the North Pamir in the Mid-Late Miocene (Klocke et al., 2015).
At present, the Tajik basin is subject to west-east compression, as testified by arcuate folds in the basin's Neogene strata (Hamburger et al., 1992; Gagala, 2014), GPS measurements (Mohadjer et al., 2010; Zubovich et al., 2010; Ischuk et al., 2013) and the slip-vectors of intra-basin earthquakes (Schurr et al., 2014). This is in contrast to the formerly connected Tarim block, now located east of the Pamir, where GPS vectors indicate no shortening in the sediments (Yang and Liu, 2002). The compression in the Tajik basin was attributed to the westward oriented gravitational collapse of the Pamir (Stübner et al., 2013a; Schurr et al., 2014). This push results in Neogene folding at shallow levels, i.e. thin-skinned shortening of basin sediments above the evaporite decollement (Schurr et al., 2014). The decollement crops out at some location within the Peter I. range at the northeastern termination of the Tajik basin (Hamburger et al., 1992). Ongoing salt tectonics within the basin is evident by the presence of several salt domes (Leith and Simpson, 1986b). The Jurassic decollement might be heterogeneous and partly removed, testified by brittle rupture at the base of the decollement (Schurr et al., 2014).
At the basin's rims, deformation is currently accommodated by the sinistral transpressional Darvaz Fault and the dextral reverse Illiac Fault zone to the east and north of the Tajik basin, respectively. Recent geophysical studies imaged a relatively thick crust of the Tajik basin (35-40 km; Sippl et al., 2013a; Schneider, 2014), which delaminates and rolls back forming a northwestward convex arc beneath the Pamir (see also Chapters 5 and 6 for more details regarding the Tajik basin).

Directly northward of the Tajik basin and the Alai Valley extends the NW-SE trending Tian Shan mountain range, separated by the Tajik basin through the Gissar suture (Allen et al., 1993). As the Hindu Kush, the Tian Shan is an old mountain range, reactivated during the India-Asia collision. In contrast to the Hindu Kush, the Tian Shan does not lie directly at the former active margin, but 1500 km to the north (Tapponnier and Molnar, 1979). The reactivation of the Tian Shan occurred in the Neogene, thus delayed relative to the onset of India-Asia collision (Avouac and Tapponnier, 1993; Sobel et al., 2006). Uplift started probably around 23 Ma (Hendrix et al., 1994; Yin, 2010; van Hinsbergen et al., 2011a) but was accelerated later (∼10-12 Ma; Abdrakhmatov et al., 1996; Sobel et al., 2011). North-south shortening across the Tian Shan is estimated to be ∼200 km (Avouac and Tapponnier, 1993).
The Tian Shan is split by the prominent, but currently inactive NNW-SSE trending dextral Talas-Fergana Fault (Zubovich et al., 2010). The Talas-Fergana Fault lies in continuity of the western rim of the Tarim basin and isolates the Pamir-Hindu Kush system from the regions further to the east. Cenozoic shortening is thought to increase from east to west in the Tian Shan, resulting in a rotation of the whole block relative to Kazakhstan (Avouac and Tapponnier, 1993).

2.3 Intermediate depth seismicity and mantle structure

Despite the northward offset of the Pamir relative to the Hindu Kush and the outskirt position of the latter, probably the most striking feature that sets the Pamir-Hindu Kush apart from its surroundings is the intense intermediate depth seismicity that occurs exclusively beneath these two orogens (Billington et al., 1977; Pegler and Das, 1998; Sippl et al., 2013b; Bai and Zhang, 2015). At first glance, and in map view the seismically active zone appears continuous (Fig. 1.1). However, the Cenozoic tectonic history of the Pamir and Hindu Kush differ (see Section 2.2), which suggests that the lithospheric structure beneath Pamir and Hindu Kush might differ as well. The following section aims to provide a brief overview to the existing concepts.

Observations: The mantle structure beneath Pamir and Hindu Kush was primarily derived from geophysical investigations, which gained increasing precision over the last decades due to more available data and advancement in analysis methods. Figure 2.6 shows two seismic tomography cross sections through Pamir and Hindu Kush from Villaseñor et al. (2003): a northward- to vertically-dipping high velocity anomaly (HVA) is imaged underlying the Hindu Kush. It penetrates the mantle down to 600 km and seems still to be attached to the lithosphere of the Indian plate. At the longitudinal range of the Pamir, a shallower and more diffuse HVA was imaged (see also Mohan and Rai, 1995; Mellors et al., 1995; Van der Voo et al., 1999; Koulakov and Sobolev, 2006; Koulakov, 2011).
Intermediate depth seismicity forms an arc-like structure beneath the Pamir, with a dip shifting from west-east beneath the Tajik basin to purely north-south at the longitude of 73°E. Under the Hindu Kush, the seismic zone dips north, strikes west-east and features earthquakes as deep as 280 km over its whole longitudinal extent (e.g. Sippl et al., 2013b; Bai and Zhang, 2015). The instrumentally recorded largest earthquakes, including

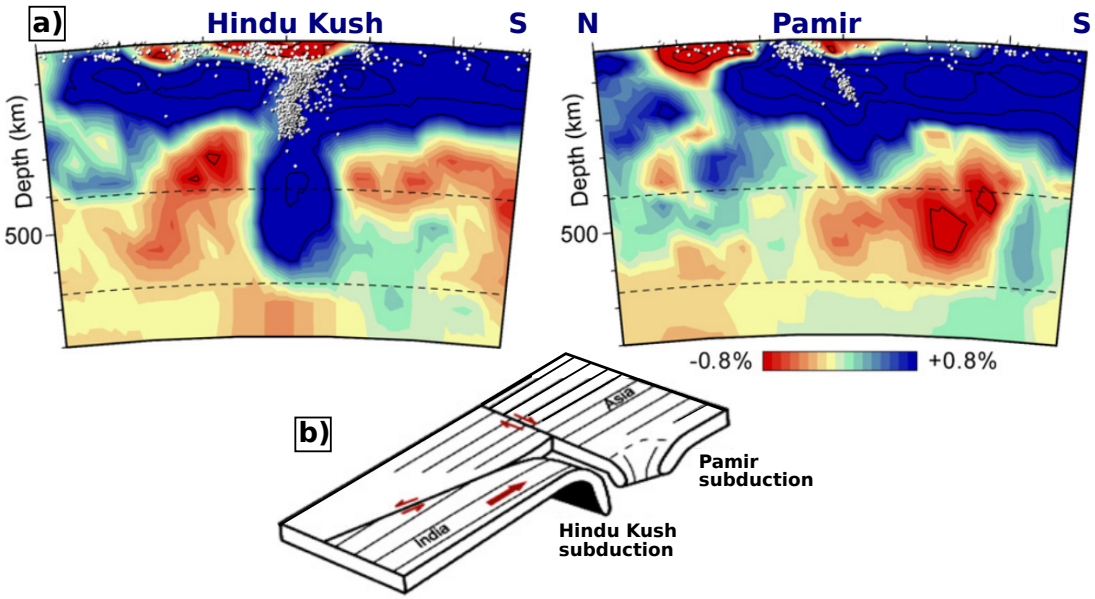

Figure 2.6: a) Vertical cross sections of the global P-wave tomographic model of Villaseñor et al. (2003) through the Hindu Kush and Pamir regions; the contours highlight 1% anomalies. Cross sections are north-south oriented at 70.5°E and 74.5°E for the Pamir and Hindu Kush, respectively. Dots are earthquake hypocenters. **b)** Schematic sketch, showing the geometry of lithospheric plates modified from Mattauer (1986). All figures are taken from Negredo et al. (2007).

the recent M_w 7.5 event (231 km depth, October 2015; USGS, 2016), generally cluster in the deepest portion of the seismogenic region. Local tomography resolved low velocity material below the Hindu Kush and Pamir (Roecker, 1982; Sippl et al., 2013a), possibly coinciding with the zone of earthquakes. In the Pamir, a recent receiver function study (which is more sensitive to abrupt velocity changes than seismic tomography) confirmed that at least the Pamir earthquakes must be located in a 10 km thick dipping low velocity channel descending beneath the Pamir from the Asian side (Schneider et al., 2013).

Tectonic models for the Pamir-Hindu Kush region: Due to the slab-like character of the earthquake zones and the HVA beneath the mountains, there is a universal agreement that the mantle anomalies in the Pamir-Hindu Kush must result from a currently active process of mantle lithosphere removal. Given that Pamir-Hindu Kush are located in a continental setting and no remains of an ocean basin were found in the geological record (Tapponnier et al., 1981; Burtman and Molnar, 1993), it was suspected that upper mantle processes in the Pamir-Hindu Kush must involve the subduction of continental crust to some extent. However, simple density calculations have shown that continental lithosphere with an average thickness of 35 km on its own is too buyout to subduct (McKenzie, 1969; Molnar and Gray, 1979). Thus, other scenarios have been brought forward, including the subduction of thinned crust (e.g. 30 km crust; Cloos, 1993), subduction of parts of the crust (e.g. detachment of the upper and lower crust), and the pulling of the continental

material to depth by an external mechanism (e.g. attached older oceanic lithosphere).

Beneath the Hindu Kush, the configuration of tomographically imaged HVAs and seismicity has been interpreted as slab break-off (Lister et al., 2008; Koulakov and Sobolev, 2006), but also as the drop-like removal of mantle lithosphere (Koulakov, 2011). Due to the northward dip of the seismically active zone in its upper part, the Hindu Kush anomaly has been mostly associated with the subduction of an Indian-derived slab. However, based on tectonic reconstructions, Gaina et al. (2015) proposed the subduction of an Asian-derived continental fragment beneath the Hindu Kush. Thus, neither the exact mechanism of lithosphere removal nor the affinity of the Hindu Kush mantle anomalies is clear yet.

The northward offset and the southward-dipping seismic zone in the Pamir has puzzled researchers even more, especially as finding of crustal xenoliths give evidence for the deep subduction of Asian crust (∼90 km; Gordon et al., 2012). Asian-sided subduction would be against the long established direction of Indian underthrusting/subduction beneath Asia. Thus, no older, earlier subducted lithosphere could force the descent of buoyant crustal material. To overcome this problem, Pegler and Das (1998) and Pavlis and Das (2000) argued for one tilted, Indian derived subduction zone beneath Pamir and Hindu Kush. However, based on the results of the recent TIPAGE deployment (Mechie et al., 2012, see location map of the stations in Fig. 1.2), these models can be excluded, as receiver functions, local tomography and high precision seismicity images (Schneider et al., 2013; Sippl et al., 2013a,b) clearly resolved Asian units, subducting beneath the Pamir. Eclogitization of these crustal fragments, and the associated density increase could provide an additional driving mechanism for deep subduction of continental crust.
Despite the models introduced above, which generally focus on either Pamir and Hindu Kush, different studies aimed to understand the seismotectonic behavior beneath both mountain ranges as a single entity. Negredo et al. (2007), for instance, argued that the shallower seismicity in the Pamir might result from different subduction velocities (Fig. 2.6b shows their working hypothesis regarding lithospheric geometry). Replumaz and Tapponnier (2003) regard the Hindu Kush HVA in the mantle as a remnant of an incomplete break-off at the western edge of the collision system.

To conclude, a great variety of tectonic models exist for the Pamir-Hindu Kush region, which might partly be attributed to the fact that existing data of the last century were sparse and could thus be interpreted in different ways. Some of the older models can probably now be ruled out due to better data available, especially in the Pamir due to the TIPAGE experiment (Mechie et al., 2012). However, Pamir's relation to the deep and shallow structure of the Hindu Kush and the tectonic evolution history of the region as a single entity requires further investigation. In the following chapters I will attempt to answer these questions using primarily data from the TIPTIMON seismic network (Schurr et al., 2012, 2013) as a base for my analysis.

3 Methods and seismological background

In this thesis I use seismological methods as a tool to understand seismotectonic processes in the Pamir and Hindu Kush region. In Figure 3.1, two example seismograms of a local and a teleseismic earthquake recorded by the TIPTIMON stations are shown. These two types of records formed the basis for my work: teleseismic earthquakes occur at epicentral distances greater than 30° relative to the recording stations, local resp. regional earthquakes at distances smaller than ∼13°. Whereas seismic waves from teleseismic earthquakes up to ∼95° epicentral distance have traveled mainly through the relatively homogeneous mantle, regional seismograms are strongly influenced by the shallow crustal structure and crust-mantle interactions (Lay and Wallace, 1995). Thus, both records contain different types of information regarding the subsurface. The following chapter shortly introduces the different methods used here to analyze these local and teleseismic records, as well as the underlying physical concepts. For detailed theoretical background the reader is referred to e.g. Lay and Wallace (1995), Aki and Richards (1980) or Stein and Wysession (2009).

The ground motion u, measured at the seismometers at a given time t, can be expressed as the convolution of effects from the source $s(t)$, the path $g(t)$ and the recording instrument $i(t)$:

$$u(t) = s(t) * g(t) * i(t) \tag{3.1}$$

The response of a seismometer $i(t)$ is a device specific function that is known for each seismometer type and can hence easily be accounted for by deconvolving it off the data. In contrast, if the recorded signal is an earthquake, both the rupture mechanism and the propagation path are unknowns. Seismology uses physical concepts to describe and understand these terms and thus gain valuable information about the structure and dynamics of the earth's interior (Stein and Wysession, 2009). Here, Section 3.2 is concerned with methods to extract source information $s(t)$, Section 3.1 with the propagation path $g(t)$.

Many seismological problems, which will be discussed in the following sections, can be formulated as inverse problems, where the *best* model (e.g. the velocity model which best explains the observed travel times) is derived based on a certain number of observations:

$$y_i = X_j(\vec{x}, \beta_k) + \epsilon_j \tag{3.2}$$

Equation (3.2) states the most general formulation of the inverse problem where the observations y_j are related to the model X_j, which depends on a set of model parameters β_k at the location $\vec{x}$, but also on the errors ϵ_j, which include model and data errors (after Lay and Wallace, 1995; Aki and Richards, 1980). Theoretically, the model parameters can be derived by minimizing the difference between the measurements and the model predictions

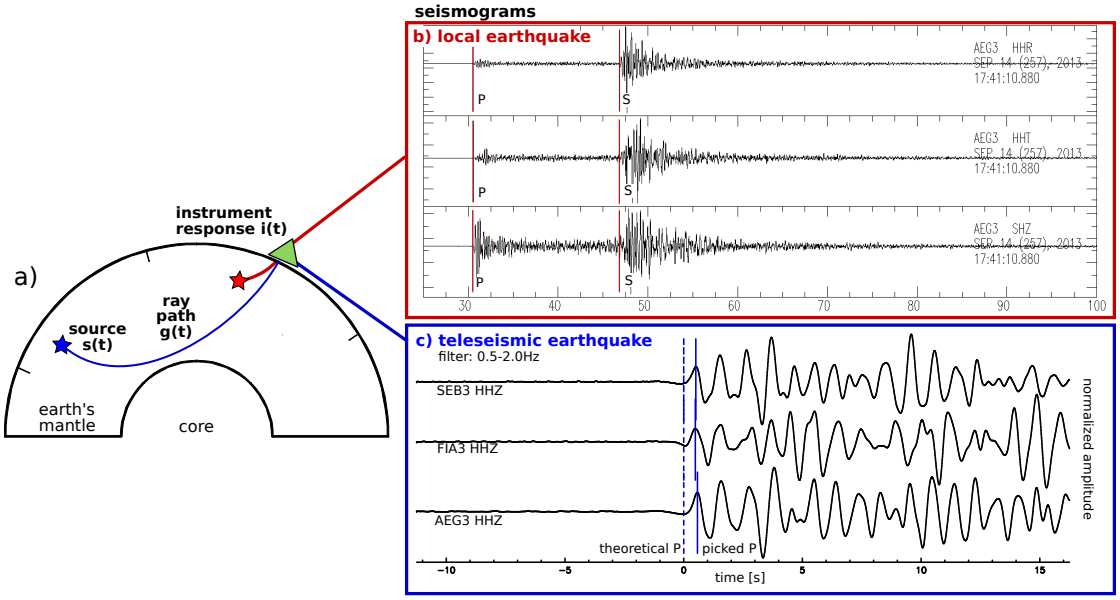

Figure 3.1: a) Cartoon illustrating the contributions influencing the seismic records according to Equation (3.1). **b)** Example of an intermediate depth Hindu Kush earthquake (36.32°N/71.14°E, M_L = 3.0, 109 km depth) registered at one of the TIPTIMON stations in Afghanistan. The horizontal components (radial - HHR, transverse - HHT) are rotated relative to the earthquake; the vertical component HHZ is oriented downward. *P* and *S* are the onsets of P- and S-phase, respectively. These P- and S-travel times were used e.g. for event location and local earthquake tomography (Chapters 5 and 7). **c)** Vertical records of an earthquake used for teleseismic tomography in Chapter 4 that occurred near Sumatra at 2013-07-06 05:05:06. Filtered at low frequencies, the first seconds after the P-phase appear very similar at adjacent stations. Instead of the emergent, and thus more difficult to determine, first onset, the first maximum of the waveforms was picked. Only the travel time residuals between the picked and a theoretical onset were then used for teleseismic tomography.

$$\sum_j M(y_i - X_j(\vec{x}, \beta_k)) \stackrel{!}{=} min. \tag{3.3}$$

where $M()$ is any measure for the goodness of the fit. The methods available to solve Equation (3.3) depend on the character of the model X_j. If X_j is linear and the errors are Gaussian, the result can be gained by least square minimization. By contrast, if the problem is underdetermined (viewer observation than model parameters), like in seismic tomography where certain model nodes might not be crossed by rays (data), the problem can be reformulated, so that it can ultimately be written as

$$\vec{y} = \tilde{G}\vec{\beta} \quad \Leftrightarrow \quad \vec{\beta} = \tilde{G}^{-i}\vec{d} \tag{3.4}$$

where a certain number of observations, which are bundled in the data vector $\vec{y}$, are related to the model vector $\vec{\beta}$ by the operator $\tilde{G}$. The superscript $-i$ stands for the inverse of $\tilde{G}$ (e.g. the regular inverse if $\tilde{G}$ is square or the pseudo-inverse). A formulation as in Equation (3.4) could be obtained by adding additional constraints to the data or by linearizing the problem. In earthquake tomography, for instance, the problem is linearized

by starting from a first guess and only inverting for the residual between predictions and observations. If a problem is formulated as in Equation (3.4), it can then be solved by inverting the matrix $\tilde{G}$. This can be done using e.g. singular value decomposition (SVD), which is a possibility to invert the model matrix by factorization and yields an exact solution. Other methods only approximate the solution, and might be used if the systems of equations become huge. The most commonly used of these approximating solutions is the sparse equations and least squares method (LSQR method; e.g. Paige and Saunders, 1982; Menke, 1984).

3.1 Determination of earth's structure

3.1.1 Seismic tomography

Earthquake tomography uses seismic waves to generate a three dimensional velocity image of the earth's subsurface. Here I performed a teleseismic and a local earthquake tomography, two different types of body-wave travel time tomography. Figure 3.2a illustrates the basic principle of ray based tomography after Aki et al. (1977): the heterogeneous subsurface is separated into several blocks with constant slowness u (slowness=1/velocity) and ray theory is used to calculate the travel time of a specific phase between each station and each earthquake. The total travel time ΔT of a ray i can be calculated by summing up the travel times through the blocks which are crossed by the ray:

$$\Delta T_i = \sum_{j=1}^{J} l_{ij} \Delta u_j \tag{3.5}$$

where J is the total number of model parameters, u_j is the slowness in the model element j and l_{ij} is the length of the path i through the element j. To constrain the slowness u, seismic tomography usually starts from a known model, predicts travel times and uses the difference between observed and predicted travel times to subsequently improve the model. Thus, seismic tomography involves three main steps (Rawlinson and Sambridge, 2003): parametrization of the true earth in a model space (e.g. blocks or nodes), calculating theoretical travel times (ray tracing) and solving the inverse problem.

If the earthquakes are located inside the study region (local tomography), the ray paths, and thus the travel times, depend not only on the slowness of the blocks but also on the position of the earthquakes, which, however, are additional unknown parameters. Thus, local earthquake tomography has to solve iteratively for earthquake locations and velocity model. In contrast, in teleseismic tomography (schematically in Fig. 3.2b), the earthquakes used for the analysis are located outside the study volume in an epicentral distance from 30-90°. The region outside the volume is considered as 'standard earth', whose properties are known. Even if the earthquake locations were not very well constrained, the travel times at the different stations would be offset by a constant value. Such offsets are normally mapped into an additional inversion parameter, the station or event corrections. Consequentially, teleseismic tomography does not have to solve for earthquake locations, but the resulting velocity model features only relative velocities.
Despite these different inversion tasks, the main difference between the two approaches is

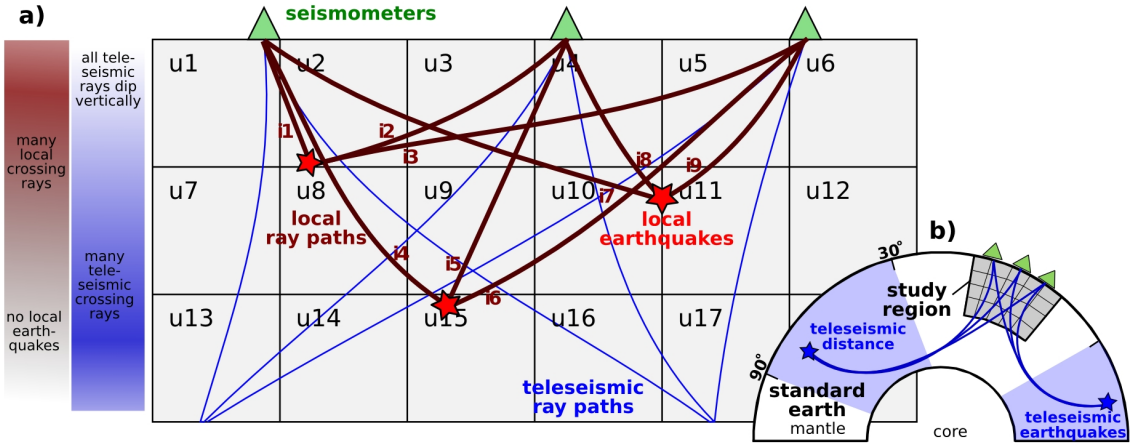

Figure 3.2: Simplified parametrization for ray-based seismic tomography: the subsurface is split into several blocks with a constant slowness u. The observed travel times between earthquakes and seismic stations are used to constrain the slowness of these blocks according to Equation (3.5). **a)** For local earthquake tomography, the study region encompasses the seismic sources. Their locations yield additional inversion parameters. **b)** Teleseismic tomography uses earthquakes from an epicentral distance between ∼30-90° but only inverts the travel time residuals that accumulated inside the study region.

the resolved area: in local tomography the lower resolution limit is defined by the deepest earthquakes. Resolution is usually good in the crust, due to the abundant seismicity. In teleseismic tomography, the deepest resolution limit depends on the aperture of the seismic network, which restricts the maximum depth of crossing rays. The shallow structure can not be resolved at high vertical resolution because all ray paths dip vertically directly beneath each station.

In this thesis I used the *teleLOTOS* code (Koulakov, 2009; Jakovlev, 2009) for the calculation of a teleseismic tomography (Chapter 4), and *simulps* (Thurber, 1983, 1993; Eberhart-Phillips, 1993; Evans et al., 1994) for local earthquake tomography (Chapter 5). In both software packages, theoretical travel times are calculated based on the Fermat principle of travel time minimization. Not the whole wave equation is solved, but the wave front is approximated as a ray (high frequency approximation; e.g. Stein and Wysession, 2009), which allows the application of principles from geometrical optics. Ray paths are calculated by (pseudo-) bending algorithms to determine the minimal value of travel time. In contrast to early tomographic studies, where the subsurface was parametrized in blocks (Aki et al., 1977), modern algorithms prefer to use nodes at a defined location and with a discrete velocity value. The velocities between the nodes are then interpolated. In *teleLOTOS*, the ray paths which were determined from the ray tracer are used directly to derive an inversion grid. The grid nodes are then distributed in the model domain depending on the ray coverage and well resolved areas are covered by a denser network of model nodes. Velocities between the nodes are approximated linearly. In contrast, *simulps* uses a rectangular grid and tri-linear interpolation. Adjacent nodes can be linked to overcome the problem of poorly sampled grid nodes. Thus, the main difference between the *teleLOTOS* and *simulps* approaches for model parametrization and travel time calculation are

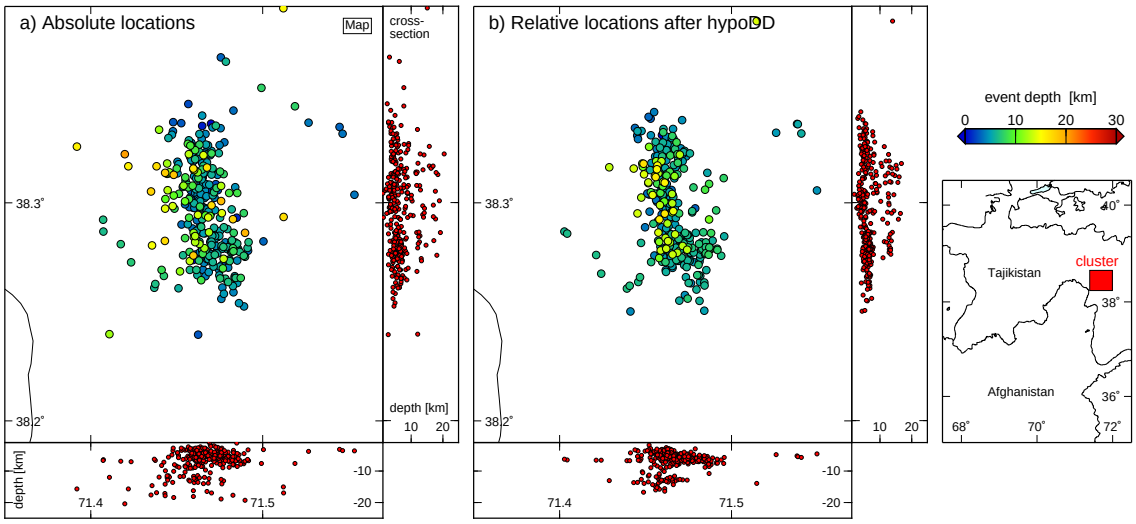

Figure 3.3: Example to demonstrate the effect of double difference relocation. **a)** Absolute locations gained by relocating single events in the 3D velocity model of Chapter 5 (events are color coded by depth in map view and plotted as red circles in the two west-east and north-south striking vertical cross sections). **b)** The same event cluster after double difference relocation in the same velocity model.

that *teleLOTOS* can deal with any parametrization of the velocity perturbation, *simulps* is restricted to the rectangular grid.
Inversion in *teleLOTOS* is performed using an LSQR algorithm (Paige and Saunders, 1982), which yields a numerical, thus not exact, solution for the system of linear equations. *Simulps* directly solves for the inversion matrix, using a parameter separation method to overcome the coupled hypocenter-velocity structure problem (Pavlis and Booker, 1980). This approach allows the calculation of the full resolution matrix, which can then be used e.g. to define a threshold value for resolution (Chapter 5). In *teleLOTOS*, the resolution is usually constrained based on synthetic tests alone (e.g. Koulakov and Sobolev, 2006; Jakovlev, 2009; Bianchi et al., 2013).

3.1.2 Earthquake locations

Like seismic tomography, earthquake location involves the solution of the inverse problem. The data vector is formed by the travel time observations, the unknowns are the hypocenter coordinates and the origin time of the event. Approaches for event location can be subdivided into absolute and relative and further into single-event and multi-event location schemes. Each of these techniques relies on certain assumptions and has its specific (dis)advantages.
Single event absolute locations strongly depend on the velocity model used for travel time calculation and might further be affected by other path-dependent effects, e.g. seismic anisotropy. Most modern programs implement ray-based location schemes, where the location problem is linearized by improving the hypocenter location in increments, starting from a first guess. Depending on the solution approach, the result is either a preferred hypocenter and an uncertainty, calculated based on e.g. Gaussian statistics (Aki

and Richards, 1980) or alternatively, a probability density function (PDF), indicating the likelihood of the location. In multi-event absolute location schemes the dependency of the location on the velocity model is partly overcome as they implement a joint-inversion for all hypocenters.
Relative methods, e.g. double difference (DD) techniques, can be used to obtain high precision relative earthquake hypocenters, which are not contaminated by path-dependent effects or any further model errors. However, to allow a stable inversion, relative locations strongly depend on reliable initial event locations. DD techniques take advantage of the fact that the inter-event distance is small relative to the station-event distance. Thus, instead of solving the inverse problem for the whole travel time path, only the travel time difference of pairs of earthquakes registered at a common station is considered. If different earthquakes occur at small inter-event distances, they can be grouped into event networks (clusters), in which all events are relocated relative to each other. One of the most commonly used programs is *hypoDD(3D)* (Waldhauser and Ellsworth, 2000; Waldhauser, 2001), which minimizes the double difference residuals for pairs of earthquakes at each station by weighted least squares. For inversion either the SVD or the LSQR method can be used.

For the local event locations of the TIPTIMON data I applied a combination of the methods described above, aiming to make use of their different advantages to obtain high precision earthquake locations and reliable errors. Absolute locations were initially derived from the ray-based location program *hypo71* (Lee and Lahr, 1975), which is the location software implemented in the location chain of Sippl et al. (2013b). Single event absolute locations were further refined using the *simulps* relocation routine, which allowed the event relocation in a 1D and 3D velocity model in combination with station corrections. To constrain the absolute location errors, I preferred to rely on the error estimate from the probabilistic location software *NonLinLoc* (Lomax, 2008) instead of *simulps*-derived errors. *NonLinLoc* locations were calculated using the inversion approach of Tarantola and Valette (1982, equal differential time estimate). The *NonLinLoc* errors can be given in terms of a confidence interval of the PDF and thus do not depend on any assumption regarding the error-distribution.
Relative locations were obtained with *hypoDD3D* (Waldhauser and Ellsworth, 2000; Waldhauser, 2001), which allowed me to perform double difference relocation in the same 3D velocity model as used for single event location earlier on. For double difference relocation I used the LSQR method, as some data clusters were huge (e.g. most of the intermediate depth Hindu Kush events form one cluster), but relocated subsets of the event clusters in SVD mode, to derive a reliable error estimate. SVD allows inverting directly for the resolution matrix and thus to obtain a proper least squares error estimate, whereas the LSQR method yields an approximated solution with the effect that no reliable error estimate can be given (Waldhauser and Ellsworth, 2000).
Figure 3.3 shows a data example of one earthquake cluster, which is part of the shallow event catalog discussed in Chapter 6. The double difference relocation does not severely change the centroid coordinates of the event cluster, indicating a stable single event location. However, after double difference relocation the seismogenic structures appear more focused (Fig. 3.3b) compared to the absolute hypocenters (Fig. 3.3a). Thus, solid absolute event locations are the basic requirement before double difference relocation schemes

should be applied.

In order to provide the basis for a stable inversion in the local earthquake tomography (Chapter 5), I used the multi-event absolute location scheme *velest* (Kissling et al., 1994). *Velest* allows inverting jointly for event location and velocity model. Thus, the derived velocity model is a *minimum* model in the sense that calculating event locations with this model (and possibly including station corrections) yields the smallest misfit. Using such locations is an important requirement for local earthquake tomography as it secures that the best fit 3D velocity model represents the absolute minimum and not only a local minimum in the misfit function.

3.2 The seismic source

To describe the effect of the seismic source on the seismogram in Equation (3.1), it is not necessarily required to constrain the true rupture mechanism of an earthquake. Instead, the radiation pattern of seismic energy in the far-field can be represented by a *body force equivalent*, which means by forces that would cause the same displacement signal at a seismometer as the true rupture (Aki and Richards, 1980). A seismic source in the subsurface (internal source) has to satisfy the condition of zero net force and zero net rotation. Thus, the simplest possible equivalent force would be a double couple (two perpendicularly arranged dipole sources which consist of two point sources in opposite direction, separated by a small distance along the axis of the forces). To achieve a generalized formulation, aiming to describe a source of arbitrary orientation, three different dipoles can be summarized in the seismic moment tensor:

$$\mathbf{M} = \begin{pmatrix} M_{xx} & M_{xy} & M_{xz} \\ M_{yx} & M_{yy} & M_{yz} \\ M_{zx} & M_{zy} & M_{zz} \end{pmatrix} \tag{3.6}$$

The seismic moment tensor $\mathbf{M}$ represents the source as a combination of nine force couples, which allow to reproduce exactly the same displacement field as slip on an internal fault would cause in the far field. Due to the requirements of zero net force and zero net movement, only six of its nine components are independent. Information about the seismic source can be drawn from the analysis of eigenvalues and vectors of the moment tensor. The eigenvectors, for instance, define three orthogonal axes, which correspond to the principal directions of maximum, intermediate and minimum tension (P, B, T axes), whose orientation is often used as indicators for the regional stress field (see e.g. Chapter 4).

If one of the eigenvalues equals zero, the moment tensor represents a pure double couple force and the remaining moment tensor components M_{ij} can then be rewritten in terms of a scalar moment M_0 and the components of the unit normal vector of the fault plane ($\hat{\mathbf{n}}$) and the unit slip vector ($\hat{\mathbf{d}}$):

$$M_{ij} = M_0(n_i d_j + n_j d_i) \tag{3.7}$$

The scalar seismic moment M_0 links the energy release due to the earthquake to the rigidity (μ), the average slip on the fault ($\bar{D}$) and the fault surface area (S):

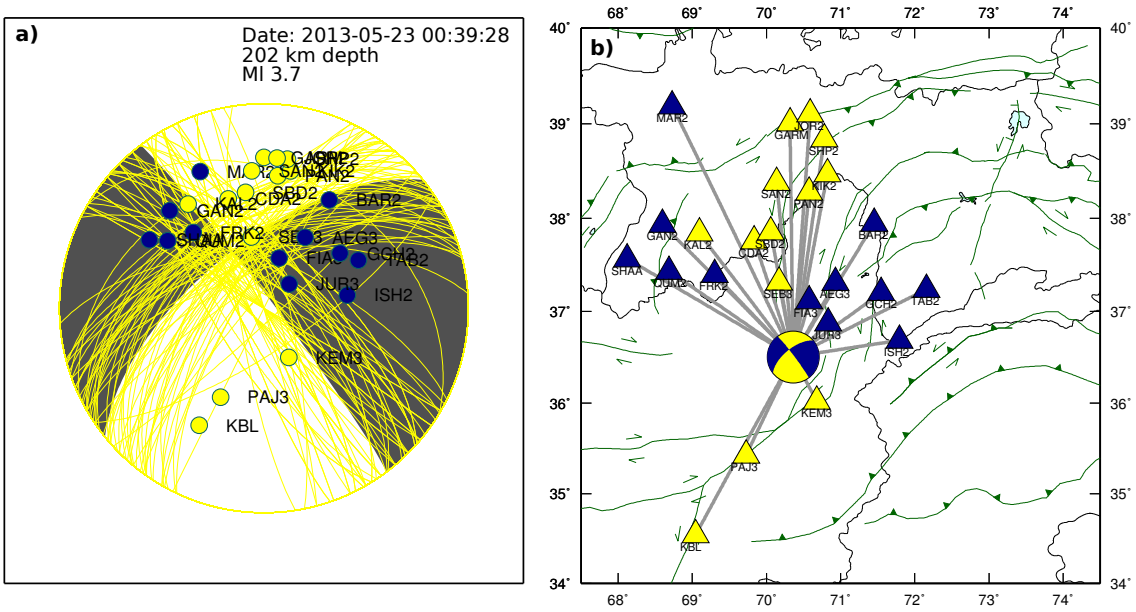

Figure 3.4: Example focal mechanism determined from first motion polarities picked at the TIPTIMON stations. **a)** Preferred mechanism (shaded in gray) and locations (azimuth and take-off angle) of the first motion P picks of the stations on the stereonet. Blue circles - onset up; yellow circles - onset down; yellow lines - focal planes of all acceptable mechanisms which fulfill certain quality criteria. **b)** Station and earthquake location; triangles at the stations are colored according to the polarity of the first motion onset at the specific station. Political boundaries in gray, faults from Schurr et al. (2014) in green.

$$M_0 = \mu \bar{D} S \tag{3.8}$$

Thus, the scalar seismic moment and the associated moment magnitude M_w are a physical measure for the size of the earthquake, whereas other magnitudes, e.g. the local magnitude M_L, are derived based on waveform amplitudes. Equation (3.7) also links the seismic moment to the fault geometry (e.g. strike, dip, rake and slip of the fault plane), characteristics that can be easily expressed in stereonet plots, the well known *beach ball* representation for an earthquake rupture mechanism (see e.g. Fig. 3.4 or Chapters 5 and 7).

3.2.1 Determination of rupture mechanism

Seismic records at different azimuths and distances to an earthquake can be used to deduce information regarding the rupture mechanism, which I determined here applying two different methods: waveform modeling (Chapters 6 and 7) for the largest earthquakes in the dataset and by first motion polarities for several smaller events (Chapter 7).

In waveform modeling, the rupture mechanism of an earthquake is derived from a least-square type inversion based on the misfit between real data and synthetic seismograms. To calculate synthetic seismograms, the ground displacement can be expressed as a sum over the different moment tensor components. Equation (3.1) can be reformulated to:

$$u_n(x,t) = s(t) * i(t) * \sum_{i=1}^{5}(m_i G_{in}(t)) \tag{3.9}$$

where u_n is the vertical, radial or tangential displacement measured at the seismic station, m_i are the five elements of the moment tensor, which are left when assuming no isotropic component, and $G_{in}(t)$ are the *Green's functions* (Lay and Wallace, 1995). Each of the Green's functions describes the displacement response at the seismometer caused by an impulse source oriented according to the corresponding moment tensor element, thus describes the path dependent effects on the waveform. Assuming that the instrument response and source time function are known, Equation (3.9) can be rewritten in matrix form similar to Equation (3.4). Thus, deriving the moment tensor involves the solution of an inverse problem, the calculation of Green's functions and the assumption of a source time function.
As local seismograms are subject to a lot of complexity, waveform modeling is normally undertaken at low frequencies (see e.g. the difference between the unfiltered local and the filtered teleseismic earthquake in Fig. 3.1), which implies that the method only works for earthquakes bigger than a certain minimum size. The smallest event for which I determined a mechanism via waveform modeling in the TIPTIMON dataset has a moment magnitude of 3.1 (see Chapters 4 and 6). For smaller events, a satisfying match was not possible any more.

I used first motion polarities and the software *HASH* (Hardebeck and Shearer, 2002) to derive the mechanisms of several smaller Hindu Kush intermediate depth earthquakes. Figure 3.4 shows an example for a double couple mechanism constrained from first-motion P polarities. In contrast to the waveform modeling, here only the polarity of the P onset on the vertical component of each station is used to constrain the mechanism. The result is not the deviatoric moment tensor but only its double couple components (i.e. expressed as strike, dip and rake). Based on the polarity picks, take-off angles and event-station azimuths *HASH* determines a set of acceptable mechanisms which would explain the observed polarities based on a grid search. The spread of the possible solutions (*yellow* lines in Fig. 3.4a) determines the quality or robustness of the solution. As can be seen in Figure 3.4, the quality of the solution strongly depends on the number of available stations, the azimuthal coverage and the take-off angles, which determine how complete the stereonet is covered with picks, and thus how unique the preferred mechanism is. In contrast, waveform modeling is less dependent on good azimuthal coverage.

Both methods above assume that the rupture dimension of the considered earthquake is small enough to be described as a point source, which does not hold for large earthquakes. One possible approach to describe the rupture process of large earthquakes is the superposition of various point sources along a hypothetical rupture interface. The result is a *finite fault model*, which captures the varying spatio-temporal distribution of displacement on the fault surface. Results for such a model derived for the M_w 7.5 October 2015 Hindu Kush earthquake by Yong Zhang and Rongjiang Wang are shown in Chapter 7.

3.2.2 Strain rate from seismic moments

Seismic moments can not only be used to derive valuable information about the earthquake rupture mechanism, they can also be used to draw conclusions regarding the state of stress in a given seismogenic volume. Assuming all seismic slip from multiple earthquakes would occur on one single interface, the cumulative seismic slip s in a given time can be calculated directly from the sum of all moments (Brune, 1968):

$$\sum s = \frac{1}{\mu A_0} \sum M_0 \tag{3.10}$$

where A_0 is the area of a specific shear zone, μ is the shear modulus and M_0 are the scalar seismic moments of all earthquakes in a specific time interval. If deformation occurs along a framework of many faults, it is more adequate to consider a deforming volume. Following Kostrov (1974), the average strain-rate tensor within a specific volume can be calculated by summing the moment tensors of individual earthquakes with hypocenters within this volume:

$$\dot{\bar{\varepsilon}}_{ij} = \frac{1}{2\mu V t} \sum_{k=1}^{N} M_{ij}^{(k)} \tag{3.11}$$

where N is the total number of earthquakes in a given time, V is the considered volume, t is the time interval and M_{ij}^{k} are the seismic moment tensor elements of the kth event. I used the Kostrov (1974) formulation in Chapter 7 to calculate the strain rate in the volume containing the Hindu Kush intermediate depth seismicity.

4 Deep India meets deep Asia: Lithospheric indentation, delamination and break-off under Pamir and Hindu Kush (Central Asia)

This chapter is the final version of Kufner et al. (2016) before submission to Earth and Planetary Science Letters

Abstract
Subduction of buoyant continental lithosphere is one of the least understood plate-tectonic processes. Yet under the Pamir-Hindu Kush, at the northwestern margin of the India-Asia collision zone, unusual deep earthquakes and seismic velocity anomalies suggest subduction of Asian and Indian lithosphere. Here, we report new precise earthquake hypocenters, detailed tomographic images and earthquake source mechanisms, which allow distinguishing a narrow sliver of Indian lithosphere beneath the deepest Hindu Kush earthquakes and a broad, arcuate slab of Asian lithosphere beneath the Pamir. We suggest that this double subduction zone arises by contrasting modes of convergence under the Pamir and Hindu Kush, imposed by the different mechanical properties of the three types of lithosphere involved. While the buoyant northwestern salient of Cratonic India bulldozes into Cratonic Asia, forcing delamination and rollback of its lithosphere, India's thinned western continental margin separates from Cratonic India and subducts beneath Asia. This torn-off narrow plate sliver forms a prominent high-velocity anomaly down to the mantle transition zone. Our images show that its uppermost section is thinned or already severed and that intermediate depth earthquakes cluster at the neck connecting it to the deeper slab, providing a rare glimpse at the ephemeral process of slab break-off.

Keywords
(1) Pamir-Hindu Kush, (2) India-Asia collision, (3) Slab break-off, (4) Lithosphere delamination, (5) Intermediate depth seismicity, (6) Tomography

Highlights
1) We evaluate seismic data and derive a tectonic scenario for the Pamir-Hindu Kush.
2) Pamir-Hindu Kush host two opposite dipping zones of intermediate depth seismicity.
3) The Hindu Kush earthquakes are due to the slab-detachment of Indian lithosphere.
4) The Eurasian Pamir slab is pushed north, stretched and torn apart by cratonic India.
5) The rheological properties of the lithosphere involved cause this contrasting behavior.

4.1 Introduction

The Pamir and Hindu Kush, located northwest of Tibet, are part of Earth's largest active continental collision (Fig. 4.1a). As in Tibet, the Pamir-Hindu Kush crust comprises terranes that rifted from Gondwana (the Gondwana terranes of Fig. 4.1b) and then amalgamated to the southern margin of Asia (Tapponnier et al., 1981; Burtman and Molnar, 1993; Schwab et al., 2004). Unlike Tibet, the Pamir-Hindu Kush mantle exhibits vigorous intermediate depth (>100 km) seismicity (Billington et al., 1977; Chatelain et al., 1980; Pegler and Das, 1998; Sippl et al., 2013b) (Fig. 4.1a) and strong velocity anomalies down to the bottom of the transition zone (Koulakov and Sobolev, 2006; Negredo et al., 2007). Fifteen earthquakes with magnitude greater than 7.0 have occurred in the Hindu Kush deep seismic zone in the last 100 years, including the recent destructive October 2015 M_w 7.5 Badakhshan, Afghanistan event (ISC, 2013; USGS, 2016). Intense intermediate depth seismicity is generally confined to oceanic subduction zones and its occurrence in-

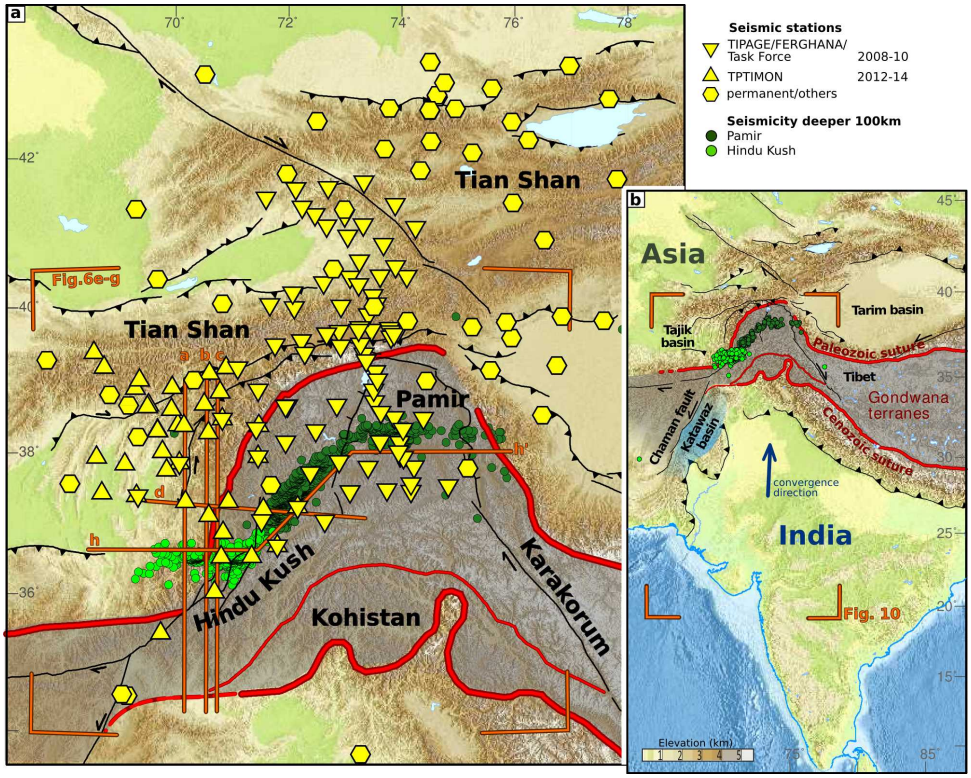

Figure 4.1: Seismicity and seismic station used in this study plotted onto a topographic map of Central Asia. a) Yellow symbols mark seismic stations. Northern red line follows the Late Paleozoic-Triassic suture separating cratonic Asia in the north from the Gondwana terranes (shaded grey) in the south. Southern line is the Cenozoic Indus-Yarlung suture, separating Indian from Asian rocks. Thin red line marks the Shyok suture. Seismicity (Sippl et al., 2013b) for depths greater than 100 km is plotted in light and dark green under the Hindu Kush and Pamir, respectively. Orange markers locate the sections in Figure 4.6. **b)** India and its collision with Asia. Deep (>100 km) seismicity for the last 50 years from a global catalog (Engdahl et al., 1998).

side a continent is enigmatic (Billington et al., 1977; Vinnik et al., 1977; Chatelain et al., 1980; Roecker, 1982; Burtman and Molnar, 1993; Pegler and Das, 1998). The Pamir and Hindu Kush earthquakes form two separate zones (Fig. 4.1); the provenance of the Hindu Kush earthquakes is debated (Pegler and Das, 1998; Sippl et al., 2013b), but in the Pamir they are associated with continental Asian plate subduction (Schneider et al., 2013; Sippl et al., 2013a). This contradicts the plate-tectonic paradigm that continental lithosphere does not subduct to significant depth without the pull-force of a leading, negatively buoyant oceanic plate. The understanding of the origin of these anomalies is a key to the deep-seated processes of the India-Asia collision and continental dynamics in general.

We present a regional tomographic model, new earthquake hypocenters and source mechanisms, all based on recent seismic experiments. The detailed lithospheric structure revealed by the tomography and seismicity, and the stress field inferred from earthquake focal mechanisms allow us to deduce the geodynamic processes currently acting under the Pamir and Hindu Kush. We propose a tectonic scenario that led to the unique constellation observed today, suggesting a solution to the long-standing controversy on slab provenance and explaining the formation of the peculiar double subduction zone.

4.2 Data

Our results were obtained from the analysis of seismic data recorded by three temporary networks (Fig. 4.1a), namely the TIPAGE (Mechie et al., 2012) and FERGHANA (Feld et al., 2015) networks operated between 2008 and 2010 in the Pamir and Tian Shan, and the TIPTIMON network (Schurr et al., 2012, 2013) from 2012-2014 in the western Pamir, Tajik basin and Hindu Kush. TIPTIMON operated 33 broadband stations in Tajikistan and eight short period sensors in Afghanistan (Mark L-3D, 1 Hz natural frequency) and shared seven sites with the TIPAGE network. The stations in Afghanistan were situated on top of the Hindu Kush intermediate depth seismic zone, allowing to constrain its geometry at high resolution. Additional permanent station data were collected for the operating periods of the temporary networks (Fig. 4.1b). In total, we analyzed data from 180 seismograph sites with a spacing between ∼20 km along a north-south profile in the central Pamir and 40-60 km in the western Pamir, Hindu Kush and Tajik basin. Waveforms from the permanent stations were accessed via the GEOFON, IRIS and Chinese Earthquake Network data centers.

4.3 Earthquake analysis

4.3.1 Extended earthquake catalog

We augmented the existing Pamir-Hindu Kush earthquake catalog (Sippl et al., 2013b), which is based on the TIPAGE and FERGHANA networks, with the events located during the TIPTIMON experiment between 2013 and 2014, i.e. while the Afghan stations were recording. The superior event-station geometry of this network in relation to the Hindu Kush earthquakes significantly improved their locations. For the earthquake-catalog production, we followed essentially the same automated procedure applied for the TIPAGE catalog (see details in Sippl et al., 2013b). Here, we aimed to improve the image of the

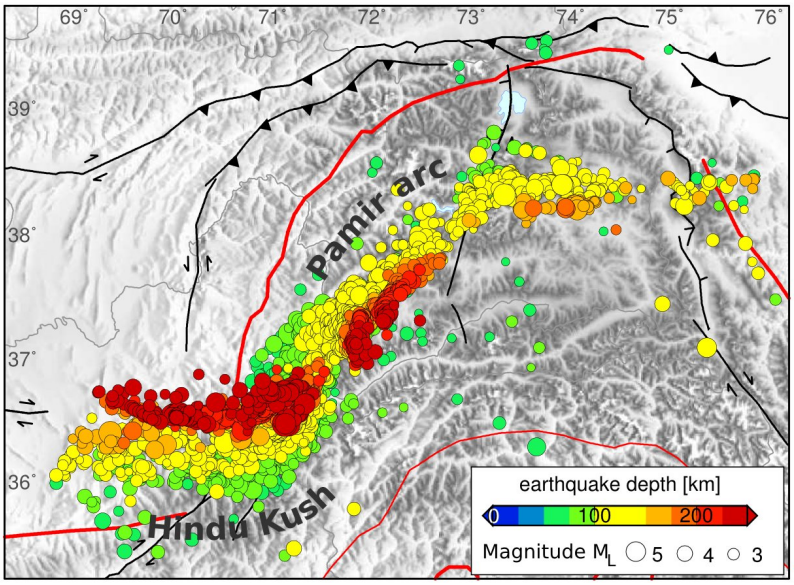

Figure 4.2: Updated earthquake catalog for the Pamir and Hindu Kush. Earthquake catalog at sub-crustal depths with hypocenters deeper than 50 km. Size of the symbols corresponds to local magnitude, color to depth. Hypocenters are sorted by depth where deepest earthquakes are plotted on top. Main tectonic features as in Figure 4.1a.

Hindu Kush seismic zone, therefore only earthquakes that were registered by at least one of the seismic stations in Afghanistan and located west of 71.8°E, the approximate border between the Pamir and Hindu Kush seismic zones, were added to the combined catalog. To ensure location quality, at least eight P-picks, one S-pick and a root mean square (RMS) residual smaller than one second, based on the initial single event location, were required for event selection. This yielded ∼3700 new earthquake hypocenters (Supplementary Fig. B1a, b), which were merged with a subset of the existing event catalog (Supplementary Fig. B1c). West of 71.8°E, the TIPAGE subset is restricted to events with a maximum backazimuthal gap of 120°, to retain only the best locations under the Hindu Kush. The merged catalog (Fig. 4.2) was relocated in a regional 1D velocity model (Sippl et al., 2013b). We applied the double difference location algorithm (hypoDD; Waldhauser and Ellsworth, 2000) to improve the relative location of intermediate depth seismicity (for hypocenters deeper than 50 km). This joint relocation not only ensures the consistency of the whole catalog but also improves the relative locations of individual events with larger backazimuthal gap due to the common recording stations of the different temporal networks.

Absolute location errors were assessed using a probabilistic relocation scheme (NonLinLoc; Lomax et al., 2000), where a probability density function (PDF) for the location of each single event is calculated. Commonly, the 68% error ellipse of this PDF serves as a measure for the absolute location uncertainty of the events (Lomax et al., 2000). The average volume of the PDF error ellipses of all events is 270 km^3 (equivalent to a sphere with 4 km radius); the average RMS is 0.31 s. 91 percent of all intermediate depth earthquakes could be relocated with the double difference scheme. The relative location errors of these were

obtained by running hypoDD in the singular value decomposition mode on subsets of the event clusters, yielding an average relative error of 1.3 km. For those events not relocated with hypoDD, mainly isolated events not belonging to a cluster, the single event locations were used.

In the updated earthquake catalog (Fig. 4.2), the sub-crustal seismicity forms two separate zones: (1) A roughly 90° arc under the Pamir that dips from the Asian side due south in the northeast and due east in the southwest (described in detail by Sippl et al., 2013b); (2) a narrow, slab-like, east-striking and north-dipping structure under the Hindu Kush. In the uppermost mantle, the latter dips clearly north, steepening to sub-vertical at depths greater than ∼140 km. Seismicity in this deepest Hindu Kush cluster is very intense, e.g., producing almost one third of all detected intermediate depth earthquakes in our catalog, despite its compact size.

4.3.2 Focal mechanisms and stress inversion

We derived earthquake source mechanisms for intermediate depth earthquakes in the time period from 2008 to 2010 in two ways. For 72 events, which were strong enough (M_w 3.9-6.2) to produce sufficient signal at long periods (>10 s), we inverted complete displacement seismograms from all broadband stations in the time domain for the deviatoric moment tensor (Schurr and Nábělek, 1999). All inversions were done interactively to allow quality control of the data and the fit. For 166 events, which were too small for moment tensor inversion, yet had enough coverage in station azimuth and distance range to constrain the two nodal planes, we determined fault-plane solutions from first-motion polarities (Hardebeck and Shearer, 2002). The first motions were picked manually. We kept only earthquakes with more than eight measurements, a maximum azimuthal gap of 150°, and a maximum take-off angle gap of 60° for the focal-mechanism determination. In total, 8200 P-polarities were determined, yielding an average of 49 polarity picks per earthquake. We accepted the best-fit mechanism only if all possible fault-plane solutions had a RMS fault-plane uncertainty smaller than 35° with a maximum of 5% polarity outliers. Maps with event locations, data examples and a comparison of the results obtained from both methods can be found in the Supplementary Material Figure B2.
In Figure 4.3a, we project the tensional (T) axes of the individual source mechanisms on a crooked cross section following the strike of the seismic zones, which is also later used for displaying the tomographic model. Although there is significant scatter, a clear pattern is recognizable. For deep (depth >150 km) events, the T-axes plunge in general steeply but vary slightly between the Hindu Kush and the western and eastern Pamir clusters (Fig. 4.3a). For the central Pamir earthquakes, T-axes plunge more horizontally. The scatter in the stress axes from the individual source mechanisms is expected, because pre-existing weaknesses, probably randomly distributed, allow ruptures to deviate from optimal geometries for the ambient stress field. To estimate the regional stress field, we inverted the fault-plane data for stress tensors (Figs. 4.3b-f). To satisfy the assumption of a uniform stress field, the mechanisms were subdivided into four sub-regions according to their hypocenter locations and clustering of the T-axis orientations (Fig. 4.3b). One sub-region encompasses all Hindu Kush earthquakes (52 mechanisms); the other sub-regions follow the Pamir seismicity along strike (western, central and eastern Pamir: 107, 42 and

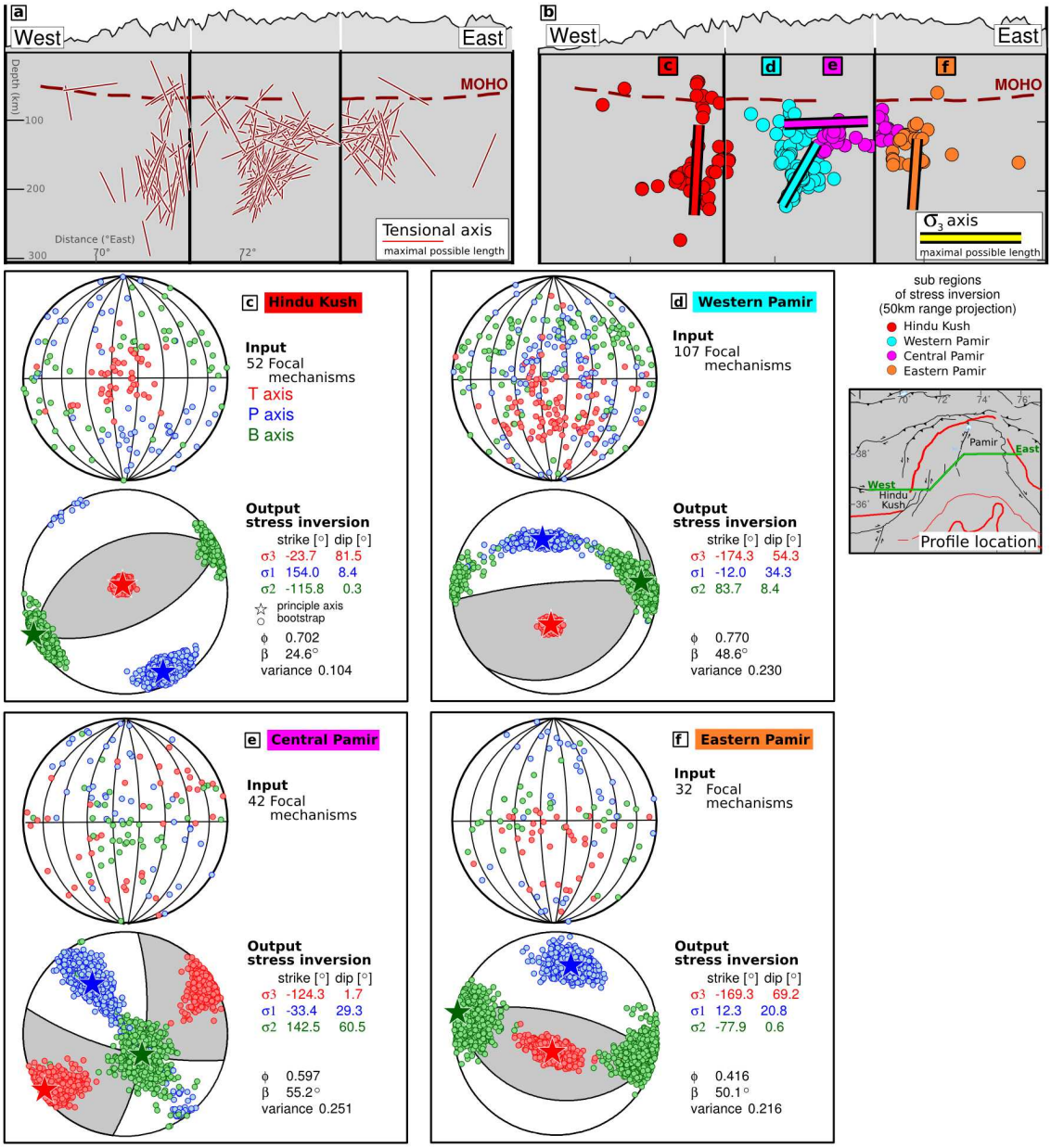

Figure 4.3: Earthquake tensional axes and stress inversion. **a)** σ_3 axes (T-axes) from 238 earthquake focal mechanisms projected onto cross section of Figure 4.6h. Length of vectors scales with in-plane proportion of their amplitudes (longest possible vector is 100% in-plane, point means perpendicular to plane). **b)** Partitioning of earthquakes in four sub-regions (color coded) for the stress inversions and resulting σ_3 axes projections. **c-f)** Top panels: Principal axes of focal mechanisms in a stereonet used as input to the stress inversion. Bottom panels: Inverted stress tensors plotted as beachball and with principal stress axes (stars). $\Phi=(\sigma_2-\sigma_1)/(\sigma_3-\sigma_1)$ is the relative stress magnitude, β the average rotation angle. Colored circles indicate results of bootstrap inversions, providing a measure of inversion robustness.

37 mechanisms). The linear inversion minimizes the total amount of rotation around an arbitrary axis necessary to rotate the focal mechanisms to fit the stress tensor using the software slick (Michael, 1987).

To inspect the robustness of the inversion results, we applied a bootstrap test, re-sampling the data set 1000 times and flipping the selected fault and slip directions 10% of the times. Parameters that quantify the quality of the stress tensors are the average rotation angle β and the variance. As the focal mechanisms for the Hindu Kush earthquakes exhibit overall a very similar orientation, the resulting stress tensor is well defined (Fig. 4.3c), expressed by a low variance (0.104) and a small average rotation angle (24.6°). Re-sampled bootstrap inversions show very stable orientations of the stress axes (σ axes). The mechanisms for the central, western and eastern Pamir (Figs. 4.3d-f) are more scattered, but all three stress tensors yielded a variance smaller than 0.26. The σ_3 axes confirm the pattern seen in the T-axes ensemble. For the deeper clusters under the Hindu Kush, western and eastern Pamir, they plunge steeply to sub-vertically, while for the shallower central Pamir events σ_3 lies sub-horizontally.

4.4 Teleseismic tomography

4.4.1 Travel times

For the regional seismic tomography, we used P-wave travel-time residuals from 1029 teleseismic earthquakes (30-90° epicentral distance, M_w >5.5, Fig. 4.4a). Earthquake parameters were obtained from the USGS global PDE catalog. Waveforms were corrected for seismometer response and bandpass filtered between 0.5 and 2.0 Hz. P wave travel times were picked semi-automatically on all available vertical records by detecting the nearest extremum of the waveform to the theoretical onset (Bianchi et al., 2013). We inspected all picks visually and discarded uncertain and noisy ones. In total, 36,339 valid travel-time observations were made, yielding on average 35 picks per earthquake and 200 picks per station. To ensure that events from the two major recording periods were linked, we always required picks from stations that were active during both periods (i.e., re-occupied temporary and permanent stations).

4.4.2 Tomographic inversion

Our P-wave velocity model was calculated using a modified version of the LOTOS code (Koulakov, 2009), allowing for the inversion of teleseismic data (Bianchi et al., 2013). The inversion for velocity perturbation was performed on a grid with 30 km horizontal and variable vertical node spacing dependent on the ray coverage. To determine the node positions, the ray density was calculated in cubes of 30 km edge length (Fig. 4.4b). This ray density grid was then scanned along vertical columns, summing up the cumulative ray length, until it exceeded the average ray-length value (here 907 km per cube). Then, a grid node was introduced, the sum was set back to zero and the scanning was continued. This procedure resulted in dense node spacing in well resolved regions and ensured that inversion nodes were only introduced if enough rays were available. The velocity between the nodes is defined by linear interpolation using tetrahedral volumes around the nodes.

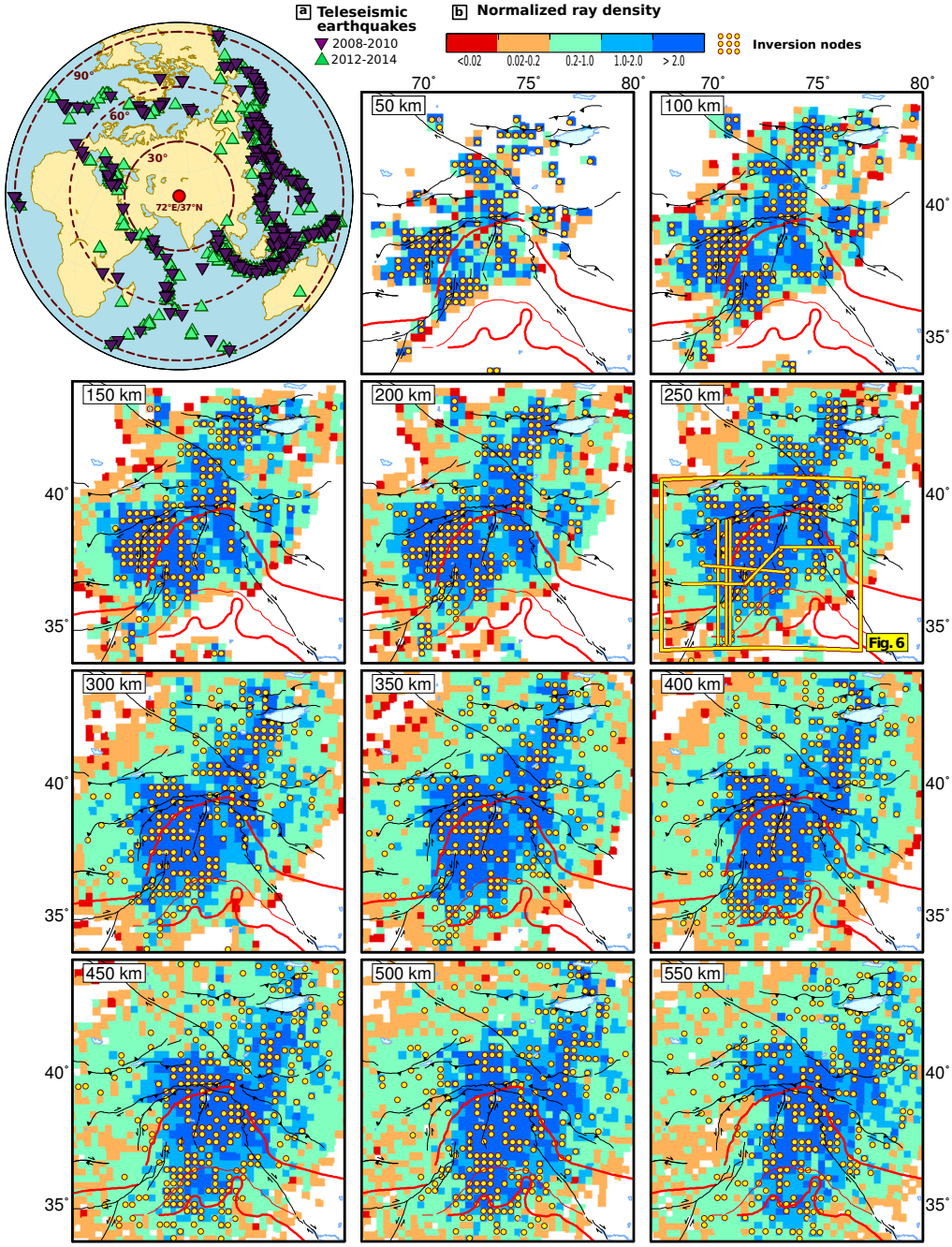

Figure 4.4: Distribution of teleseismic earthquakes and ray coverage. a) Location of teleseismic earthquakes used in tomography. Colors differentiate the two recording periods. **b)** Ray coverage: cumulative ray length in each 30 km cube, normalized by the average length. Yellow dots mark the node positions in the inversion grid (vertical projection width: ±25 km). The positions of the cross sections shown in Figure 4.6 are plotted for orientation in the 250 km slice. Main tectonic features as in Figure 4.1a.

In the final tomographic model, we only show velocity anomalies that are less than 25 km away from the nearest node, in order not to blur the image by extensive anomalies caused by sparse ray and node density.

Travel-time residuals were calculated from the initial picks including elevation and crustal corrections for each event-station pair separately. For the crustal correction, we constructed a smoothed Moho map based on receiver functions from the TIPAGE, TIPTIMON and FERGHANA deployments (Schneider, 2014) and additional data from the CRUST1x1 model (Laske et al., 2013). The resulting map has a maximum/minimum Moho depth of ∼85/∼45 km in the western Pamir and Tajik basin, respectively. The crustal velocities of the background 1D velocity model (ak135; Kennett et al., 1995) were stretched to the depth where the ray penetrates the Moho. Theoretical travel times were then calculated in this modified velocity model. We took the elevations of the recording stations into account by reducing the picked travel times by the theoretical travel time from zero elevation to the station (assuming a P-wave velocity of 5.86 km/s). After applying these corrections, the average residual was subtracted for each event to generate relative travel-time residuals.

The inversion matrix contains elements for the velocity perturbation at each node, elements for station corrections and a regularization block. Station corrections were strongly damped to avoid a trade-off with the shallow mantle structure. The inversion was performed simultaneously for velocity perturbations and station corrections using the LSQR method (Paige and Saunders, 1982). After each iteration, the ray paths and travel-time residuals were recalculated for the updated velocity model. The inversion converged after five iterations. To avoid possible artifacts from grid orientation, we performed the whole inversion procedure on four individual grids, where the x-y coordinate system used for the calculation of ray density and node position was rotated by 0°, 22°, 45° and 67°, respectively (Fig. 4.4b shows for example the first of these grids). The velocities from these individual inversions were re-sampled on a rectangular grid and then averaged to obtain the final model.

4.4.3 Evaluation of optimum inversion parameters and checkerboard test

We determined the optimum parameter for flattening by computing synthetic and real models over a set of different flattening values. The optimum parameter yielded the best trade-off between the competing influences of the reduction in RMS travel-time residuals and the increase of model variance (see trade-off curve in Supplementary Fig. B3). The optimum damping parameter and the extent of the well-resolved regions were evaluated from synthetic tests. We calculated theoretical travel times for the resolution tests by 3D ray tracing through a synthetic velocity model using the same station-event geometry as in the real data. Noise was added to the synthetic travel times according to the unmodelled residuals after the inversion of the real data.

Figure 4.5 shows two sets of checkerboard tests calculated with the optimum flattening parameter (big checkerboard pattern: cubes of 150 km edge length with alternating anomalies of ±3%, separated by a 50 km wide neutral zone; small checkerboard pattern: 100 km anomaly edge length and 25 km wide neutral zone). With our preferred regu-

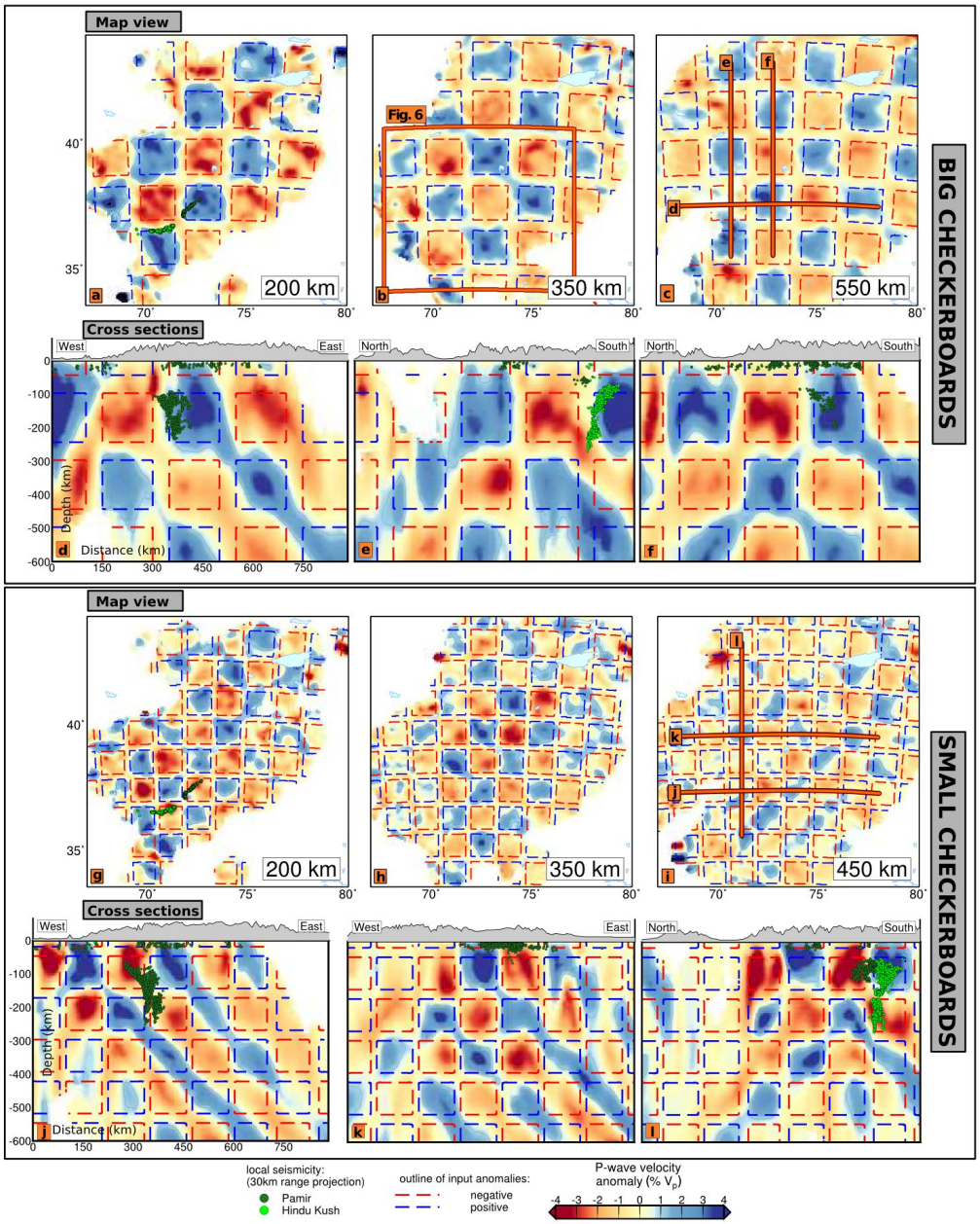

Figure 4.5: Checkerboard tests. The recovered output velocity model is color coded as in Figure 4.6. Seismicity from Figure 4.2 is plotted for orientation. **a-f)** Input anomalies (dashed, ±3%) are cubes of 150 km edge length separated by a 50 km wide neutral zone. **g-l)** Cubes with edge length of 100 km separated by 25 km wide neutral zone.

larization parameters for flattening and damping, amplitude recovery decreased slightly with depth (amplitudes of big checkerboard anomalies at 550 km are ∼35% smaller than at 150 km), but the pattern and especially the neutral zone between the anomalies can still be resolved. As expected for teleseismic tomography, vertical smearing exceeds horizontal smearing, and the horizontal extent of the anomalies is accurately mapped in

most of the model domains. Only in the deeper layers beneath the western Hindu Kush (∼450-600 km, west of ∼70°E), the lower ray coverage allows resolution of only the larger checkerboard anomalies. With this set of regularization parameters, the total variance reduction of the travel-time residuals of the real data was 63%. The final station corrections are overall small due to the high damping (extreme values of -0.11 s at station KBU in Kabul/Afghanistan, 0.04 s at EKS2 near Bishkek/Kyrgyzstan and a median of 0.003 s).

4.4.4 The mantle velocity structure and its relation to the Pamir and Hindu Kush seismic zones

Our three-dimensional teleseismic P-wave model shows a complex high-velocity structure at sub-crustal depths (Fig. 4.6; see also Supplementary Fig. B4 and Supplementary section B for the whole tomographic model, which also includes parts of the Tian Shan). We interpret the relative velocity anomalies as mainly due to temperature differences (Sobolev et al., 1997), i.e., high velocity anomalies (HVAs) likely represent subducted cold lithosphere. Figure 4.6 displays sections through the tomographic velocity model together with the projected earthquake hypocenters and the σ_3-axes of the stress inversion.

Under the Hindu Kush a strong, narrow high-velocity anomaly reaches from the base of the earthquake zone at ∼250 km depth to the bottom of the mantle transition zone at ∼600 km depth (anomaly *HK'* in Fig. 4.6). The Hindu Kush seismic zone itself occurs within neutral velocity material (G_{HK} in Fig. 4.6). This is in contrast to oceanic subduction zones, where intermediate depth earthquakes occur inside the high-velocity slabs. Slightly displaced southward, adjoining the seismic zone, lies a shallower HVA (*HK*) that connects upwards to the crust and thins from west to east. It is connected to the deeper *HK'* anomaly by a narrow neck of high-velocity material, which appears to be almost severed in the easternmost section through the Hindu Kush (Figs. 4.6a-c). For the Hindu Kush earthquakes, σ_3 of the stress tensor points vertically down toward the deepest HVA *HK'*, paralleling the sub-vertical dip of the seismic zone and the velocity anomalies, indicating down-dip extension (Fig. 4.6h). With synthetic tests, we assessed to what extent the neck in the anomaly is resolvable. We built a model with a gap separating the anomalies *HK* and *HK'* as well as one with a continuous HVA between Pamir and Hindu Kush (Figs. 4.7a, b). Both cases are well resolved, hence, the gap in the HVA containing the Hindu Kush earthquakes and the observed thinning of the anomalies *HK* and *HK'* does not appear to be an artifact. To test the possibility of the presence of a highly thinned lithospheric layer near the Hindu Kush earthquakes, we built a third synthetic model with a 15 km thick high and 15 km thick low velocity layer, simulating a thinned crust-mantle lithosphere compound at the position of the Hindu Kush seismicity (Fig. 4.7c). Such a thin structure could not be recovered; instead, the extent of the adjacent high-velocity zone is slightly decreased.

In contrast to the Hindu Kush, the deepest Pamir earthquakes coincide with a prominent velocity anomaly (*P* in Fig. 4.6), crossing the Pamir from the Tarim basin in the east to the Pamir-Hindu Kush syntaxis in the west, where its deepest section *P* abuts against the deep *HK'* anomaly below ∼350 km depth. It overlaps with the Pamir earthquakes in its upper part but penetrates deeper, to ∼400 and ∼450 km depth in the east and southwest,

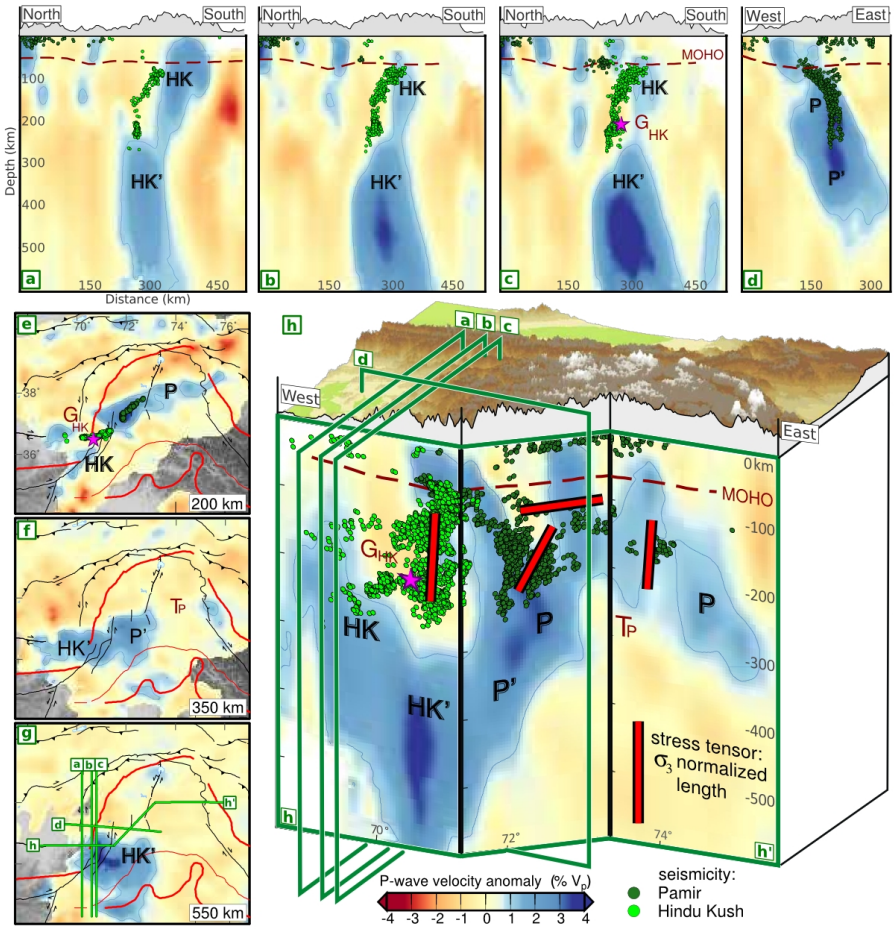

Figure 4.6: Tomographic velocity model, seismicity and stress axes. a-d) Vertical sections. **e-g)** Depth maps. **h)** Vertical section along the Hindu Kush and Pamir slabs (+1% anomaly of the velocity model is contoured). Earthquakes of the Pamir (dark green) and Hindu Kush (light green) seismic zones (30 km swath width) and σ_3 (tension) axes (red bars) from stress inversions of 238 focal mechanisms projected onto the cross-section planes. Capital letters mark anomalies described in the text. Pink star marks the hypocenter of the recent October 2015 M_w 7.5 Badakhshan, Afghanistan event (USGS, 2016). Discrepancy between USGS event locations and our catalog is less than 10 km at this depth.

respectively (Figs. 4.6d, h). In the center of the Pamir anomaly, a vertical tear (T_P) splits the slab from ∼200 to ∼400 km depth (Figs. 4.6f, h). All synthetic models (Fig. 4.7) show only little vertical smearing at the bottom of the Pamir anomaly, rendering the shape of the slab, the inferred tear and the junction of the Pamir and the Hindu Kush anomalies reliable (*P*, *P'*, *HK* and T_P in Fig. 4.6). The σ_3 axes of the Pamir stress tensors vary from dominantly vertically plunging in the western and eastern Pamir to a sub-horizontal orientation in the central Pamir, just above the vertical tear T_P. Hence, the stress field in the Pamir slab appears more complex compared to the Hindu Kush, involving both down-dip stretching at the outer wings of the slab, as well as along-arc stretching and tearing in its curved center (Fig. 4.6h).

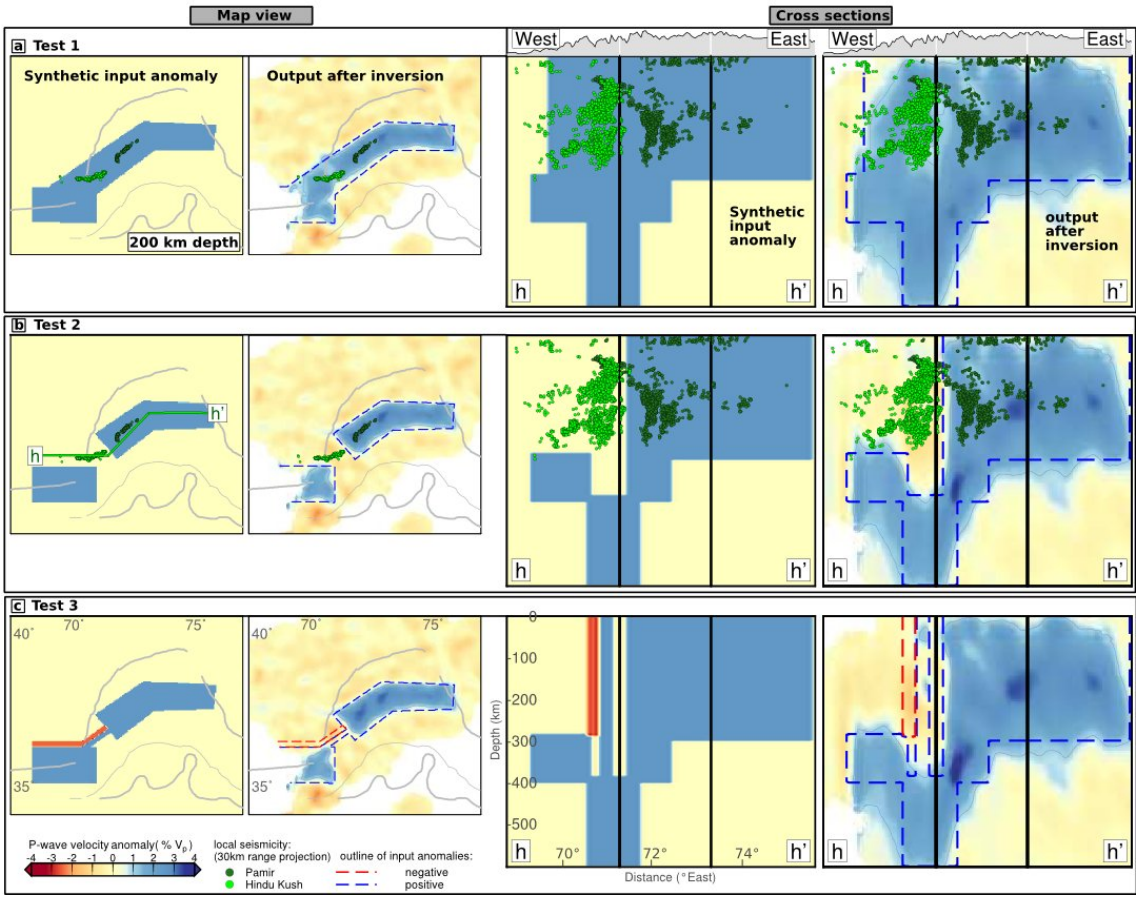

Figure 4.7: Synthetic tests to assess the reliability of the features discussed in the text. Left panels show the input synthetic anomalies, right panels the recovered models (input anomalies dashed). Map view and cross-section as in Figures 4.6e, h. Earthquakes and tectonic features as in Figure 4.6. **a)** Scenario 1: Pamir-Hindu Kush anomalies are connected in the upper mantle. **b)** Scenario 2: Pamir-Hindu Kush anomalies are separated in the upper mantle and the Hindu Kush earthquakes occur in the gap. **c)** Scenario 3: A ∼15 km thick low and a ∼15 km thick high velocity zone occupy the zone between the Pamir and Hindu Kush anomalies.

4.5 Discussion and interpretation

Combining our observations on lithospheric structure, occurrence of earthquakes, and the intra-slab stress field, we aim to understand the geodynamic processes acting under the Pamir and Hindu Kush. Starting out from this current state, we go back in time to sketch a possible late Cenozoic tectonic history of the western part of the India-Asia collision, which can explain the formation of the major structural characteristics observed today.

4.5.1 Lithospheric stretching and slab-detachment under the Hindu Kush

In the Hindu Kush, our observation of an inclined upper, downward steepening and thinning HVA, accompanied by increasingly intense seismicity, match numerical simulations

of slab detachment following subduction and collision (Duretz et al., 2012; Magni et al., 2012). In these models, shortly before detachment, the slab steepens to near vertical in the deeper part and the subducting lithosphere is highly thinned at the point where the final break-off will happen. Strain localizes where the lithosphere is thinnest. Although the transition between a leading oceanic and subducted continental plate is the preferred zone for slab break-off, subsequent break-offs might occur when continental lithosphere continues to subduct, as has been the case for the Indian plate (Capitanio and Replumaz, 2013). Slab break-off had already been suggested in the Hindu Kush (e.g. Koulakov and Sobolev, 2006; Lister et al., 2008). Here, we confirm this idea and provide clear images of this often postulated but rarely observed tectonic event. Figure 4.8 shows the synoptic interpretation of our results. The consistent down-dip extensional stress field of the Hindu Kush earthquakes, all the way to the bottom of the crust, indicates that the massive deeper lithospheric fragment (anomaly *HK'*) has to be still attached to its thin, upper continuation (*HK*). This part underlies the inclined upper part of the Hindu Kush seismicity and dips from the Indian side (Figs. 4.6a-c). The gap between the shallow and the deep HVA (G_{HK}) likely represents the part of the slab where the mantle lithosphere is thinned to an extent that it can no longer be imaged by teleseismic tomography (<30 km; see synthetic example in Fig. 4.7c). The north-dipping Hindu Kush seismic zone is partly separated from the underlying HVA *HK* by a narrow neutral zone (Figs. 4.6a-c). This offset might mark the resolution limit of our tomography and could arise from a crustal layer (see synthetic test in Fig. 4.7c), pulled to depth by and still attached to the mantle lithosphere as has been suggested by Roecker (1982). The earthquakes, particularly in the upper inclined section, may actually occur in subducted lower crust, as they do under the Pamir (Schneider et al., 2013). This crustal layer is likely too thin to be resolved by tomography Sippl et al. (2013a). In a synthetic test, a 15 km thick crustal layer together with a thin remnant lithospheric mantle layer reproduces the observed neutral to slightly reduced velocities (Fig. 4.7c). The most active seismicity clusters and largest earthquakes both in our catalog (Figs. 4.2, 4.6) and global catalogs (e.g., the recent October 2015 M_w 7.5 event, Fig. 4.6h) occurred adjacent to the thin neck between the *HK* and *HK'* anomalies (Figs. 4.6a-c) in a depth range between ∼180 and 220 km. This agrees well with detachment depths predicted by numerical models for moderate lithospheric ages and convergence rates (e.g. Duretz et al., 2011, 2012). Seismicity is less intense in the western Hindu Kush where the deep and shallow anomalies (*HK* and *HK'*) appear to be still connected (Fig. 4.6h). This might indicate that the largest earthquakes under the Hindu Kush are directly associated with the final pinching-off (Lister et al., 2008). We might in fact witness the point in time, where the Hindu Kush slab is just about to break free. Although viscous necking is likely to be the dominant deformation mechanism (Duretz et al., 2012), strain localization may produce such high strain rates that brittle failure is enabled.

Assuming that the Hindu Kush anomalies once formed an intact lithospheric slab, the thinning and necking of the upper part of the Hindu Kush slab implies that the initial length of subducted lithosphere was less than its current penetration depth. Thus, the total length of the lithosphere has to be corrected for stretching in any paleogeographic reconstruction. We estimated the first-order magnitude of this extension under simplified assumptions. The Hindu Kush slab is significantly thinned in its upper part between ∼50 and 300 km depth. Here, it is on average less than 50 km thick, compared to a thickness of

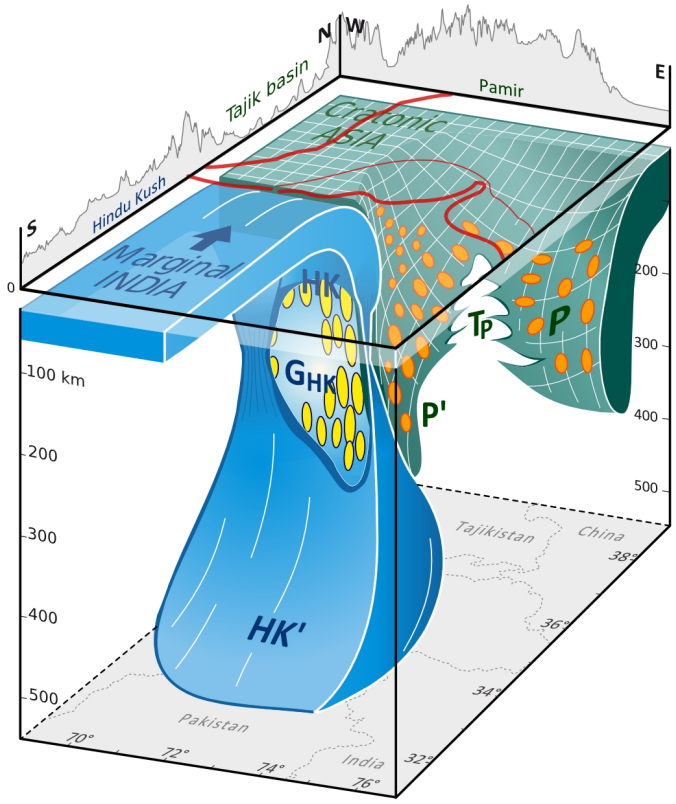

Figure 4.8: Synoptic interpretation of the tomographic model. Blue: The Indian-plate sliver detaching under the Hindu Kush. Earthquakes (yellow) cluster in regions of stretching and necking where lithosphere is extremely thinned. Green: Asian plate delamination and rollback under the Pamir, with along-arc stretching and central tearing; Pamir earthquakes in orange. Capital letters mark the velocity anomalies described in the text and annotated in Figure 4.6.

~150 km below ~300 km depth. This amounts to ~66% thinning assuming plane strain (schematically shown in Fig. 4.9a). Restoration would hence shorten the upper 250 km of the slab to ~83 km length. Between 250 and 300 km, the slab is already that thin, that it can be neglected. The total slab penetration is ~600 km (Fig. 4.6; Koulakov and Sobolev, 2006; Negredo et al., 2007) and the total restored slab length is hence ~380 km (Fig. 4.9b). Subducting ~380 km of slab at ~34 mm/yr (Molnar and Stock, 2009) takes ~11 Myr, suggesting that the Hindu Kush slab is a young feature in the India-Asia collision history. Obviously, this is a rough estimate, as slab-thickness measurements are affected by uncertainties in the tomographic model, although the lateral resolution is very good in this region (Fig. 4.7). The lower portion of the Hindu Kush slab could have been shortened, which would lead to an overestimation of its original thickness. The Pamir anomaly, which penetrates to ~400 km depth, is apparently less affected by vertical stretching, as no significant thinning of the HVAs *P* and *P'* is observed (Fig. 4.6d). Thus, the restored Hindu Kush slab (Fig. 4.9b) and the Pamir slab (Fig. 4.6d) appear to have a similar length.

4.5.2 Slab provenance - one or two plates?

The complex topology of the seismic planes under the Pamir and Hindu Kush has puzzled scientists for a long time. Interpretations ranged from the juxtaposition of two subduction zones of opposite polarity (Chatelain et al., 1980; Burtman and Molnar, 1993; Negredo et al., 2007) to one-plate models either of Indian (Billington et al., 1977; Pegler and Das, 1998) or Asian provenance (Sippl et al., 2013b). Our new data together with other recent results help to clarify the situation. The Hindu Kush earthquake zone outlines a structure that dips moderately, but clearly to the north between the Moho at ∼60 km depth and ∼140 km depth (Figs. 4.2, 4.6a-c). This is in agreement with the observations of Pegler and Das (1998), who inferred an Indian origin of the Hindu Kush slab based on the dip of the earthquake zone. That the north-dipping seismic zone is underlain by high velocity material on its southern side (Fig. 4.6a-c) strongly supports this interpretation. Any other configuration, e.g., a contorted and overturned slab of Asian origin would not comply with this geometric relation. Consequently, we infer that the Hindu Kush mantle anomalies belong to lithosphere that came from the south, from the Indian side.

Compared to the Hindu Kush, the Pamir velocity anomalies are bent and offset northwards (Fig 4.6), just as the Pamir seismic zone (Fig. 4.2) and tectonic structures (Fig. 4.1). Recent geophysical studies related the Pamir seismic zone (Sippl et al., 2013b) and associated mantle anomalies to depths of ∼180 km to subduction of Asian lithosphere (Sippl et al., 2013a; Schneider et al., 2013). The deeper Pamir velocity anomalies imaged here (Figs. 4.6d, e) likely represent the continuation of the same down-going Asian plate, as they overlap in the upper part with the structures imaged by Sippl et al. (2013a) and Schneider et al. (2013). Together with our inference on the provenance of the Hindu Kush slab, the currently available observations strongly suggest a two-plate model, where the Hindu Kush slab is subducting from the Indian side, detaching and abutting against the western edge of the arcuate Asian Pamir slab at depth. This configuration is sketched in Figure 4.8.

4.5.3 A scenario for the recent tectonic history of the western India-Asia collision

The problem remains how the peculiar configuration of two narrow plates of different continental origin subducting next to each other in opposite directions formed. While the Hindu Kush slab is straightforwardly explained as part of the subduction of the Indian slab, the retro-side subduction and along-arc stretching and tearing of the Asian Pamir slab is more difficult to explain. We suggest that the peculiar configuration of two slabs of different tectonic origin (Fig. 4.8) arises quite naturally when considering the shape, structure and rheology of India and Asia during the collision history. Paleomagnetic reconstructions, geological balancing, and global tomography (Van der Voo et al., 1999; Guillot et al., 2003; van Hinsbergen et al., 2011a) demand that before the Indian cratonic lithosphere (*Cratonic India* in Fig. 4.10) arrived at the Asian margin, some 1000 km of a (super-)extended passive margin, so-called Greater India, was subducted. Cratonic India's buoyancy, with its thick and stable Proterozoic crust and depleted mantle lid (Kumar et al., 2007), presumably choked the subduction zone, leading to the break-off of the Greater Indian slab (DeCelles et al., 2002; Stearns et al., 2013, 2015). Its remains are

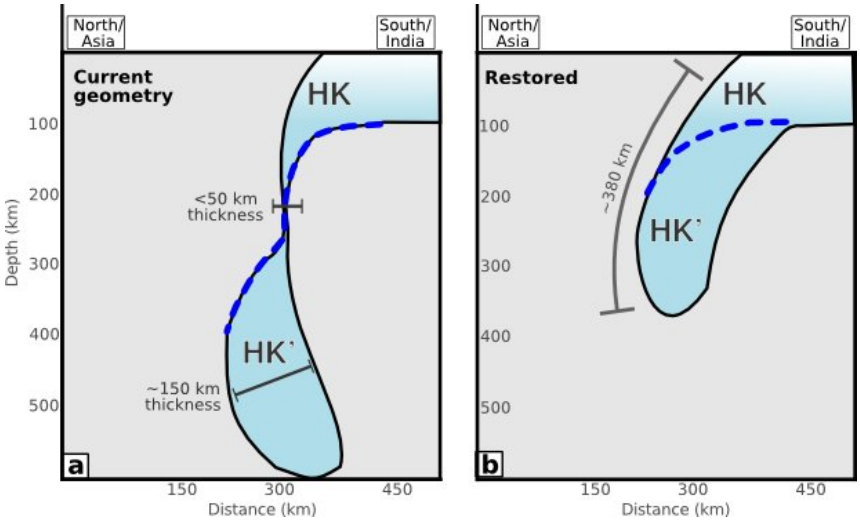

Figure 4.9: Sketch of slab-restoration for the Hindu Kush. a) Current situation similar to imaged Hindu Kush slab (Figs. 4.6a-c). **b)** Restored slab. Although addressing the mechanism of slab stretching is beyond the scope of this article, current geometry may have been achieved by simple shear extension as sketched; the final detachment is probably due to necking.

apparently resting now just below the mantle transition zone (Van der Voo et al., 1999; Replumaz et al., 2010; Capitanio and Replumaz, 2013, schematically sketched in the inset of Fig. 4.10a). After break-off of Greater India, the mode of convergence switched from subduction to underthrusting. Underthrusting of India might have been facilitated by the constitution of Asia's southern margin at the time. It was built by the amalgamated Gondwana terranes that form the Pamir, Karakorum and Tibet crust today (Guillot et al., 2003; Schwab et al., 2004). The lithosphere of these terranes was rheologically weakened by a long history of subduction, accretion, arc formation and tectonism (e.g., Schwab et al., 2004; Schmidt et al., 2011; Smit et al., 2014; Stearns et al., 2015). Although Asian and Indian rocks now abut along the Indus-Yarlung suture at the surface (Fig. 4.1), Indian mantle lithosphere and possibly lower crust underthrusted Asia several hundred kilometers further north (Nábělek et al., 2009; Kind and Yuan, 2010), reaching the Tarim basin in westernmost Tibet (Li et al., 2008) and also underthrusting the Pamir (Mechie et al., 2012; Sippl et al., 2013a). We suggest that the Tarim-Tajik cratonic lithosphere (*Cratonic Asia* in Fig. 4.10) constituted the first real obstacle for advancing Cratonic India as the Gondwana terrane collage further to the south likely lacked a lithospheric keel (e.g., Schwab et al., 2004; Schmidt et al., 2011; Smit et al., 2014; Stearns et al., 2015). Then, the first contact between Cratonic Asia and Cratonic India must naturally have occurred along India's western promontory. Its imprint is still visible in topography and structural grain from the western Himalaya to the northern Pamir (Fig. 4.1). As the two cratons started to collide here, it must have had consequences for the style of deformation.

We estimated that the central portion of the Pamir slab and the restored Hindu Kush slab have roughly a similar length (Section 4.5.1, Fig. 4.9). Rolling back the collision by this amount places the underthrusted Indian lithospheric spur along the straight line con-

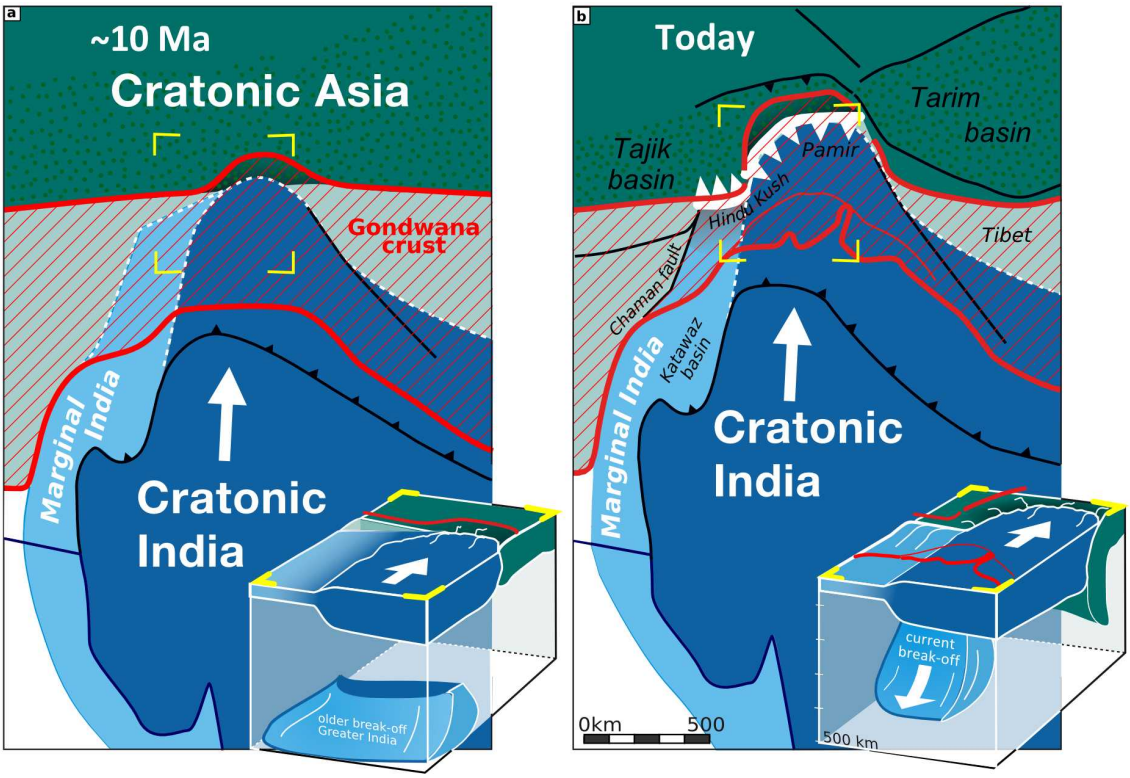

Figure 4.10: Evolution scenario of the western India-Asia collision zone for the ~10 Myr of collision history. Sketches outline the tectonic plates at depth, which differ from the boundaries at the surface (sutures as in Fig. 4.1). Insets focus on the Pamir-Hindu Kush, illustrating the plate interaction in perspective view (region and view point as in Fig. 4.8) **a)** At ~10 Ma, the Indian cratonic lithosphere (Cratonic India) impinges on Asian cratonic lithosphere (Cratonic Asia, comprising the basement of the Tarim and Tajik basins), pushing thickened crust, comprising rheological weak Gondwana crust (hatched red) on top. The previously subducted Greater Indian lithosphere (extended passive margin of India) has already detached along the entire collision front, allowing a rearrangement of the continental subduction system. **b)** Present: Cratonic India has underthrusted the Pamir, shortened the Gondwana crust, and indented Cratonic Asia, which delaminates and rolls back. The thinned and less buoyant crust of the western passive margin of India (Marginal India) tears off from Cratonic India and subducts under Asia.

nection between today's southern Tajik basin and southern Tarim basin (Fig. 4.10a). We suggest that this was the southern margin of Cratonic Asia, which got subsequently indented, forcing the Asian lithosphere to roll-back and forming the Pamir slab (Fig. 4.10b). India's western salient is delimited on its western flank by a deformed margin, which terminates at the present plate boundary along the Chaman fault system (Fig. 4.1b). The structure of this margin is well exposed in Pakistan's Katawaz basin (Fig. 4.1b), where strongly folded marine sediments overlie a thin transitional basement (Tapponnier et al., 1981; Treloar and Izatt, 1993; Mitra et al., 2006). It probably constitutes a vestige of India's extended continental margin (Replumaz et al., 2010), akin in structure and rheology to the vanished Greater India. Extrapolating India's now underthrusted western margin to the north, it naturally connects to the Hindu Kush earthquake zone (Fig. 4.1). We

consequently propose that the narrow slab that subducts under the Hindu Kush is India's extended western continental margin (*Marginal India* in Fig. 4.10). Convergence between India and Asia must have been accommodated differently for Cratonic and Marginal India due to their difference in buoyancy. While Cratonic India's buoyant spur penetrated into Cratonic Asia, Marginal India's thinner crust and denser lithosphere separated from Cratonic India and subducted beneath Cratonic Asia. At this point (at ∼10 Ma), the Pamir crust, which was pushed onto Cratonic Asia (the former connection of the Tajik and Tarim basins), was already critically thickened (Schmidt et al., 2011; Smit et al., 2014; Stearns et al., 2013; Stübner et al., 2013a; Stearns et al., 2015). Its load depressed the Asian lithosphere, initiating its subduction. Hence, to the extent that Cratonic India advanced into Asia and forced the Asian lithosphere to roll back under the Pamir, Marginal India subducted under the Hindu Kush, forming the two oppositely dipping slabs (Fig. 4.10b). The process of pushing back and bringing down the Asian plate is thus more akin to delamination than classic plate subduction, driven initially not primarily by gravitational instability but by the penetration of India. Rollback of the Pamir slab must have caused along-arc extension, recorded by the more shallow Pamir earthquake mechanisms (Fig. 4.6h). As the Pamir slab was forced to retreat in its center and was bent around the western corner of advancing Cratonic India, it tore apart in the middle (Fig. 4.8). If the Pamir slab became partly eclogitized (Sippl et al., 2013a), negative buoyancy would accelerate the roll-back and tearing.

4.6 Conclusion

The Pamir and Hindu Kush are the only place in the India-Asia collision zone where deep earthquakes occur, strong velocity anomalies penetrate deeply into the mantle and continental crust subducts to at least 150 km depth without the help of a leading oceanic plate. We evaluated seismic data from recent temporary deployments in the Pamir and Hindu Kush in order to understand why this happens. Using detailed seismicity, earthquake source mechanisms and stress inversions, and high-resolution tomographic images, we show that the Hindu Kush earthquakes are caused by the detachment of a foundering lithospheric plate sliver that once was India's continental margin. In contrast, the velocity anomaly under the Pamir is caused by Asian lithosphere (Cratonic Asia), which is forced to delaminate and roll back by the northward advancing promontory of Indian lithosphere (Cratonic India). While buoyant Cratonic India bulldozes into Cratonic Asia, the heavier Marginal India lithosphere tears off from Cratonic India and subducts. Hence, the different mechanical properties of the adjacent lithospheres (Marginal India versus Cratonic India) activated the two contrasting modes of convergence, side by side and coevally under Pamir and Hindu Kush, forming the two juxtaposed subduction zones observed today.

5 Upper and lower plate at once - a local earthquake tomography from the Hindu Kush-Pamir-Tajik basin continental subduction region

Abstract
The Tajik basin is locked at three sides between Central Asia's Tian Shan, Pamir and Hindu Kush mountains. At sub-crustal levels, the basin's lithosphere subducts eastward beneath the Pamir, but at the same time acts as backstop for Indian continental subduction beneath the Hindu Kush to the south. Both subduction processes are driven by the ongoing northward convergence of India towards Asia and are accompanied by intense intermediate depth seismicity. Here we want to illuminate the basin's lithospheric structure, aiming to understand why the lithosphere can feature such contrasting tectonic behaviors. We use ∼5300 local earthquakes, recorded by temporary seismic networks over four years to derive v_p (P-wave velocity) and v_p/v_s (P- to S-wave velocity) ratio models, which resolve the mantle at sub-crustal depths down to ∼280 km. In our velocity models, the intra-continental subduction zones are manifested as dipping low velocity zones, originating from crustal troughs and terminating at ∼160 km, although intermediate depth seismicity penetrates deeper. We interpret the two opposite dipping low velocity zones beneath the Pamir and Hindu Kush as subducted crustal material of Asian and Indian origin, respectively. The increase in seismic velocities deeper than ∼160 km might be attributed to the partial eclogitization of the subducted material. The Hindu Kush subduction seems to have pulled middle crustal fragments to depth, which detach deeper in the mantle due to their buoyancy. The Tajik basin's lithosphere exhibits a velocity change from a high velocity mantle lid to a heterogeneous low velocity domain at ∼120-140 km, then back to high velocities below this zone. This mid-lithospheric, sub-horizontal low velocity zone additionally exhibits anomalously low v_p/v_s characteristics and was interpreted as the MLD (midlithospheric discontinuity).

5.1 Introduction

The Pamir and Hindu Kush mountains, located north of the western Himalayan syntaxis, host the region of most intense intra-continental intermediate depth seismicity, worldwide (Fig. 5.1). The Pamir seismic zone had been associated to the subduction of Asian lower crust and mantle lithosphere (Sippl et al., 2013a; Schneider et al., 2013). The Hindu Kush zone arises from Indian-sided subduction and an ongoing slab break-off (Koulakov and Sobolev, 2006, Chapter 4), possibly also including the subduction of crustal material (Roecker, 1982). The Tajik basin, locked between the Pamir to its east, the Hindu Kush

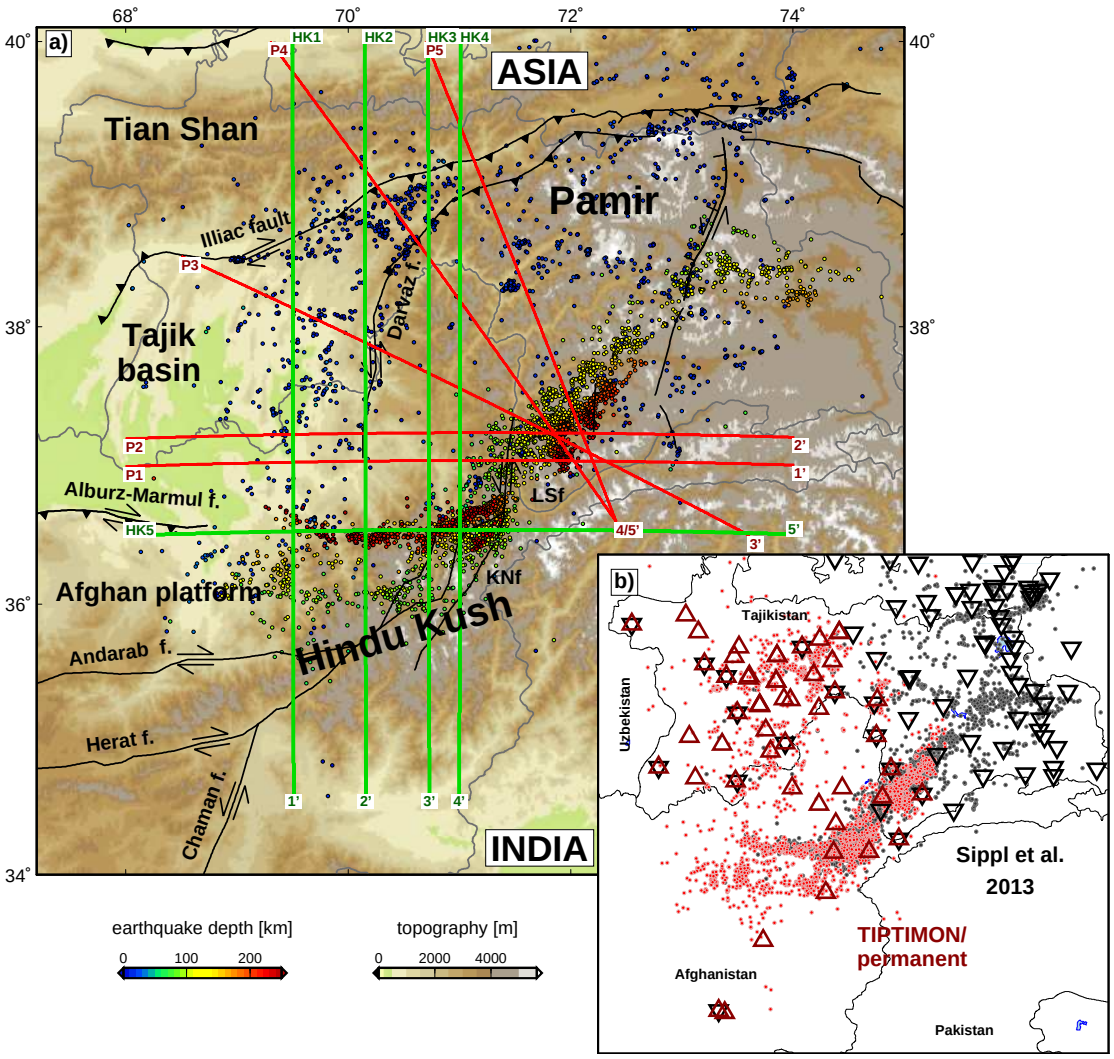

Figure 5.1: a) Tectonic setting, earthquakes used for tomography and cross section locations of Figures 5.9 and 5.10. LSf - Lake Shiwa Fault; KNf - Kapisa-Nuristan Fault. Faults after Schurr et al. (2014) and Chapter 4. **b)** Input earthquakes (circles) and stations (triangles), separated by color into the dataset already used by Sippl et al. (2013a) in gray and the new data added in this study (red).

to its south, and the Tian Shan to its north, plays a key role in the context of ongoing collision and continental subduction: on the one hand, the Tajik-basin lithosphere was shown to delaminate and rollback beneath the Pamir (Sippl et al., 2013b,a; Schneider et al., 2013), on the other hand it seems to form the hanging wall of the north-dipping Hindu Kush subduction (Chapter 4).

Here we want to understand how continental lithosphere can exhibit such contrasting properties in response to deformation within an extremely narrow spatial extent (e.g. ~150 km west-east extent of the Hindu Kush seismic zone). To achieve this, we make use of the deep sub-crustal seismicity, which is unusual for an intra-continental setting and provides the

unique possibility to study the deep lithospheric structure of an intra-montane basin and its interaction with its surroundings using the method of local earthquake tomography.

5.2 Tectonic setting

The Tajik basin forms an approximately 400 x 400 km wide crustal block occupying parts of Tajikistan, Uzbekistan, and Afghanistan (Fig. 5.1) and is covered by an up to 10 km thick, southward thickening sedimentary sequence. Within this sedimentary package, a layer of Jurassic evaporites decouples a mostly Neogene thin-skinned thrust-and-fold belt in post-Jurassic strata from Proterozoic-Jurassic units, largely undeformed during the Cenozoic (Hamburger et al., 1992; Gagala, 2014).
During the Paleozoic and Mesozoic, the Tajik and Tarim basins formed a continuous unit, the Tajik-Yarkand basin (Burtman and Molnar, 1993), which collided against Asia at ∼300 Ma, forming the Gissar suture. After suturing, the basin's lithosphere was heated from ∼290 to 240 Ma, possibly by a mantle plume (Sun et al., 2008; Zhang et al., 2011; Käßner et al., 2016). The North Pamir terrane collided against the southern edge of the Tajik-Yarkand basin in the Paleozoic, followed by the successive accretion of the other Pamir units. Different hypotheses exist on the early tectonic history of the basin, ranging from a Mesozoic marginal basin (Tapponnier et al., 1981) over a thinned passive continental margin (Leith and Alvarez, 1985; Kaz'min et al., 2010) to a foreland basin, already since the Mesozoic (Hamburger et al., 1992). India-Asia collision, initiating at ∼50-55 Ma (van Hinsbergen et al., 2011a), resulted in the northward indentation of the Pamir, overriding the Tajik-Yarkand basin and reactivating older sutures zones to strike-slip faults in the Hindu Kush (Treloar and Izatt, 1993) and as thrust faults in the Pamir (Burtman and Molnar, 1993). The onset of basin inversion initiated probably not earlier than ∼25-16 Ma (Sobel and Dumitru, 1997; Coutand et al., 2002). At ≤13 Ma, inversion of the Tajik basin, together with enhanced deformation of the southwestern Tian Shan, began (Käßner et al., 2016). Deformation was accompanied by counterclockwise vertical-axis rotation of the central and particularly the eastern Tajik basin strata (Pozzi and Feinberg, 1991; Bazhenov et al., 1994; Thomas et al., 1994).
Currently, the connection between the Tarim and Tajik basins is nearly severed and the Tajik basin is subject to west-east compression (Mohadjer et al., 2010; Zubovich et al., 2010; Ischuk et al., 2013), caused by the westward oriented gravitational collapse of the Pamir (Stübner et al., 2013b; Schurr et al., 2014) as well as to north-south compression due to the ongoing Indian indentation. These forces are accommodated by the sinistral transpressional Darvaz Fault and the dextral reverse Illiac Fault Zone to the east and north of the Tajik basin, and by the dextral-transpressional Alburz-Marmul and Andarab faults south of the Tajik basin in northern Afghanistan (see Fig. 5.1 for the location of these faults). The sinistral Kapisa-Nuristan and Lake Shiwa faults between the Pamir and Hindu Kush might translate the northward push from the Indian indentation, propagating along the Chaman Fault, into the central Pamir (Schurr et al., 2014).
At sub-crustal depths, the Tajik basin is framed by the Hindu Kush seismic zone to the south and the Pamir seismic zone to its east. Recent geophysical studies imaged a relatively thick crust of the Tajik basin (35-40 km; Sippl et al., 2013a; Schneider, 2014), which delaminates and rolls back forming an northwestward convex arc beneath the Pamir. At the same time, the basin lithosphere acts as a kind of backstop in the south, where

it abuts against the Hindu Kush seismic zone, which had been inferred to result from northward directed Indian lithosphere subduction and break-off (Koulakov and Sobolev, 2006, Chapter 4).

5.3 Data and method

5.3.1 Earthquake catalog

We reassessed earthquake catalogs recorded by several temporary and permanent seismic networks within Central Asia from 2008 to 2014 to generate input travel time picks for the local earthquake tomography: the core of this network was formed by the TIPAGE (Mechie et al., 2012), FERGHANA (Feld et al., 2015) and TIPTIMON (Schurr et al., 2012, 2013) seismic deployments. Further stations were added from all available regional networks summing up to 153 stations used here (Fig. 5.1b). Waveforms of the permanent stations were downloaded from the GEOFON, IRIS and Chinese Earthquake Network data centers. Most stations recorded with 100 Hz; spacing was ∼40-60 km in the western Pamir and Tajik basin.
Our combined dataset consists of arrival times of 5298 local earthquakes, yielding ∼101.000 P and ∼45.000 S picks (Figs. 5.2a, b). This input data is composed of two different subsets from networks operating between 2008-2010 (TIPAGE, FERGHANA) and 2012-2014 (TIPTIMON; see Fig. 5.1 for the components of these subsets). The data recorded by the TIPTIMON network was first used here for local earthquake tomography (LET). Picks from 2766 earthquakes had already been used by Sippl et al. (2013a) to calculate a LET focused on the Pamir. We include these travel times in the current study because the different networks share several common stations in the western Pamir and Tajik basin. Thus, the combined dataset will have a higher diversity of crossing rays beneath the basin and high resolution at the basin/Pamir transition where the TIPTIMON network terminates. Further, the output model will be a combined velocity model for the whole Pamir-Hindu Kush system which is of advantage for other seismological methods (e.g. precise earthquake relocation). The discussion here, however, will focus on the western part of the study region, for which no local earthquake tomography results have been published so far.

All phase picks were obtained using an automatic picking routine for local earthquakes (Sippl et al., 2013b). Strict selection criteria were applied to the automatically obtained picks: for the 2632 earthquakes finally included from the TIPTIMON dataset, we allowed only events with a minimum of 10 and 15 observations for shallow (<50 km) and deep events, respectively, an initial maximal root mean square (RMS) misfit of 1.2 and a maximal azimuthal gap of 240°. Additionally, we applied a de-clustering routine to the data so that not all events registered by the TIPTIMON network but only a high quality subset of the whole catalog was included. This step was aimed at reducing the number of events which would not add additional information but possibly introduce low quality picks and increase computation time during inversion.

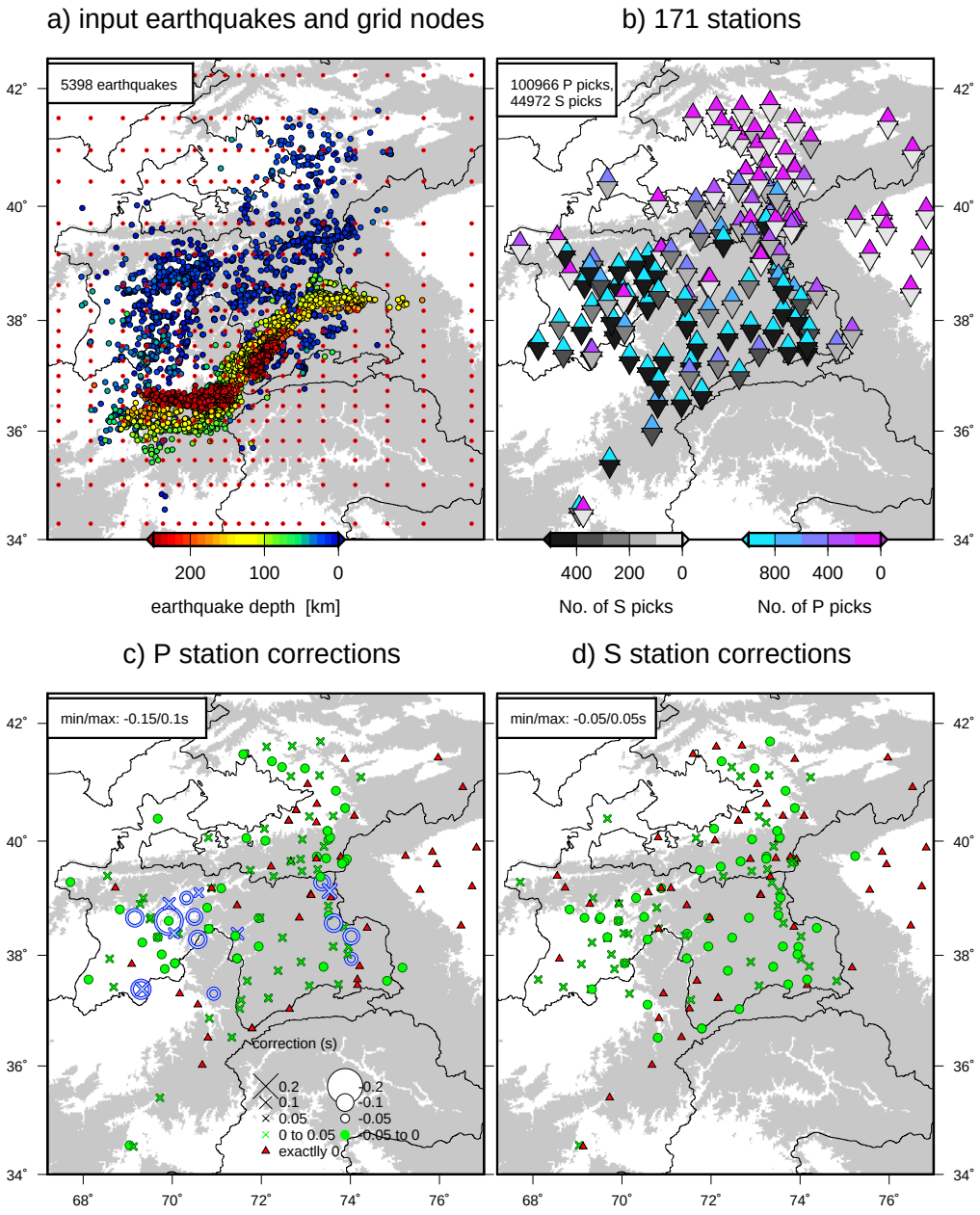

Figure 5.2: a) Input earthquakes for local tomography. The earthquakes were jointly relocated in the minimum 1D velocity model of Figure 5.3. Red dots are the locations of inversion grid nodes in map view. Topography higher than 2500 m in gray. **b)** Stations used, color coded by the number of picks obtained at the specific station. **c/d)** Final station corrections.

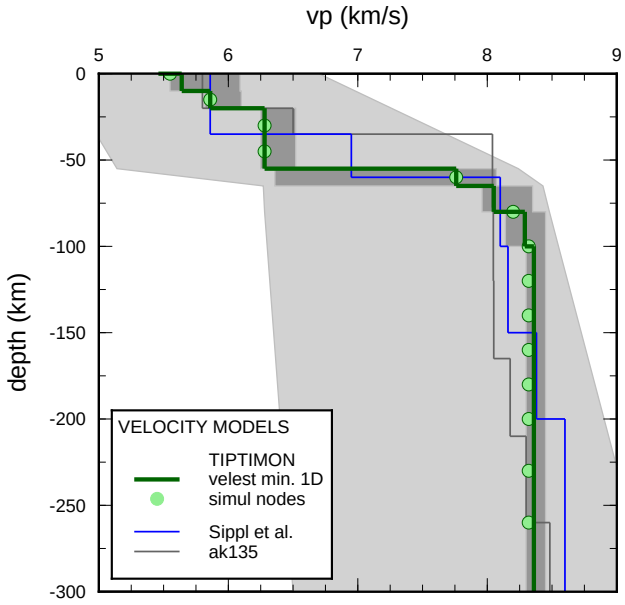

Figure 5.3: Minimum 1D P-wave velocity models from this study (green line; see also Supplementary Tab. C1) and from Sippl et al. (2013a) in blue. The light gray shaded area represents the range of input models tested during the inversion for the minimum 1D model here. The dark gray area represents the range of output models after inversion. Green circles are the velocities defined at the input nodal points for tomographic inversion. The global ak135 velocity model (Kennett et al., 1995) is shown for reference.

5.3.2 Local earthquake tomography

Tomographic inversion was performed with the software *simulps* (Thurber, 1983, 1993; Eberhart-Phillips, 1993; Evans et al., 1994). In *simulps*, v_p (P-wave velocity) and v_p/v_s (P- to S-wave velocity) ratio, hypocenter coordinates and origin times are calculated from the residuals between observed and predicted travel times using the least squares method (Menke, 1984). Ray tracing is performed by pseudo-bending (Um and Thurber, 1987). The velocity models are represented in Cartesian coordinates in a rectangular grid, consisting of nodes at fixed depth and x-y positions. Between the grid nodes, velocities are interpolated by linear b-splines. The roughness of the resulting velocity model can be adjusted using damping parameters for station terms, v_p and v_p/v_s.

The model presented here consists of 19x19x17 nodes in x- (positive in west direction), y- (positive north) and z- (depth; positive down) direction. Node spacing at the center (37°N/71.5°E) of the model domain is 35 km, which roughly equals to the average station spacing in the Tajik basin, and increases towards the edges. In the Pamir and Tian Shan, grid nodes were set up coarser than station spacing would allow as this study focuses on the Tajik basin. Depth layers were implemented in 15 km intervals in the crust and increased to 20 and finally to 30 km intervals in the mantle. A starting minimum 1D P-wave velocity

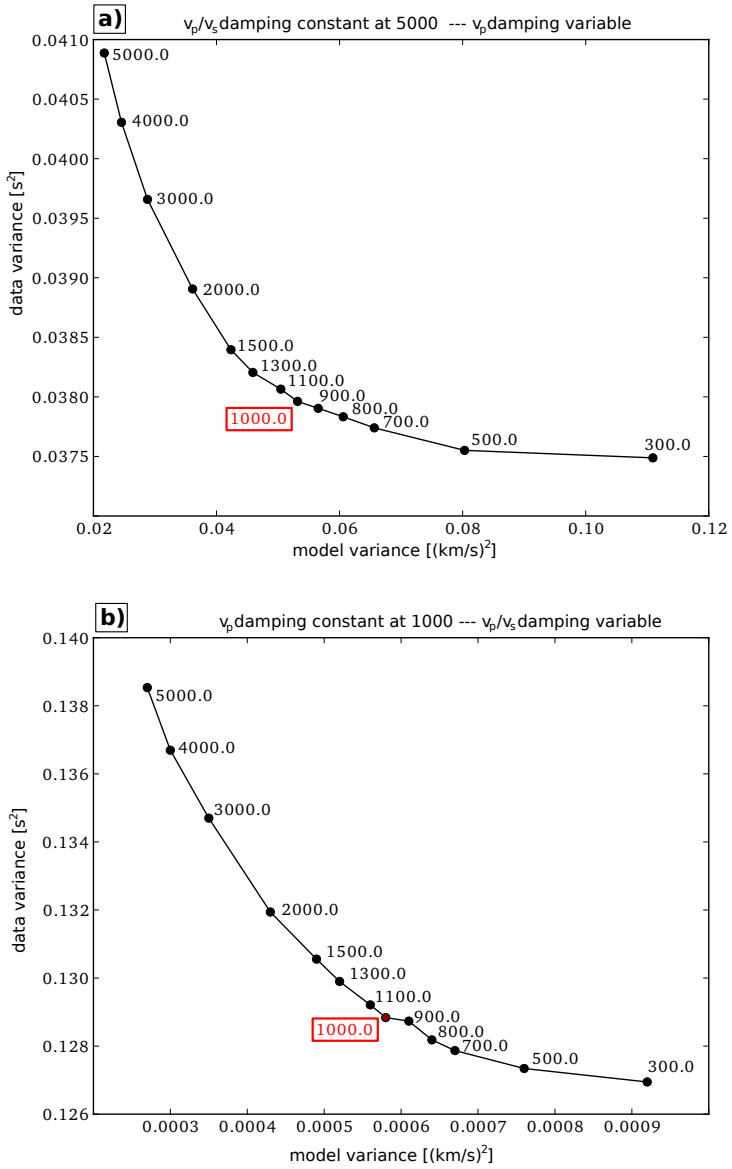

Figure 5.4: Trade-off curves between model and data variance to determine the best set of damping parameters. **a)** v_p-damping is varied with highly damped v_p/v_s. **b)** v_p/v_s-damping is varied while v_p-damping is set to the previously determined value (here: 1000).

model and initial v_p/v_s ratio was derived from a handpicked subset of the TIPTIMON catalog using the software *velest* (Kissling et al., 1994) and from a Wadati-diagram (see Supplementary Section C for more information regarding the minimum 1D model). As the minimum 1D model (Fig. 5.3; Supplementary Tab. C1) represents the average seismic properties of the region, it was used to relocate the whole input earthquake catalog and as a starting model for tomographic inversion. Suitable damping parameters were determined from trade-off curves in a multi-step procedure: we initially calculated several models using different damping values for v_p and over-damped v_p/v_s, to keep the v_p/v_s model

at its starting value of 1.72. The preferred v_p damping was determined from a trade-off curve (Fig. 5.4a), seeking to find the optimum between model roughness and data variance. Once the optimum v_p-damping was evaluated, a new set of inversions was run, keeping v_p damping at its optimum value and varying v_p/v_s damping (Fig. 5.4b). The best damping parameter was again determined from the trade-off curve. Station corrections were damped to a point where no systematic variation with tectonic structures could be observed any more (Fig. 5.2c, d), aiming to map relevant travel time residuals into the velocity anomalies rather than into the station corrections.
To further ensure a stable inversion, we kept the initial earthquake hypocenters fixed for the first two iteration steps. The inversion with the best set of damping parameters yielded a reduction of the data variance by 80% and 77% for v_p and v_p/v_s, respectively, after the 10th iteration. Additionally, we ran various inversions with slightly different grid spacing or damping parameters which yielded results very similar to the model presented here, aiming to ensure that the velocity structures discussed in the following were stable features.

5.3.3 Resolution and synthetic tests

The model resolution mostly depends on the ray coverage and the diversity of rays from different azimuths within a specific area. A single measure which contains information from both these quantities is the *spread* value, which we therefore used to assess the model resolution. We calculated the spread from the contributions of the non-diagonal elements of the model resolution matrix weighted by their distance from a specific grid node (Toomey and Foulger, 1989; Michelini and McEvilly, 1991). Off-diagonal elements in the model resolution matrix quantify the amount of smearing between different model parameters. Thus, the smaller the spread value, the better a specific node is resolved.
We used synthetic tests to determine a suitable threshold spread value to identify well resolved areas in our model domain. Synthetic travel times for these tests were calculated with a *simulps*-internal routine by ray tracing through a self-created velocity model. Gaussian noise was added to the synthetic travel times, scaled with the standard deviation of picking quality assigned earlier by the automatic picking routine (e.g. standard deviation of 0.05 for highest quality P picks and 0.8 s for lowest quality S picks; Sippl et al., 2013a,b). We tested two sets of synthetic models: first, ordinary checkerboards to constrain the overall extent of the resolved area. The checkerboard models (Fig. 5.5) consist of alternating positive and negative velocity anomalies, specified at each grid node relative to the background 1D velocity models. The P-wave velocity model varies by ±10%, the v_p/v_s ratio by ±5%, which is slightly less than the maximum amplitudes in the real data. Additionally, we designed more complex models (Fig. 5.6), whose geometry was inspired by the results gained from the inversion of the real data. Our considerations for the setup

Figure 5.5: Recovered anomalies from synthetic checkerboard tests for all nodal planes at crustal (**a**) and mantle depths (**b**). The amplitude of the synthetic input anomalies equals to the maximal range of the color scales (±10% for v_p and ±5% for v_p/v_s). v_p and v_p/v_s output anomalies are contoured in 2.5% and 0.025 intervals, respectively. Thick colored contours denote different spread values. Green circles are relocated earthquakes projected onto the depth section with a range of ± the half width of each section.

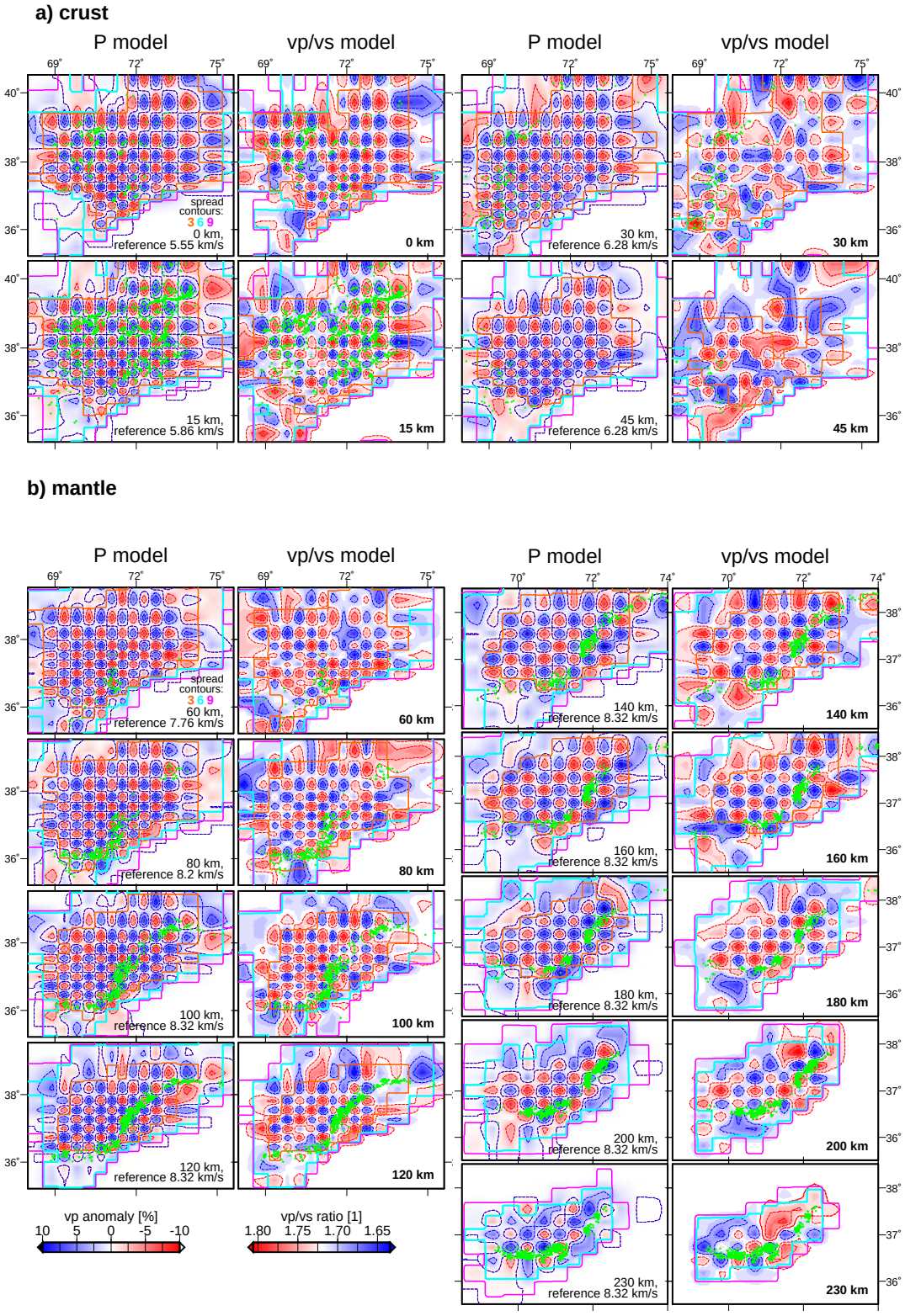

Figure 5.5: Checkerboard tests. See Figure caption on the previous page.

of these synthetic test will be explained in more detail in Section 5.5.1, after the presentation of the results. Here, we want to use the test only to constrain a suitable spread value. Checkerboards do not represent a realistic distribution of velocity anomalies in the subsurface, but the optimum damping used for inversion strongly influences the amount, size and amplitude of the anomalies within a domain. Thus, a new damping value for each set of synthetic tests had to be determined via trade-off curves. First, we varied v_p damping, while keeping v_p/v_s damping high and inverted with the optimum value. Then the same procedure was repeated for the v_p/v_s model. For the inversion of the complex synthetic tests, we used the same set of inversion parameters as for the real data. We consider this approach more useful in this case, as the synthetic tests were designed to mimic the real structures.

In Figures 5.5 and 5.6, the output velocity model after inversion and three contours of the associated spread value are shown in all node depth levels (Fig. 5.5) as well as in three representative cross sections (Fig. 5.6). The checkerboards are very well resolved within the contour with the smallest spread (orange in Figs. 5.5 and 5.6) and smeared but still distinguishable up to the middle spread value (turquoise contour). Within the middle spread value, the larger anomalies of the complex synthetic tests are still sharply resolved. Thus, we chose the intermediate spread value (turquoise contour) as resolution limit for further plotting, being aware that anomalies with less than ∼30 km (like the checkerboard anomalies) might be smeared at the edges of the domain.
In two subsurface areas, this spread value does not coincide with the well resolved model domain: in the 30 and 45 km depth layers of the v_p/v_s model, the resolution is particularly bad because only few earthquakes and less S picks than P picks were available in these depth ranges. Despite this lower resolution, we decided to install grid nodes in these layers to keep the same model geometry for v_p and v_p/v_s models and also to avoid a too big depth jump between two subsequent nodal depths. The second problematic area is the northernmost part of the mantle beneath the Tajik basin. Here, even the large anomalies in the synthetic test can hardly be resolved, probably due to too few crossing rays at the outermost periphery of our network. These dataset specific limitation have to be taken into account while interpreting the results and will be discussed in more detail subsequent to the results section.

5.3.4 v_p-v_p/v_s cross-plotting

The output of our inversion are two 3D velocity models for v_p and v_p/v_s. However, from laboratory measurements and numerical modeling studies, it is known that many natural rocks or metamorphic reactions within these rocks can be identified due to their specific v_p-v_p/v_s characteristics (Sobolev and Babeyko, 1994). Thus, the joint interpretation of v_p and v_p/v_s models yields better insights into the underlying processes than the interpretation of the models individually. To assess the v_p-v_p/v_s characteristics of our model in a more objective way than just comparing the individual plots, we introduced v_p-v_p/v_s cross-plots (Fig. 5.7). In these plots, we counted the occurrence of all v_p-v_p/v_s combinations in our tomographic model and identified areas with similar v_p-v_p/v_s characteristics based on local clusters and general lithological considerations (Fig. 5.7a, b). These regions were then projected back to their positions in the model domain using different colors

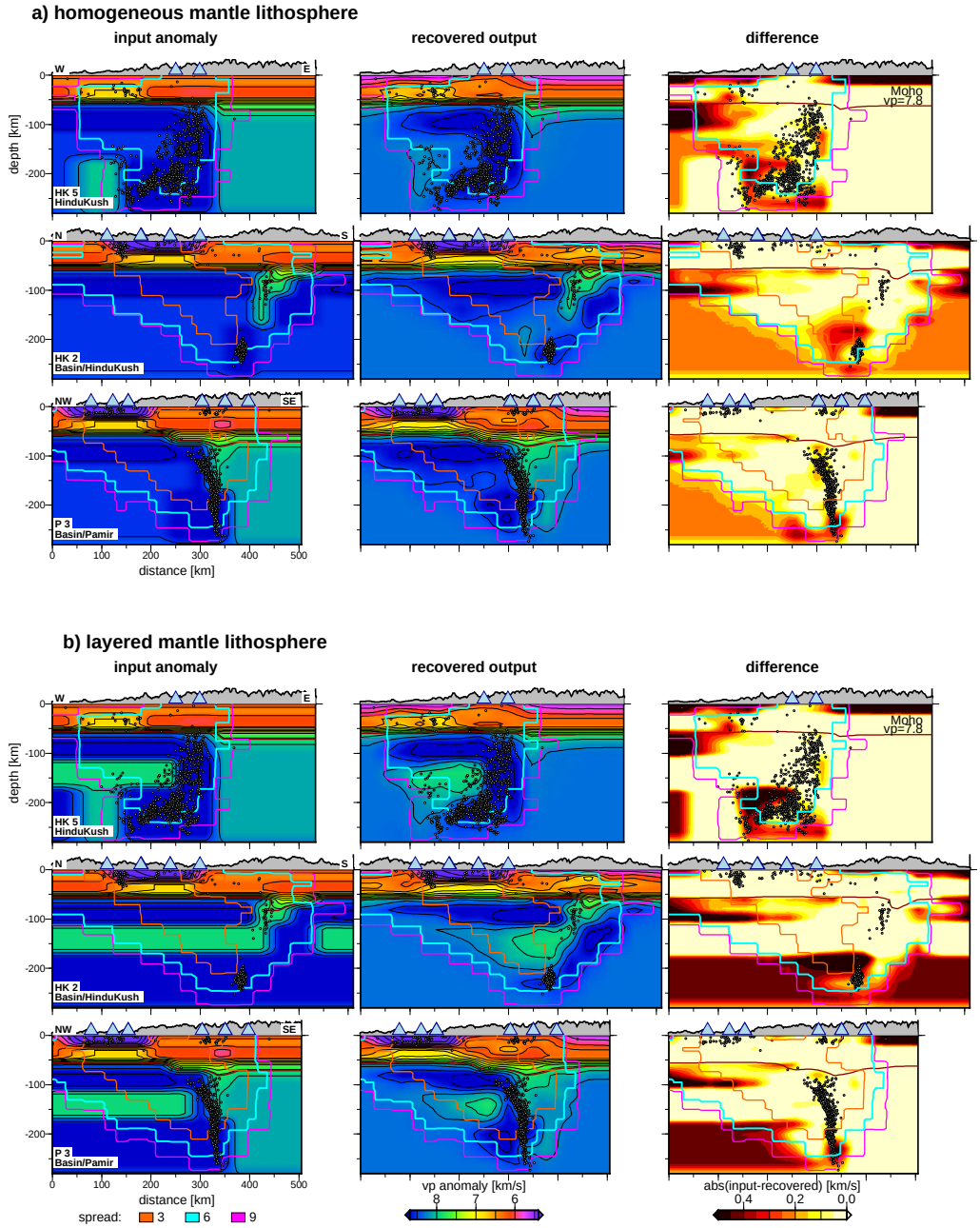

Figure 5.6: Synthetic tests to assess the reliability of the features discussed in the text (see Fig. 5.1 for the profile locations). *left column:* input model; *middle column:* output after inversion; *right column:* Difference between the two models. v_p and v_p/v_s output anomalies are contoured in 2.5 and 0.025 intervals, respectively. Projection range of seismic stations (blue triangles) and earthquakes (black circles) is ±15 km. Projected topography in gray. The dark red line in all plots is the 7.8 km/s contour, roughly representing the Moho depth constrained from receiver functions (Schneider, 2014). **a)** v_p model with homogeneous mantle lithosphere beneath the Tajik basin. **b)** v_p model with layered mantle lithosphere. **c)** v_p/v_s model from Sub-figure a).

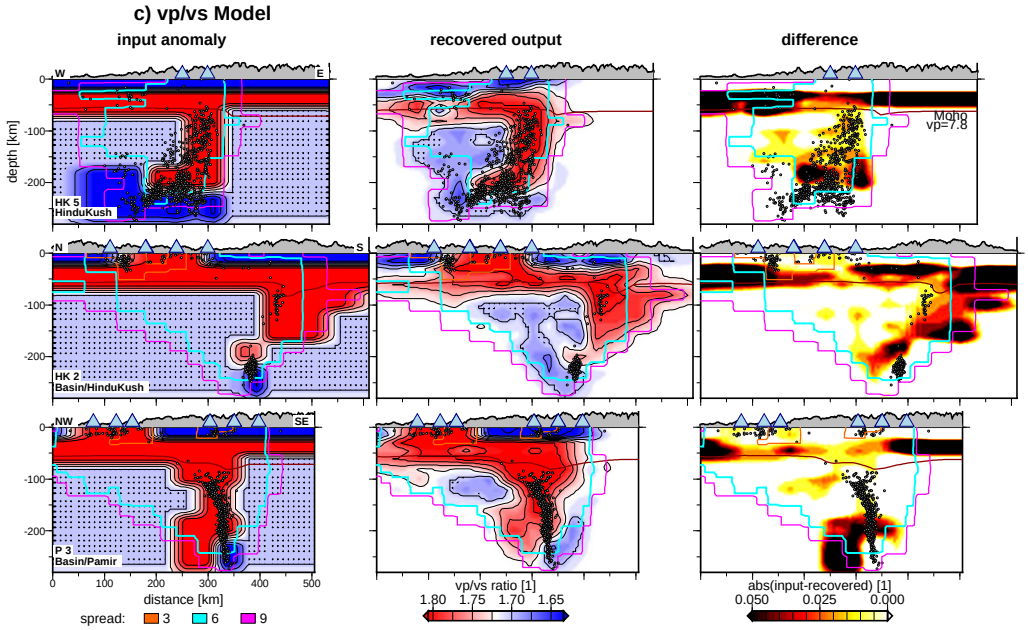

Figure 5.6: Continued.

(Fig. 5.7c, d). Such an approach allows identifying areas with a similar v_p-v_p/v_s pattern and interpret them in terms of lithology and possibly rheology.

Initially, we set up a master cross-plot (Fig. 5.7a), combining all v_p-v_p/v_s combinations from north-south profiles (from 40°-34.5°N) along the inversion nodes within the longitudinal range considered here (∼69°-73°E) and within the resolution limits, defined by the spread values in Section 5.3.3. In Figure 5.7a we can identify three separated main peaks. At low v_p (∼5.4-6.8 km/s), v_p and v_p/v_s are clearly linearly correlated (Peak 1 in Fig. 5.7a). At very high v_p (∼8-8.8; Peak 3), this correlation is less clear. The intermediate velocity peak (∼6.8-7.8; Peak 2) is approximately circular and has a relatively high v_p/v_s ratio (∼1.75).
Attributing these peaks to values measured from true rock samples is not straight forward, because the resolution and amplitude recovery of anomalies in tomography depends on the size and position of the initial anomaly as has been shown in the synthetic tests. Nevertheless, some first order relations can be inferred: the low and high velocity peaks (Peak 1 and 3) represent the contributions from crustal and mantle rocks. The positive linear v_p-v_p/v_s relation in the crust is an effect of increasing pressure and temperature with depth resulting in an increase of metamorphic grade and a decrease in silica content of the rocks (Sobolev and Babeyko, 1994; Christensen and Mooney, 1995). The intermediate peak (Peak 2) might represent lower crustal material (Mooney et al., 2002). The high velocity mantle peak (Peak 3) must encompass lithosphere and asthenosphere, as it spans a relatively large v_p interval. Given that seismic velocity variations in the mantle are mainly due to temperature and pressure changes, variations are expected to be much smaller than in the crust. Based on these considerations, we bundle the v_p-v_p/v_s domain into different units, separated by different color coding (Fig. 5.7b): crust, lower crust and

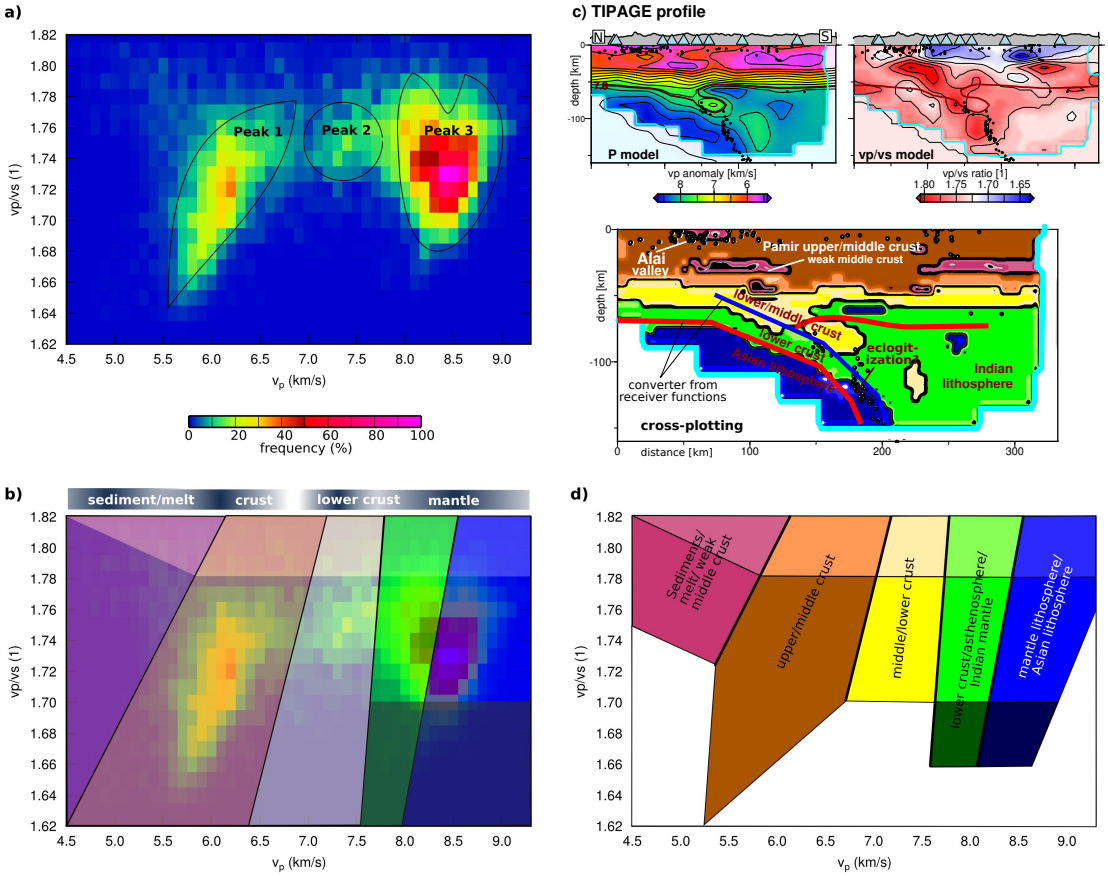

Figure 5.7: v_p-v_p/v_s cross-plots. **a)** v_p-v_p/v_s combination of the tomographic model, color coded by the frequency of occurrence. **b)** Separation of the v_p-v_p/v_s cross-plots into different units, based on the frequency peaks in Sub-figure a) and rheological considerations. Labeling of the sub-units after Sobolev and Babeyko (1994); Christensen and Mooney (1995) and Mooney et al. (2002). **c)** Cross-plotting scheme applied to the N-S TIPAGE profile along the central Pamir (Sippl et al., 2013a). Features in the v_p and v_p/v_s plots as in Figure 5.6. Labels in the cross-plot profile are based on the interpretations by Sippl et al. (2013a) and Schneider et al. (2013). **d)** Final color scheme for cross-plots and possible lithological interpretation.

mantle (composed of asthenosphere and lithosphere). The domain with lowest v_p and highest v_p/v_s does not fit into any of these categories as it does not follow the linear trend of the crustal peak. Thus, it was coded in a separate color (pink).

Before applying the cross-plotting scheme to our velocity model, we tested the classification on the probably best constrained transect of our study region: the north-south oriented TIPAGE profile through the central Pamir (Mechie et al., 2012; Sippl et al., 2013a; Schneider et al., 2013). Based on local earthquake tomography, numerical simulations and receiver function analysis (Sippl et al., 2013a; Schneider et al., 2013), it has been shown that Asian mantle lithosphere subducts beneath the Pamir, pulling a layer of

lower crust with it. This crust hosts the Pamir intermediate depth seismicity and partly eclogitizes at depth. Together with the lower crust, middle crustal material is dragged to shallow mantle depths.
Visualizing this tomographic image from Sippl et al. (2013a) using our cross-plotting units, we can clearly see advantages and restrictions (Fig. 5.7c): the crust, the subducted middle crust, the subducted mantle lithosphere and the different characteristics of the Indian lithosphere beneath the Pamir are distinguishable. It is not possible to resolve the contrast between subducting lower crust (∼10 km thickness) and the Indian mantle lithosphere because the thin crustal layer is below the resolution limit of local tomography (Sippl et al., 2013a). Nevertheless, the subducted crust shows up with a different color between middle crust and mantle lithosphere until the point where the crust eclogitizes (transition from green material, coinciding with the earthquakes, to blue material). This transition also coincides with the steepening of the dip of the seismically active region and might even be connected to a localized increase in v_p/v_s ratio at constant v_p (light blue patch in the cross-plots). In the crust, the sediments of the Alai valley and mid-crustal, possibly partly molten regions, stick out in pink.

Based on this example and the considerations in the paragraph above, we can annotate the color coded cross-plotting units with lithological characteristics (Fig. 5.7d). The separation is not totally unique. Particularly the distinction between high velocity lower crust and low velocity mantle is not defined within the color domain of our model. However, the cross-plotting clearly helps to identify certain trends in the v_p and v_p/v_s velocity models.

5.4 Results

Tomographic inversion of the real data resolves a complex 3D geometry in the subsurface beneath the Tajik basin and its surroundings. Figure 5.8 shows horizontal sections to illustrate the overall geometry of velocity anomalies. Further, we show two sets of profiles to illustrate the eastward and southward transition of the Tajik basin's lithosphere into the Pamir and the Hindu Kush, respectively (see Fig. 5.1 for profile location).

5.4.1 Crustal structure

At shallow crustal depths (Fig. 5.8a), the Tajik basin clearly sets itself apart from the surrounding mountains due to its low v_p and high v_p/v_s ratio, compared to the high v_p, low v_p/v_s upper crust in the Pamir, Tian Shan and Hindu Kush. At 0 km, the transition sharply matches the surface expressions of the Illiac Fault to the north and the Darvaz Fault to the east. At 15 km depth, the low velocity basin material already extends further under the Pamir mountains than the bounding fault at the surface. The high/low velocity partitioning between basin and mountains reverses in the middle and lower crust, where the Tajik basin basement is largely characterized by a high v_p anomaly, the mountains by low v_p, although the sub-division is less sharp and strict than in the uppermost crust.

The cross sections along the Pamir arc (Fig. 5.9) show a sub-horizontal continuation of the basement unit of the Tajik basin (*light brown* in the cross-plots) beneath the Pamir rocks (*dark brown*; in the following, colors in brackets always refer to the cross-plot colors).

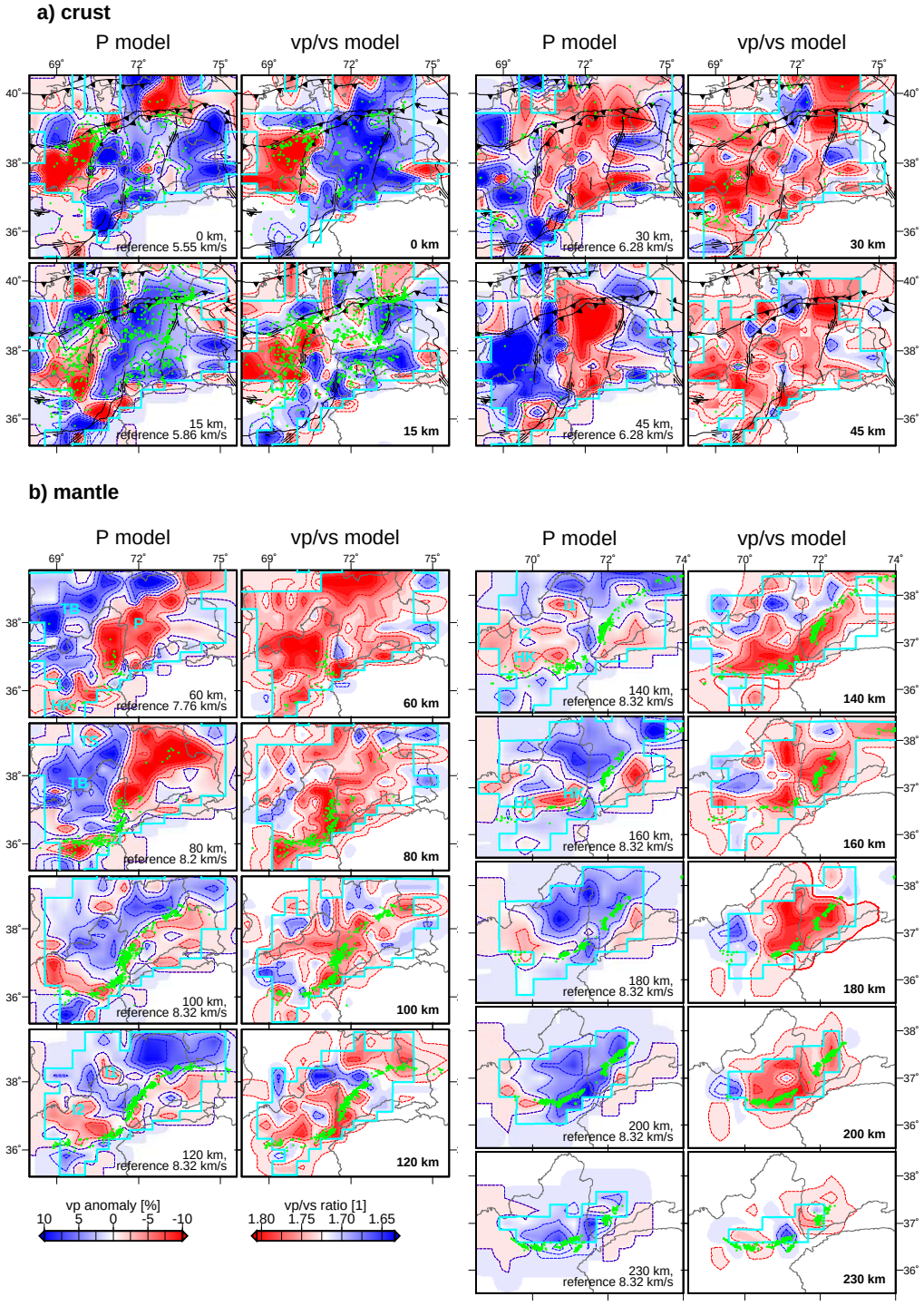

Figure 5.8: v_p and v_p/v_s depth maps from the inversion of the real data. The turquoise line marks the resolution limit. Letters refer to remarks in the text. Tectonic features as in Figure 5.1. All other plotted features as in Figure 5.5.

Eventually, the underthrust basin units bend further downward and find their geometric continuation in the Pamir seismic zone (profiles P1/P2). In contrast, the sediment layer (*pink*) on top of the basement units primarily abuts at the Darvaz Fault. Following the Pamir arc towards the northeast, the width of the Tajik basin and the amount of underthrusting beneath the Pamir subsequently decreases, but the crustal thickness directly on top of the intermediate depth earthquakes increases (*yellow* in profile P5).
In the south, the Tajik basin basement seems to underthrust the Hindu Kush crustal rocks (*light brown* units in profile HK1 of Fig. 5.10), building a south-dipping ramp, which, however, does not bend towards the mantle, as it is the case beneath the Pamir. Instead, the Hindu Kush seismic zone dips from the counter side, originating from a narrow crustal trough beneath the Hindu Kush (*yellow* units in profile HK1). Whereas the crustal seismicity at the basin-Pamir transition cuts off at ∼10-15 km along the Darvaz Fault, crustal seismicity penetrates deeper in the Hindu Kush.
In the north, where the Tajik basin abuts against the Tian Shan, basin sediments and basement form a south-dipping ramp (HK1/2). The western termination of the Tajik basin is outside the resolution limit of this study.

5.4.2 Mantle structure

The 60 km and 80 km depth sections (Fig. 5.8b) show the transition from crustal to mantle velocities, also accompanied by the onset of intermediate depth seismicity beneath the Pamir and Hindu Kush. These two domains, however, are clearly spatially separated (anomalies P/HK in Fig. 5.8). Beneath both mountain ranges, the uppermost intermediate depth earthquakes are associated with the thickest crust (*yellow* in Figs. 5.9 and 5.10). Deeper in the mantle, the thickened crust then evolves into zones of low v_p and elevated v_p/v_s (*green*), which enclose the intermediate depth seismicity. At ∼150 (Pamir) and ∼180 km (Hindu Kush) depth, the low velocity zones terminate and the seismogenic regions beneath Pamir and Hindu Kush are located in a high velocity domain (*blue*). These seismically active areas are still mostly associated with an elevated v_p/v_s ratio. The change from high velocity to low velocity also coincides with the steepening of the dip of the seismically active regions and is accompanied by a localized high v_p/v_s patch (small patchy *light blue* domain).

Despite these overall similar features, the Hindu Kush low velocity structure exhibits clearly lower velocities in the mantle than the Pamir structure (e.g. *yellow* patches in profile HK3/5 at 160 km depth) and a different geometry: at depths shallower than ∼160 km, the low velocity zone forms a dipping band of ∼40 km thickness which widens at ∼160 km depth to a blob-like low velocity domain (*green* in profile HK2). At its up-dip limit at 65 km depth, v_p is as low as ∼7.1 km/s. Within this low velocity band, the seismic velocity is generally between 7.8-8.0 km/s, but locally lower than 7.6 km/s in the center of the low velocity nest at ∼160 km depth (*yellow* domain in profile HK3). The steepening of the seismogenic region beneath the Hindu Kush is much sharper than in the Pamir and associated with an aseismic region at ∼160-180 km, which spans over the whole longitudinal range of the Hindu Kush seismicity. The renewed onset of the deeper intermediate depth seismicity is then closely connected with the upper contour of the underlying high

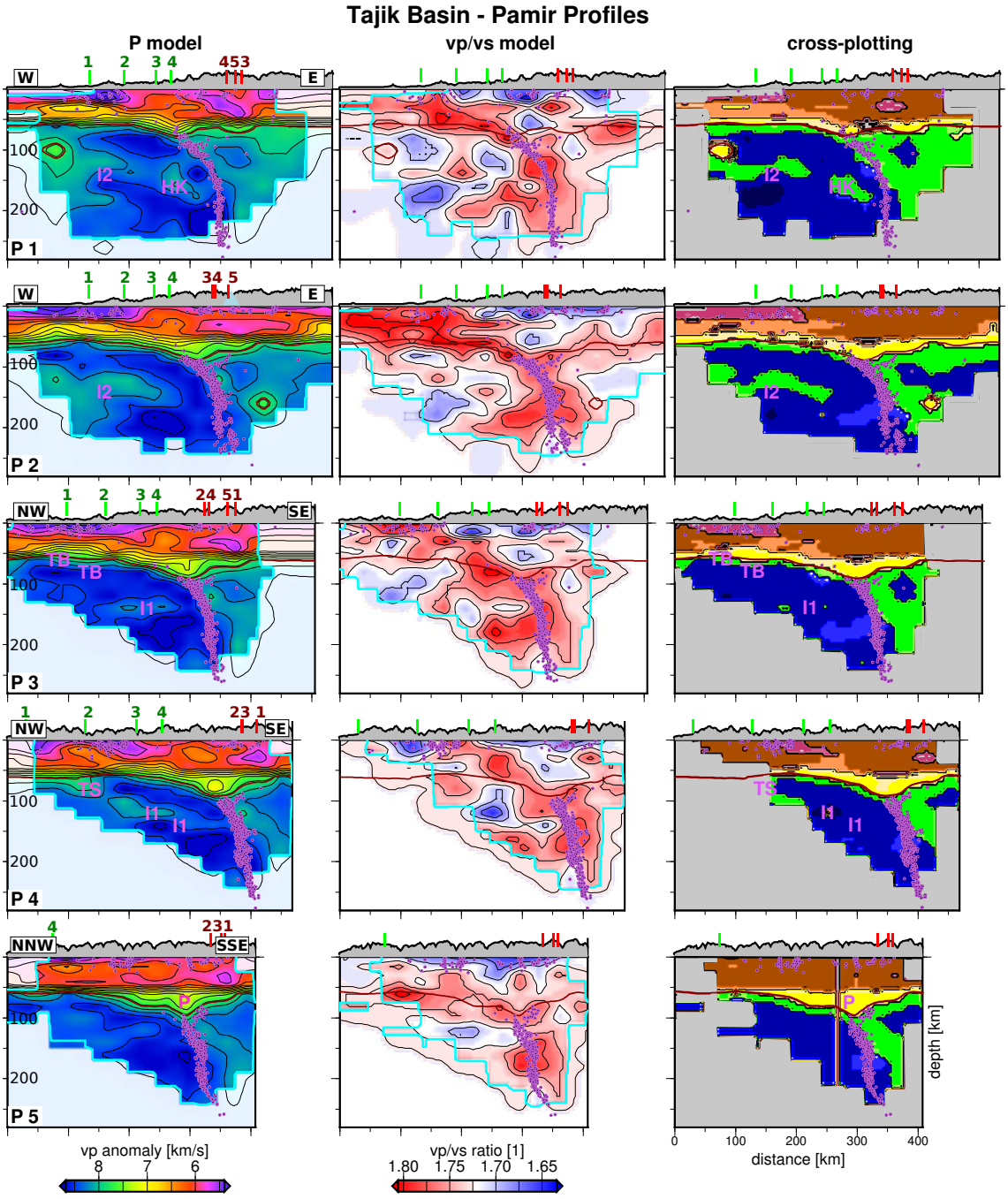

Figure 5.9: Vertical profiles for v_p (*left column*), v_p/v_s (*middle column*) and cross-plots (*right column*), cross-cutting the Tajik basin and Pamir perpendicular to the Pamir seismic zone (see Fig. 5.1 for the profile locations). Turquoise line marks the resolution limit. Letters refer to the remarks in the text and are projected from Figure 5.8 into the cross section. Earthquakes in the cross-plots in pink, color coding according to the legend of Figure 5.7d. Vertical ticks on top of the cross sections mark the position of crossing profiles (green: Hindu Kush profiles; red: Pamir profiles). All other features as in Figure 5.6 (except the seismic stations, which are not projected onto the topography here).

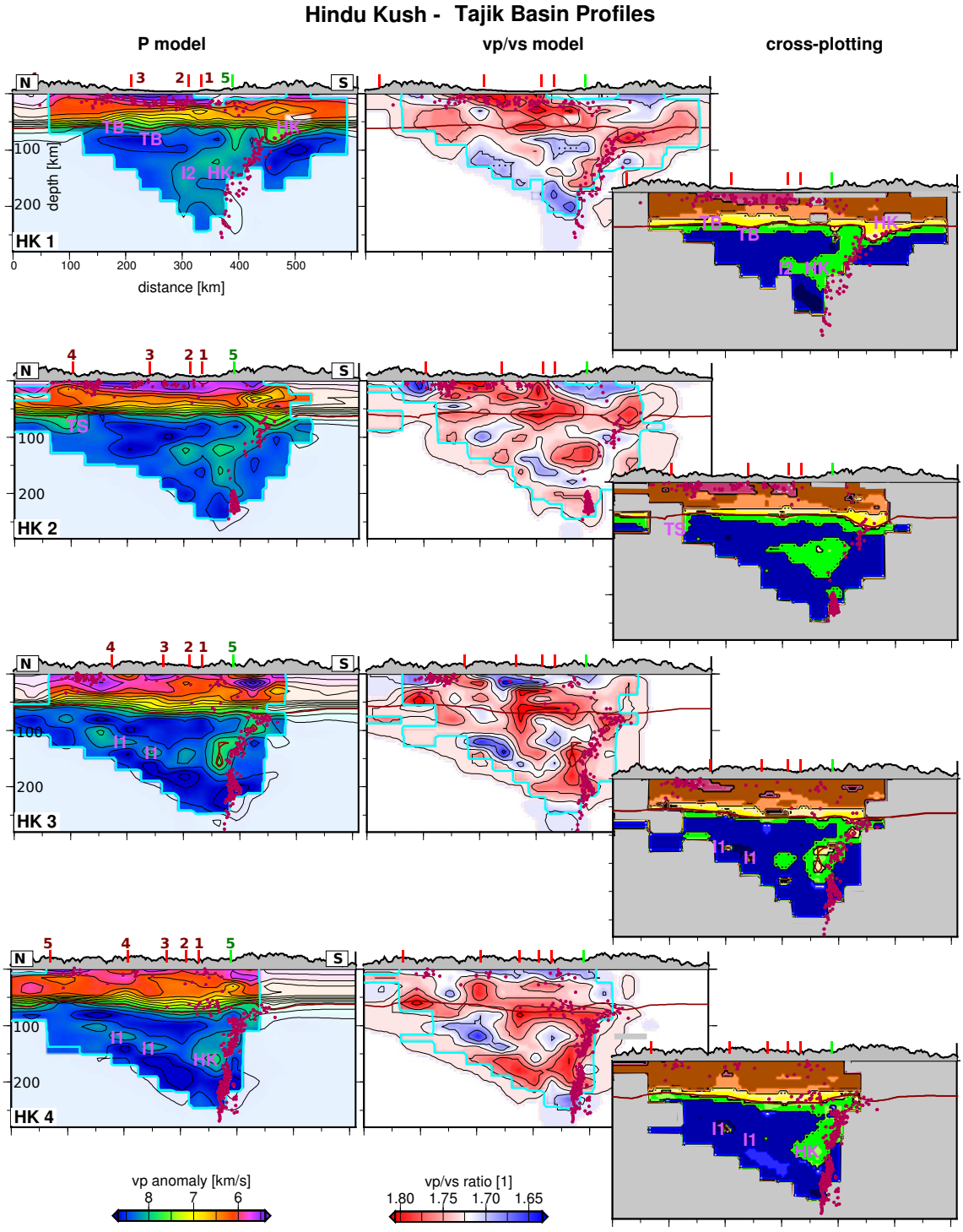

Figure 5.10: Vertical profiles cross-cutting the Hindu Kush and Tajik basin (see Fig. 5.1 for the profile locations). All other plotted features as in Fig. 5.9.

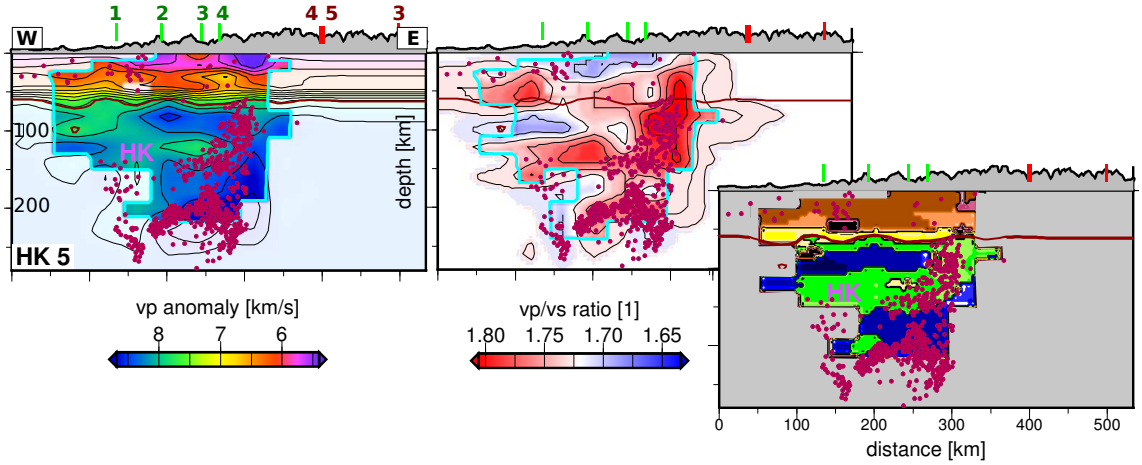

Figure 5.10: Continued.

v_p domain (profile HK5).

Sub-crustal units beneath the Tajik basin have clearly higher v_p than those beneath the Pamir (dominantly *blue* vs. *green* in the cross-plots) and approximately similar v_p as the lithosphere south of the Hindu Kush intermediate depth seismicity. The Tajik basin lithosphere is internally split into three parts: (1) a high velocity lid (60-100 km depth in Fig. 5.8b), which surrounds the Pamir low velocity anomaly in an arc like shape and terminates sharply against the Hindu Kush low velocity anomaly (e.g. 80 km section in Fig. 5.8). (2) A discontinuous sub-horizontal layer of lower velocities at ~120-140 km, consisting of spatially restricted low v_p patches (*I1* and *I2* in Fig. 5.8b). These patches feature partly very low v_p/v_s ratios. (3) Beneath this discontinuous layer, the Tajik basin's mantle exhibits higher velocities again.
Tracking the low velocity domain beneath the Tajik basin in the cross sections only based on the v_p characteristics is difficult, as these profiles cut through the different isolated low velocity patches in the Tajik basin's mantle (*I1/2*) and the thickened crust (*P/HK/TS*) in a partly oblique manner. However, due to their different orientations or different v_p/v_s characteristics, the features are separable (compare e.g. the v_p and cross-plot of profile P4).

5.5 Discussion and interpretation

5.5.1 Reliability of the resolved anomalies

As already noted in Sections 5.3.3 and 5.3.4, the resolution depends not only on the size and amplitude of a specific anomaly, but also on the position and amplitude of the adjacent anomalies. Outside the resolution limit, the velocity in the output model just equals the background 1D velocity model. Here we want to investigate to which extent the features just described are resolvable in our model and how they are influenced by the starting velocity model.

The synthetic models in Figure 5.6 mimic the most striking features of the real data: the Tajik basin, consisting of sediments and basement; the thickened crust beneath Pamir and Hindu Kush and a layer of crustal material dipping into the mantle, underlain by high velocity lithospheric slabs; additionally, a low velocity mantle beneath the Pamir. To clarify to which extent the sub-horizontal low velocity zone in the Tajik basin's mantle is resolvable, we vary the character of the basin's lithosphere in two separate synthetic models to have homogeneous high velocities or to feature a velocity alternation from high to low and back to high velocities (Fig. 5.6a and b, respectively). In both models the v_p/v_s ratio is low in the upper crust beneath the mountains and elevated in the upper mantle as well as in the subducting lithosphere. Further, the v_p/v_s ratio is high in the sediments and crust beneath the Tajik basin (Fig. 5.6c).
Results (middle panel in Fig. 5.6) show that the v_p resolution in the whole crust is particularly good. Despite the complex pattern, the variation between the input and recovered anomalies is smaller than 0.1 km/s (right panel in Fig. 5.6). The Moho contour could be clearly recovered, even in the domains of localized crustal thickening beneath Pamir and Hindu Kush. Thus, the underthrusting of the Tajik basin basement and the crustal thickening directly on top of the intermediate depth seismicity is resolvable. In the v_p/v_s model (Fig. 5.6c), the transition from low to high v_p/v_s ratios beneath the mountains is generally resolved, however, the sharp contrast in the input anomaly is slightly smeared. These crustal layers had already been identified in the checkerboard recovery as less well resolved (Fig. 5.5).
At mantle depths, the general pattern of anomalies is well recovered (e.g. the difference between Pamir, Tajik basin and Hindu Kush mantle). However, especially deeper than ~100 km, the amplitudes of the recovered anomalies of v_p and v_p/v_s are overall smaller than the input. This amplitude decrease has the highest impact on thin structures. The low v_p zones surrounding the intermediate depth seismicity, for instance, appear to terminate at shallower levels (profile HK2 in Fig. 5.6). Thus, the low velocity features beneath the Hindu Kush might either penetrate deeper or be thicker than resolved here. Mantle anomalies near the northwestern resolution limit of the tomography (western Tajik basin) are less well recovered (difference between input and output more than 0.2 km/s for v_p), and amplitudes nearly drop back to the background velocity model. In the real data, the deep Tajik basin mantle shows up with higher velocities than the background model (e.g. profiles HK3/4 in Fig. 5.10). Given the generally smaller recovered amplitudes at this position in the synthetic tests, the true velocities in the deep Tajik basin mantle are probably even higher than resolved here. The model with the layered mantle lithosphere (Fig. 5.6b) resolves the alternating pattern, albeit the deeper velocity change being slightly more smeared than the shallow one. Thus, neither the high velocities deep in the mantle below the Tajik basin nor the low v_p intersection seem to be an artifact.

The second test series deals with the reliability of absolute velocities: during inversion, the *simulps* code seeks to minimize the overall misfit by solving for hypocenter locations, v_p, v_p/v_s ratio and station terms. The initial velocity model affects the inversion as the input earthquakes are initially relocated in this model and theoretical travel times are calculated on the basis of the underlying velocities. The initial velocity model used here is a minimum 1D velocity model focusing on the Tajik basin and Hindu Kush (green curve in Fig. 5.3; Supplementary Section C). Compared to ak135 (gray curve in Fig. 5.3), it

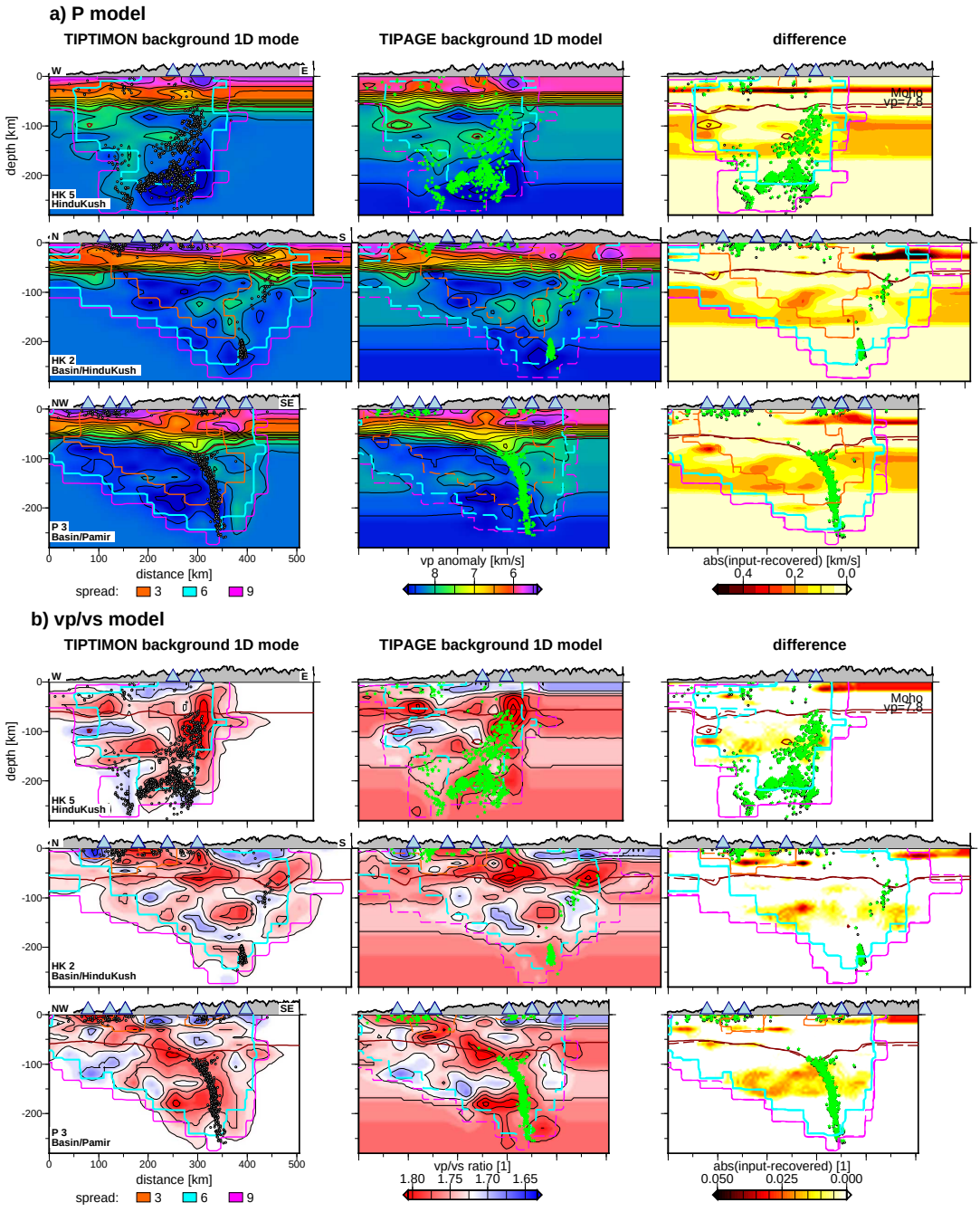

Figure 5.11: Comparison between the output velocity models for two different starting 1D velocity models. TIPTIMON refers to the minimum 1D model derived in this study, TIPAGE to the Sippl et al. (2013a) model (Fig. 5.3). Relocated earthquakes plotted in black and green for the two models. Spread and Moho contours in the model based on the TIPAGE 1D model are dashed. **a)** v_p, **b)** v_p/v_s models. All other plotted features as in Figure 5.6.

has strikingly high upper mantle velocities. Such an effect could arise because ray paths used to deduce the local model were mainly sampling the high velocity mantle lid of the Tajik basin. Starting with such a model might affect the whole inversion. Thus, to assess this dependence we run the inversion additionally with the TIPAGE minimum 1D model (black curve in Fig. 5.3), constructed by Sippl et al. (2013b), focusing on Pamir and Tian Shan. This model has lower velocities in the upper mantle and a different crustal structure (black curve in Fig. 5.3).
Figure 5.11 shows the comparison of the two inversion results. The general arrangement of low/high velocity anomalies is conserved for the v_p as well as for the v_p/v_s model. In the crust, the absolute velocities and the Moho depth agree very well. However, especially in the mantle deeper than 100 km, the amplitude of the anomalies is partly shifted towards the initial velocities of the background model. Nevertheless, in both models the dipping low velocity material and the velocity alternation in the Tajik basin lithosphere are clearly resolved. The geometrical shape of the deeper anomalies in the mantle, however, might vary in the order of several kilometers.

5.5.2 The Tajik basin's crust and its response to deformation

The Tajik basin's crust can be clearly identified due to its low velocity sedimentary cover and the high velocity basement compared to the surrounding mountains. Crustal thickness is ∼40 km and does not change significantly in north-south direction, indicating that no pronounced north-south oriented crustal thickening occurs in the basin interior. At its northern and southern termination, the sediment-basement package builds two south-dipping ramps. To the north, Tian Shan rocks underthrust the basin along the Illiac Fault. To the south, the basin underthrusts the Hindu Kush beneath the North Afghan Platform (e.g. profile HK1). To both sides, the underthrusting does not penetrate further than ∼50 km beneath the mountains. Instead, crustal thickening occurs within the adjacent lithological units north and south of the Tajik basin (anomalies HK and TS below Hindu Kush and Tian Shan). The position of this localized thickening in the crust resolved here is also in good agreement with crustal thickness maps constrained by receiver functions (Schneider, 2014). The northern anomaly of these, the west-east striking anomaly TS, directly underlies the Illiac Fault, suggesting that the crustal thickening at the basin's northern margin could be related to the reactivation of the Paleozoic Gissar suture, which obviously represents a zone of weakness. To the south, the Hindu Kush thickened crust grades into the Hindu Kush continental subduction zone, also a zone of weakness. Thus, the northward push of the Indian indenter seems to result in enhanced north-south deformation in the tectonic units at the edges of the basin crust but not in internal thickening of the basin itself. Crustal seismicity in the Hindu Kush penetrates deeper than in the basin. This might indicate intense deformation in the Asian units squeezed between the Tajik basin and the Hindu Kush subduction or a colder geotherm than in the Pamir.
In contrast, at the eastern termination of the Tajik basin, the upper part of the sedimentary cover terminates at the Darvaz Fault, but the basement rocks of the Tajik basin underthrust sub-horizontally further beneath the Pamir crust, implying a certain degree of decoupling along an interface within the basin units. Schurr et al. (2014) suggested the evaporite decollement near the base of the sediments as a possible candidate. Seismicity mapped here in the basin indeed clusters along a horizontal interface at ∼10-15 km, sup-

porting this hypothesis.

Thus, deformation in the Tajik basin crust seems to be partitioned sharply at the edges and within the basin (as schematically sketched in Fig. 5.12): in north-south direction, the Tajik basin crust acts as a strong, rigid block, which transmits the stresses, rather than deforming internally. In west-east direction, the basement underthrusts beneath the Pamir. Whereas the bounding faults at the north and south of the Tajik basin appear as crustal scale features, the Darvaz Fault to the east decouples upper crustal and deeper processes. This is in good agreement with the intense folding of the sedimentary cover on top of the evaporites and the smaller amount of deformation in the underlying units (Hamburger et al., 1992; Gagala, 2014).

5.5.3 Subduction of continental crust in the Hindu Kush

We further want to assess how the localized crustal thickening south of the Tajik basin beneath the Hindu Kush is related to the intermediate depth seismicity. In the Pamir, a similar configuration (Moho trough and a low velocity layer hosting the intermediate depth seismicity) has been attributed to the subduction of continental crust (Sippl et al., 2013a). In the Hindu Kush, subduction of continental crust has been already suggested by Roecker (1982) based on a low velocity domain imaged by early local earthquake tomography and by Mishra et al. (2012) from gravity anomalies. In accordance with Roecker (1982), we imaged a pronounced low velocity zone beneath the Hindu Kush (anomaly HK), which partly falls together with the intermediate depth seismicity. Following the annotation of the cross-plots (Fig. 5.7), this green domain could be associated to lower crust or asthenosphere. The synthetic tests showed that the amplitudes of thin mantle anomalies are generally underestimated. Thus, the seismic velocities in this layer might be lower than the 7.8-8.0 km/s resolved here. As the low velocity domain also features elevated v_p/v_s ratios and appears as a continuous zone that connects to the crust at its up-dip limit, a crustal origin of the anomaly seems more likely. The blob-like structure at ∼160 km, which features the lowest velocities (7.6 km/s), however, appears fragmented and has clearly too low velocities for mantle material. Thus, the low velocity layer beneath the Hindu Kush could encompass two units of the crust, which behave differently at depth: the blob-like anomaly associated to the yellow domain might be middle crust, as it is aseismic and its v_p-v_p/v_s characteristics are similar to the mid-crustal material mapped in the TIPAGE profile across the Pamir (Fig. 5.7c). The bulk of the sheet-like green domain could be subducting lower crust, as it hosts the intermediate depth seismicity and clearly differs from the underlying mantle lithosphere. Further, the thickness of this subducting crustal unit seems to be less than the total crustal thickness in the Hindu Kush. Thus, the relatively deep crustal earthquakes we here imaged beneath the Hindu Kush might not only occur due to the squeezing of the Asian backstop units as suggested above, but could also result from the decoupling and accretion of the upper crust, which is too buoyant to subduct (see schematic sketch in Fig. 5.12).

Despite some similarities, the Hindu Kush subduction zone differs from the Pamir. In the western Pamir, no velocities lower than 7.8 km/s occur at sub-Moho depth (profile P1/2). In the central Pamir (TIPAGE profile; Fig. 5.7c; Sippl et al., 2013a) the low velocity patch

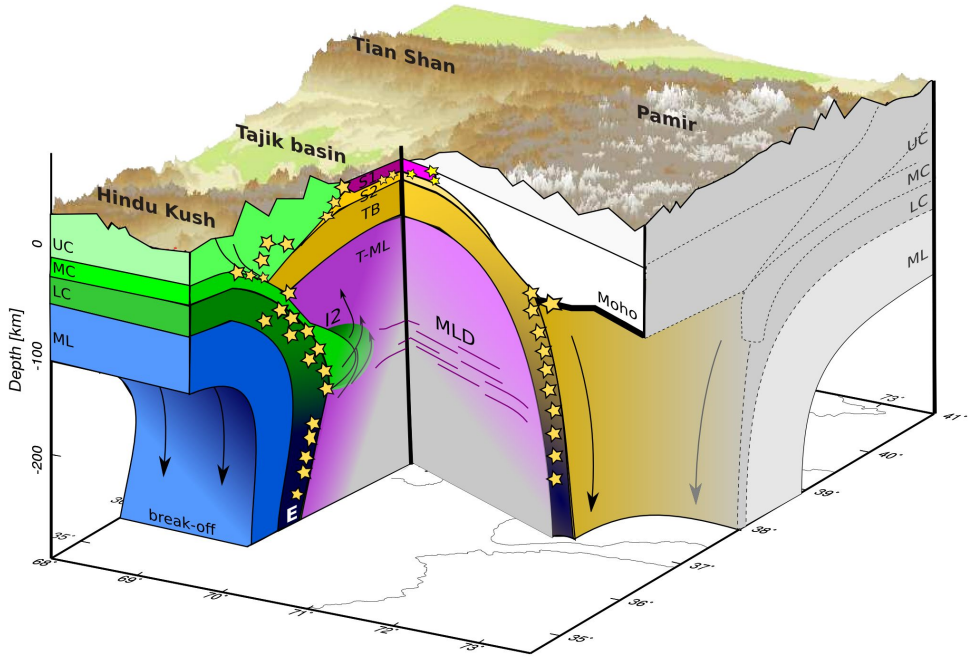

Figure 5.12: Simplified sketch of our interpretation, cross-cutting the Pamir-intermediate depth seismicity and the Hindu Kush intra-continental subduction zone in its western part. Hindu Kush units in green and blue (UC/MC/LC - upper, middle and lower crust; ML - mantle lithosphere); Pamir units in gray (adopted from Sippl et al., 2013a). Tajik basin units in brown/yellow and pink (S1/S2 - post- and pre-Jurassic sediments; TB - basement; T-ML - mantle lithosphere; the gray shaded region in the deep Tajik basin marks the resolution limit of the tomography presented in this study): Indian-sided subduction and entrainment of lower and middle crustal material beneath the Hindu Kush causes the local weakening and possibly asthenospheric inflow into the Tajik basin's mantle lithosphere (I2). The subducted crustal material partly subducts and eclogitizes (E), partly detaches. The Tajik lithosphere at the same time subducts eastward beneath the Pamir. A midlithospheric discontinuity (MLD, label I1 in the Figures showing results) splits the high velocity mantle lithosphere of the Tajik basin at ∼120-140 km depth. Stars mark regions of seismic activity. At crustal depths, the Tajik basin shows little internal thickening. It is overridden by the Pamir and Hindu Kush mountains asymmetrically: the whole crust forms a ramp to the south (Hindu Kush), whereas the Post-Jurassic sedimentary cover detaches from the basement in the east (Pamir). Only the pre-Jurassic and basement units subduct beneath the Pamir.

in the mantle, which has been interpreted as middle crustal entrainment, is still connected to the thickened crust of the Pamir. In contrast, parts of middle crustal material seem to be pulled to greater depths in the Hindu Kush. It has been shown in numerical simulations that middle crust can be pulled to such depths despite its buoyancy if the coupling between middle and lower crust is relatively strong or if convergence rate is relatively fast (Duretz and Gerya, 2013). The second of these reasons might be the case in the Hindu Kush, as the subducting Indian slab is in the process of break-off (Chapter 4). This break-off, in turn, might be accompanied by an accelerated of the subduction velocity at depth (Duretz et al., 2012). Accelerated subduction velocities in turn could be responsible for the deep subduction of crustal material. The accumulation of low velocity material at ∼160 km

might represent the point where the forces between gravitational driven upward drag and downward pull from the detaching slab level off.
The abrupt change from low v_p values surrounding the local earthquakes to high v_p in the deeper portion of the Hindu Kush slab could then arise due to eclogitization of subducting mafic lower crust, similar as proposed in the Pamir (Sippl et al., 2013a). Eclogitization increases the seismic velocities of a specific material to values higher than typical mantle velocities (Hacker et al., 2011) and increases its density (Sobolev and Babeyko, 1994; Krystopowicz and Currie, 2013), thus decreases its resistance to subduction. Further, the fluid phase, released during the metamorphic reaction, was suggested to trigger the decoupling between the lower and middle crustal layer (Labrousse et al., 2011), which might then either pond at depth or relaminate (Hacker et al., 2011). Such a process could explain the blob-like low velocity zone resolved here, as it is located directly above the change from low to high velocity material surrounding the seismicity. However, the abrupt cut-off of seismicity at ∼160-180 km and the over-steepening of the seismic zone in the Hindu Kush might be caused by an additional effect connected to the ongoing break-off[1].

5.5.4 The character of the Tajik basin's mantle lithosphere

The subduction and possibly exhumation of crustal material beneath the Hindu Kush must affect the Tajik basin mantle lithosphere to its north, which might manifest itself in the low velocity domain I2 at the western edge of the Hindu Kush seismic zone. The anomaly is geometrically connected to the Hindu Kush crustal subduction, but is more diffuse and has lower amplitudes. Thus, it could represent a weakened zone in the Tajik basin's mantle lithosphere that formed in response to the crustal entrainment. Metamorphic reactions in the mantle lithosphere might, for instance, be triggered by fluid infiltration. As the anomaly I2 is located at the western termination of the Hindu Kush subduction zone, the lower velocities could also arise due to asthenospheric inflow at the edge of the collision system (e.g. Docherty and Banda, 1995).

In its center, we imaged the Tajik basin lithosphere consisting of a high velocity upper mantle lid (anomaly TB in Figs. 5.8, 5.9 and 5.10) and the flat lying anomaly I1, underlain by high velocities again. High seismic velocities underlying the crust of the Tajik basin are in accordance with global seismic studies (Pasyanos, 2010). The reliability of the low velocity domain in the mantle has been shown in the synthetic tests (Section 5.5.1). In addition, receiver function studies image a sub-horizontal reflector at the position of the anomaly I1 (Schneider, 2014). Thus, there is little doubt that the low velocities at the base of the high velocity lid are a resolvable feature.
The anomaly I1 is unlikely to represent the lithosphere-asthenosphere boundary (LAB), because seismic velocities in the Tajik basin increase again directly underneath the anomaly. Further, the asthenosphere should be much thicker than ∼30 km (Gung et al., 2003). Additionally, it is suspicious that the v_p/v_s ratios in the anomaly I1 are extremely low. This might hint towards an artifact in the velocity model, which could arise e.g. from the unmodeled effects of seismic anisotropy (Bezada et al., 2014). Thus, instead of the LAB, the anomaly I1 might represent the midlithospheric discontinuity (MLD; Yuan and Romanowicz, 2010; Rader et al., 2015, schematically sketched in Fig. 5.12). The MLD

[1]These characteristics will be discussed in detail in Chapter 7

has been mainly found in thick, continental lithosphere in depth ranges between ∼60 and 160 km (Rader et al., 2015). Although different hypotheses on its formation exist, the MLD seems to be generally connected to the accumulation of crystallizing volatile-rich melt in a confined depth range of the mantle lithosphere (Rader et al., 2015). Hansen et al. (2015) and Hopper and Fischer (2015), for instance, imaged the MLD beneath the northern U.S. craton, as a horizontally layered, sharply confined but discontinuous low velocity layer. These characteristics are in good agreement with our observations in the Tajik basin's mantle (discontinuous sub-horizontal anomaly, possibly anisotropic), as well as with its formation history (see Section 5.2).

5.6 Conclusion

We present local tomographic v_p and v_p/v_s models gained from the inversion of ∼100.000 P and ∼40.000 S picks, covering large parts of the Hindu Kush, Pamir, Tajik basin and southwestern Tian Shan. Our seismic velocity images resolve a pronounced difference between the Tajik basin's sedimentary cover (low v_p, high v_p/v_s) and mafic basement (high v_p) to the felsic upper crust of the mountains. Whereas the basin basement and parts of the sediments underthrust eastward under the Pamir, they abut to the south against the Hindu Kush seismic zone (schematically shown in Fig. 5.12). The Hindu Kush intermediate depth seismicity falls together with a sheet-like low v_p, high v_p/v_s layer, dipping from the counter-side and connecting to the Hindu Kush crust. We interpret this constellation as subduction of continental crust beneath the Hindu Kush. Crustal subduction probably also involves the entrainment of middle crust, which might penetrate as deep as ∼160 km before it detaches from the subducting units. The lower crust might undergo eclogitization and subduct deeper due to the increased density. The whole process of crustal subduction is possibly locally accelerated by the ongoing slab break-off beneath the Hindu Kush.
We resolve two low velocity zones in the mantle beneath the Tajik basin. One of these anomalies is spatially closely associated to the Hindu Kush subduction zone and might be attributed to the local weakening of the mantle units due to the subduction of crustal material, possibly allowing the entrainment of asthenosphere at the western edge of the subduction zone. In contrast, a discontinuous, sub-horizontal low velocity anomaly, splitting the high velocity mantle lithosphere of the Tajik basin at ∼120-140 km depth, likely represents the MLD (midlithospheric discontinuity; Rader et al., 2015).

6 Seismotectonics of the Tajik basin and surrounding mountain ramps

Abstract
We use seismological data to investigate active deformation in the Tajik basin and the surrounding Pamir and Hindu Kush mountains in Central Asia. The region is strongly affected by the ongoing India-Asia collision, which formed two oppositely dipping continental subduction zones at sub-crustal levels. We want to understand how crustal deformation is influenced by the deeper lithospheric processes and how it is partitioned between the basin, its rims and the mountains. Here we show hypocenters of ∼2400 crustal earthquakes, located in a regional 3D velocity model, and ∼130 earthquake source mechanisms of the largest of these events, derived from data recorded by temporarily deployed seismic networks over four years. Crustal seismicity can be divided into three sub-regions, which exhibit different seismotectonic behavior in response to the far field stresses exerted by the India-Asia collision: 1) In the Tajik basin, deformation is partitioned between seismically active strike-slip faults at its northern and eastern rim, which converge in the seismically extremely active Garm region, and the basin's interior. Within the basin, seismicity occurs mainly along a horizontal interface at ∼10-12 km depth, with the most active cluster coinciding with the region of active salt diapirism. Pressure (P) axes and slip vectors of these events parallel the west-east oriented GPS-velocity vector field, suggesting that seismogenic deformation along the salt decollement is controlled by the westward oriented gravitational collapse of the Pamir. 2) Crustal seismicity at the basin's southern margin is sparse. Instead, seismic deformation might be shifted further to the south, beneath the Hindu Kush, where hypocenters reach up to ∼40 km depth. These deep crustal earthquakes seem to be related to the ongoing continental subduction underneath. 3) The Hindu Kush-Pamir transfer system features a zone of NNE-SSW oriented strike-slip faults, and accordingly oriented strike-slip events. The location of this zone of distributed shear coincides with the earlier proposed (Chapter 4) contrast of Marginal and Cratonic Indian lithosphere at sub-crustal depths, suggesting that crustal tectonics in the Pamir and Hindu Kush seem to be linked to the lithospheric-scale processes.

6.1 Introduction

The Tajik basin in Central Asia is surrounded at three sides by the Tian Shan, Pamir and Hindu Kush mountains (Fig. 6.1). Cenozoic deformation is controlled by the ongoing India-Asia collision, which manifested itself by different styles of deformation in each of these mountain ranges. The northward push of India resulted in the northward offset of the Pamir (Burtman and Molnar, 1993) and intense crustal thickening (van Hinsbergen et al., 2011a; Schmidt et al., 2011), lateral escape along strike-slip faults in the Hindu Kush (Tapponnier et al., 1981; Treloar and Izatt, 1993; Hildebrand et al., 2000) and reac-

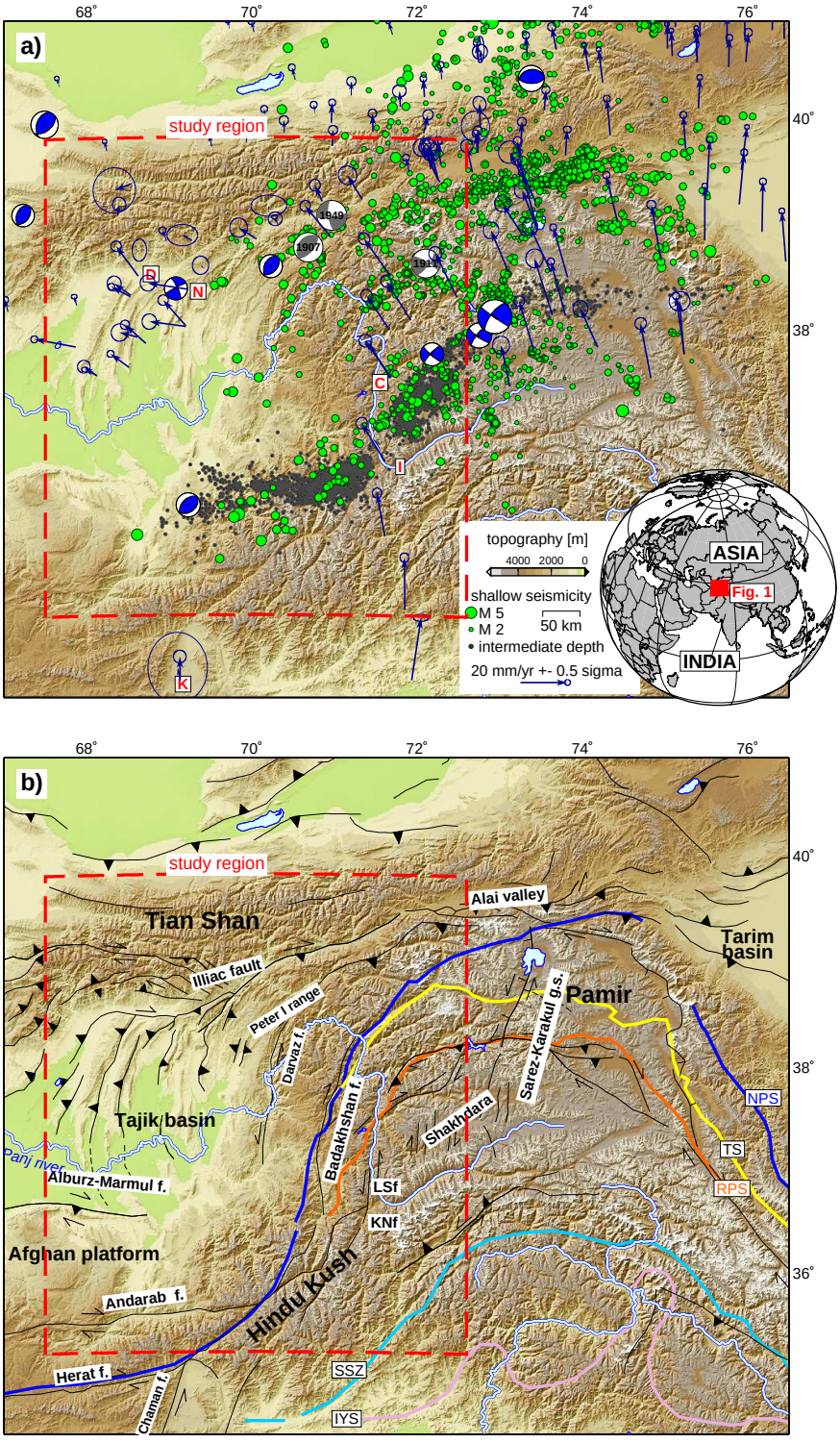

Figure 6.1: Overview maps of the Hindu Kush-Pamir-Tajik basin collision system. See Figure caption on the subsequent page.

Figure 6.1: Topographic maps of the Hindu Kush-Pamir-Tajik basin collision system. **a)** Seismicity and GPS vectors: GPS velocity vectors (blue) from Mohadjer et al. (2010); Zubovich et al. (2010); Ischuk et al. (2013) and Zubovich et al. (2016). For campaign points, the most recently published one is plotted. Shallow (<40 km depth) and intermediate depth (>120 km depth) seismicity from Sippl et al. (2013b) and Chapter 4, respectively. Blue beach balls represent the double couple components of all available moment tensors from the GEOFON catalog (GEOFON, 2016) from July 2012 to April 2016. Their size is scaled by moment magnitude with minimum and maximum values of 4.2 and 7.2, respectively. The largest of these events was the December 2015 Sarez earthquake. Gray mechanisms represent the three largest instrumentally recorded events in the region (Khait, 1949, m_b= 7.6; Sarez, 1911, m_b= 7.3; Karatag, 1907, m_b= 7.5; according to Kulikova, 2016). Rivers in light blue. Red letters in boxes refer to selected cities: C - Chorugh; D - Dushanbe; I - Ishkashim; K - Kabul; N - Nurek. **b)** Tectonic features: faults (black) after Schurr et al. (2014). LSf - Lake-Shiwa Fault; KNf - Kapisa-Nuristan Fault; Sarez-Karakul g.s. - Sarez-Karakul Graben System. Sutures (bold, colored lines) after Schwab et al. (2004); Yin and Harrison (2000) and L. Ratschbacher (pers. comm.): NPS - North Pamir; TS - Tanymas; RPS - Rushan Pshart; SSZ - Shyok; IYS - Indus Yarlung.

tivation of the Tian Shan (Avouac et al., 1993; Sobel et al., 2006; Käßner et al., 2016). At sub-crustal levels, two oppositely dipping zones of intermediate depth seismicity formed beneath the Pamir and Hindu Kush, which have been attributed to the subduction of Asian and Indian material, respectively (Koulakov and Sobolev, 2006; Sippl et al., 2013a; Schneider et al., 2013, Chapter 4). Within this framework of deforming units, the Tajik basin was postulated to behave as a relatively rigid block (van Hinsbergen et al., 2011a). However, its sub-crustal lithosphere has a complex architecture, featuring delamination and rollback beneath the Pamir (Sippl et al., 2013b,a; Schneider et al., 2013), but acting as a kind of rigid backstop for the northward dipping Hindu Kush subduction zone at the same time (Chapter 4). This situation was proposed to be primarily caused by an internal lithological contrast in the advancing Indian lithosphere: while a narrow sliver of India's stretched margin subducts beneath the Hindu Kush, cratonic Indian lithosphere pushes the Pamir northwards (Chapter 4).

Seismotectonics of the Pamir have been described in detail by Schurr et al. (2014) based on field mapping and the seismic data acquired during a two-year local seismic deployment (the TIPAGE network; Mechie et al., 2012). Schurr et al. (2014) stated a segmentation of the Pamir along the north-south striking Sarez-Karakul Graben System into an eastern part, which moves northward *en bloc*, and a western part which exhibits a higher amount of seismic deformation. This deformation has been explained by the gravitational collapse of the western Pamir and the lateral extrusion of Pamir rocks into the Tajik basin, causing west-east shortening and thin skinned folding there. According to Schurr et al. (2014), the segmentation of the Pamir might be caused by the northeastward propagation of India's western margin into Asia, linking deformation in the Pamir to the Chaman Fault in Afghanistan (see Fig. 6.1 for its location). The mechanism of the most recent M_w 7.2 earthquake, which ruptured the Sarez-Karakul system in December 2015 (GEOFON, 2016) strongly supports this suggestion.
Figure 6.1 shows the crustal seismicity derived from the TIPAGE network (Sippl et al., 2013b) together with Cenozoic faults (Schurr et al., 2014), GPS vectors (Mohadjer et al.,

2010; Zubovich et al., 2010; Ischuk et al., 2013; Zubovich et al., 2016) as well as the three largest instrumentally recorded earthquakes since the beginning of the last century (Khait, 1949, m_b= 7.6; Sarez, 1911, m_b= 7.3; Karatag, 1907, m_b= 7.5; according to Kulikova, 2016). Two of these earthquakes locate at the Pamir's northwestern margin, where it abuts against the Tian Shan along the Peter I. range (Garm region). However, the frequency of earthquakes recorded by the TIPAGE catalog decreases in the Garm region. This drop marks not the ceasing of seismogenic deformation but rather the westward termination of the local TIPAGE network. Studies based on teleseismic data (Burtman and Molnar, 1993; Fan et al., 1994) reveal seismic activity in the basins and its rims, however, can not reach the location precision of a local seismic network. Very regional studies along the Peter I. range based on old Soviet catalogs (Leith and Simpson, 1986b; Hamburger et al., 1992; Lukk et al., 1995; Lukk, 2011) resolve intense seismic activity but in turn lack the broader regional context. Thus, to a certain extent, the Tajik basin and its margins form a white spot on the seismicity map, which, however, we will fill in the following.

Our analysis is based on the recordings of the local seismic TIPTIMON network (Schurr et al., 2012, 2013), which was deployed in the Tajik basin and Hindu Kush between 2012 and 2014. In particular, this study will focus on the seismic deformation of the Tajik basin, its margins and the interaction between deep and crustal deformation.

6.2 Tectonic setting

During the Paleozoic and Mesozoic, the Tarim and Tajik basins were connected, forming the Tajik-Yarkand basin (Burtman and Molnar, 1993). The basin's former rims are currently outlined by the Gissar suture to the north and the North Pamir suture to the south (see Fig. 6.1 for the geological terms described in the following). South of the North Pamir suture, the Pamir-Hindu Kush mountains comprise a sequence of Gondwana derived terranes and island arcs (bold lines in Fig. 6.1), which accreted during the Cimmerian orogeny (Schwab et al., 2004; Yin and Harrison, 2000) and were later further deformed in response to the India-Asia collision, which initiated at ∼50-55 Ma (e.g. van Hinsbergen et al., 2011a). The units at the longitudinal range of the Pamir and Hindu Kush reacted differently to the deformation, resulting in an asymmetric pattern of Cenozoic deformation: the Pamir was northward-offset, probably not starting earlier than ∼25 Ma (Sobel and Dumitru, 1997; Coutand et al., 2002), overriding the earlier connected Tajik and Tarim basins (Burtman and Molnar, 1993). In contrast, suture zones in the Hindu Kush were re-activated as strike-slip faults, accommodating escape movement of these blocks towards the west (Tapponnier et al., 1981; Treloar and Izatt, 1993; Hildebrand et al., 2000). The Tajik basin experienced little crustal thickening (Chapter 5) and rather transmitted deformation to the Tian Shan further to the north (Avouac et al., 1993; Sobel et al., 2006; Käßner et al., 2016). Reactivation of the Tian Shan started probably around 23 Ma (Hendrix et al., 1994; Yin, 2010; van Hinsbergen et al., 2011a) but was accelerated later (∼10-12 Ma; Abdrakhmatov et al., 1996; Sobel et al., 2011). Deformation in response to the India-Asia collision is still ongoing as evident from WSW-ENE striking thrust earthquakes (Fig. 6.1).

The Tajik basin's and North Afghanistan's sedimentary cover recorded the timing of these different tectonic events: the North Afghan Platform is overlain by Jurassic clastic sediments which change upward into a carbonate rich sequence. As the basin became restricted at the end of the Mesozoic, carbonate shelf sediments deposited in the Tajik-Yarkand basin. The transition to redbeds then represents the uplift of the North Afghan Platform in response to the Indian collision. Whereas the platform is sharply restricted by the Herat Fault in the south, it shows a more gradual transition into the Tajik basin to the north (Brookfield and Hashmat, 2001). However, the Alburz-Marmul Fault, which separates these units, must have been active recently as it cuts in the Tajik basin's Neogene strata (Nikolaev, 2002).
The Tajik basin is filled with an up to 10 km thick sedimentary sequence that thickens towards the south, resting on a pre-Triassic, heterogeneous basement built of oceanic and continental blocks (Burtman, 1975; Brookfield and Hashmat, 2001). The sedimentary cover consists of a dominantly marine Late Triassic to Oligocene pre-orogenic epicontinental sedimentary infill, overlain by syn- and post-orogenic Neogene to Quaternary continental clastics (Brookfield and Hashmat, 2001; Nikolaev, 2002; Carrapa et al., 2015; Klocke et al., 2015). A decollement along Jurassic evaporites decouples a mostly Neogene thin-skinned thrust-and-fold belt in post-Jurassic strata from Proterozoic-Jurassic units, largely undeformed during the Cenozoic (Hamburger et al., 1992; Gagala, 2014). Folds form westward convex arcs, initiating near the Peter I. range at the Pamir-Tian Shan syntaxis and terminating at the Alburz-Marmul Fault in Afghanistan (Nikolaev, 2002). These arcuate folds suggest that they had their origin in detachment along the salt strata. To its north, the basin is bounded by the dextral-reverse Illiac Fault Zone, which translates into the Vakhsh Thrust System further east. The latter represents the active thrust front of the Pamir, which features a shallowly dipping decollement along Jurassic evaporites. Several detachment faults cut its hanging wall (Hamburger et al., 1992; Schurr et al., 2014). The Tajik basin is separated from the Pamir to its east by the sinistral transpressive Darvaz Fault. The Darvaz Fault must have accommodated much of the northward offset of the Pamir, but knowledge regarding its current activity is sparse. Ischuk et al. (2013) derived ∼10 mm/yr from GPS measurements, but due to the large separation of the GPS points it is not clear where the deformation localizes.

In the Hindu Kush, most of the prominent west-east trending dextral strike-slip faults are inactive today. Displacement was suggested to have jumped north from the Herat to the Andarab Fault already at 23 Ma possibly as reaction to the northward displacement of the Pamir (Şengör et al., 1988; Boulin, 1988, 1991). Along the Pamir-Hindu Kush transition, the offset of the Pamir was absorbed by a network of roughly north-south trending strike-slip faults (e.g. the left-lateral Lake-Shiwa and Kapisa-Nuristan fault systems; see Fig. 6.1).

6.3 Earthquake analysis

6.3.1 Local seismicity

The earthquake catalog presented here comprises all shallow (<50 km) earthquakes registered during the TIPTIMON seismic experiment, which was deployed from 2012 to 2014 in the Hindu Kush and Tajik basin (Schurr et al., 2012, 2013). Additionally, it includes a

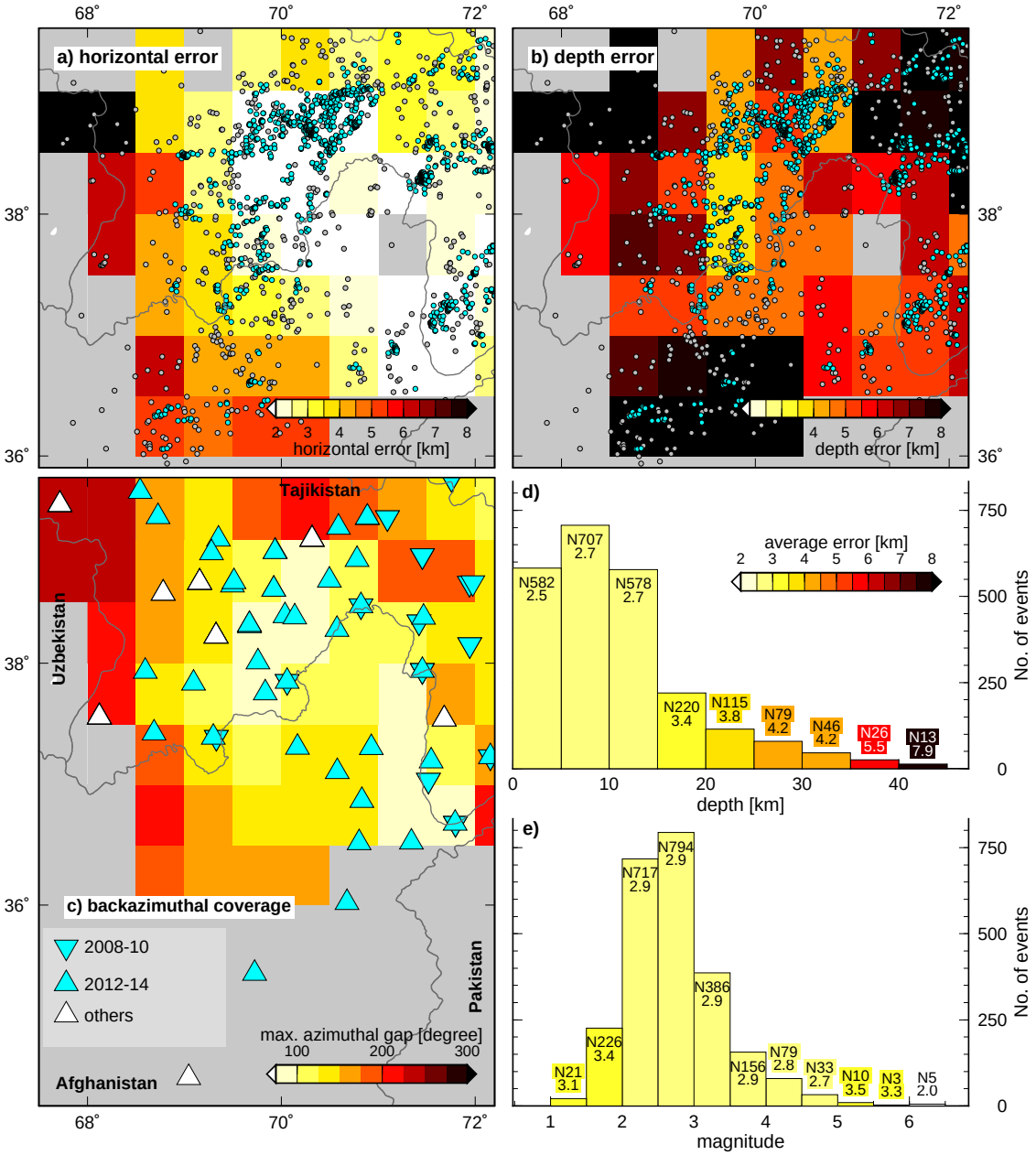

Figure 6.2: Earthquake location quality: **a/b)** Absolute errors are the axes length of the error ellipsis in the specific direction from the probabilistic location scheme averaged over all earthquakes in 0.5°x0.5° bins. The horizontal error is the average over longitudinal and latitudinal direction. Only bins with at least three events are shown. Events which could/could not be double difference relocated are plotted in blue and gray, respectively. Political boundaries in dark gray. **c)** Station locations and largest azimuthal separation between two stations used to locate a specific earthquake, for the events shown in Sub-figures a/b), averaged in 0.5°x0.5° bins. **d/e)** Depth and magnitude histograms color coded by location error. The upper number at the top of each bin refers to the number of events (N), the lower number is the averaged location error in kilometers (radius of a sphere with the same volume than the error ellipsis).

subset of the TIPAGE catalog (Sippl et al., 2013b; Schurr et al., 2014), which covers the Pamir and southwestern Tian Shan. As TIPTIMON and TIPAGE share several common stations in the western Pamir (see Fig. 6.2c), the different datasets were combined to also include the eastern periphery of our study region.

Earthquake location procedure: We obtained earthquake hypocenters by a multi-step location procedure: initial earthquake locations were determined using an automated location chain (Sippl et al., 2013b), in which possible earthquakes are detected from a continuous time series and initial locations are subsequently improved. In several iterative loops, P and S picks are updated or rejected based on quality criteria. Earthquakes, included from the TIPTIMON recording period here, were required to have a root mean square (RMS) residual smaller than two seconds, at least five P picks and at least one S pick in this initial detection step. These restrictions were sufficient to ensure that a triggered event was indeed a local earthquake and not e.g. accidentally correlated noise or a teleseismic event. The regional 1D velocity model of Sippl et al. (2013b) was used for initial event detection but locations of the joint catalog were then improved by event relocation in the 3D P- and S-wave velocity models from Chapter 5. Given the highly variable crustal velocity structure in the study region, this step was essential in order to accurately determine event depths. Relative locations were obtained from a double difference relocation scheme, aiming to improve the inter-event location quality. Individual and double difference event relocation was performed with the software *simulps* (Thurber, 1983, 1993; Eberhart-Phillips, 1993; Evans et al., 1994) and *hypoDD3D* (Waldhauser and Ellsworth, 2000; Waldhauser, 2001), respectively. We assessed the absolute location error by calculating probabilistic, non-linear earthquake locations using the software *NonLinLoc* (Lomax, 2008). The 68%-confidence ellipsoids of the maximum-likelihood hypocenters served as a measure for location uncertainty. Relative location errors were taken directly from *hypoDD3D*, relocating subsets of clusters in the singular value decomposition mode based on the posterior analysis of the covariance matrix (Waldhauser and Ellsworth, 2000). Local magnitudes were calculated from the maximum amplitudes in the waveforms according to Hutton and Boore (1987).
In total, 1590 shallow earthquakes, which occurred between July 2012 and April 2014, could be detected (Supplementary Fig. D1c). These events were partly already plotted in Chapter 4 and were used for local earthquake tomography in Chapter 5. However, as these chapters focused on other aspects, neither the complete shallow seismicity was shown nor was it discussed in detail. The catalog presented here consists of 2381 events (west of 72.2°E), 65.3% thereof registered by the TIPTIMON deployment. The other earthquakes are relocated events that happened between 2008-2010 (see Supplementary Section D for the description of the subset) but were relocated together with the TIPTIMON events.

Error analysis: The mean RMS residual of the events in our joint catalog is 0.23 s. Figure 6.2 shows the absolute location errors from the probabilistic relocation scheme *NonLinLoc* (Lomax, 2008). Average location uncertainty estimated from the *NonLinLoc* error ellipsoids is ±2.95 km (this value refers to the radius of a sphere with the same volume as the error ellipsoids calculated in *NonLinLoc*). In general, average horizontal

errors are smaller than vertical errors (average of ±2.7 km and ±2.5 km in longitudinal and latitudinal directions versus average of ±6.2 km in depth direction). The location errors correlate well with the largest azimuthal gap between stations used for the event location of a specific event (Fig. 6.2a-c), whereas no obvious correlation occurs between magnitude and average location error (Fig. 6.2e). Event location quality seems to decrease with depth (Fig. 6.2d), although the last statement might be partly biased, as about half of the deepest crustal earthquakes are located in the Hindu Kush, where azimuthal coverage is bad. Errors are smallest (horizontal $< \pm 2$ km; vertical ±3-5.5 km) in the center of the network. This region includes the Tajik basin, the Peter I. range and the western Pamir. East of the Peter I. range, location quality decreases, together with the frequency of seismicity. Thus, it is questionable to which extent the decrease in seismicity there arises from the decrease in resolution. The same concern might apply for the western Tajik basin and for the southern Hindu Kush, where errors are largest (horizontal ±5-6 km; vertical $\sim \pm 10$ km).

In the joint catalog, 76% of all earthquakes were double difference relocated (blue circles in Figs. 6.2a, b). The average relative error of these events is ±0.7 km. The events not relocated with the double difference scheme were mainly isolated events that could not be associated to any event cluster. Thus, the basic assumption for the method was not fulfilled.

6.3.2 Earthquake source mechanisms

We derived earthquake source mechanisms for the strongest events in the shallow TIPTIMON catalog from moment tensor inversion (Nábělek and Xia, 1995; Schurr and Nábělek, 1999). For the inversion procedure, the instrument response was deconvolved, seismograms were bandpass filtered, down-sampled to 1 Hz, cut to 256 data points per trace and rotated to a radial-transverse aligned coordinate system based on the initial event location. The initial filter bandwidth was adjusted depending on the size of the event, from a lower limit ranging from 10-15 s to an upper limit between 30-50 s.
Synthetic seismograms were obtained from the convolution of an assumed source time function (here three triangular peaks of initially 1 s length) and the Green's functions calculated based on the used velocity model (here the minimum 1D model from Chapter 5). The match between observed and calculated waveforms was measured in terms of the normalized variance, which describes the residuum between data and model, normalized by the data power. Thus, the variance is comparable for all events and can vary between 0 to 1, where 0 corresponds to the best achievable correlation. We derived the best-fit mechanism in a least-square type inversion, starting from an arbitrary first guess. Time shifts between the true and synthetic seismograms were allowed as they depend mainly on the used velocity model and event location.
Once the mechanism with the smallest variance was determined, the whole inversion procedure was repeated automatically for several depth steps around the initial hypocentral depth. The depth that yielded the smallest variance was taken as the final centroid depth of the specific event. Prior to inversion, all data traces were inspected visually and obvi-

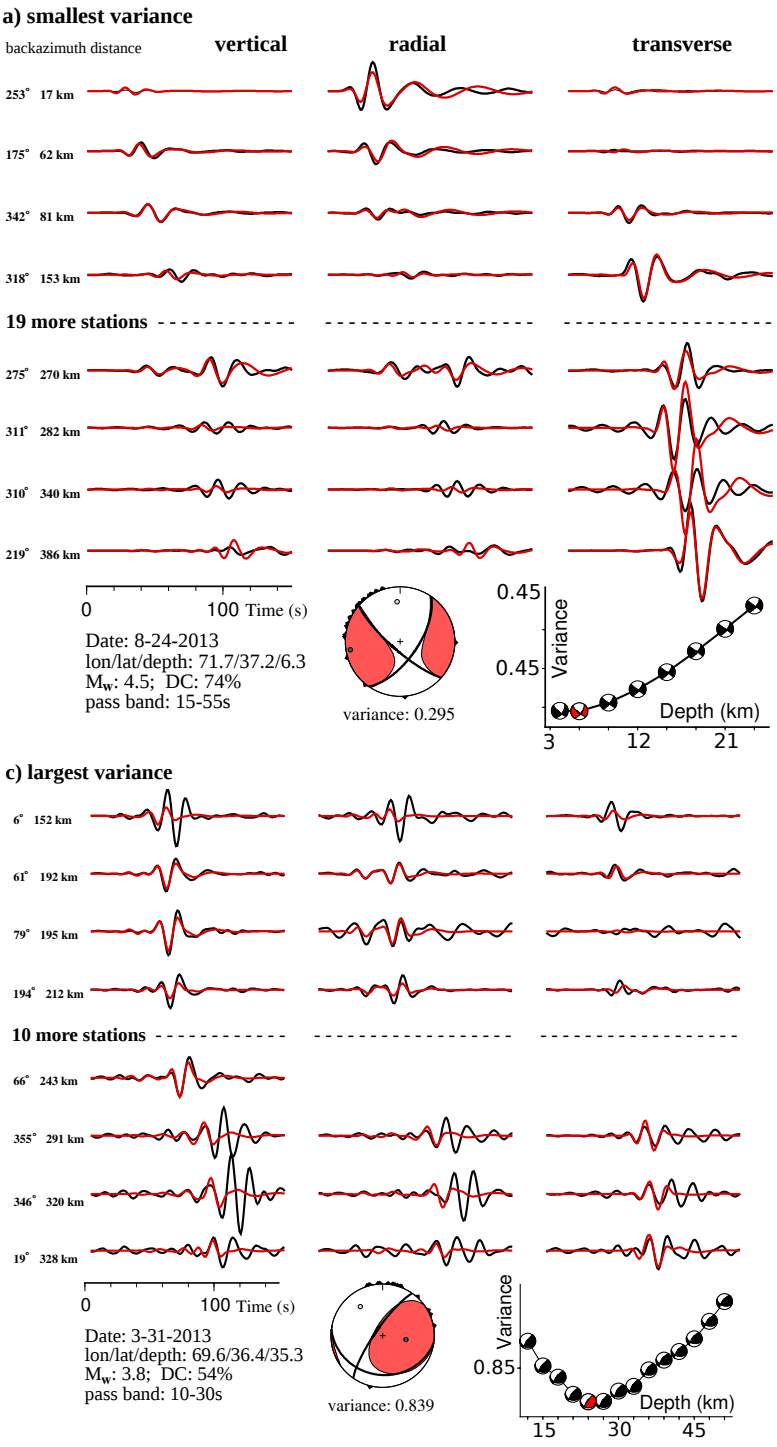

Figure 6.3: Examples for earthquake mechanism determination by waveform modeling. **a)** The event that yielded the mechanism with the smallest variance ($\hat{=}$ best quality). **b)** The mechanism with the biggest variance. For each mechanism, only records from eight stations are shown. The upper four are example stations of the nearest epicentral distance, the lower four are examples from the most distant stations.

ously problematic traces were removed.

Earthquake source mechanisms could be determined for 81 shallow events. Mean M_w (moment magnitude) is 3.63 (smallest/biggest value of 3.1/4.8). The larger an event is, the higher is its energy content at long periods. This allows waveform matching at longer periods as well, which generally yielded better solutions. Accordingly, in our dataset the moment magnitude of the events is approximately linearly correlated to the variance (quality of solution). Mean variance of all events is 0.62 (smallest/biggest value of 0.30/0.84), including events with a double couple percentage ranging from 22% to 100% (average of 71%).
Figure 6.3 shows example traces of the events with the smallest and biggest variance in the TIPTIMON dataset. For each event we plot only eight stations; four in the nearest epicentral distance, four from the most distant stations. For the event with the smallest variance (Fig. 6.3a), the general shape of all waveforms is matched accurately. Some variation in the absolute amplitudes might be due to local near-station subsurface heterogeneity. For the event with the largest variance (Fig. 6.3b), the dominant first peak in the waveform is well modeled but the correlation decreases for the subsequent peaks, especially for the larger epicentral distances. Nevertheless, the mechanism was stable over the different depth levels and the variance was smallest at the preferred depth (see variance vs. depth plot in Fig. 6.3b), thus it was included in the final results.

In addition to the mechanisms determined from the TIPTIMON dataset, we include further data from Schurr et al. (2014), who derived mechanisms for the period of the TIPAGE deployment. A specific earthquake was included if it was in our jointly relocated event catalog. The mechanism was then plotted at the updated hypocenter position. For the study region considered here (west of 72.2°E), these two datasets sum up to 127 source mechanisms, 63% of them from the TIPTIMON period (see Supplementary Fig. D1 for the components of the two different subsets).

6.4 Results and interpretation

Figure 6.4 shows the earthquake catalog as well as the pressure and tension axes of all mechanisms determined from the local seismic data. In Figure 6.5, the seismicity and the beach ball representation of these mechanisms are plotted together with all available mechanisms from the global CMT project which includes ∼40 years of data (Dziewoński et al., 1981; Ekström et al., 2012). However, the depths and locations of the CMT mechanisms should be interpreted with caution as they were not relocated relative to our results. Additionally to these overview maps, Figures 6.7 to 6.10 zoom into sub-domains of our study region, showing the seismicity together with the velocity model used for relocating the events, which puts additional constraints on lithological boundaries possibly associated with the seismicity (Chapter 5).
The earthquake catalog reveals seismic activity not only along the active faults flanking the Pamir and Tian Shan mountains but also in the basin's interior (Fig. 6.4a). Despite sparse deeper earthquakes mainly below the North Afghan Platform, upper crustal seismicity clearly dominates in our catalog, with ∼75% of all events being shallower than

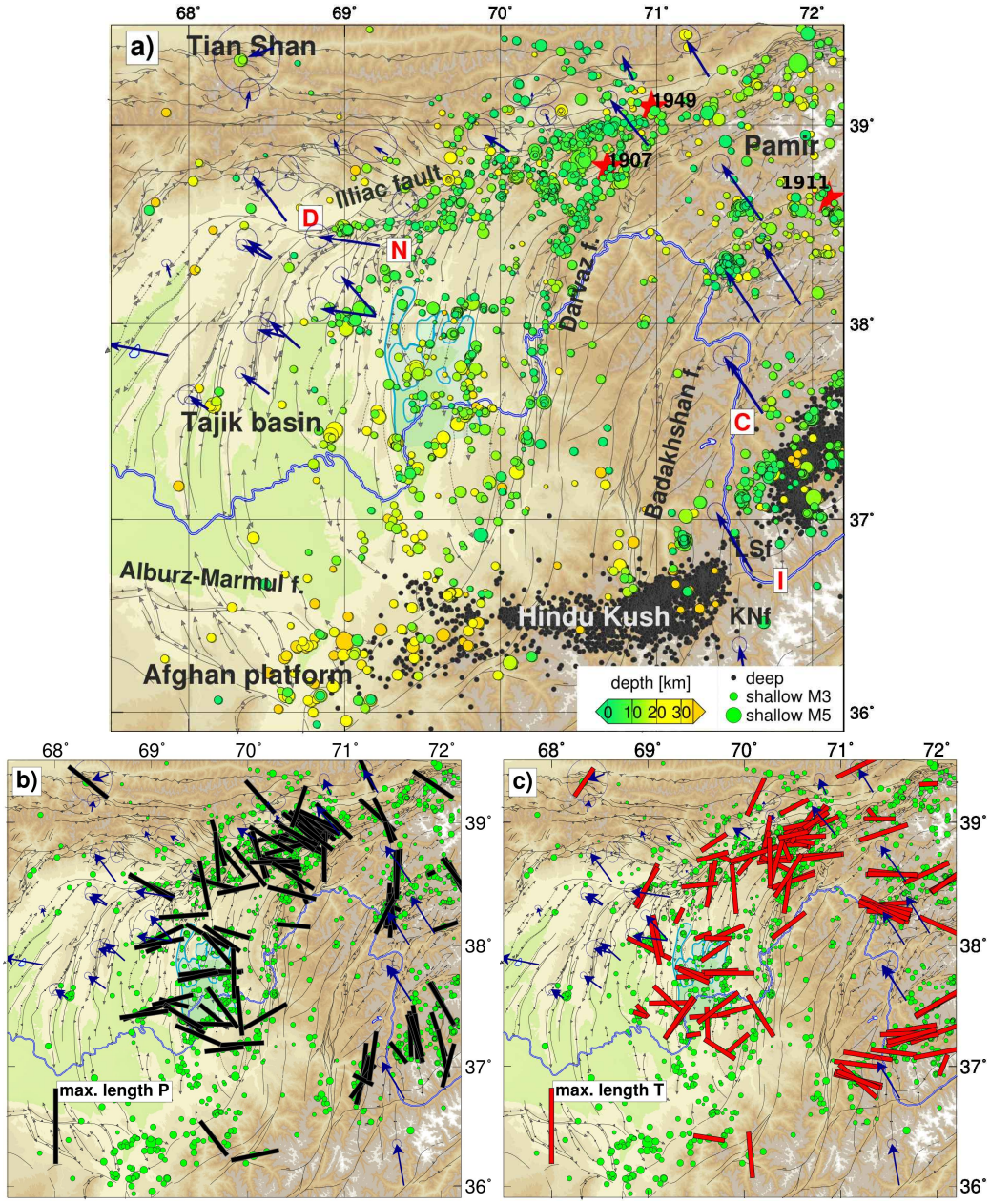

Figure 6.4: a) Earthquake catalog covering the years 2008/10 and 2012/14 derived from temporary seismic deployments. Shallow events color coded by depth and scaled by magnitude; deep events from Chapter 4. Stars indicate the three largest instrumentally recorded events (Khait, 1949, m_b= 7.6; Sarez, 1911, m_b= 7.3; Karatag, 1907, m_b= 7.5; according to Kulikova, 2016). Faults in the Tajik basin from S. Abdulhameed (pers. comm.) and from Schurr et al. (2014) in the Pamir. The blue domain in the Tajik basin encloses the area of salt diapirs (L. Ratschbacher; pers. comm.). All other features as in Figure 6.1. **b/c)** Pressure (black) and tension (red) axes from the moment tensors plotted in Figure 6.5. Lengths of the axes are normalized to one and projected into the horizontal map. Shallow seismicity in green.

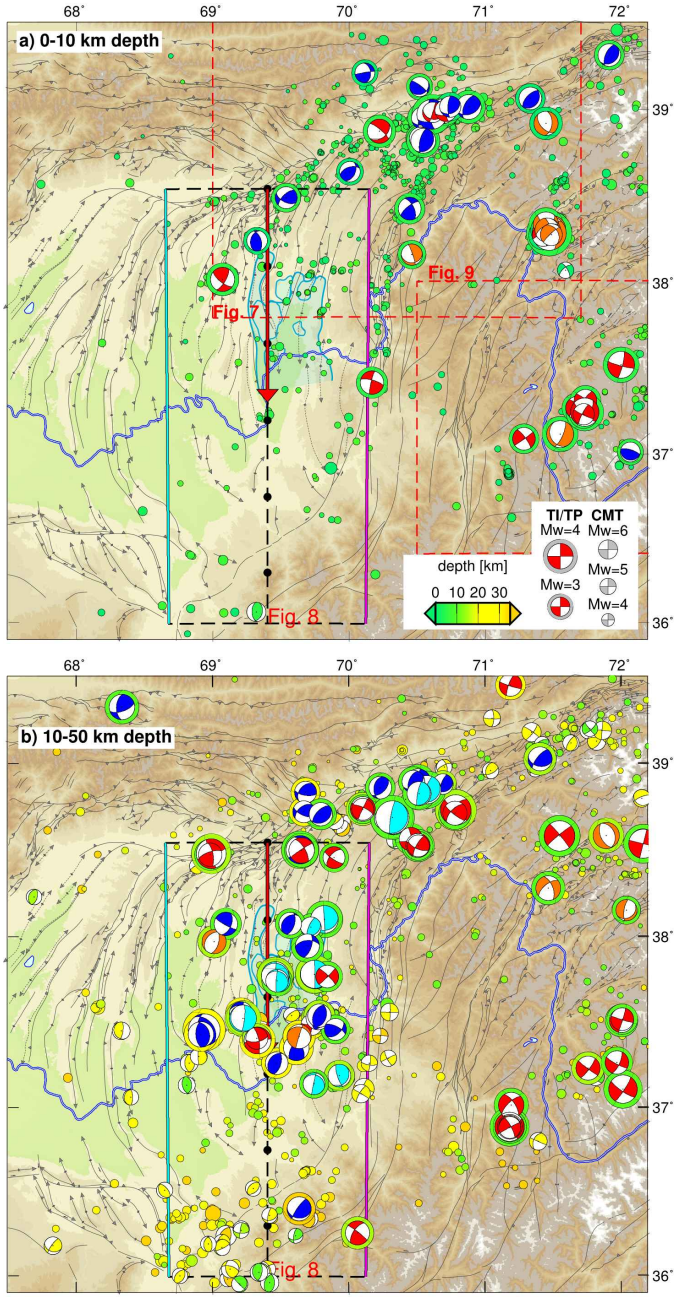

Figure 6.5: The double couple component of the moment tensors determined in this study (TI/TP - larger mechanisms, surrounded by a color corona) and from the global CMT database (Dziewoński et al., 1981; Ekström et al., 2012). The corona of the TI/TP events and the color of the CMT events corresponds to their hypocentral depth. The TI/TP mechanisms are further grouped after their faulting type: red - strike-slip; orange - normal; blue - thrust; turquoise - thrusts with one sub-horizontally dipping fault plane. Local seismicity and faults as in Figure 6.4. **a)** Events shallower than 10 km. **b)** Deeper events.

12 km (Fig. 6.2d). The majority of the events have local magnitudes between two and three (Fig. 6.2e). The number of events with largest magnitude successively decreases, as expected from the Gutenberg-Richter law, which predicts an exponential decay of event number with magnitude. The completeness threshold in our catalog is approximately at $M_L = 2.4$ (see Supplementary Fig. D1e).

To assess how representative this catalog (derived based on four years of data) is for the seismic activity in the basin, we compare it to two global catalogs, recorded over the same and a much longer time period (Fig. 6.6). From these, the EHB catalog (Fig. 6.6b; Engdahl

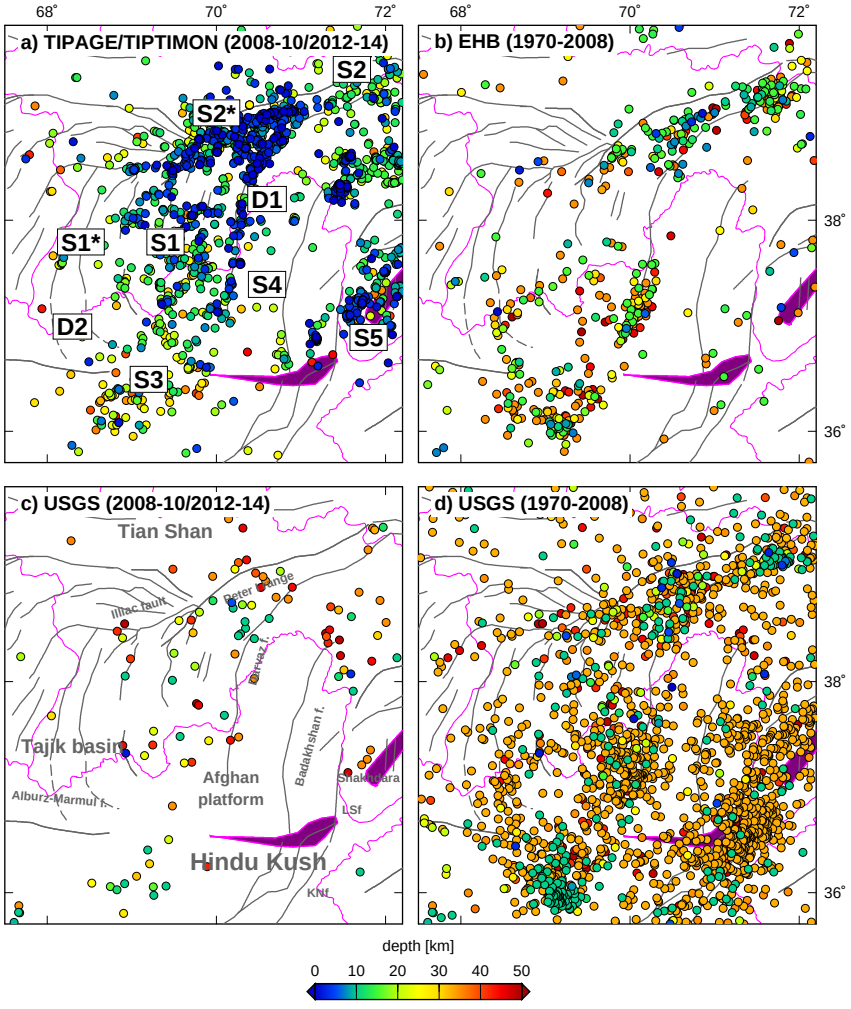

Figure 6.6: Comparison between different earthquake catalogs. **a)** This study. The labels refer to similar (S) and differing (D) features between our catalog and the global ones (see further discussion in Section 6.4). **b)** All events listed in the global EHB bulletin (Engdahl et al., 1998). **c/d)** Events listed in the USGS catalog (USGS, 2016) during the time of the temporary deployments used here and during the same time period as the EHB catalog. Political boundaries in pink, faults in gray (as in Fig. 6.1). Dark pink outline indicates the location of the Pamir and Hindu Kush intermediate depth seismicity (from Chapter 4).

et al., 1998) contains fewer earthquakes, but their locations, especially the depths, are better determined than the USGS ones (Fig. 6.6c, d). A lot of events in the USGS catalog cluster at the same depth, indicating that the depth was set to a standard predefined value during event location and is probably badly constrained. Despite this, EHB and USGS catalogs map generally similar features, except for the region around the Shakhdara gneiss dome, where the USGS catalog contains more shallow events. Given that this region is directly above the Pamir intermediate depth seismicity, the USGS events might in fact partly be mis-located deeper events.
The most prominent differences to our catalog are labeled with *D* in Figure 6.6, main similarities with *S*. The main contrast to our catalog arises at the western transition from the Hindu Kush to the basin (*D2*), where USGS and EHB catalogs show a north-south striking seismically active lineament following one of the fold axes into the basin, which does not appear in our data. Given that this feature does neither appear in the USGS data from the same time period (Fig. 6.6c), the earthquakes in domain *D2* might be either relatively small or the activity might occur in pulses. As in our catalog, seismicity in the global catalogs decreases towards the west in the Tajik basin (*S1/1⋆*) and seismic activity decreases east of the Peter I. range (*S2/2⋆*). These domains have been identified in Section 6.3.1 as those with the worst resolution in our catalog. However, as the global catalogs indicate similar characteristics, these domains seem to be represented by our local catalog sufficiently well. In the following, we will discuss different seismogenic sub-regions in more detail.

6.4.1 Tian Shan and Pamir margins

The Darvaz Fault, which separates Tajik basin and Pamir, is seen along its entire north-south extent as a seismically active steep lineament with a penetration depth of around 10 km (Fig. 6.4). As the fault bends around the Pamir orogen in the north, seismogenic depth increases to ∼15 km and the seismically active part of the fault dips north (map in Fig. 6.7 and cross sections in Fig. 6.8). The largest events (those with moment tensors) seem to cluster at the down-dip limit of the seismically active domain and exhibit strike-slip mechanisms, generally in accordance with the sinistral shear inferred from geological and GPS observations (Ischuk et al., 2013; Kuchai and Trifonov, 1977; Trifonov, 1978). Whereas these GPS measurements were too sparse to assess where exactly deformation occurs, the aligned seismicity resolved here could indicate that deformation might focus on one localized fault interface. In contrast, the central portion of the Darvaz Fault appears seismically inactive in the global catalogs (*D1* in Fig. 6.6), suggesting that this fault segment might feature smaller events or is partly locked. None of the earthquakes for which the CMT catalog provides solutions show thrusting, whereas one of our mechanisms has a thrust component. Thus, thrusting, as suggested by Thomas et al. (1994) could also happen during smaller earthquakes or aseismically.
Like the Darvaz Fault, the Illiac Fault in the north, which separates the basin from the Tian Shan, forms a near-vertical seismogenic structure. However, its seismogenic portion penetrates deeper to ∼15-18 km depth (Fig. 6.9). Thus, in contrast to the Darvaz Fault, the Illiac Fault seems to cut through the whole sedimentary package covering the Tajik basin, which should not be deeper than ∼10 km at the northern edge of the basin (Burtman

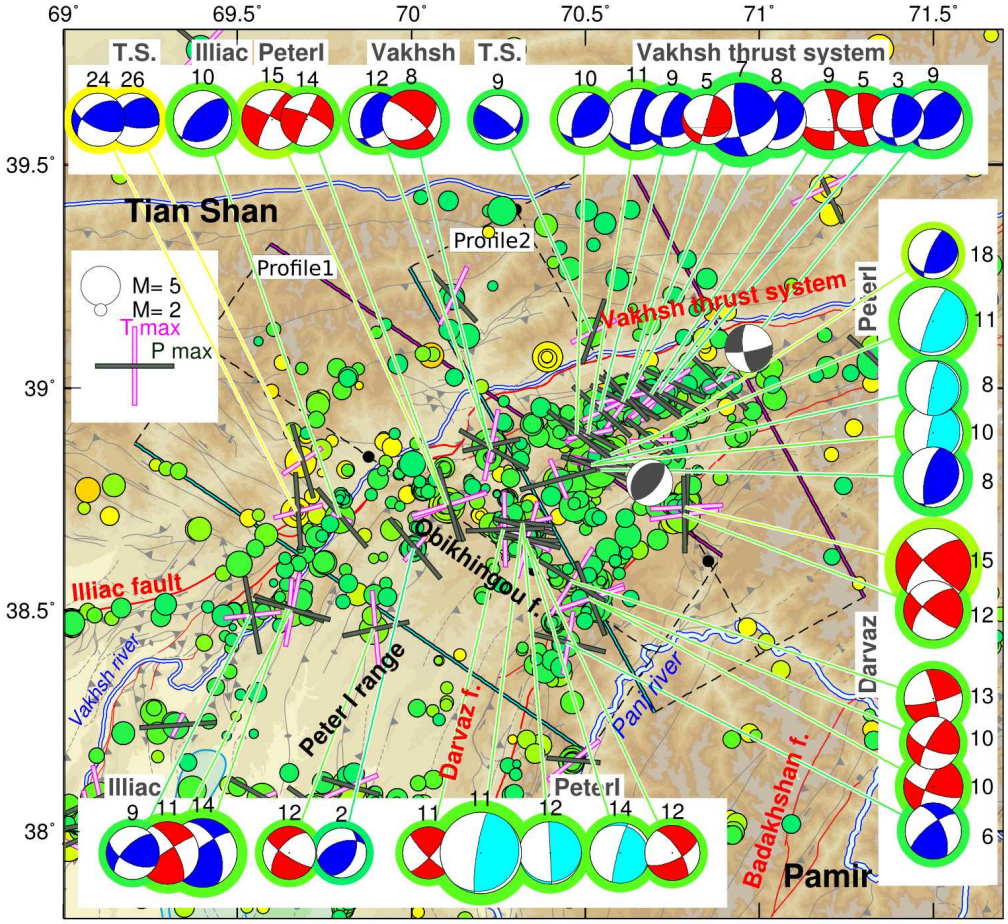

Figure 6.7: Zoom into the Peter I. range (see Fig. 6.5 for map location): color coding of seismicity with depth as in Figure 6.5. Pressure (P) and tension (T) axes of the events with focal mechanism are normalized to one and projected into map view. The number on top of the associated beach balls and the surrounding colored circle indicate the hypocentral depth of the earthquake. The color of the mechanisms indicates their faulting type (see the annotation in Fig. 6.5). The two gray mechanisms plotted directly in the map are the focal mechanisms determined by Kulikova (2016) for the 1949 Khait (m_b 7.6, strike-slip mechanism) and 1907 Karatag (m_b 7.5, thrust) earthquakes. Active faults in red (Schurr et al., 2014, L. Ratschbacher, per. comm.). Other faults and topography as in Figure 6.5. Boxes indicate the profile locations of Figures 6.8 a/b. Dots along the central black line of these boxes are 50 km tick-marks.

and Molnar, 1993), and possibly into the basement. Earthquake mechanisms confirm the dextral-shear displacement postulated from field observations (Schurr et al., 2014).

6.4.2 Garm region

Seismic activity of the Illiac and Darvaz faults intensifies as they converge in the Garm region, where the northward offset Pamir nearly abuts against the Tian Shan (Peter I. range). Figures 6.7 and 6.8 show a close up map of the Peter I. range and two strike-perpendicular cross sections, together with the P-wave velocity constrained by local tomography (Chap-

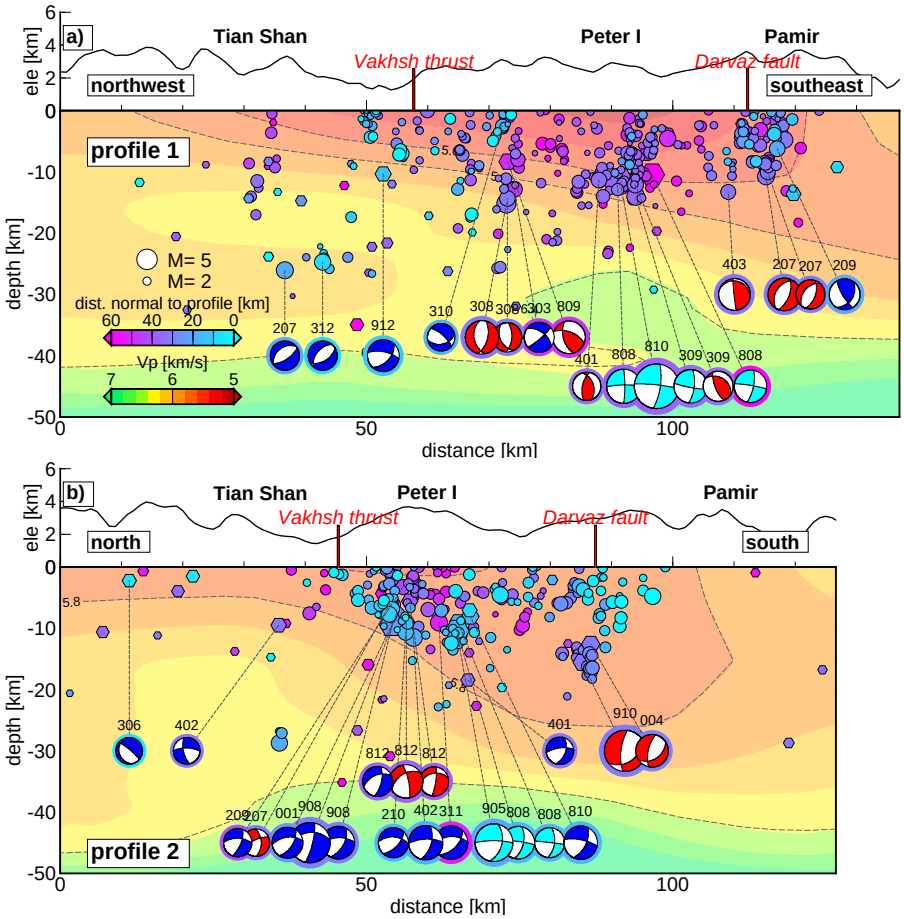

Figure 6.8: Vertical profiles through the Peter I. seismicity (see Fig. 6.7 for profile locations). Focal mechanisms are projected into the hemisphere behind the vertical plane of the cross section. The number on top indicates the last digit of the year and the month in which the earthquake happened (e.g. 010 for October 2010). Color coding of the earthquakes and the circles surrounding the focal mechanisms indicates their profile-normal distance. The background map shows the P-wave velocity model derived in Chapter 5 (along the center of the profiles), which was used here to relocate the earthquakes. Contour interval is 0.2 km/s. The 5.6, 5.8 and 6.4 contours are dashed. Black lines on top of the profiles are the projected topography.

ter 5): the seismically active domain coincides with low P-wave velocity (v_p), which very likely represents the Tajik basin's sediments (Chapter 5), now squeezed between Pamir and Tian Shan (Hamburger et al., 1992; Burtman and Molnar, 1993). Seismicity within the low velocity zone aligns on three interfaces, which feature different source mechanisms:

1. As the vertically dipping dextral Illiac Fault translates into the Vakhsh Thrust System, hypocenters align on a southward dipping ramp. Earthquake mechanisms along this ramp indicate mainly thrusting and to a minor extent dextral strike-slip movement (Fig. 6.8b). Their P-axes accurately parallel the GPS velocity vectors (Fig. 6.4b). This seismogenic ramp falls together with a dipping P-wave velocity contrast (Fig. 6.8), suggesting that it seems to build at the contact between the

sediments of the Tajik basin (low v_p) and the basement of the Tian Shan (high v_p). Thus, these earthquakes might indicate the over-thrusting of the sediment package over the Tian Shan basement.

2. The zone of low v_p is bounded to the south by the Darvaz Fault, which features sinistral strike-slip earthquakes. However, whereas the Darvaz Fault dips vertically along most of the Tajik basin's rim (e.g. in its north-striking branch as discussed above), it is tilted to the north only in the Peter I. range. Further, hypocenters reach deeper than in the vertically dipping segment.

3. A third branch south of the Vakhsh Thrust System and north of the Darvaz Fault (named *PeterI* in Figs. 6.7 and 6.8) mainly features earthquakes with one of the possible fault planes sub-horizontal, suggesting that these events might occur at the detachment horizon at the base of the sediments. However, these *PeterI* events align to a vertically dipping structure, clearly separated from the seismogenic traces of the Vakhsh and Darvaz faults (Fig. 6.8a). In contrast to the two other seismogenic branches, the *PeterI* events do not cluster along a seismic velocity contrast. Thus, instead of sliding along a sub-horizontal interface, these events could also be associated to folding within the sediments of the Peter I. range. Consequently, the rupture might occur on the more vertical of the two fault planes.

The three fault branches converge in the east as the Peter I. range further narrows and are cut across by a strike-slip fault in the west as the Peter I. range widens into the Tajik basin (Obikhingou Fault in Fig. 6.7; after Burtman and Molnar, 1993). Due to this constellation, the triangular block of the Peter I. range is to a certain extent isolated from the rest of the Tajik basin. Sparse seismicity apart from these three main branches might be associated to the numerous detachment folds that cut through the range (Schurr et al., 2014).

The Garm region had been the focus of many seismological studies during Soviet time, resulting in an event catalog spanning ∼30 years of data (e.g. Lukk et al., 1995). This catalog shows a similar segmentation in branches as presented here shallower than ∼15 km. The Soviet catalogs additionally locate deeper diffuse seismicity in the basement, which had been interpreted by Lukk (2011) as fluid intruded wave-guide, by Hamburger et al. (1992) as intra-continental subduction. Our catalog also contains some of these diffuse basement events. The only two events with source mechanisms have thrust mechanisms, featuring a different strike than the events associated to the Vakhsh Thrust System (named T.S. in Fig. 6.7). Thus, these events might indicate deformation in the foot wall of the Tian Shan. However, given that these basement events are much sparser than the shallower seismicity, we do not dare to follow or contradict either of the suggested interpretations of Hamburger et al. (1992) and Lukk (2011).

In Figure 6.7, the two biggest instrumentally recorded earthquakes along the Pamir thrust system are plotted as well. Locations and mechanisms have been reconstructed by Kulikova (2016) based on analog seismograms. These mechanisms fit generally into the short temporal snapshot of seismicity presented here: the 1949 Khait strike-slip earthquake (m_b 7.6) locates on the branch of the Vakhsh system. One of the possible fault planes of the Khait event coincides roughly with the surface trace of the Darvaz Fault and with

the strike-slip mechanism derived here. In other publications, the Khait earthquake is described as a reverse event with one steeply southward dipping plane (Gubin, 1960), which would rather agree with its hypocenter on the Vakhsh Thrust System. The 1907 Karatag earthquake (m_b 7.5) has a thrust mechanism and its epicenter is located near the seismicity associated to the Darvaz Fault. Considering the error range of approximately ±40 km, the Karatag earthquake might be associated to the Vakhsh Thrust System as suggested by Kulikova (2016).
In any case, the presence of these two large earthquakes indicates that the Peter I. range seems to be the crustal region which suffers the most intense seismogenic deformation along the Tajik basin's rims, not only during our observational window of four years but also over longer time spans. As can be seen from the separation of seismicity in different branches, the influences from northward push and westward escape of the Pamir seem to be partitioned at the northern and southern sides of the intensely folded Tajik basin sediments.

6.4.3 Tajik basin's interior and Hindu Kush margin

In contrast to the bounding faults, most seismicity within the Tajik basin aggregates along a slightly southward deepening interface from ∼10 km in the north to ∼15 km in the south (see label *BasinInterface* in the north-south cross sections of Fig. 6.9). This interface roughly falls together with the 5.6 km/s contour of the P-wave velocity model derived in Chapter 5. Many rupture mechanisms of events on this interface have thrust mechanisms with one horizontal dipping fault plane. Seismicity shallower than the interface is sparse and has smaller magnitudes. Seismicity deeper than this interface tends to occur in patches. The most intense of these patches occurs at the Tajik-Afghan border (Figs. 6.4 and 6.5 and label *deep patch* in the cross sections of Fig. 6.9) and features thrust but also dextral strike-slip mechanisms. Deeper than the $v_p = 6.4$ km/s velocity contour, seismicity becomes much sparser.

None of the source mechanisms in the basin's interior shows west-east striking thrust mechanisms like along the Northern Pamir Thrust front and in the Garm region just described above. In map view, the compressional-axes (P-axes) of the earthquake source mechanisms accurately parallel the west-east oriented pattern indicated by horizontal GPS velocity vectors in the basin (Fig. 6.4b). This GPS pattern has been interpreted as the response of the basin's sediments to the gravitational collapse of the Pamir orogen causing the Neogene folding of the Tajik basin's sediment cover (Schurr et al., 2014). Given that the basin earthquakes here indicate the same stress pattern as outlined by the GPS vectors, seismogenic deformation seems to be controlled mainly by the westward oriented push of the Pamir. As the basin earthquakes clearly align on a sub-horizontal interface, it is likely that the horizontal plane of the source mechanisms forms the rupture interface. These interface earthquakes could indicate horizontal movement along an intra-sedimentary contact or along the basement (as schematically sketched in Fig. 6.9b). Schurr et al. (2014) suggested that such an interface might be the Jurassic evaporite layer within the basin's strata. Deformation would occur seismogenically where the salt layer is thinned or absent and pre- and post Jurassic sediments are in contact.
Most of the *BasinInterface*-earthquakes mapped here locate in the southeastern part of the

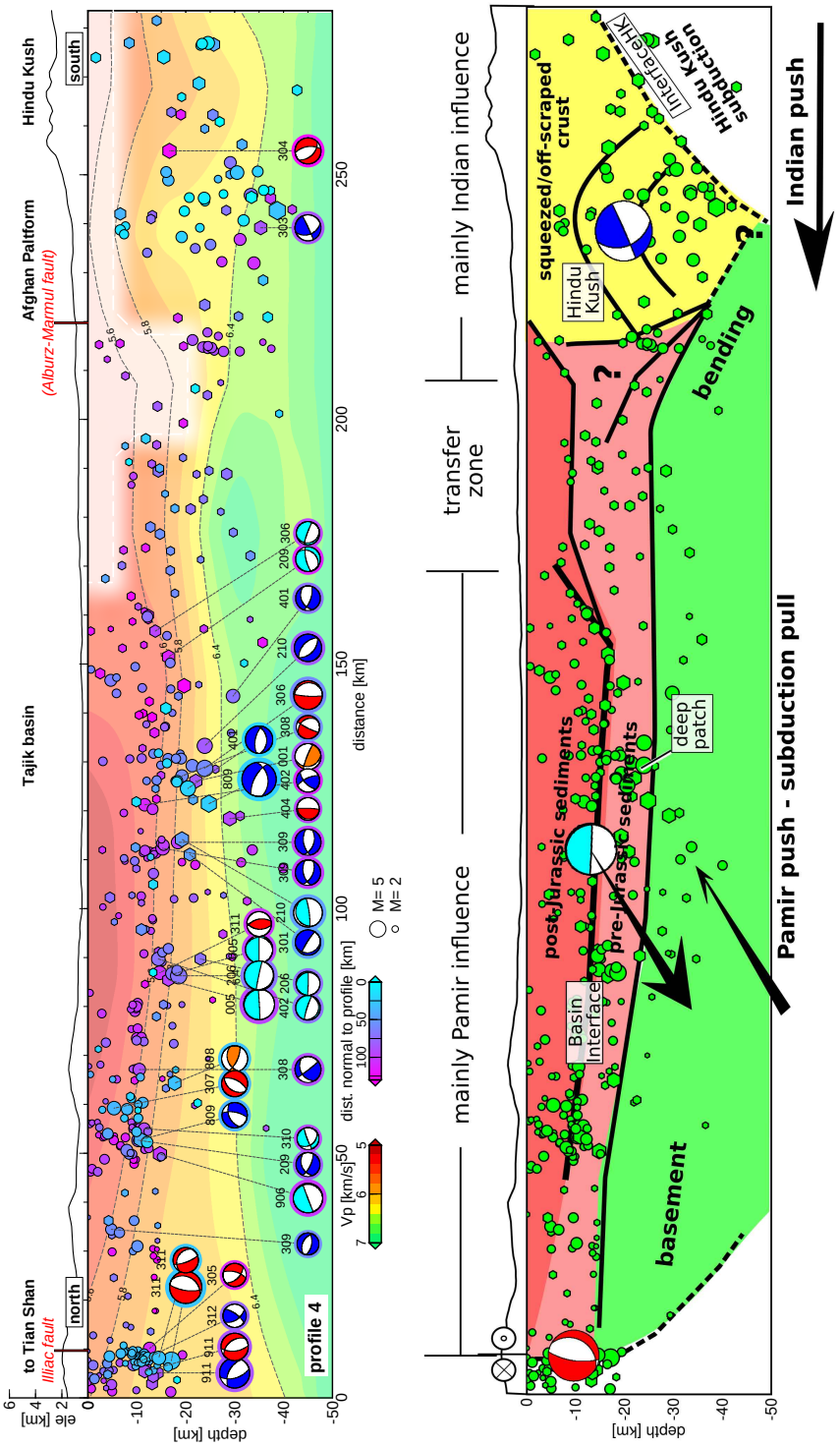

Figure 6.9: North-south oriented cross section through the Tajik basin (see Fig. 6.5 for profile location). **a)** Real data, annotations as in Fig. 6.8. The domain dashed in white encloses badly resolved areas of the velocity model. **b)** Schematic interpretation sketch. Dashed lines were constrained from the interpretation of the local tomography combining v_p and v_p/v_s data (Chapter 5). Earthquakes as in Sub-figure a). See Sections 6.4.3 and 6.5 for further explanation.

Tajik basin, accurately outlining the domain of salt diapirism (Leith and Simpson, 1986a, marked as blue domain in Figs. 6.4 and 6.5). Their clustering likely indicates that the salt horizon at depth is less continuous in this part of the basin. Thus, the horizon outlined by the seismicity provides a direct measure for the thickness of the post-Jurassic cover of the Tajik basin. Local earthquake tomography showed that the basin's basement and possibly the pre-Jurassic sediments underthrust beneath the Pamir (Sippl et al., 2013a, Chapter 5). Consequently, the events deeper than the *BasinInterface*-earthquakes (*deep patch*) imaged here, which show strike-slip and thrusting mechanisms, might indicate deformation during underthrusting, possibly due to bending of the basement units.

The gradual southward deepening trend of hypocenters in the basin culminates in a west-east striking band of deepest seismicity beneath the North Afghan Platform which is, however, spatially separated from the basin events (Fig. 6.4; see label *Hindu Kush* in the cross sections of Fig. 6.9). This deep crustal seismicity occurs only east of the surface expression of the Marmul Fault and west of the most intense intermediate depth seismicity (Fig. 6.4). Hypocenters of the deep crustal earthquakes penetrate as deep as 40 km and terminate along a northward dipping interface (see label *InterfaceHK* in the north-south cross sections of Fig. 6.9). The deep crustal seismicity is further associated with an upward bending of the velocity contours relative to the regions north and south (Fig. 6.9). We could determine only one source mechanism for these deeper crustal earthquakes (a NNE-SSW striking thrust mechanism), but mechanisms in the global CMT catalog also indicate overall thrusting (Fig. 6.5). These deepest Hindu Kush events should be interpreted with caution, as the location errors are bigger than for the basin events. However, also in the global catalogs, deep crustal seismicity clusters further south beneath the Hindu Kush and the North Afghan Platform.

6.4.4 Shakhdara region

The Shakhdara region (see close up map and cross section in Fig. 6.10) is characterized by dominantly strike-slip earthquakes. Hypocenters align to northeast striking structures, generally in accordance to the mapped faults. One cluster of seismicity is located at the northern edge of the Badakhshan Fault, the other patches do not directly coincide with structures described by Schurr et al. (2014). However, the north-striking Lake-Shiwa Fault is marked by a pronounced velocity contrast: the middle crust of the Pamir is underlain by a low P-wave velocity zone (also described by Sippl et al., 2013a). West of the Lake-Shiwa Fault, velocities in the Hindu Kush are clearly higher. Accordingly, seismicity on the Pamir side does not occur deeper than ∼10 km but upper crustal seismicity further west penetrates to ∼15 km. This seismicity and seismic velocity distribution might indicate a shallower brittle-ductile transition in the Pamir crust than in the crust beneath the Hindu Kush mountains.

The overall sinistral strike-slip mechanisms of the events mapped here suggest that seismogenic deformation is accommodated on a network of interconnected faults. We could not determine any rupture mechanism for the events on the Badakhshan Fault, but earthquakes between the Badakhshan and Lake-Shiwa faults indicate strike-slip mechanisms with fault planes rotated relative to the Shakhdara events further east. The mechanisms

in the cluster west of the Lake-Shiwa Fault show little variation during our deployment period (e.g. earthquakes recorded in 2010 and 2013 have similar mechanisms). Given that this earthquake patch is located between the dextral-transpressional Badakhshan and the sinistral Lake-Shiwa Fault, their tilted mechanisms could indicate distributed deformation in the transfer zone.

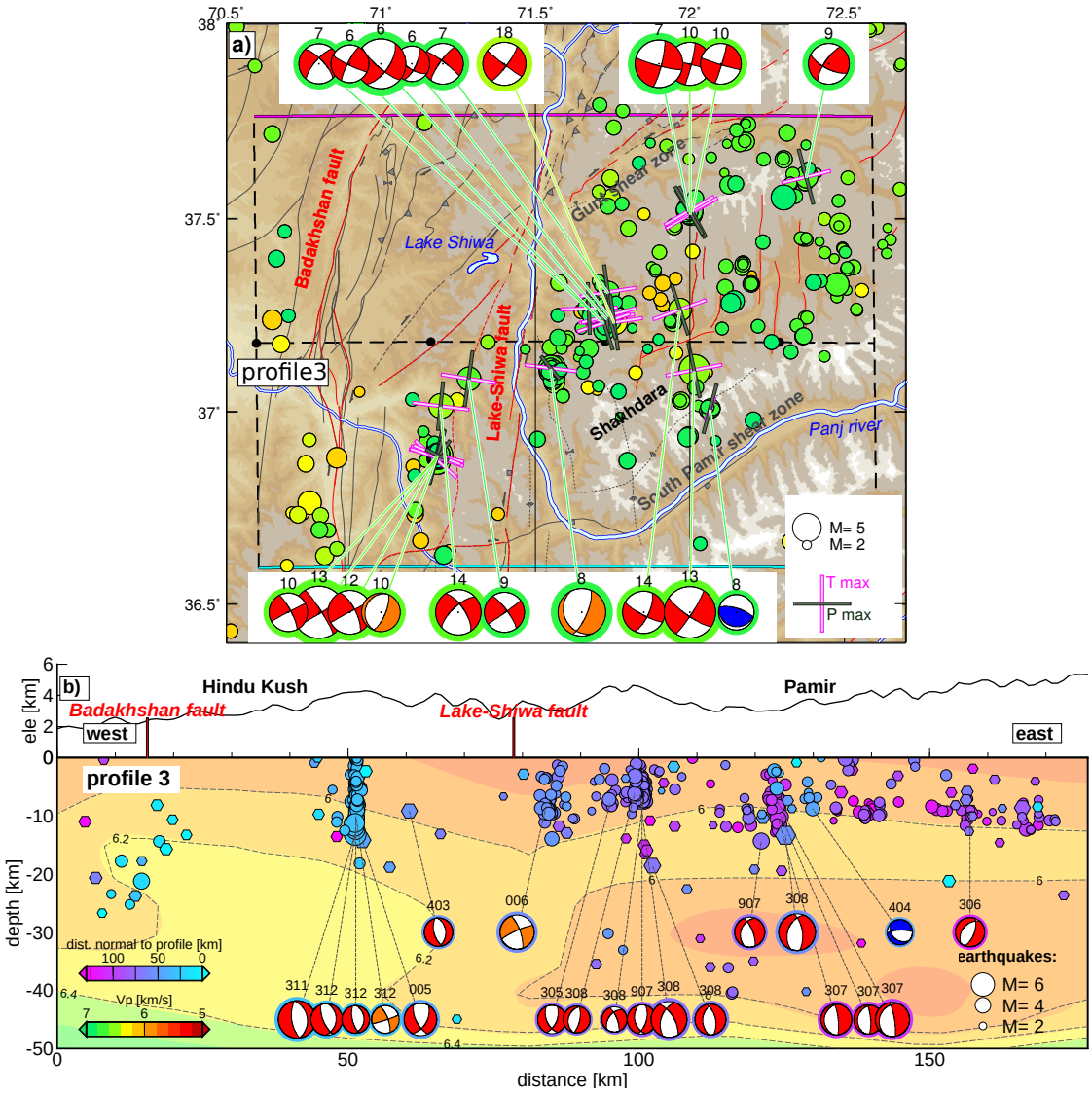

Figure 6.10: Zoom into the Shakhdara region and surroundings (see Fig. 6.5 for map location). Annotations as in Figures 6.7 and 6.8. **a)** Map view. **b)** Vertical profile along the section indicated as a box in Sub-figure a). The dotted velocity contours are at 6.0, 6.2 and 6.4 km/s.

6.5 Crustal deformation and mantle processes

Figure 6.11 shows the combined crustal seismicity catalog from the TIPTIMON and TIPAGE deployments, together with the intermediate depth seismicity. The lack of thrusting north of the Hindu Kush versus pronounced thrusting to its east, north of the Pamir, might be understood considering the broader tectonic context, which has been suggested earlier based on seismic tomography (Chapters 4 and 5). At mantle depths, the peculiar seismotectonic constellation of two oppositely dipping zones of intermediate depth seismicity was suggested to be created due to two distinct units making up the Indian lithosphere: whereas the northward advancing cratonic Indian lithosphere (Cratonic India) forces the subduction of the Asian lithosphere beneath the Pamir, a narrow sliver of India's stretched margin (Marginal India) currently subducts and detaches beneath the Hindu Kush. The map view extent of these units is sketched in Figure 6.11 as proposed in Chapter 4. The transition from Cratonic to Marginal India falls together with the zone of distributed crustal shearing between Pamir and Hindu Kush (Section 6.4.4). Further, the P-wave velocity contrast between higher velocities in the Hindu Kush middle crust versus lower velocities in the Pamir along the Lake-Shiwa Fault (Fig. 6.10) also correlates with

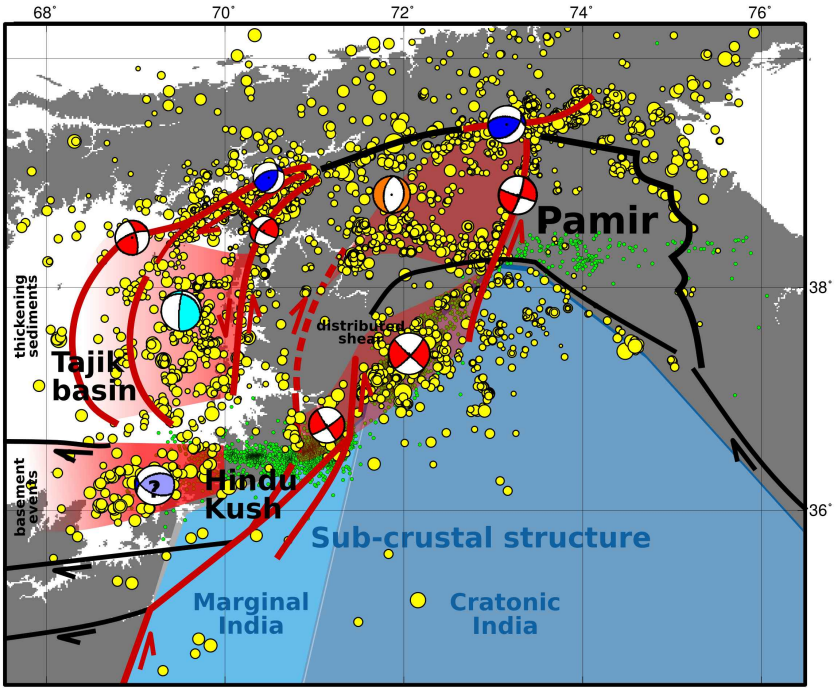

Figure 6.11: Joint earthquake catalog and schematic interpretation sketch for the seismic deformation. Crustal earthquakes in yellow; intermediate depth seismicity in green. The gray domain represents topography higher than 2000 m. The blue bodies sketch the outline of India's lithosphere at sub-crustal depths according to Chapter 4. The map region, the simplified tectonic features and intermediate depth seismicity are the same as in Figure 6.1, but crustal seismicity from the updated catalog is plotted. The simplified interpretation sketch shows deforming regions in red and the style of dominant deformation as focal mechanisms. See Section 6.5 for a detailed description.

this transition. This suggests that the different behavior of the two distinct Indian units at sub-crustal levels can be traced into the Asian crust on top. The zone of distributed strike-slip deformation at the Pamir-Hindu Kush transition might be the crustal reaction to the tearing of India's lithosphere underneath.
We did not resolve seismic activity along the Badakhshan Fault, although it was described to be active from the offset of morphological features (Schurr et al., 2014). In global catalogs, the Afghan part of the Pamir likewise appears seismically inactive (*S4* in Fig. 6.6). This domain of crustal seismic quiescence coincides with the longitudinal extent of the most intense intermediate depth seismicity (Fig. 6.4a), suggesting that the current deformation due to the push of India is not transferred further to the north but seems to be accommodated by processes related to the Hindu Kush subduction. The Hindu Kush subduction was shown to also involve parts of the middle and lower crust, whereas the upper crust might be scraped-off and accreted (Chapter 5). In this context, the deepest crustal earthquakes mapped here beneath the North Afghan Platform could occur due to the squeezing of the Asian units between the rigid Tajik basin and the Hindu Kush subduction. The earthquakes along the northward dipping interface (*InterfaceHK*) might outline the intra-crustal contact along which subduction and possibly crustal off-scraping occurs (also sketched in Fig. 6.9).

The crustal seismicity in the central and eastern Pamir, also shown in Figure 6.11, has been described in detail by Schurr et al. (2014). They proposed that the Sarez-Karakul Graben System might split the Pamir in two parts. Whereas the eastern Pamir deforms *en bloc*, the western Pamir experiences internal seismic deformation explained by the gravitational collapse of the western Pamir into the Tajik basin. As shown here, the seismogenic deformation due to this collapse is most pronounced in the Garm region, where a triangular sedimentary package is squeezed between the oppositely dipping ramps of the Vakhsh Thrust System and the tilted Darvaz Fault. Additionally, the collapse causes seismicity on a gliding interface in the Tajik basin's strata.
At sub-crustal levels, the Schurr et al. (2014)-separation into western and eastern Pamir coincides with a change in strike of the intermediate depth seismicity and a vertical tear which develops in the Asian subducted lithosphere (Chapter 4). Thus, as in the Hindu Kush and at the Pamir-Hindu Kush transition, mantle processes and the style of seismogenic deformation in the crust seem to be interconnected in the Pamir as well.

6.6 Conclusion

Based on four years of temporarily deployed seismic networks, we derived an earthquake catalog and source mechanisms for shallow seismicity within the Tajik basin and the adjacent Pamir, Hindu Kush and Tian Shan orogens. We interpret the seismogenic features together with the velocity structure derived by local earthquake tomography (Chapter 5) and relative to the sub-crustal processes.
Seismic deformation in the basin and its rims is strongly partitioned: The basin's bounding faults to the north and east (Illiac and Darvaz faults) have mainly strike-slip components. At the northeastern termination of the Tajik basin, where the Pamir and Tian Shan mountains converge, the Illiac and Darvaz faults translate into a zone of thrusting along

the Peter I. range. This region hosts not only the largest instrumentally recorded earthquakes along the basin's rims (Kulikova, 2016), but also exhibits the most frequent crustal seismicity in our catalog. This seismicity was interpreted to occur in response to the northward pushing Indian indenter and the westward escaping Pamir rocks. Hypocenters in the basin show a gradual southward deepening trend, probably outlining the Jurassic evaporite decollement, as most of these earthquakes cluster in the region of active salt diapirism. Deepest crustal seismicity occurs beneath the North Afghan Platform, spatially separated from the basin events. The Afghan Pamir exhibits little seismogenic deformation.
These different seismogenic domains might arise as the far field stress exerted by the ongoing Indian indentation into Asia is accommodated differently by the individual units involved in the collision: The stress regime indicated by seismicity in the basin coincides with west-east oriented GPS-velocity vectors, indicating that seismotectonics in the Tajik basin are mainly influenced by the westward escape of the western Pamir. Thus, west-east directed shortening is much more pronounced in the basin than the far field deformation from the Indian collision. In contrast, seismicity at the basin's southern margin is shifted further south below the Hindu Kush, and might be connected with the ongoing Hindu Kush continental subduction. A domain of interconnected strike-slip faults in the Pamir-Hindu Kush transfer zone might accommodate the relative movement between the two segments of the tearing horizontally Indian lithosphere at sub-crustal levels (Cratonic and Marginal India in Fig. 6.11). Thus, crustal deformation in both the Pamir and Hindu Kush seem to be strongly influenced by sub-crustal processes.

7 Zooming into the Hindu Kush slab break-off

Abstract
Intermediate depth earthquakes (∼60-300 km depth) occur in regions where pressure-temperature conditions are expected to promote ductile deformation rather than brittle failure. To explain this seismogenic behavior, either dehydration embrittlement due to phase transformations of hydrous minerals or thermal runaway, where localized viscous creep results in weakening and slip on a narrow shear-zone, were suggested. Here, we present a detailed case study of the Hindu Kush slab break-off, which features the most active nest of intra-continental intermediate depth seismicity worldwide, and suggest that in the Hindu Kush-case both processes might be capable triggering earthquakes. Which one of them is dominantly active, however, depends on the depth interval to which crustal material is subducted and on the advance of the slab-detachment. We use the records of temporarily deployed seismic stations over four years to deduce a high precision earthquake catalog and source mechanisms for many of these earthquakes. We then relocate the largest Hindu Kush earthquakes of the last 30 years relative to our local catalog, including the most recent M_w 7.5 Badakhshan event in October 2015 and 21 of its aftershocks. Our results reveal different characteristics in the shallower and deeper part of the seismogenic domain, the geometry of which narrows with depth from a diffuse north dipping earthquake zone (∼60-180 km depth) to a localized vertically dipping and partly overturned interface on which the events cluster (∼180-270 km). From a strain rate analysis using 30 years of data available from the GCMT catalog, we deduce that the deep portion of the slab is in the process of detaching from the shallower fragment. The deeper domain is seismically much more active and hosts the largest earthquakes. Fault planes of these, as well as the aftershocks of the M_w 7.5 Badakhshan event, indicate shearing on the plane outlined by the catalog seismicity. Based on tomographic images, we suggest that seismicity in the shallow part coincides with the domain of subduction of crustal rocks. Whereas the buoyant crust in the shallower part likely resists subduction, the earlier subducted mantle lithosphere pulls from underneath. Thus, the deeper seismogenic domain could represent a shear-zone that develops through the subducting mantle lithosphere in response to this vertical force. In such a slab-shearing scenario, metamorphic reactions in the subducted crust might provide a possible fluid source to trigger seismicity in the shallower domain, whereas earthquakes on an intra-lithospheric interface might likewise be attributed to thermal runaway.

7.1 Introduction

The Pamir-Hindu Kush in Central Asia forms, besides Vrancea in Romania, the only region worldwide where intermediate depth seismicity (seismicity in the range of ∼60-

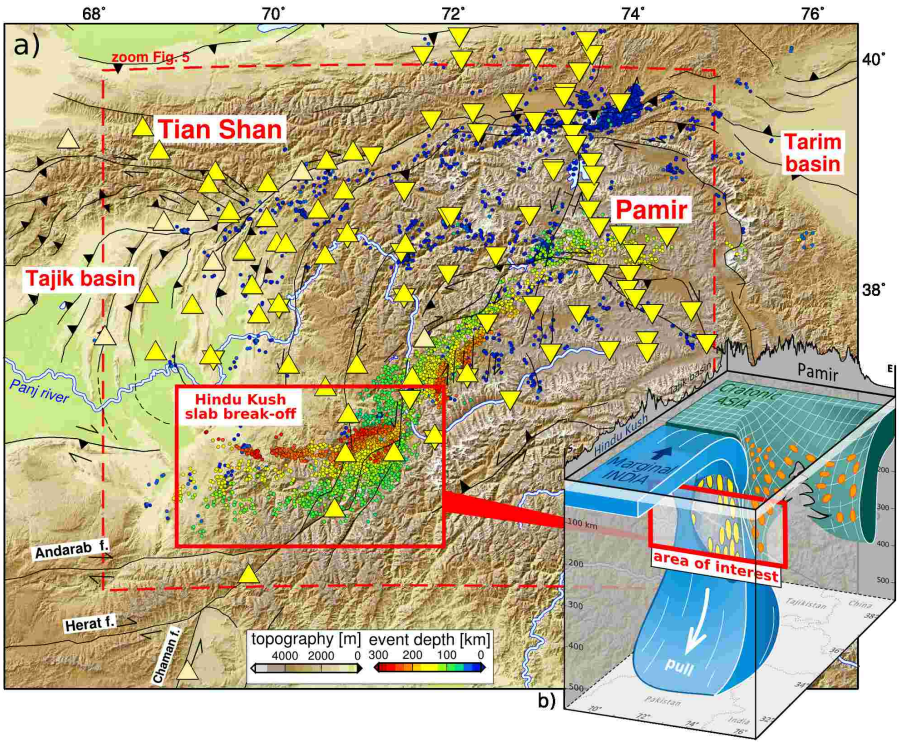

Figure 7.1: a) Topographic map of the Hindu Kush and surroundings. Yellow triangles are the local seismic stations used in this study (normal triangles - TIPTIMON; inverted triangles - TIPAGE/FERGHANA; light yellow - permanent stations; see Section 7.3.1 for a detailed description of the network). Intermediate depth seismicity from Chapter 4 and shallow seismicity from Sippl et al. (2013b) is color coded by depth. Tectonic features as in Chapter 6. **b)** Sketch from Chapter 4, illustrating the regional tectonic context: beneath the Hindu Kush, an earlier subducted fragment of India's thinned continental margin (blue) is currently in the process of detaching, causing the intermediate depth seismicity (yellow). Beneath the Pamir, the Asian plate (green) delaminates and forms an arcuate slab, which tears horizontally in its center. Pamir earthquakes are sketched in orange.

300 km depth) is not clearly associated with ongoing oceanic subduction. Instead, the removal of mantle lithosphere has been suggested as main driving mechanism for the frequent earthquakes (Wortel and Spakman, 2000; Koulakov and Sobolev, 2006; Lister et al., 2008; Lorinczi and Houseman, 2009). In the Hindu Kush, slab-detachment seems to be the most likely scenario (Chapter 4). However, the physical processes causing the associated seismicity are enigmatic as the pressure at the hypocentral depths of these events would require very large differential stresses to allow brittle failure. These are unlikely to be reached as ductile deformation should occur in the temperature regime of the upper mantle (Thielmann et al., 2015). Two main processes have been suggested to explain intermediate depth seismicity: dehydration embrittlement due to phase transformations of hydrous minerals (Kirby et al., 1996; Yamasaki and Seno, 2003; Hacker et al., 2003), and thermal runaway, where localized viscous creep might result in temperature increase, subsequent weakening and finally slip on a narrow shear-zone (Kelemen and Hirth, 2007; Braeck and Podladchikov, 2007; John et al., 2009). In the Hindu Kush, seismicity has

been suggested to result from the enhanced strain rate during the slab break-off (Lister et al., 2008). The involvement of crustal material in the subduction process (Schneider et al., 2013; Sippl et al., 2013a, Chapter 5), in turn, might widen the range of possible metamorphic rock reactions, which could promote earthquake triggering by dehydration embrittlement.
Numerical simulations, dealing with the dynamics during slab break-off, reveal that the spatio-temporal evolution of the detachment depends on multiple input parameters, i.e. the imposed convergence rate, the involved rheology, slab thickness and the consideration of 3D effects (van Hunen and Allen, 2011; Duretz et al., 2012; Duretz and Gerya, 2013). Thus, relating intermediate depth seismicity to a physical rupture process requires the detailed knowledge of the (tectonic) framework in which the break-off happens. This, however, is by far not yet clear in the case of the Hindu Kush.

We aim to illuminate the dynamics of the Hindu Kush slab break-off by deducing a high precision snapshot of its seismotectonic characteristics. This then enables us to put constraints on the possible driving mechanisms for seismicity. Our results are mainly gained from the analysis of seismic records from the temporarily deployed stations of the TIPAGE (Mechie et al., 2012) and TIPTIMON (Schurr et al., 2012, 2013) networks (see station locations in Fig. 7.1), which allowed us to determine the geometry of the seismically active domain, the rupture mechanisms of many of these earthquakes and the velocity structure of the surrounding material. We additionally used available global seismic data to relate our observations, representing a temporal snapshot of four years, to a longer observation period. In particular, we calculated the strain rate within the seismogenic portion of the slab based on the geometry established before and relocated the largest digitally recorded Hindu Kush earthquakes relative to our catalog. This last point also includes a detailed analysis of the most recent M_w 7.5 Badakhshan earthquake (26.10.2015) and several of its aftershocks.

7.2 Tectonic setting

The Hindu Kush is located north of the western syntaxis of the India-Asia collision system. It is a geodynamic peculiarity along the whole collision front due to the occurrence of intense intermediate depth seismicity and vertically dipping seismic velocity anomalies down to the transition zone (Van der Voo et al., 1999; Koulakov and Sobolev, 2006, Chapter 4), which have been related to the subduction of Indian lithosphere, i.e. India's thinned continental margin as suggested in Chapter 4. The Hindu Kush slab seems to be very close to breaking-off (Koulakov and Sobolev, 2006; Bai and Zhang, 2015, Chapter 4), causing intense intermediate depth seismicity. The first order features of the Hindu Kush seismic zone have been described over the last years by several authors with increasing precision (Billington et al., 1977; Pegler and Das, 1998; Sippl et al., 2013b; Bai and Zhang, 2015): It appears as a continuous, west-east striking feature of very narrow along-strike extent (i.e. 150 km). In the shallower part (i.e. between 60-160 km depth), the seismogenic zone dips moderately north, but steepens to near vertical deeper than ∼180 km (see Fig. 7.1). The Pamir zone of intermediate depth seismicity, located north-east from the Hindu Kush, has been associated to Asian subduction (Schneider et al., 2013; Sippl et al., 2013a),

possibly forced to delaminate by a northward penetrating Indian indenter (Chapter 4), and is thus only indirectly associated with the Hindu Kush slab break-off.

7.3 Seismicity analysis

7.3.1 Local earthquake catalog

Our local earthquake catalog comprises all earthquakes registered during the TIPTIMON seismic deployment (Schurr et al., 2012, 2013), jointly relocated with a subset of the already published event catalog from Sippl et al. (2013b), whose results are mainly obtained from the data recorded by the TIPAGE seismic network. TIPTIMON was deployed between 2012-14 in the Tajik basin, Hindu Kush and western Pamir; TIPAGE between 2008-10 in the Pamir and Tian Shan. TIPAGE and TIPTIMON share several common stations in the western Pamir. Thus, the joint network allows us to illuminate the subsurface beneath both Pamir and Hindu Kush at high precision (see Fig. 7.1 for the location of the stations and Supplementary Fig. E1 for a detailed description of the catalog subsets from different deployment times).
For event location and error assessment, we chose the same approach and selection criteria as in Chapter 6: hypocenters were initially obtained using an automated location chain for event detection (Sippl et al., 2013b). All events included in the final TIPTIMON catalog from this initial step were required to have a root mean square (RMS) residual smaller than two seconds, at least five P picks and at least one S pick. These initial locations were improved by single event and double difference relocation in the regional 3D velocity model of Chapter 5 using the software *simulps* (Thurber, 1983, 1993; Eberhart-Phillips, 1993; Evans et al., 1994) and *hypoDD3D* (Waldhauser and Ellsworth, 2000; Waldhauser, 2001), respectively. Errors were constrained in *NonLinLoc* (Lomax, 2008) and *hypoDD3D*. The joint catalog west of 71.8°E, which will be primarily discussed in the following, consists of 4369 events, 94% thereof from the TIPTIMON deployment. The mean RMS of the single event locations is 0.23 s. The average absolute location uncertainty is 4.9 km (this value refers to the radius of a sphere with the same volume as the error ellipsoids calculated in *NonLinLoc*). Figure 7.2 shows a detailed analysis of the location errors: the vertical uncertainty generally exceeds the horizontal one (average of 5.1, 4.9 and 7.4 km in latitudinal, longitudinal and depth direction, respectively). The shallowest intermediate depth events in the western part of the Hindu Kush have the largest location errors, due to the unfavorable station-event geometry. The whole catalog exhibits no obvious correlation between average location errors and magnitude or depth.
In total, 90.3% of all events could be relocated with the double difference scheme (green circles in Figs. 7.2a-c). The average relative error of the double difference relocated events is ±1.9 km, which was derived by running *hypoDD3D* in the singular value decomposition mode. The events which were not relocated in the double difference scheme were mainly isolated earthquakes that could not be attached to any of the double difference clusters.

7.3.2 Earthquake source mechanisms

We determined earthquake source mechanisms for 158 of the events that occurred during the time of the TIPTIMON deployment. For the 114 largest of these events (M_w between

3.5 and 5.6; average of 4.3), the mechanisms were constrained via waveform modeling as described in Chapters 4 and 6. For 44 smaller events with favorable station-event geometry, the mechanisms were determined from manually picked first motion polarities using the software *HASH* (Hardebeck and Shearer, 2002). Based on an input set of polarity picks, event-station azimuths and take-off angles, *HASH* determines a set of mechanisms

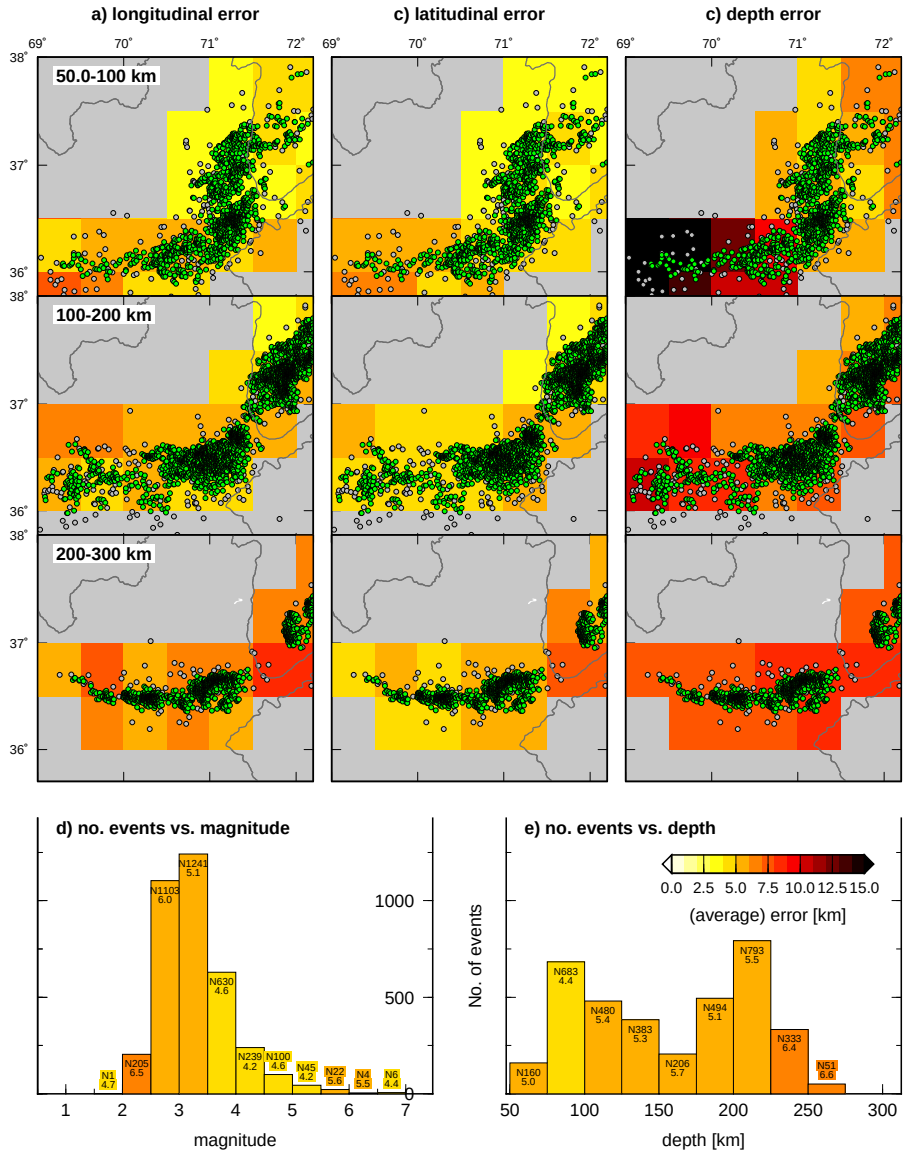

Figure 7.2: a-c) Absolute horizontal and vertical location errors of local earthquakes. Errors are constrained from the axis length of the error ellipses in the specific direction gained from the probabilistic location scheme averaged over all earthquakes in 0.5°x0.5° bins. Only bins that contain more than six earthquakes are plotted. Events which could/could not be double difference relocated are plotted in green and gray, respectively. Political boundaries in dark gray. **d/e)** Depth and magnitude histograms color coded by averaged location error. The upper number at the top of each bin (N) refers to the number of events, the lower number is the averaged location error (radius of a sphere with the same volume as the error ellipsis).

which would explain the observed polarities based on a grid search. The spread of all possible solutions relative to the preferred one determines the quality of the solution. This quality can be expressed in terms of the RMS fault plane uncertainty, which is the RMS angular difference of the acceptable fault planes from the preferred plane (Kilb and Hardebeck, 2006). Here, we derived 1329 first motion picks, yielding an average of 30 picks per event. Take-off angles and event-station azimuths were calculated in *NonLinLoc* based on the 3D velocity model from Chapter 5. All obtained mechanisms were visually inspected to ensure that the possible fault planes indicated the same faulting type than the preferred mechanism. Otherwise the event was disregarded. The average RMS fault plane uncertainty of the 44 mechanisms shown here is 44° (minimum/maximum values of 20°/60°).
In addition to the mechanisms determined based on TIPTIMON data, we further included all mechanisms from the TIPAGE recording period in the plots shown here (the same data as used in Chapter 4 for the stress inversion), summing up to 264 mechanisms. All mechanisms were plotted at their hypocentral position in the relocated event catalog. Supplementary Figures E2 and E3 show further detail regarding the subdivision of the mechanisms with respect to recording time and the used method.

7.3.3 Relocation of all magnitude seven earthquakes since the 1980s

The deep Hindu Kush was repeatedly struck by large earthquakes with magnitudes larger than seven. None of these, however, occurred in the deployment time of our networks. The hypocenters of these events, as listed in global bulletins, can not be compared directly to our results as locations in different catalogs generally vary due to differences in the location method used, the set of phase picks and the underlying velocity model. Thus, we introduced station corrections at the global stations to transfer these events to our local framework, aiming to interpret the large Hindu Kush earthquakes in the context of our high precision local event catalog. These station corrections were calculated based on 15 earthquakes from our local catalog, also registered in global catalogs (*master events*; Fig. 7.3). The master events were chosen to be representative for the whole spatial extent of the deepest Hindu Kush seismic zone, where most of the large earthquakes are located. Station corrections at the global stations were derived by calculating the travel time difference between the event location of the master events from our catalog and in the global catalog at each specific station. The average travel time difference from all master events at one station was used as a station term. Relocating an earthquake starting from its global catalog position using these station terms should ideally transfer the event to the framework of our local event catalog.
Two independent sets of station corrections were derived for the ISC and the GEOFON catalogs, respectively. We used both catalogs as the ISC catalog has the longer recording time but is not updated for the most recent event (terminating in 2013). The GEOFON catalog then fills the missing years until 2016. Additionally, earthquakes registered in both catalogs can be used for quality control for the method applied here. To prevent complications from misinterpreted phase picks, only P, pP and S picks in the epicentral distance smaller than 90° were used. For the ISC events, residuals bigger than 9.5 seconds were excluded due to possible picking errors. All phase picks from the GEOFON data had been visually reinspected and did not show such big residuals. For each master event, all

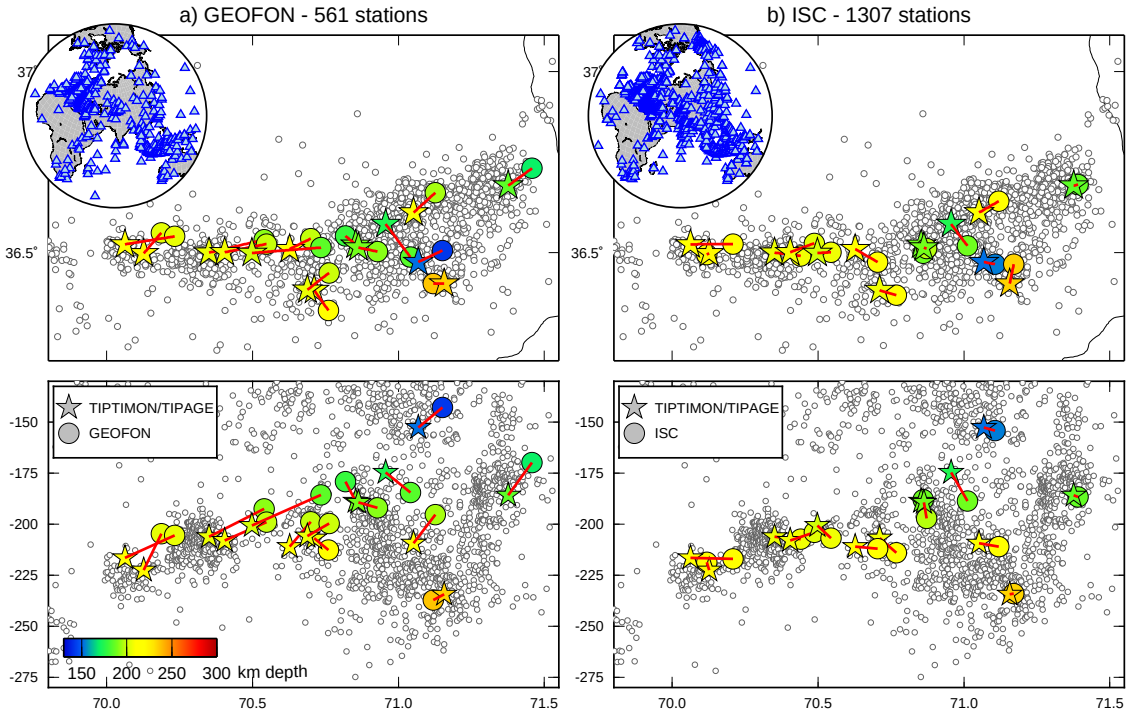

Figure 7.3: Master events used to deduce station corrections for event relocation of the largest Hindu Kush earthquakes of the last 30 years. **a)** Location of the master events in the local and in the GEOFON catalog (*top* - map view; *bottom* - longitude-depth section). Small gray circles are all other earthquakes from the local event catalog for orientation. The inset-globe shows the location of the 561 global stations used by GEOFON to locate the master events. **b)** The same information as in a) but showing the ISC locations of the master events instead.

residuals of the same phase were reduced to have zero mean. The final correction term at each station was calculated as the median of all available residuals. For a station to be included in the set of final station corrections, we required at least two phase picks from the master events and the standard deviation (std) from all residuals to be smaller than 0.5 s. This combination yielded the maximum number of stations that could be used for relocation, but ensured that stations with erroneous picks were excluded. Figure 7.4 shows the final sets of station corrections after applying these quality criteria. In total, 680 (614 P, 47 pP and 19 S) and 572 (487 P, 78 pP, 7 S) station terms from 639 and 487 stations could be determined for the ISC and GEOFON catalogs, respectively. Although the initial offset of our locations relative to the ISC locations is smaller than to the GEOFON locations (Figs. 7.3a, b), the two different station correction sets show overall very similar large scale trends (Fig. 7.4). This is expected as both datasets are based on station networks with a large overlap.

For all steps involving travel time calculation, the software *NonLinLoc* (Lomax et al., 2000) was used. The other steps were executed using *python/obspy* (Beyreuther et al., 2010; Wassermann et al., 2013). Supplementary Table E1 lists further detailed information regarding the master events.

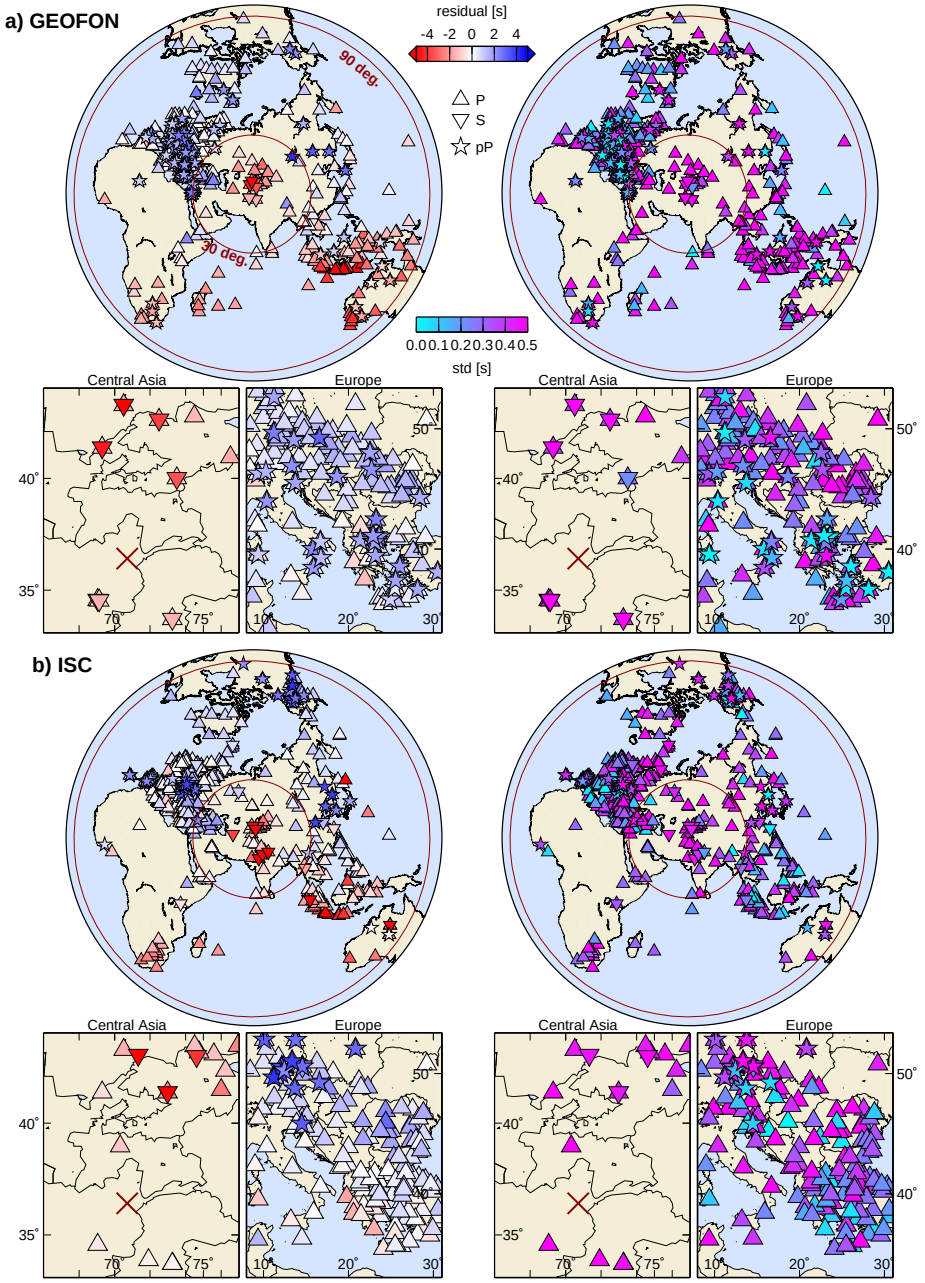

Figure 7.4: Station terms: **a)** *left:* Averaged travel time residuals between the GEOFON locations of the master events and their location in the local event catalog (see Fig. 7.3a for the location of the master events). Residuals were reduced to zero mean. Only stations that fulfilled the quality criteria described in Section 7.3.3 are plotted. The different symbols indicate the type of the phase pick (triangle - P; inverted triangle - S; star - pP). *Right:* the color coded standard deviation of the associated residuals at each station. The red cross in the 'Central Asia' map marks the position of the recent 2015, M_w 7.5 event for orientation. **b)** The same information as in a) but showing the station corrections derived from the ISC catalog.

Using these station corrections, we relocated the five largest Hindu Kush events since the 1980s (according to their moment magnitude given in the Global Centroid Moment Tensor catalog), 21 aftershocks of the 2015 event, the foreshock of the 2002 event and one additional large event which appears in the ISC and GEOFON catalog in 2004 (see Supplementary Tabs. E2 and E3 for detailed event information). For each of these events, only a smaller number of the derived station terms could be used, dependent on the available picks of the specific event: for the aftershocks of the 2015 event, the average of used phases was 31. For the large events, we used on average 215 phases (see the column *'no. of phases'* in Supplementary Tabs. E2 and E3).

To assess the quality and the error of the relocated events, we implemented three types of tests: for the first test we changed the set of station terms by varying the quality criteria for selection (maximum std from 0.5 to 1.0 s; minimum number of picks of two or three). This test should serve as a measure of how vulnerable the method is to wrong picks or how much the solution depends on individual stations. It was only implemented for the large events because the aftershocks did not have sufficient stations for relocation any more if the quality criteria were restricted. The second test aimed to assess the impact of station geometry: for each master event, an individual set of station corrections from the other 14 master events was calculated. Then we relocated this specific master event from its position in the ISC/GEOFON catalog using only global stations which would mimic the same station geometry as we had used for the relocation of the large Hindu Kush earthquakes. The offset of the relocated master event and its actual position in the local catalog served as a measure for the location accuracy of a specific station-event geometry. This approach only worked if the remaining master events had enough suitable picks, thus, mainly when the smaller aftershocks were used as test events. As a final test, a magnitude 6.6 earthquake, which occurred in 2004 and was listed in both global catalogs, was relocated using the two different sets of station corrections.

Generally, the event locations were relatively robust towards the variation in quality constraints for the station correction (on average ∼0.1-4 km horizontal and ∼2-4 km depth error; see Supplementary Tables E2 and E3 for a more detailed summary of the location uncertainties). Location errors derived from relocating the master events with a specific station geometry decreased, if more phases could be used for relocation. Generally, they did not exceed 4 km. These errors were always smaller than the initial offset between the event hypocenter in the global and local catalogs. Finally, the relocated ISC and GEOFON hypocenters of the 2004 event overlap within their error ranges. Thus, the applied relocation scheme seems to be reliable in the given error range and consequentially the hypocenter position of the relocated events can be interpreted in the context of our local event catalog.

7.3.4 Results

Figures 7.5 and 7.6 (b/c, e/f) show the local earthquake catalog and the TIPTIMON and TIPAGE focal mechanisms together with the relocated events. Despite their direct vicinity, the Hindu Kush (earthquakes plotted with black outlines) and Pamir (blue outlines)

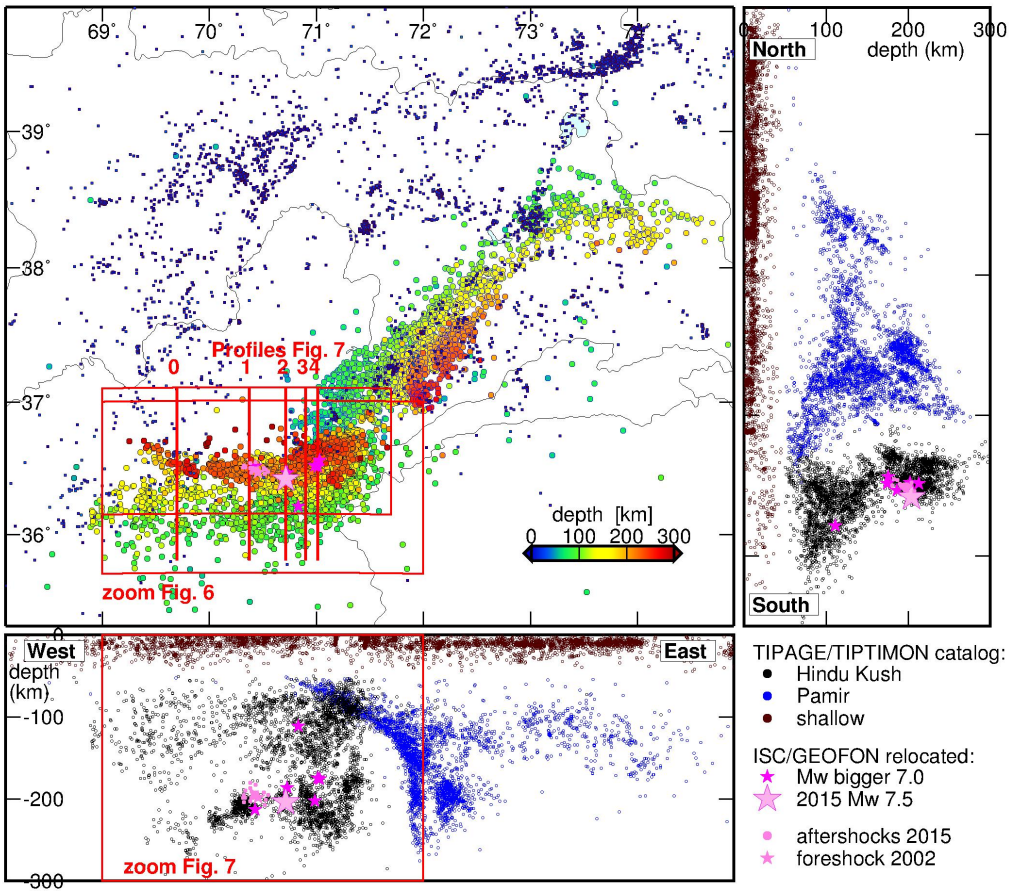

Figure 7.5: Local earthquake catalog and relocated large events in map view and projected onto two vertical sections. The events in the map are color coded by depth. The outline of the circles indicates the affinity of the specific earthquake to the Pamir or Hindu Kush seismic zone, which has been assigned manually based on the different dips of the seismogenic structures. Earthquakes shallower than ∼50 km are outlined in dark red and are associated with crustal structures (see a detailed description in Chapter 6). The relocated events from the global catalogs are plotted in pink.

seismic zones feature different dips as already pointed out in Chapter 4: the Pamir seismic zone forms an arcuate structure, northward offset relative to the Hindu Kush seismicity. The Hindu Kush seismicity appears as a west-east striking curtain of seismicity. This generally different character arises from the large-scale tectonic constellation of forced Asian-sided subduction beneath the Pamir versus Indian-sided subduction and break-off beneath the Hindu Kush (see schematic sketch in Fig. 7.1b and Chapter 4). The Pamir seismicity is described in detail in Sippl et al. (2013b). In the following, we will focus on the details of the Hindu Kush seismicity:

The west-east striking curtain of intermediate depth seismicity is split by a sub-horizontally trending seismic gap at ∼160-180 km depth, with the deeper part containing the majority of the earthquakes in the local catalog and most of the relocated magnitude seven events (Fig. 7.5). Whereas the seismically active area appears as a diffuse cloud at shallow levels (Fig. 7.6b), it narrows to a thinner structure deeper than ∼180 km (Fig. 7.6e). In the

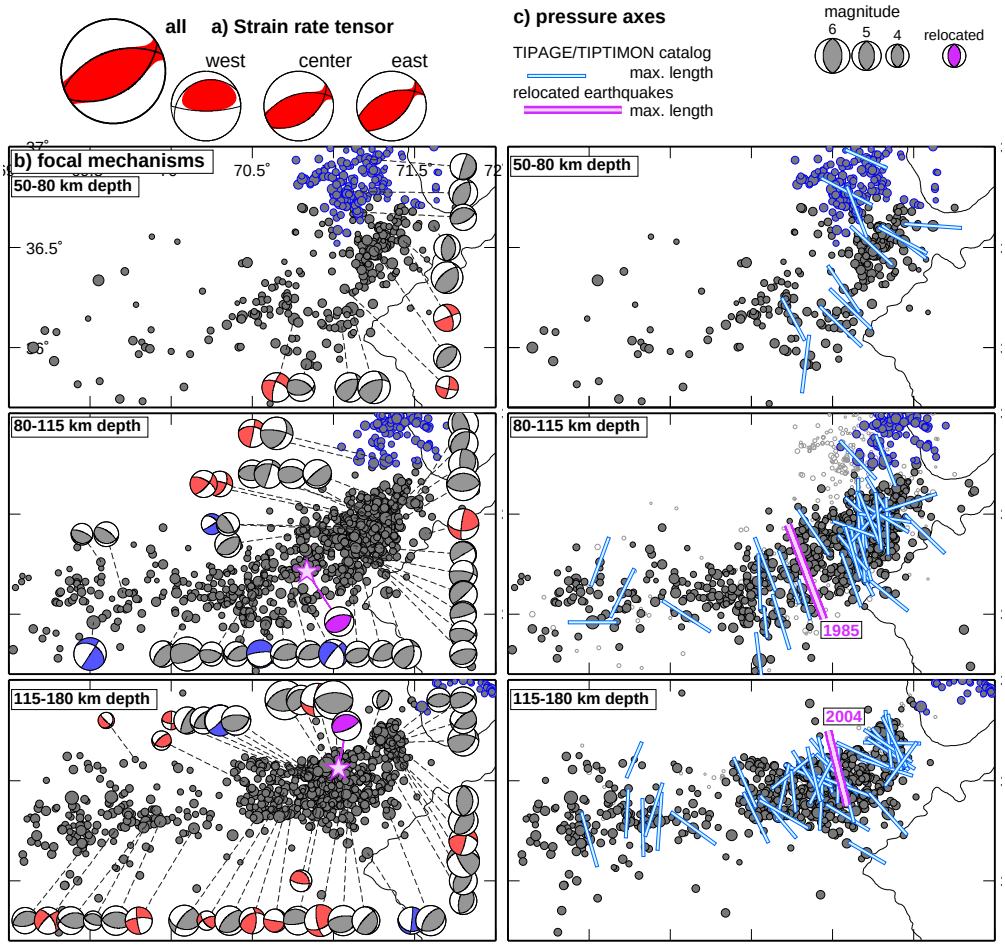

Figure 7.6: Map view sections through the different depth levels of the Hindu Kush seismicity together with the derived focal mechanisms and the results of the strain rate inversion (see Fig. 7.5 for the location of the map excerpt). **a)** Stereonet plot of the strain rate tensor (red) obtained using the approach of Kostrov (1974) and moment tensors listed in the GCMT catalog since 1977. The double couple component of the strain rate tensor is additionally outlined in black. Here the results for the shallower depth interval of intermediate depth seismicity (60-180 km depth) are shown, considering *all* available mechanisms and splitting them into sub-sections along-strike (*west/center/east*; see Section 7.5 and Table 7.3 for further information). **b)** Local seismicity and beach ball representations of the focal mechanisms. The mechanisms are color coded according to their faulting type (red - strike-slip; blue - normal; gray - thrust). Seismicity associated with the Pamir and Hindu Kush seismic zone is outlined in blue and black, respectively. Hypocenters and beach balls of large relocated events in purple. **c)** Pressure (P) axes of the events with focal mechanism from the local catalog (black) and the relocated large events (purple, with year of the event) are normalized to one and projected into map view. Seismicity in each depth level is plotted as in Sub-figure b). The faint gray circles additionally indicate the location of seismicity in the depth interval above. **d-f)** Map view sections through the deeper patch of intermediate depth seismicity. All annotations as in Sub-figures 7.6a-c.

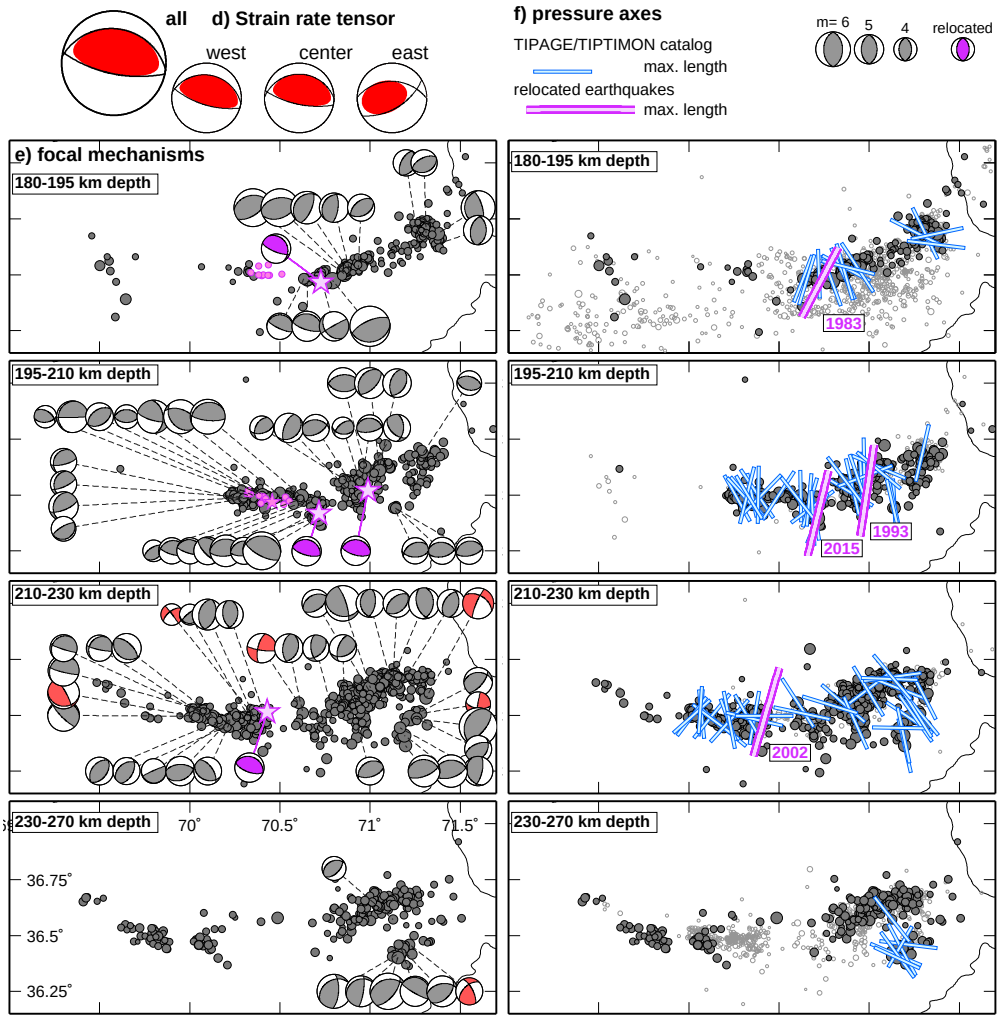

Figure 7.6: Continued.

following, we will refer to the upper seismogenic portion of the Hindu Kush slab as the *shallow* part (∼60-180 km depth), to the deeper portion as *deeper* part (∼180-265 km depth).

All large relocated Hindu Kush earthquakes have down-dip extensional mechanisms (Fig. 7.6b, e) with pressure (P) axes indicating north-south compression. Focal mechanisms derived from the local data of the TIPTIMON/TIPAGE deployments show slightly more scatter but generally similar characteristics: mechanisms are down-dip extensional with P-axes oriented roughly perpendicular to the strike of the seismogenic structure. Strike-slip events in map view, which would correspond to along-strike extension in a vertically dipping structure, seem to be restricted to exterior domains of the seismogenic structures.

Zooming into the Hindu Kush seismicity (Fig. 7.7), the deeper seismogenic patch appears fragmented and seismicity clusters in several vertically oriented *fingers* (labels F1-F4 in

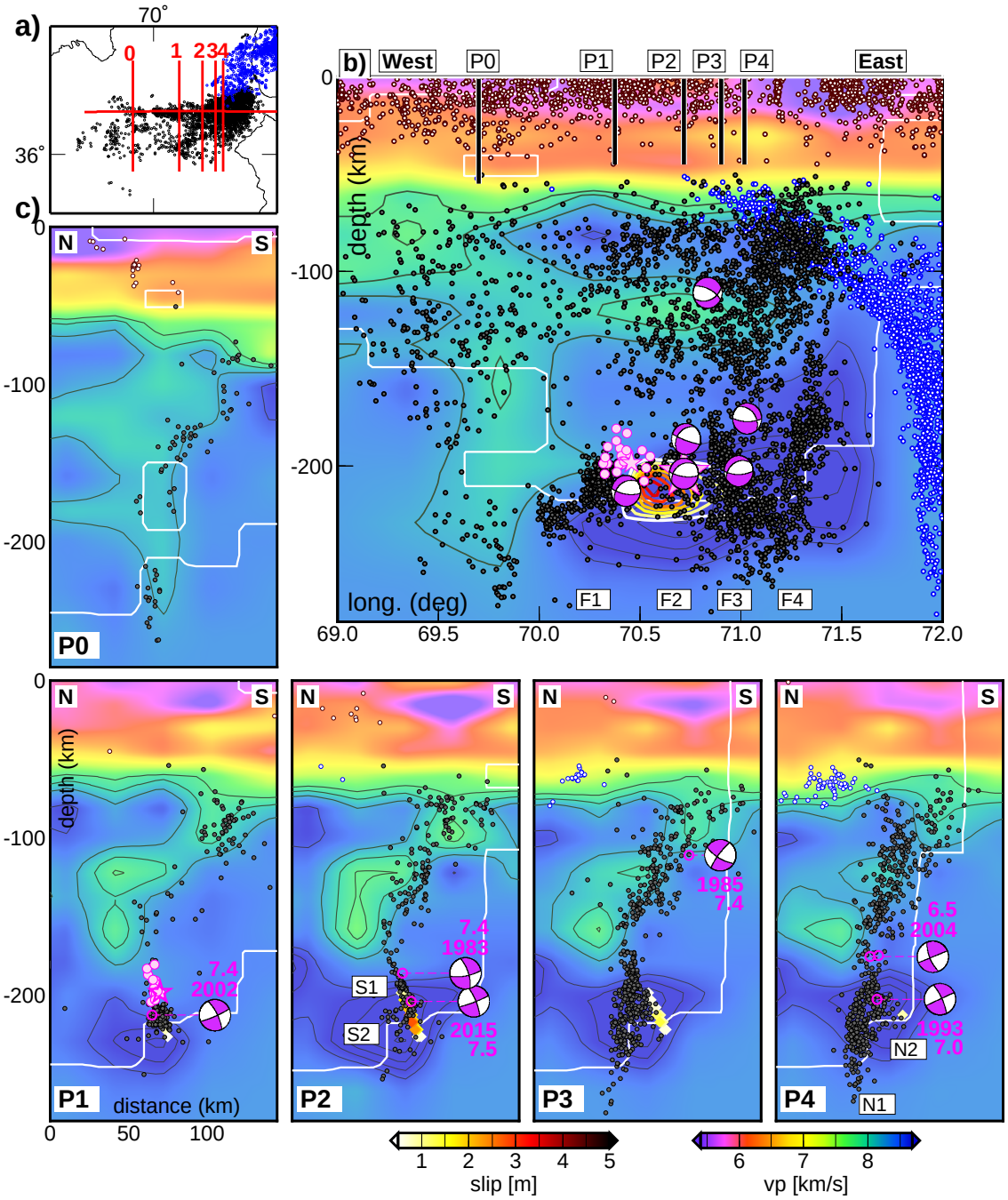

Figure 7.7: See Figure caption on the subsequent page.

Fig. 7.7b), which are seismically highly active, closely spaced patches, separated by areas with little or no background seismicity (*gaps*). The hypocenters of the relocated large events seem to cluster at the edges of these seismic gaps. On a west-east striking cross section (Fig. 7.7b), approximately parallel to the strike of the seismic zone, the seismogenic fingers appear arranged roughly parallel to each other. In dip-parallel cross sections, each of these fingers is separated into domains with different dips outlined by the earthquake

Figure 7.7: Zoom into the Hindu Kush intermediate depth seismicity. **a)** Location map of the plotted profiles. Hindu Kush seismicity in black, Pamir seismicity in blue as in Fig. 7.5. **b)** West-east cross section, projecting the local seismicity onto a tomographic image along 36.45°N. Contours in the sub-crustal low velocity domains (green) are from 7.8 to 8.2 km/s in 0.2 km/s intervals and from 8.6 to 9.0 km/s in 0.1 km/s intervals in the high velocity domains (blue). Thick white contour depicts the minimum resolution limit of the tomography according to Chapter 5. Pink beach balls are projected focal mechanisms of the large relocated events. The big pink star marks the October 2015 M_w 7.5 earthquake; pink circles are its relocated aftershocks. The red-to-white contours denote the slip of the October 2015 event constrained from a finite fault inversion (Y. Zhang and R. Wang; pers. comm.). The smaller pink star marks the foreshock of the 2002 event. The labels *F1-F4* refer to features mentioned in the text. **c)** North-south cross sections with 15 km projection range. The labels on top of the beach balls refer to the moment magnitude and the year of the specific event. The 2004-event is plotted twice at its relocated position using GEOFON and ISC data, respectively, to illustrate the accuracy of the relocated events. The labels *S1/2* and *N1/2* refer to features mentioned in the text. All other annotations as in Sub-figure b).

hypocenters (Fig. 7.7c): in the center (Profiles 1 and 2 in Fig. 7.7c), the deeper fragment appears overturned in one segment (labels S1/2) and is separated by a sharp kink from the shallower north-dipping seismicity. In the east (Profiles 3 and 4), the separation of the shallow and deep patches is less pronounced, but the deep seismicity is split into a north- and a southward dipping sub-branch (labels N1/2). In contrast, in the very west (Profile 0), seismicity is less frequent, no large earthquakes occur and no sharp gap cuts the seismicity.

The relation between seismically active and aseismic regions in the deepest portion of the Hindu Kush slab can be further explored by investigating the October 2015, M_w 7.5 Badakhshan earthquake, which is the largest and most recent of the large Hindu Kush earthquakes. The 2015 event locates on the same seismogenic finger as the second largest event (1983, M_w= 7.4; Finger *F2* in Fig. 7.7b) and both earthquakes have a similar focal mechanism.
In Figure 7.7, in addition to the local seismicity and the relocated events, a finite fault slip-model for the earthquake rupture derived by Y. Zhang and R. Wang is plotted. The model was constrained from 48 seismic stations with epicentral distances between 15-90°. The hypocenter determined by GEOFON and the focal mechanism given in the GCMT catalog (Dziewoński et al., 1981; Ekström et al., 2012) were used in the joint inversion following the method of Zhang et al. (2012). In Figure 7.7, we plot the steeper of the two tested nodal planes (dip of 69°), which fit the data almost equally well (Y. Zhang and R. Wang, pers. comm.). On slab-perpendicular north-south cross section (Fig. 7.7c), this fault plane has the same dip as the southward dipping structure outlined by the aftershocks. This dip also accurately parallels the plane outlined by the background seismicity. Thus, we considered the sub-vertical nodal plane the more likely fault plane. The finite fault solution indicates that maximum slip occurred west of the hypocentral location. Displacement propagated westward into the seismic gap and drops back to zero where seismicity in the local catalog and the relocated aftershocks cluster (Fig. 7.7b).

7.4 Seismic velocity structure

In Figure 7.7, we plot the results of the seismicity analysis together with the P-wave velocity (v_p) model derived in Chapter 5, which was also used for earthquake relocation here. The pronounced sub-crustal low velocity zone beneath the Hindu Kush has been interpreted as subducting crust (Roecker, 1982, Chapter 5). Interestingly, the penetration depth of the low velocity zone coincides with the separation between the shallow and the deep cluster of intermediate depth seismicity introduced here: the shallower intermediate depth earthquakes cluster in or at the bottom of this low velocity anomaly, the earthquakes of the deeper segment occur in a high velocity zone, not distinguishable from the ambient mantle velocities.

The shape and the amplitudes of the anomalies resolved in local earthquake tomography depend on the overall resolution, the presence of adjacent anomalies or on the initial velocity model as discussed in Chapter 5. Synthetic tests are an important tool to quantify these effects. Here we want to constrain the character and the shape of the Hindu Kush low velocity zone in more detail by setting up an additional synthetic test series based on the local earthquake tomography of Chapter 5. In these tests, we consider one more factor that might affect the outcome of synthetic tests, which is the ray tracer and grid discretization used to deduce the synthetic travel times.
In Chapter 5, the synthetic travel times were calculated in the same grid as later used for the inversion by applying the *simulps* ray tracing scheme (Thurber, 1983, 1993; Eberhart-Phillips, 1993; Evans et al., 1994). Such an approach is justified as these tests were set up to constrain the velocity architecture of the whole region. Here, we aimed at constraining synthetic anomalies finer than the grid spacing of the inversion grid. Thus, we followed the approach of Haberland et al. (2009) and used a three-dimensional finite difference simulation code for ray tracing on a grid with 1x1 km spacing (Podvin and Lecomte, 1991; Tryggvason and Bergman, 2006). After calculation of the synthetic travel times, we added Gaussian noise, scaled with the standard deviation of the quality class which had been assigned to each pick (Chapter 5).

The synthetic velocity model implemented here contains two lithospheric slabs, dipping with opposite polarities beneath Pamir and Hindu Kush. Each of these slabs consists of a layer of mantle lithosphere, overlain by a crustal layer (see input geometry in Fig. 7.8b). The geometry of these anomalies was constrained by interpolating two planes through the seismicity 'curtains' of Pamir and Hindu Kush and creating envelopes of different thickness, based on the interpolation points. These envelopes were then transferred to bodies with different velocity in the synthetic model for ray tracing[1]. Thus, the position of the synthetic anomalies is directly connected to the earthquake geometry.
To constrain the character of the Hindu Kush low velocity zone, we tested four end member cases (Figs. 7.8c-f) by varying thickness (10 and 20 km) and intensity (v_p= 7.3 and 7.7 km/s, which is ∼10% and 5% slower than the surrounding mantle) of the low velocity structure. Additionally, in one test, aiming to deduce the amount of smearing between the shallower and the deeper domain, the low velocity layer terminated at 160 km; in the other tests at 280 km. The geometry of the other features was not changed: the Hindu

[1] all steps executed using *vtk*-tools: http://www.vtk.org/Wiki/VTK_Tools

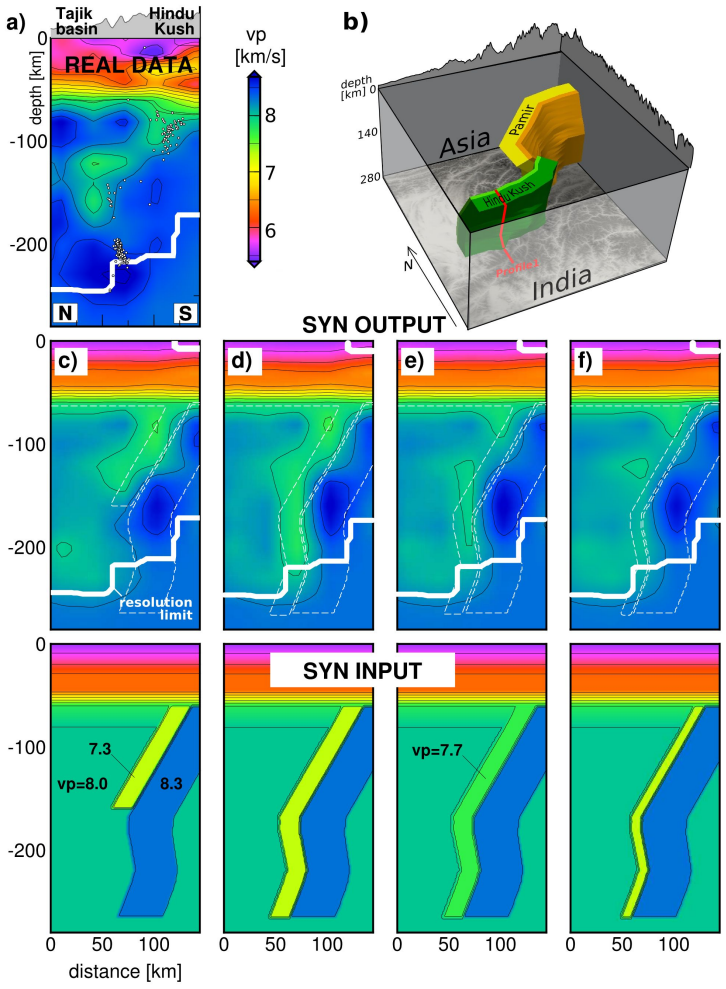

Figure 7.8: Synthetic tests to re-evaluate the resolution power of the local earthquake tomography of Chapter 5 with respect to a thin low velocity structure in the mantle: **a)** real data along profile P1 of Figure 7.7c. Contours in 0.25 km/s intervals. Thick white line depicts the resolution limit as described in Chapter 5. **b)** Geometry of the input anomalies for the synthetic test, constrained by interpolating planes through the seismicity: the Hindu Kush (green) and Pamir (yellow) anomalies consist of a package of crust and mantle lithosphere. During the synthetic test, the penetration depth and the amplitude of the Hindu Kush crustal anomaly are varied. **c-f)** Four end member tests: the bottom panels show the input anomaly (v_p refers to the P-wave velocity of the different structures). The top panels show the output after inversion. Dashed white lines depict the outline of the input anomalies.

Kush and Pamir mantle lithosphere had v_p= 8.3 km/s and 50 km thickness, the Pamir crust a v_p of 6.9 km/s and 20 km thickness as its character is very well constrained from previous studies (Schneider et al., 2013; Sippl et al., 2013a). For all tests, the minimum 1D velocity model from Chapter 5 was used as a background model and the P-wave to S-wave velocity (v_p/v_s) ratio was held constant at 1.73.

The test results along Profile 1 of Figure 7.7 are plotted in Figures 7.8c-f. Only one profile is shown as the others exhibit similar characteristics as discussed in the following: for all tests, the amplitudes of the recovered low velocity zones are lower than the input anomalies. The amplitude underestimation is largest deeper than ∼100 km. In the test with a very thin subducted crustal layer and the one with the smallest low velocity amplitude (tests *e* and *f*), the recovered low velocity zone is hardly distinguishable from the background velocities. In the case of the thin (10 km) low velocity layer, this effect arises because the thickness of the structure is below the resolution limit of the tomography and the localized low velocity is smeared in the surrounding structures. In the case of the less pronounced low velocity zone (v_p= 7.7 km/s), the geometry of the anomaly could be recovered but the amplitude decreases to an extent that the anomaly can hardly be separated from the mantle velocities to its north.
In the two tests with a thicker low velocity zone and a higher v_p contrast (tests *c* and *d*, 20 km thickness, v_p= 7.3 km/s), the recovered anomaly appears as a continuous low velocity zone. The geometry of the input anomalies is slightly smeared, but can still be recognized. The model with the shallower terminating low velocity layer (test *c*, penetration depth = 160 km) can clearly be distinguished from the model featuring a deeper penetrating low velocity zone. The shallower terminating anomaly is not smeared vertically, but rather the opposite effect arises: due to the amplitude decrease at the edge of the low velocity zone it appear to terminate ∼20 km shallower in the recovered velocity model.

Comparing the output of these synthetic tests with the real data (Fig. 7.8a), the descending low velocity layer appears thicker and more intense than in any of the synthetic tests, but does terminate at ∼160-180 km. Thus, we can conclude that a layer of low velocity material, probably thicker than ∼20 km and/or velocities lower than 7.3 km/s might be hosted in the mantle beneath the Hindu Kush. This zone, however, does clearly not penetrate as deep as the deeper part of the seismicity and probably terminates at ∼180 km depth.

7.5 Strain rate from seismicity

Due to the geometry of the seismically active domain, it seems likely that the Hindu Kush intermediate depth earthquakes occur in a sharply defined, spatially restricted volume. Following Kostrov (1974), we can obtain the average strain-rate tensor in such a volume by summing up the moment tensors of the earthquake that occurred in the specific volume (see Chapter 3 for more detail):

$$\dot{\varepsilon}_{ij} = \frac{1}{2\mu V t} \sum_{k=1}^{N} M_{ij}^{(k)} \tag{7.1}$$

where N is the total number of earthquakes in a given time, V is the considered volume, t is the time interval and M_{ij}^{k} are the seismic moment tensor elements of the kth event.

We used all earthquakes listed in the Global Centroid Moment Tensor (GCMT; Dziewoński et al., 1981; Ekström et al., 2012) catalog from 1976 to 2013 (see the earthquake locations in Supplementary Fig. E4) to calculate the strain rate in the seismogenic portion of the

Hindu Kush slab. Among different available catalogs, also including this study, we chose the GCMT catalog because of its long coverage. The largest event in the GCMT catalog has M_w= 7.39 (1983/12/30), nine events are bigger than M_w 6.5 and the smallest event has M_w 4.79. Thus, the catalog might be complete from $M_w \sim 5$. To extend the catalog until present, we additionally consider the October 2015 M_w 7.5 event in the strain rate calculation (no other earthquake between 2013 and autumn 2015 was stronger than M_w 6.0, thus would significantly affect our calculation). This combined data set yielded a total recording period of $t = 40$ years.
As sub-crustal earthquakes shallower and deeper than 180 km are hosted in material with clearly different P-velocity characteristics (see Fig. 7.7 and Section 7.4), we considered these two depth domains separately. To constrain the volume (V in Equation (7.1)), we started from the plane fitted through the local seismicity, which had also been used as a base to construct the synthetic tests (Fig. 7.8b). Along the seismogenic portion of the Hindu Kush slab (69-71.5°E), we derive an area of $32,041$ km^2 for the shallow and $17,956$ km^2 for the deep part. This probably represents a maximum estimate as the area was determined by fitting a plane through our local catalog and the larger events registered in the GCMT enclose a smaller area (see comparison in Supplementary Fig. E4). As most earthquakes seem to occur in a thin layer, we used a seismogenic thickness of 15 km, as a compromise between the possibly greater thickness in the upper part and the narrowing seismogenic thickness with depth. The shear modulus was set to $\mu = 6.6 \times 10^{10}$N/m^2, which is approximately its value in the upper mantle according to the PREM earth model (Dziewoński and Anderson, 1981). Calculations were executed in a Cartesian coordinate system (x-axis positive in north direction; y-axis in east; z-axis downward; Aki and Richards, 1980) and tensor elements listed in the GCMT solutions are changed accordingly (see e.g. Holt, 1995; Lorinczi and Houseman, 2009).

The results of the strain rate calculation are summarized in Tables 7.1-7.3: Table 7.1 lists all equivalent strain rate tensor components for the two depth intervals. From these we

Depth (km)	Coeff.	$\dot{e}_{xx}$	$\dot{e}_{yy}$	$\dot{e}_{zz}$	$\dot{e}_{xy}$	$\dot{e}_{xz}$	$\dot{e}_{yz}$
60-180	10^{-14} s^{-1}	-0.1691	-0.0297	0.1988	0.0873	-0.0246	-0.0121
180-265	10^{-14} s^{-1}	-0.8858	-0.0785	0.9642	-0.1435	0.8893	0.2038

Table 7.1: Seismic strain rate tensor components in the deep and shallow depth interval of the Hindu Kush seismic zone according to Equation (7.1). Indexes refer to a Cartesian coordinate system where the x-axis is positive in north direction, y-axis positive in east and z-axis positive downward (Aki and Richards, 1980). Components have to be multiplied with the corresponding coefficient (coeff.).

Depth (km)	Coeff.	$\dot{e}_1$	$\dot{e}_2$	$\dot{e}_3$
60-180	10^{-14} s^{-1}	-0.2118	0.0099	0.2019
180-265	10^{-13} s^{-1}	-0.1281	-0.0055	0.1336

Table 7.2: Eigenvalues (Principal strain rates) from Tab. 7.1. The eigenvalues correspond to the maximum compression ($\dot{e}_1$), intermediate ($\dot{e}_2$), and maximum extension ($\dot{e}_3$) rate, respectively. Components have to be multiplied with the corresponding coefficient (coeff.).

Sub-region name (longitudinal range)	West (70-70.6°E)	Center (70.6-71.0°E)	East (71-71.5°E)	All (69-71.5°E)
shallow (60-180 km)				
Dimension (km^2)	7,803	3,904	6,158	32,147
No. mechanisms	10	16	29	62
$\dot{e}_3$ (1/s)	0.1331	0.1535	0.3723	0.2019
Coeff.	10^{-14}	10^{-13}	10^{-15}	10^{-14}
Maximum vertical extension rate (% per Myr)	4.20	48.41	1.17	6.37
Relative vertical displacement rate at 180 km (mm/yr)	5.04	58.09	1.41	7.64
deep (180-265 km)				
Dimension (km^2)	4,618	2,140	3,442	17,943
No. mechanisms	14	62	38	114
$\dot{e}_3$ (1/s)	0.1133	0.8223	0.5818	0.1336
Coeff.	10^{-13}	10^{-13}	10^{-14}	10^{-13}
Maximum vertical extension rate (% per Myr)	35.74	259.32	18.35	42.12
Relative vertical displacement rate at 265 km (mm/yr)	35.41	278.52	17.0	43.44

Table 7.3: Strain rate results from Tables 7.1 and 7.2, separated into sub-regions, following the Hindu Kush seismicity along-strike. The area of the sub-region is determined from a plane interpolated through the Hindu Kush seismicity (Fig. 7.8b). *No. mechanisms* refers to the number of earthquake mechanisms in the GCMT catalog that fall into the specific sub-region. The components of $\dot{e}_3$ have to be multiplied with the corresponding coefficient (coeff.). The *maximum vertical extension rate* (MER; in % per Myr) is another way to write $\dot{e}_3$ (in 1/s). These two values can be converted directly into each other: MER= $\dot{e}_3 \times 24 \times 60 \times 60 \times 356 \times 10^6$. The *Relative vertical displacement rate* (RDR) refers to a point at the base of the specific block and was calculated by integrating the vertical strain rates across all blocks above. *Note:* values listed here for MER and RDR were calculated from $\dot{e}_3$ before it was rounded to the fourth decimal place (as it is given in this Table).

computed the Eigenvalues (Tab. 7.2), which correspond to the maximum compression (−), intermediate, and maximum extension (+) rate, respectively. In Table 7.3, the results are summarized and the same calculation is repeated, subdividing the shallow and deep domain of the Hindu Kush seismic zone into three patches along-strike, corresponding roughly to the seismogenic fingers identified in the local earthquake catalog (Figs. 7.7).

In Figures 7.6a and d, the strain rate tensors derived here are plotted in a stereonet, next to the focal mechanisms from the local earthquake catalog. As already visible from the individual earthquake source mechanisms, the strain rate tensors reveal a down-dip extensional, north-south compressional regime. NW-SE compression dominates in the shallow part and NNE-SSW compression dominates in the deeper part, which accurately corresponds to the P-axes of the large earthquakes (Figs. 7.6c, f), emphasizing that these events had the largest impact on the strain rate calculation. As most of the large earthquakes were located in the deeper patch, the highest strain rate also occurs in the deeper depth interval. The maximum vertical extension rate is 42% per Myr ($0.1336\times10^{-13}\mathrm{s}^{-1}$) and 6% per Myr ($0.2019\times10^{-14}\mathrm{s}^{-1}$) in the deeper and shallower part, respectively (Tab. 7.3). As the orientation of the maximum extension is approximately vertical, we can calculate the relative vertical displacement of a point at the base of the shallow and deep domain by integrating all vertical strain rates above this point. The relative vertical displacement rate of a point at 265 km is 43 mm/yr and 8 mm/yr for a point at 180 km (see Tab. 7.3 for detailed information).
Splitting the seismogenic structure additionally into three segments along-strike, the largest strain rate occurs in the central portion of the deep Hindu Kush seismicity (70.6-71.0°E). The hypocenter of the October 2015 event was located in the same patch. Further, in this patch, the plane outlined by the catalog seismicity appears overturned (S1 in Fig. 7.7).

To constrain the uncertainty of these calculations, we ran a sensitivity analysis by varying the most important input parameters: the seismogenic volume (between 75% and 125% of the value given in Tab. 7.3), the shear modulus (between $6.74 \times 10^{10}\mathrm{N/m}^2$ and $7.57 \times 10^{10}\mathrm{N/m}^2$, which are the values at 80 and 265 km in the PREM earth model) and the time span t (excluding the last and first 10 years of data). This last point, for instance, basically corresponds to including or excluding the largest Hindu Kush event in 2015. The effect of changing the seismogenic volume by 25% and excluding 10 years of data have an equally strong impact (changing the vertical displacement rate or $\dot{e}_3$ by ∼20%). The effect of changing the shear modulus is less severe and only changes the vertical displacement rate by ∼5%. However, despite this variability in the absolute values, the strain rate ratio between the deep and the shallow domain remained relatively stable.

The maximum strain rate values in the order of 0.1 to 0.8 $10^{-13}s^{-1}$ calculated here are comparable with strain rates obtained for the Vrancea seismic nest (Oncescu et al., 1999; Lorinczi and Houseman, 2009), which has also been suggested to accommodate an active slab break-off, and about two orders of magnitude larger than values obtained for the Tonga subduction zone (Holt, 1995). Holt (1995) considered his estimate of the seismic strain rate to represent a large fraction of the total strain rate budget within the seismogenic zone because it is in the order of theoretical values expected from bending of a descending spherical plate. Thus, the break-off regions seem to feature locally much higher seismic

strain rates than expected from the subduction and associated bending of a lithospheric slab. The total strain rates might be even higher than the values obtained here due to aseismic deformation involved in the detachment. Further, the shear zone might be more localized than we assumed.

7.6 Discussion and interpretation

The synthetic tests of Section 7.4 indicated that the low velocity zone in the Hindu Kush mantle is very likely thicker than 20 km, does not penetrate deeper than ∼180 km and might feature P-wave velocities lower than 7.3 km/s at depths greater than 100 km. Dependent on the composition, such seismic velocities might occur in lower or middle crust (Sobolev and Babeyko, 1994; Hacker et al., 2011). According to our synthetic tests, the crustal layer in the mantle beneath the Hindu Kush is thicker than expected for lower crust alone, but is in turn thinner than the whole Hindu Kush crust. Thus, these tests support the scenario suggested in Chapter 5, where the subduction of a package of lower and middle crust was stated based on coarser synthetic tests, cross plots to combine v_p and v_p/v_s models and a comparison between Pamir and Hindu Kush. From similarly low seismic velocities associated with Pamir's intermediate depth seismicity in combination with petrophysical modeling, Sippl et al. (2013a) concluded that lower and middle crustal rocks are likely to be subducted to mantle depths. The abrupt cut-off of the low velocity zone and the change to high v_p in the deeper seismogenic parts has been explained with the eclogitization of the mafic lower crust, which would feature v_p equal to or higher than the surrounding mantle. Eclogitization would result in a density increase, adding to the slab-pull of the subducted mantle lithosphere (Sobolev and Babeyko, 1994; Krystopowicz and Currie, 2013).

In the Hindu Kush, however, subduction and partial eclogitization of continental crust does not provide an explanation for the overturned dip of the deeper Hindu Kush seismic zone or its separation into two sub-branches; neither for the occurrence of large earthquakes dominantly in the deep cluster of seismicity. As such seismic characteristics can not be observed in the adjacent Pamir intermediate depth earthquake zone, they are likely to be related to the slab break-off beneath the Hindu Kush (Chapters 4 and 5).

7.6.1 Along-strike propagating slab-detachment

We suggest that the break-off splits the Hindu Kush slab into two different depth domains (shallow and deep patch), which can be separated based on their different strain rates. Using the strain rates from Table 7.3, it is possible to calculate how fast the two fragments might separate: the distance of a point at 180 km depth and a point at 265 km depth, for instance, would have increased by ∼150 km after 4 Ma. This value probably is subject to some uncertainty, which should, however, be lower than for the absolute strain rate values as the ratio between deep and shallow portion is relatively stable against variations in the input parameters (see Section 7.5). Such a fast separation is in good agreement with predictions from numerical modeling studies, which see slab-detachment as an ephemeral process (Duretz et al., 2012; Magni et al., 2012; Duretz and Gerya, 2013).
Further, in such thermomechanical numerical simulations, it has been shown that the

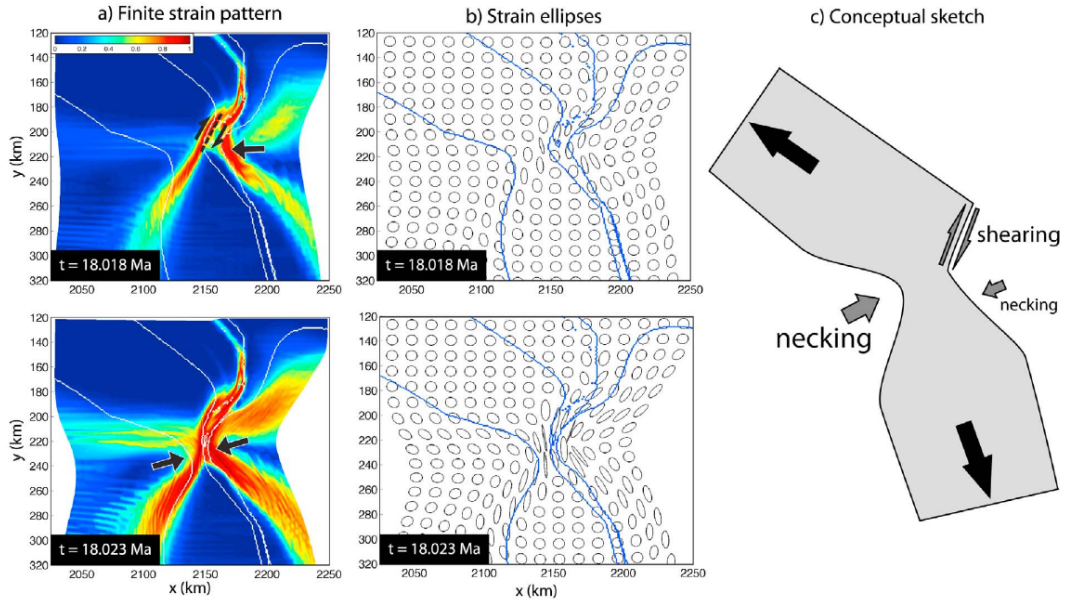

Figure 7.9: Thermomechanical model for slab-detachment after initiation of continent-continent collision from Duretz et al. (2012): **a)** Finite strain pattern during slab-detachment. (top) The initial simple shear dominated regime and (bottom) the necking dominated deformation that replaces simple shear after about 30% of across slab thinning. The white lines correspond to lithological contours (crust, mantle lithosphere, asthenosphere). **b)** Strain ellipses corresponding to the two stage intermediate depth slab-detachment. The time frames correspond to those of Sub-figure a). The blue lines correspond to the lithological contours. **c)** Conceptual sketch showing the interplay of localized shear deformation in the colder parts of the slab and distributed necking in the hotter parts.

characteristics and the dominant deformation mechanism during break-off varies in space and time: the depth of the detachment, characterized by a localized thinning of the lithosphere, depends on the competing forces of slab-pull from the subducting slab and the resistance of the buoyant continental crust entering the system at shallow levels. At the depth where these forces level off, slab break-off might initially occur in a simple-shear dominated regime, where a shear-zone through the mantle lithosphere develops (Fig. 7.9, *top*; from Duretz et al., 2012). Once the lithosphere is sufficiently thinned, the dominant deformation mechanism changes to pure-shear, resulting in the necking of the remaining thinned connection (Fig. 7.9, *bottom*).

Based on these model predictions, the along-strike variation and depth-dependent geometry of the Hindu Kush slab may be understood: the sharp kink associated with the transition from the shallower to the deeper seismogenic patch might outline the up-dip limit of a shear-zone through the mantle lithosphere. The along-strike variation of the geometry of the deeper seismic zone, in turn, could indicate that the advance of the break-off varies along strike (see the schematic sketch in Fig. 7.10a and the results in Fig. 7.7 for the following description): in the western Hindu Kush (Profile 0) we do not observe a sharp horizontal gap in the seismicity and no large earthquakes have occurred in this region in the last 30 years. Here, the break-off seems to be less advanced. In the center

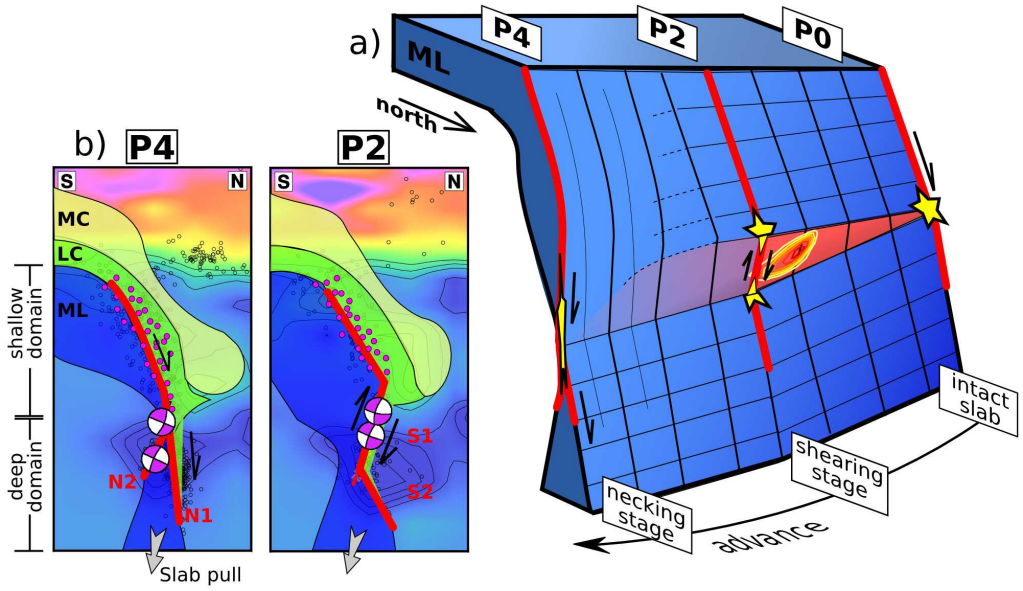

Figure 7.10: Interpretative sketch illustrating geodynamic processes during the Hindu Kush slab break-off. **a)** The along-strike varying geometry of the intermediate depth seismicity can be understood in the context of an eastward advancing slab-tearing. The bold red lines (P0/2/4) mark the interpolated interfaces through the seismicity along the profiles in Figure 7.7c. The yellow star follows the path of a fictive point on top of the mantle lithosphere, initially at the same depth level, at the different stages of the break-off process. Only the mantle lithosphere (ML) is shown here: from an initially intact slab (P0), a shearing interface develops through the mantle lithosphere (P2). As the lithosphere is thinned sufficiently, necking becomes the dominant deformation mechanism (P4). Largest earthquakes cluster on the shear-interface. The red-to-yellow contours depict the fault plane of the October 2015 M_w 7.5 event in this scenario. The terminology *intact slab* here refers to a slab in which no shearing interface has developed yet. Its mantle lithosphere might, however, already have been affected by the break-off. **b)** Interpretative sketches to demonstrate the involvement of crust in the continental subduction process, which, in turn, affects the rupture mechanisms driving seismicity. The sketches are drawn on top of the observational data shown in Figure 7.7c: the slab pull drags a package of buoyant lower (LC) and middle (MC) crust to depth, physically attached to the descending mantle lithosphere (ML). The lower crust undergoes gradual eclogitization, releasing fluids, which might trigger seismicity (small pink dots). The deeper seismogenic domain arises due to simple (profile P2) or pure (P4) shear through the mantle lithosphere. Only the denser, eclogitized fragments of the lower crust might descend, whereas the more buoyant part of the crust detaches. Larger earthquakes (pink beach balls) cluster along the shearing interface and to a minor extent in the necking zone. The labels N1/2 and S1/2 refer to the labels attached to the seismogenic structures in Fig. 7.7, describing the different seismogenic branches during break-off.

(Profiles 1, 2), we image the sharp change in dip of the plane outlined by the seismicity at ∼180 km, associated with an increase in seismic velocity and the overturning of the seismogenic structure to southward dipping (label S1 in Fig. 7.7c) and back to northward dipping (label S2) deeper than ∼210 km. The large earthquakes cluster in the S1 region. Their steeper fault planes indicate shear-movement on exactly this interface. Thus, the central Hindu Kush slab might be in the shearing dominated stage of break-off. In the east

(Profiles 3 and 4), the seismogenic structure dips near-vertically and a sub-branch splits off from the main seismogenic structure (N1/2). In contrast to the shearing stage in the central Hindu Kush, the large earthquakes have pure down-dip extensional mechanisms and none of their fault planes coincide with the dip of the seismogenic structure. This pattern suggests that the eastern Hindu Kush is already in the necking dominated stage of break-off. The splitting of the seismic zone into two branches might then indicate a strain localization at both sides of the nearly detached lithospheric fragment. Most of the large Hindu Kush earthquakes occur in the simple-shear dominated region, attesting that slab break-off seems to advance at high rates once the shearing phase initiated.
The scenario of an eastward advancing slab break-off suggested here based on local seismic data is also in good agreement with results from teleseismic tomography, which is more sensitive for the large-scale structure of the lithospheric slab as a whole. In the seismic velocity images of Chapter 4, the lithospheric fragment appeared thinned, but still more continuous in the western Hindu Kush, whereas the anomaly fainted out towards the east, where seismicity is most intense.

The slab-shearing to slab-necking scenario proposed above might also explain the sharp cut-off of the Hindu Kush low velocity zone at ∼180 km depth only in Profiles 1-4 of Figure 7.7 and not in Profile 0, where the break-off is less advanced. This sudden cut-off is to a certain extent surprising as gradual eclogitization of lower crust is expected to result in a gradual increase of seismic velocity (Finlayson et al., 1979). Possibly, once a shearing interface developed through the mantle lithosphere and the final stage of fast break-off initiated, the parts of the lower crust that were not yet eclogitized might detach from the middle crust. Such a behavior could add to the 'blob-like' thickening of the low velocity zone at ∼160-180 km that was also described in Chapter 5.

7.6.2 Processes triggering intermediate depth seismicity

Assuming that the Hindu Kush slab break-off propagates along-strike, the deep and shallow patches of intermediate depth seismicity can be attributed to the different sub-regions arising during the break-off (see Fig. 7.7 and the schematic sketches in Fig. 7.10b): the shallower patch of seismicity occurs in the region where still buoyant crustal material is involved in the subduction process. The deeper patch is located in the region dominated by either shearing or necking of the mantle lithosphere, possibly also involving a layer of eclogitized lower crust. Thus, the shallow and the deep part of the Hindu Kush differ not only regarding strain rate, but seem to differ also regarding lithology. These constraints narrow down the range of possible processes responsible for the seismicity. Suggestions regarding the underlying processes include dehydration embrittlement, mineral phase transitions or thermal runaway (see Section 7.1). Whereas the first two processes obviously depend on the availability of suitable candidates in the mineral assembly of the subducting material, thermal runaway occurs only at high differential stresses (Thielmann et al., 2015).

The deep portion (∼180-270 km depth): The investigation of the radiation patterns of the latest large Hindu Kush earthquake by Poli et al. (2016) and other large events over the past 25 years showed a two-stage rupture process for these events, where an initially slow dissipative rupture precedes a larger reduction of dynamic frictional stress. Poli et al.

(2016) also relocated the aftershocks of the October 2015 event, using a different method than in this study, and obtained, in accordance with our results, hypocenters which form a southward dipping plane northwest of the main shock. Based on this constellation and the associated radiation patterns, they proposed failure due to a thermal shear instability as the mechanism triggering the main shock. Our study revealed that one fault plane of the main shock coincides with the inverted-dipping structure (S1 in Figs. 7.7 and 7.10) outlined by the catalog seismicity. This constellation, in turn, might indicate that the rupture occurred on a shearing interface through the mantle lithosphere.
Due to the high seismic velocities at the depths of the deep seismicity, it seems unlikely that large volumes of crustal rocks are pulled to these depths. Thus, mineral phase transitions in crustal rocks, possibly releasing fluids, seem to be unlikely here. The eclogitization process, even if incomplete in continental crust, is expected to have terminated in the depth range of the deeper seismic patch (Hetényi et al., 2007). Additionally, hydrous mineral in the mantle lithosphere might be rarer than in oceanic subduction zones, where mantle dehydration has been suggested to trigger intermediate depth seismicity (e.g. Peyrat et al., 2006). Thus, dehydration embrittlement as a driving mechanism for the deep patch of Hindu Kush seismicity seems unlikely. Instead, Thielmann et al. (2015) showed from numerical modeling that grain size reduction might facilitate the initiation of thermal runaway, as it weakens the rocks. Simple shear along an intra-lithospheric interface as proposed here could cause grain size reduction. Thus, shear instability and thermal runaway might be a more likely candidate for brittle-like failure in the deep patch of the Hindu Kush seismicity.

The deeper Hindu Kush seismic zone is split into several sub-vertically dipping, distinct fingers (F1-4 in Fig.7.7c), which host the constantly occurring smaller earthquakes, whereas at least the last large earthquake in October 2015 clearly ruptured one of the seismic gaps between theses fingers. Although less sharply resolved, this partitioning also appears in global catalogs, which include longer recording times (see the comparison to other catalogs in Supplementary Fig. E5). Thus, the clustering in seismogenic fingers is unlikely to be an effect from the short deployment time of our seismic stations. Such a seismic fragmentation suggests that the seismic zone consists of distinct patches, which behave differently in response to deformation. This clustering could either occur due to inherited heterogeneities or due to ones which are created during the break-off.
In Chapter 4, it has been shown that the slab currently subducting beneath the Hindu Kush consists of lithospheric material associated with a stretched margin. Better accessible examples of (former) stretched margins, e.g. in the western Alps or the western Iberian margin, consist of zones of symmetrically arranged tilted blocks with a spacing from several to tens of kilometers (Coward et al., 1991; Pinheiro et al., 1996). Such a spacing corresponds to the spacing of the Hindu Kush fingers. Thus, they could correspond to inherited fault structures built during the formation of the margin, which now react differently to deformation than the intact blocks in between. Alternatively, the pattern might be explained by a heterogeneous state of stress in the different fragments due to former earthquakes or by the development of a boudinage-like structure in the final stage of break-off as suggested by Lister et al. (2008).

The shallow portion (∼60-180 km depth): The considerations above regarding the rupture mechanisms of the events in the deep seismogenic patch do not necessarily apply to the shallower portion of the slab. The shallow domain also features intermediate depth seismicity, although less intense and less sharply aligned than the deeper fragments. Additionally, the earthquake source mechanisms show more scatter than in the deep part (Fig. 7.6). The study of Poli et al. (2016) did not include the M_w 7.4 earthquake in 1985, the only one of the large events that very likely locates in the shallower seismic zone (Fig. 7.7). Thus, no information about its rupture propagation is available. The velocity structure constrained from the local earthquake tomography implies the existence of not yet eclogitized crustal rocks. This implies that the shallow part of the intermediate depth seismicity might feature a range of possible mechanisms promoting earthquake rupture, as rocks with different lithologies are involved in the subduction process. To a certain extent, the Bergen arc in Norway might form a currently accessible analog for the shallower intermediate depth Hindu Kush seismicity: here, a patchwork of eclogite-facies pseudotachylyte veins in exhumed lower crustal rocks gives evidence for past earthquakes, controlled by fluids penetrating into deep crustal shear-zones (Austrheim, 1987; Austrheim et al., 1996). In contrast to these rocks, partial eclogitization of subducted lower crust in the Hindu Kush could reach deeper, as colder temperatures are preserved at larger depths in the subducting slab (Sippl et al., 2013a; Tympel, 2014). Additionally, subduction velocity is accelerated by the break-off. For the Indian lower crust underthrusting beneath the Himalayas, for instance, it has been shown that eclogitization is delayed by about 100°C compared to where it is expected to occur from phase equilibria (Hetényi et al., 2007). Further, Hetényi et al. (2007) showed that the amount of eclogitization strongly depends on the hydration level of the lower crust. If the Hindu Kush slab once formed a continental margin as suggested in Chapter 4, the crust and mantle lithosphere currently subducting beneath the Hindu Kush might have a higher hydration level than the Indian crust currently underthrusting under Tibet.

7.7 Conclusion

The Hindu Kush region in Central Asia hosts a nest of intense intermediate depth intracontinental seismicity (hypocenters between ∼60 and 270 km depth; Pegler and Das, 1998; Sippl et al., 2013b) and repeating large earthquakes with moment magnitudes bigger than seven (USGS, 2016; Poli et al., 2016, Chapter 4), which have been attributed to the ongoing detachment of a lithospheric fragment (Koulakov and Sobolev, 2006; Lister et al., 2008, Chapter 4). Here, we used seismological data from temporarily deployed local and a few global stations to study the development of this slab-detachment.
On the base of local seismic deployments between 2008-10 and 2012-2014 (Mechie et al., 2012; Schurr et al., 2012, 2013), we derived a high precision earthquake catalog and focal mechanisms for many of these events. Using regional and teleseismic stations, we relocated the largest events of the Hindu Kush nest since 1983 relative our precise event catalog. To constrain the kinematics of the break-off, we used events listed in the GCMT catalog (Dziewoński et al., 1981; Ekström et al., 2012) to calculate the strain rate in the seismically active slab-segments. These results were interpreted together with the associated seismic velocities constrained from local earthquake tomography (Chapter 5).

Our results indicate, in accordance with Chapter 4, that the intermediate depth Hindu Kush seismicity is primarily driven by the down-dip extensional stress regime exerted by the detaching lithospheric slab. However, the seismicity exhibits clearly different characteristics in its shallower (∼60-180 km depth) compared to its deeper (∼180-270 km depth) part. The shallower portion is seismically less active and coincides with a zone of low seismic P-wave velocity. The seismically much more active deeper portion is hosted in a high velocity domain. Most of the large earthquakes cluster in this deeper segment. After careful re-testing of the low velocity zone, which falls together with the shallower patch of intermediate depth seismicity, in a series of synthetic tests, we conclude in accordance with Roecker (1982) and Chapter 5 that significant amounts of crustal material must be subducted beneath the Hindu Kush. The subducted package presumably involves lower and middle crustal material, but does not penetrate deeper than ∼180 km, where most of the large events cluster. From the strain rate analysis we deduce that the deep portion of the slab is separating from the shallower fragment.
Such a separation could arise as the buoyant crustal material resists subduction, whereas the earlier subducted lithospheric slab pulls from underneath. Based on the geometry of the deep seismogenic domain and taking into account numerical modeling studies (Duretz et al., 2012; Duretz and Gerya, 2013), we suggest that the separation process propagates along-strike: whereas the slab appears mostly intact in its western part, the break-off advances towards the east, featuring shearing along the mantle lithosphere and finally necking along the remaining thin connection. The rupture of the large events most likely propagates along the intra-lithospheric shearing interface, as indicated by their fault planes and the aftershock locations of the last large Hindu Kush earthquake. Along such an interface, thermal runaway, possibly facilitated by grain size reduction in the shear-zone (Thielmann et al., 2015), might be the rupture mechanism. The further internal fragmentation of the deep portion of the slab into sub-vertical structures featuring smaller earthquakes and domains ruptured by the large earthquakes might arise from inherited heterogeneities in the mantle lithosphere that date back to its formation or to such which are created during the break-off. In contrast, the shallower portion of the intermediate depth seismicity coincides with the subducting crustal layer. Thus, phase transitions and associated fluid release from the subducting crustal layer could trigger the smaller and less frequent events.

8 Conclusion and outlook

In this thesis, I examined the seismotectonics of the Pamir-Hindu Kush and Tajik basin using seismic data, mainly recorded by the temporarily deployed stations of the TIPTIMON and to a minor extent of the TIPAGE seismic networks. The Pamir-Hindu Kush region forms a tectonic peculiarity, as it is, beside possibly Vrancea in Romania, the only place worldwide where intermediate depth seismicity (i.e. seismicity between ∼60-300 km depth; Frohlich, 2006; Faccenda et al., 2012) is not directly associated to ongoing oceanic subduction. The data recorded by the local networks, in turn, forms a powerful base to analyze these seismogenic characteristics, as TIPTIMON also includes the first modern digital seismic network in Afghanistan, located directly on top of the zone of most intense intermediate depth seismicity.
Two main questions were driving my research: first of all, I was wondering which tectonic constellation might set the Pamir-Hindu Kush apart from the rest of the India-Asia collision system further east. Despite a similar Paleozoic formation history, only Pamir-Hindu Kush currently feature intense intermediate depth seismicity (Billington et al., 1977; Pegler and Das, 1998; Sippl et al., 2013b; Bai and Zhang, 2015). Only the arcuate Pamir orogen is offset north by about 300 km, compared to the surrounding mountain ranges (Burtman and Molnar, 1993). These peculiarities are then closely associated with the second question: what are the physical processes actually driving intra-continental intermediate depth seismicity as well as the involvement of crustal material in the continental subduction process?
To answer these questions, I initially had to zoom out to understand the lithospheric-scale structure and the recent formation history of Pamir-Hindu Kush in the regional context (Chapter 4), the involvement of the Tajik basin in this collision (Chapter 5) as well as the link between shallow tectonics and lithospheric scale processes (Chapter 6). With this knowledge, I could finally zoom in again to investigate the zone of intermediate depth seismicity in detail (Chapter 7).

To accurately constrain the seismogenic characteristics of the Pamir-Hindu Kush, I processed the records of the TIPTIMON stations to generate a high precision local earthquake catalog. For the largest of the events in this catalog, I derived focal mechanisms from waveform modeling and for several smaller events from first motion polarities. I used globally available data (ISC, 2013; GEOFON, 2016) to relocate the largest earthquakes over the last 30 years relative to the local event catalog and calculated the strain rate in the seismogenic portion of the Hindu Kush slab based on the events listed in the Global CMT catalog since 1977 (Dziewoński et al., 1981; Ekström et al., 2012).
At crustal levels, the Illiac and Darvaz faults bounding the Tajik basin to its north and east were imaged as seismogenic lineaments, featuring mainly strike-slip events. These two faults converge in the Garm region at the northeastern termination of the Tajik basin, which hosts not only the largest instrumentally recorded earthquakes along the basin's

rims (Kulikova, 2016), but also exhibits the most frequent crustal seismicity in the local earthquake catalog. Hypocenters in the basin align to a sub-horizontal structure, which shows gradual southward deepening. Pressure axes of these basin events parallel the west-east oriented pattern indicated by GPS velocity vectors. The Pamir-Hindu Kush transition is characterized by a region of distributed north-south oriented strike-slip events.
At mantle depths, the local earthquake catalog illuminated two separate, seismically active structures beneath Pamir and Hindu Kush, which despite their immediate vicinity exhibit different characteristics: the Hindu Kush seismicity consists of a shallower (∼60-160 km) north-dipping and a deeper (∼180-270 km), vertically dipping, partly overturned fragment, which features higher strain rates than the shallower portion. Nearly all intermediate depth Hindu Kush events have down-dip extensional focal mechanisms. Further, the largest events in the local earthquake catalog and four out of five of the relocated magnitude 7+ earthquakes in the last 30 years clustered in this deeper Hindu Kush patch. The Pamir seismicity, in turn, contained none of these large earthquakes and describes an arcuate structure, dipping from the opposite, i.e. the Asian side. Focal mechanisms in this Pamir arc indicate a transition from down-dip extension at its sides to along-arc extension in its center.

Based on the TIPTIMON as well as TIPAGE and permanent stations, I calculated a local earthquake tomography from ∼100.000 P and ∼40.000 S picks, which illuminates the subsurface structure of Pamir, Hindu Kush and the Tajik basin down to ∼230 km. I connected the obtained v_p (P-wave velocity) and v_p/v_s (P-wave to S-wave velocity ratio) model by introducing cross plots to identify domains with common v_p-v_p/v_s characteristics, which likely represent common lithological units.
In these velocity images, the Tajik basin is clearly recognizable due to its low v_p, high v_p/v_s sedimentary cover and its high v_p mafic basement compared to the felsic crust of the surrounding mountains. These basin units underthrust eastward under the Pamir and continue into a sub-crustal low velocity zone, associated with the Pamir intermediate depth seismicity. In contrast, the basin units abut to the south against the Hindu Kush seismic zone, which is associated to a low velocity layer, dipping from the Indian side. Synthetic tests showed that the sub-crustal Hindu Kush low velocity zone is very likely thicker than 20 km, does not penetrate deeper than ∼180 km and might feature P-wave velocities of less than 7.3 km/s at depths greater than 100 km. In contrast to these two sub-crustal low velocity layers beneath Pamir and Hindu Kush, the Tajik basin's lithosphere exhibits high seismic velocities at sub-crustal depths, which are, however, split in two parts by a sub-horizontal low velocity band at ∼120-140 km depth.

I used teleseismic tomography to illuminate the deeper lithospheric structure (to ∼600 km depth), using ∼1000 teleseismic earthquakes registered at the stations of the TIPTIMON and TIPAGE networks as well as at all available permanent stations. The P-wave velocity model resolves a near vertically dipping high velocity anomaly in the mantle beneath the Hindu Kush, which is, however, thinned and disconnected in its upper part, including a neutral zone (no velocity anomaly) at ∼150-250 km, just where the intermediate depth Hindu Kush seismicity is most intense. Beneath the Pamir, the tomography resolves a second high velocity anomaly, coinciding with the arcuate intermediate depth seismicity. The structure penetrates to ∼400 km and 300 km in the west and east, respectively, and

is split by a vertical tear in its center.

Bringing these observation together, I proposed that the intermediate depth seismicity can be understood in the framework of a detaching lithospheric slab beneath the Hindu Kush, which, however, is still connected to the shallower structure as can be seen from the down-dip extensional stress regime of the Hindu Kush intermediate depth earthquakes. The high velocity anomaly beneath the Pamir was interpreted as Asian lithosphere, tearing in its center. The complex sub-crustal structure of interfering lithospheric slabs might be understood by considering the different mechanical properties of the three types of lithosphere involved in the India-Asia collision: while the Asian lithosphere beneath the Pamir is forced to delaminate and rollback by the northward advancing cratonic Indian indenter, a narrow sliver of India's stretched margin tears off and subducts beneath the Hindu Kush to its side. The domain of interconnected strike-slip faults at the Pamir-Hindu Kush transfer zone at crustal levels might accommodate the relative movement between the horizontally tearing Indian lithosphere at sub-crustal levels.

In this formation scenario, the Tajik basin acts as a kind of rigid backstop for the Hindu Kush subduction but subducts beneath the Pamir at the same time. To understand this contrasting behavior, I investigated its lithospheric structure in more detail: the sub-horizontal low velocity anomaly in the Tajik basin's interior, which splits the high velocity mantle lithosphere of the Tajik basin at ∼120-140 km depth, very likely represents the midlithospheric discontinuity (MLD), which was up to now mainly observed in old cratonic lithosphere using receiver functions or surface wave tomography (Yuan and Romanowicz, 2010; Rader et al., 2015; Hansen et al., 2015; Hopper and Fischer, 2015). The intermediate depth seismicity surrounding the basin's rims and the TIPTIMON stations on top, however, allow to map the MLD in the basin using local earthquake tomography.
At crustal levels, the stress regime indicated by the seismicity in the basin coincides with west-east oriented GPS-velocity vectors, suggesting that seismotectonics in the Tajik basin are mainly influenced by the westward escape of the western Pamir as also proposed by Schurr et al. (2014). Thus, west-east directed shortening seems to be much more pronounced in the basin's crust than the far field deformation from the Indian collision.

Zooming into the Hindu Kush slab break-off, I interpreted the low velocity zone at sub-crustal depth as subducted continental crust beneath the Hindu Kush, as earlier proposed by Roecker (1982), possibly consisting of a layer of lower crust and mid-crustal fragments. These fragments might penetrate as deep as ∼160-180 km, physically attached to the lower crust, before they detach from the subducting units. The shallower portion of the Hindu Kush intermediate depth seismicity (∼60-160 km) coincides with this zone of crustal subduction, whereas the deeper (∼180-270 km), seismically far more active patch, is hosted in a high velocity domain. This vertical zoning might be understood in the context of the slab break-off, where the deeper part is pulled to depth by the deeper, earlier subducted cold lithosphere and separated from the shallower part, which contains the buoyant crustal layers. Apparently, the separation of deep and shallow domains occurs along a localized interface. Based on numerical models, such a separation was suggested to arise as a shearing interface through the mantle lithosphere develops in the final stage of break-off. Subsequently to this shearing stage, necking along the thinned lithosphere leads to the final separation of the two fragments (Duretz et al., 2012). As the overturned geometry

of the deepest Hindu Kush zone as well as the stress regime of the earthquakes accurately mimics these modeling results, I consider this shearing-and-necking-scenario likely for the Hindu Kush slab break-off. Such a scenario would further elegantly explain the different seismogenic character of the shallower and deeper Hindu Kush intermediate depth seismicity.
Based on these considerations, it seems likely that seismicity in the deep and shallow domains might be driven by two different processes: rupture in the deeper patch could be caused by thermal runaway as also suggested by Poli et al. (2016), possibly facilitated by grain size reduction along the shearing interface through the lithosphere (Thielmann et al., 2015). The less intense seismicity of the shallower patch might be triggered by phase transitions and associated fluid release as the subducted lower crust contains a larger variability of possible candidates for such reactions.

From the results presented above, I see two main paths, which could be followed for further research: given that the Pamir-Hindu Kush is one of the rare case examples of currently ongoing continental subduction and slab break-off, and given that only geophysical observations can illuminate these processes today and at sub-crustal depths, it would be highly advisable to constrain the framework in which these processes take place as accurately as possible:
A joint travel time tomography, combining local and teleseismic data, would allow to create a high resolution velocity image from crustal levels down to the transition zone: the resolution of the teleseismic tomography starts to decrease at depths shallower than ∼70 km due to fewer crossing rays, just where the extent of the domain illuminated by local tomography narrows down, due to the more narrowly clustered earthquakes. However, this is exactly the most interesting depth range to monitor the ongoing slab break-off. Thus, combining both datasets would extend the well resolved depth range over the whole domain covered by these two methods. To get further insights regarding the physical process driving the intermediate depth seismicity, it would be highly recommendable to calculate an attenuation tomography. On the one hand, such a tomography would yield, apart from v_p and v_p/v_s, a third constraint on the subsurface characteristics. Additionally, it would yield the corner frequencies, and thus the stress drops of the events. Finally, it might be interesting to study the large M_w 7.4 earthquake of 1985 in more detail. The earthquake in 1985 was the only one of the large Hindu Kush earthquakes whose hypocenter was not located in the deepest patch of intermediate depth seismicity. Thus, possible differences in the rupture characteristics relative to the deeper events could be detected, which, in turn, could give insights regarding the underlying processes triggering the seismicity.
However, to ultimately understand these underlying processes, such geophysical observations have to be combined with other geoscientific disciplines, which are e.g. petrological studies and rock experiments to understand the behavior of rocks at high pressures as well as geological field studies to constrain the amount and timing of shortening in the crust. Further, numerical modeling enables testing of different end-member scenarios. Such models, in turn, need precise geophysical observations and geologically derived parameters as input. Thus, the two different research directions suggested above actually converge again in the end.

Appendix

A.1 TIPTIMON seismic stations

The TIPTIMON network was subdivided into two field experiments. The first network was deployed in Tajikistan from 2012 to 2014 (network code 5C). During a second stage, seismometers were deployed in Afghanistan (network code 6C, 2013-2014). Tables A1 and A2 summarizes the most important station parameters.
The TIPTIMON-Tajikistan network consisted of 20 Guralp CMG-3ESP and five Nanometrics Trillium-120 seismometers. Some of the initially deployed stations were however moved during later station-services to nearby locations, mainly to improve the data quality at the specific site. In consideration of these changes, the TIPTIMON network included 34 sites during its whole deployment time, which was from June 2012 to April 2014. TIPTIMON-Afghanistan consisted of eight short period sensors (MARK L-4C-3D, 1 Hz natural frequency), operating between March 2013 and October 2014. The seismic stations of the TIPTIMON network formed independent units which could not be accessed remotely but were visited during the deployment several times to download the data. Seismometers were buried ∼1.5-2 m in the ground and were installed on bed-rock if possible. Some of the Tajik stations were deployed in rock caves and buildings, initially used for an analog seismometer network during Soviet time. Beside the seismometer, the stations consisted of a data-logger with a computer and a hard drive, a unit for energy supply (one or two car batteries and a solar panel, according to the site) and a GPS antenna. The TIPTIMON-Tajikistan network was equipped with Earth Data PR6-24 recorders (EDL) while DSS CUBE recorders were used in the TIPTIMON-Afghanistan network. All stations were sampling with a frequency of 100 Hz. More detailed information regarding these networks can be obtained via the FDSN[1] and GEOFON[2] websites. TIPTIMON data is archived at the GEOFON data management center.

Data from the permanent stations used in this study was obtained from the GEOFON, IRIS and Chinese data management centers. Specifically stations from the following networks were used: KN - 10 stations, KR-13 (Institute of Seismology, National Academy of Sciences of Kyrgyz Republic (KIS), 2007), KZ-4 (KNDC/Institute of Geophysical Research, Kazakhstan, 1994), TJ-7 (PMP International, Tajikistan, 2005), II-3 (Scripps Institution of Oceanography, 1986), IU-1 (Albuquerque Seismological Laboratory ASL; USGS,1988), CK-4, GE-1 (GEOFON data centre, 1993), KC-2 (CAIAG Central Asian Institute for Applied Geosciences, 2008) and the Chinese Earthquake Network data center (9 stations).

[1] http://www.fdsn.org/networks/
[2] http://geofon.gfz-potsdam.de/waveform/archive/index.php?type=t

Station name	Seismo-meter	Lat. (deg.)	Lon. (deg.)	Ele. (m)	City/ village	Location changed
BAL2	3ESP	38.305	69.671	971	Balchuvon	to BAC2
BAC2	3ESP	38.315	69.673	938	Balchuvon	to BAC3
BAC3	3ESP	38.315	69.673	942	Balchuvon	from BAC2
BAR2	3ESP	37.942	71.453	2091	Barushan	
CDA2	3ESP	37.757	69.834	1061	Sari-Chahma	
FRK2	3ESP	37.394	69.300	620	Farkhor	
GCH2	3ESP	37.199	71.545	2621	Gharm-Chashma	
GUL3	3ESP	38.663	69.513	1937	Gulkhor	from KID2
ISH2	3ESP	36.684	71.794	2661	Ishkashim	
JOR2	3ESP	39.102	70.591	1557	Jorf	
KAL2	3ESP	37.838	69.095	699	Uchbulog	
KHV2	3ESP	38.387	70.037	1654	Khovaling	to SAN2
KID2	3ESP	38.637	69.495	1739	Kalai-Oasht	to GUL3
KIK2	3ESP	38.468	70.822	1811	Khala-i-Khumb	
KSM2	3ESP	38.907	69.937	1604	Saidon	to KSN2
KSN2	3ESP	38.906	69.936	1607	Saidon	from KSM2
PAN2	3ESP	38.275	70.575	1141	Panj	
PES2	3ESP	38.602	69.922	1492	Pestitovo	to PES3
PES3	3ESP	38.602	69.924	1501	Pestitovo	from PES2
QUM2	3ESP	37.430	68.688	447	Qavchin	
SAN2	3ESP	38.378	70.139	1580	Sandara	from KHV2
SBD2	3ESP	37.853	70.059	2090	Shurabad	
SHU2	3ESP	38.011	69.760	695	Pushyoni-Poyon	
TAB2	3ESP	37.234	72.156	3111	Tabersem	
TAV2	3ESP	38.676	70.497	1724	Tavildara	
VAN2	3ESP	38.375	71.467	1740	Vanj	
AIN2	Tri-120	39.389	68.544	1490	Aini	to MAR2
GAN2	Tri-120	37.933	68.596	641	Quziqiyo	
HOI2	Tri-120	39.180	70.886	1653	Hoit	to HOT2
HOT2	Tri-120	39.181	70.887	1660	Hoit	from HOI2
MAR2	Tri-120	39.187	68.729	2071	Marzich	from AIN2
PIC2	Tri-120	39.006	69.353	1844	Guskef	to VIS3
SHP2	Tri-120	38.841	70.780	1831	Shpillon	
VIS3	Tri-120	38.896	69.278	1551	Viston	from PIC2

Table A1: Stations of the TIPTIMON-Tajikistan network: lat./lon./ele. are the station coordinates (latitude from north, longitude from east) and the station elevation. The sites listed in the last column were not equipped during the whole deployment time but the location was changed as indicated. No data from BAC3 was used in the teleseismic tomography as its vertical component was locked due to hardware failure of the Guralp seismometer.

Station name	Seismo-meter	Lat. (deg.)	Lon. (deg.)	Ele. (m)	City/ village
AEG3	MARK L-4C-3D	37.309	70.928	2541	Arghanchkhowa
FIA3	MARK L-4C-3D	37.110	70.577	1477	Fiazabad
JUR3	MARK L-4C-3D	36.871	70.832	1561	Jurm/Dashtak
KEM3	MARK L-4C-3D	36.020	70.678	2551	Kuran-e-Munjan
PAJ3	MARK L-4C-3D	35.426	69.724	2260	Panjshir
SEB3	MARK L-4C-3D	37.311	70.168	1728	Shur-e-Bazarg
YAM3	MARK L-4C-3D	36.520	70.801	1853	Yamgang/Gharmi
ZEB3	MARK L-4C-3D	36.527	71.342	2615	Zibak

Table A2: Stations of the TIPTIMON-Afghanistan network: lat./lon./ele. are the station coordinates (latitude from north, longitude from east) and the station elevation.

A.2 GPS timing corrections

During the TIPTIMON-Tajikistan deployment, three stations lost their GPS timing temporarily. In addition, one of these stations (KID2) ran out of energy within the time of the GPS-outage (see Tab. A3). To use the data recorded during these periods nevertheless, I corrected the EDL timing back to the GPS timing, using noise cross-correlation to adjacent stations as well as teleseismic earthquakes.

The main task of the GPS-system at each station was to ensure the correct timing of the seismic records as the EDL internal quartz clock might undergo a certain drift. The magnitude of the drift depends mainly on temperature changes. The EDL system compared its internal time with the GPS time on a regular basis of a few milliseconds. If no GPS information was available, data was recorded according to the internal EDL clock, which might be increasingly different to the GPS time the longer the antenna was disconnected. If additionally the energy supply of the station was cut, also the EDL clock stopped. If the station received enough power to operate again after such a shut down, while the GPS was still disconnected, the EDL clock received the first timing information from its internal computer clock, which, however, could be wrong by several hours.

Assuming that the travel paths of teleseismic earthquakes are very similar in the mantle, the biggest part of the travel time difference measured at adjacent stations accumulates due to the varying near station structure. The inter-station delay times measured from different teleseismic earthquakes are expected to be very similar (see Chapter 3). Knowing the average difference between two stations, it is possible to correct the temporally offset record of one station. However, teleseismic earthquakes only yield a rough estimate for the timing error and no continuous offset-function to describe the evolution of the clock drift.

The method of noise cross-correlation yields higher precision results, if two records start from the same time base, but eventually one of the records drifts away. The Green's function between a pair of stations can be obtained by the correlation of the wave field between these two stations (Sánchez-Sesma and Campillo, 2006). Under the assumption of constant site conditions, a shift in the Green's functions with time would indicate that the clocks from two neighboring stations do not work synchronously (Sens-Schönfelder, 2008).

Station	Time of GPS outage dd.mm.yy (Julian day)	Time period for reference stack	Reference stations for timing correction
FRK2	31.03.13 - 14.06.13 (090) - (165)	01.01.13 - 21.03.13 (001) - (080)	CDA2, KAL2, QUM2
KSN2	10.09.13 - 19.04.14 (282) - (109)	19.06.13 - 27.09.13 (170) - (270)	HOT2, PES3, TAV2, SHP2
KID2	11.12.12 - 09.02.13 (346) - (040)	20.10.13 - 05.12.13 (249) - (340)	MAR2, SAN2 KSN2
KID2	01.03.13 - 06.06.13 (060) - (157)	-	KSN2, KAL2, PIC2

Table A3: Stations which lost the GPS signal for longer than one day. The two last columns summarize the stations and the time interval used for noise cross-correlation. See Tab. A1 for the station names and locations.

Correcting the time shift obtained from the Green's functions in the seismic records enables to remove the error due to clock drift.

FRK2 and KSN2

The station FRK2 lost its GPS antenna by the end of March 2013 but was continuously recording data until June 2013. Then the station was serviced and a new antenna was installed. I calculated the clock drift using the method of noise cross-correlation between FRK2 and the three nearest stations (see. Tab. A3), which were located in a distance between 30 to 50 km to FRK2. Based on the work of Sens-Schönfelder (2008) and Bensen et al. (2007), I executed the following steps:

- Pre-processing was carried out hour-wise at each trace of the seismograms and included the following steps: removing of mean and trend, down-sampling (20 Hz) in order to shorten computation time and bandpass filtering (0.1 to 0.5 Hz corner frequencies) as high frequency noise is more difficult to correlate. Subsequently, I implemented an amplitude normalization scheme in the time domain to remove e.g. earthquakes from the data, using the running-absolute-mean method (with a time window of half the maximum period of the bandpass filter). Finally, spectral whitening in the frequency domain was applied to produce a homogeneous spectrum (see Bensen et al., 2007, for a detailed description of these pre-processing steps).
- After pre-processing, for each station pair (FRK2/CDA2, FRK2/KAL2, FRK2/QUM2) the hour-wise cross-correlation function in the frequency domain was calculated[3] for all possible combinations of the vertical and the two horizontal components. For each of these specific station-component combinations all hour-wise correlation functions

[3]Cross-correlation functions were calculated using the MIIC package provided by the University of Leipzig (http://theo1.geo.uni-leipzig.de/docs/index.html)

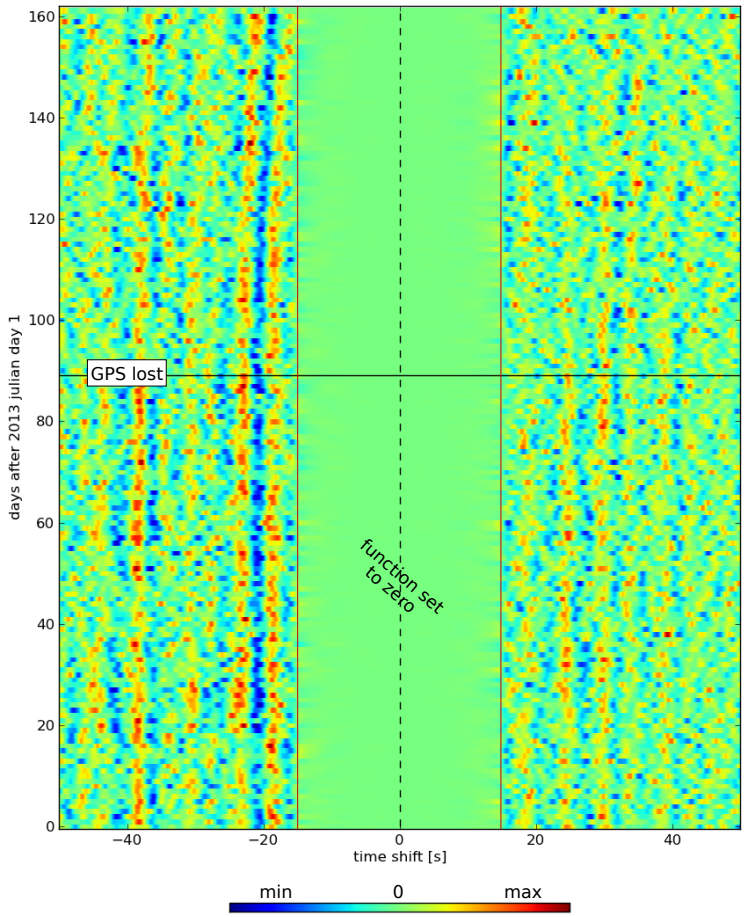

Figure A1: Daily cross-correlation functions between the east-west components of the stations FRK2 and QUM2, color coded by their amplitude. In the center, the functions are set to zero to remove the effect of the direct surface waves.

of one day were summed up to increase the signal to noise ratio. Additionally, I removed the energy in the center of these daily-stacked correlation functions, because this signal is mainly dominated by the direct surface waves between the two stations, which might have a varying source. The time limit for energy removal was calculated from the inter-station distances and assuming a seismic velocity of 3.5 km/s.
Figure A1 shows a color coded plot of the resulting Green's function of one horizontal component between the stations FRK2 and QUM2. The y-axis of this plot indicates the day for which the function was calculated. The x-axis annotates lapse time. Peaks in the lapse time provide information regarding the travel time between a noise source and the receiver. The pronounced maxima and minimum of the Green's function are rather constant during the time where both stations were equipped with GPS antennas, expressing a good reproductivity of the function (Sens-Schönfelder, 2008). After the GPS outage at day 90, a clear shift of the whole function towards positive values occurs. This indicates that the internal clock of FRK2 was running slower than the correct GPS time.

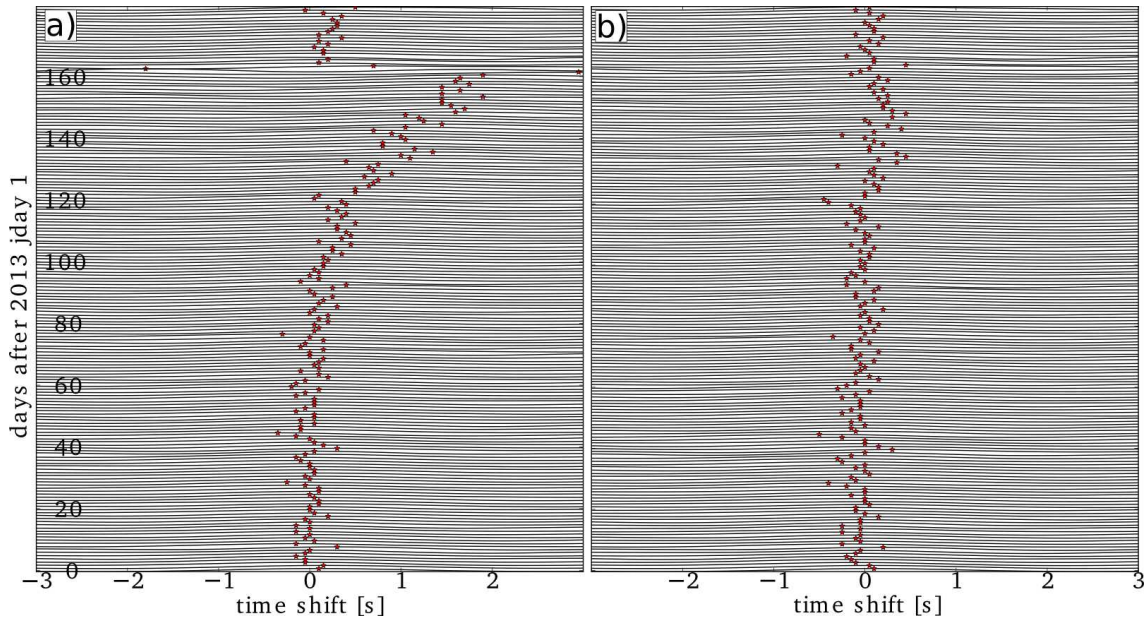

Figure A2: Cross-correlation against a reference stack for the east-west component of the cross-correlated FRK2 and QUM2 stations. For each day, the trace of the cross-correlation function is plotted in black. Red stars indicate the absolute maxima of these traces. **a)** Prior to the timing correction (the GPS antenna was lost at day 90 and re-installed at day 165). **b)** The same cross-correlation function calculated with the corrected data.

- To further enhance the relevant signal, a reference function was calculated by stacking the Green's functions from the time period before the GPS outage at both stations (see the second column in Tab. A3 for the time interval of these reference stacks). All functions were subsequently cross-correlated against this reference stack (Fig. A2). If the two clocks run synchronously, the maximum of this correlation function should be at zero lapse time. Once one clock drifts, the maximum starts to shift dependent on the difference between the clocks. The value of this time shift was determined automatically for each of the station-component combinations by searching for the absolute maximum in the cross-correlation function of each day (red stars in Fig. A2).

- Finally, the maxima of all station-components combinations were used to derive a correlation function (Fig. A3). Figure A3a shows the correlation maxima derived for the station FRK2. Despite some scatter, the shift after the GPS outage is very similar for all station-component combinations. Here I used a third-order polynomial fit to describe the offset, yielding a maximum correction value of 2.53 s. The seismic data of the station FRK2 was then shifted hour wise by the associated correction value. Figure A2b shows the cross-correlation against the reference stack for the corrected data, proving that the prominent clock drift was removed.

For the station KSN2, I applied exactly the same procedure as for FRK2 (see detailed information in Tab. A3). In contrast to the FRK2 station, the cross-correlation maxima

of KSN2 mimic a sine wave, with a maximum shift of -0.24 and 0.30 s (Fig. A3b). Thus, I fitted the data with a 5th order polynomial.

KID2

For the station KID2, the correction was complicated due to a total energy outage during its time without GPS antenna (the solar panel had been covered with snow). Therefore, the time intervals before and after the energy outage had to be considered separately:

For the time period between 11.12.12 and 09.02.13, the correction procedure was carried out similar as described above for the stations FRK2 and KSN2. The correlation function is a third order polynomial with a maximum correction value of 0.34 s (Fig. A3c).

For the time period between 01.03.13 and 06.06.13, I chose a three step approach for the correction:

- In a first correction I used two teleseismic earthquakes to gain the absolute time offset between the GPS time and the (random) time the EDL computer had used after it restarted. One of the earthquakes had happened when the station KID2 was still operating with GPS (date: 2012, Julian day 289; lat/lon: 51.90°N/159.38°E, depth: 21 km), the other at the day when it started working again after the GPS outage (date: 2013, Julian day 60; lat/lon: 50.94°N/157.51°E, depth: 41 km). A comparison

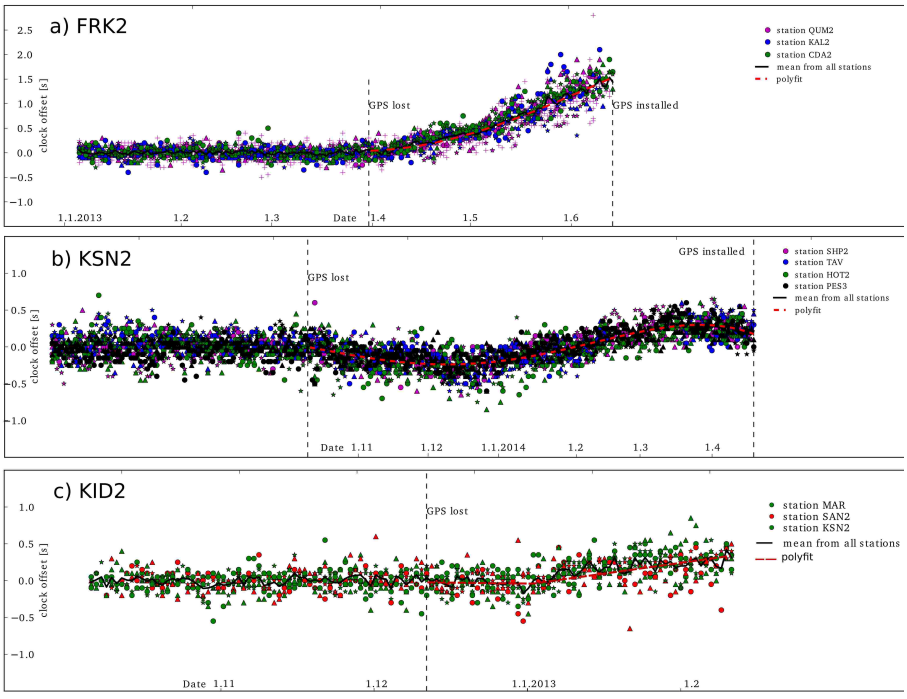

Figure A3: Maxima obtained from the cross-correlation against a reference stack (e.g. stars in Fig. A2) and derived correction function for all station-component pairs used at one station. The color of the symbols indicates the different stations, the symbol the different component-combinations.

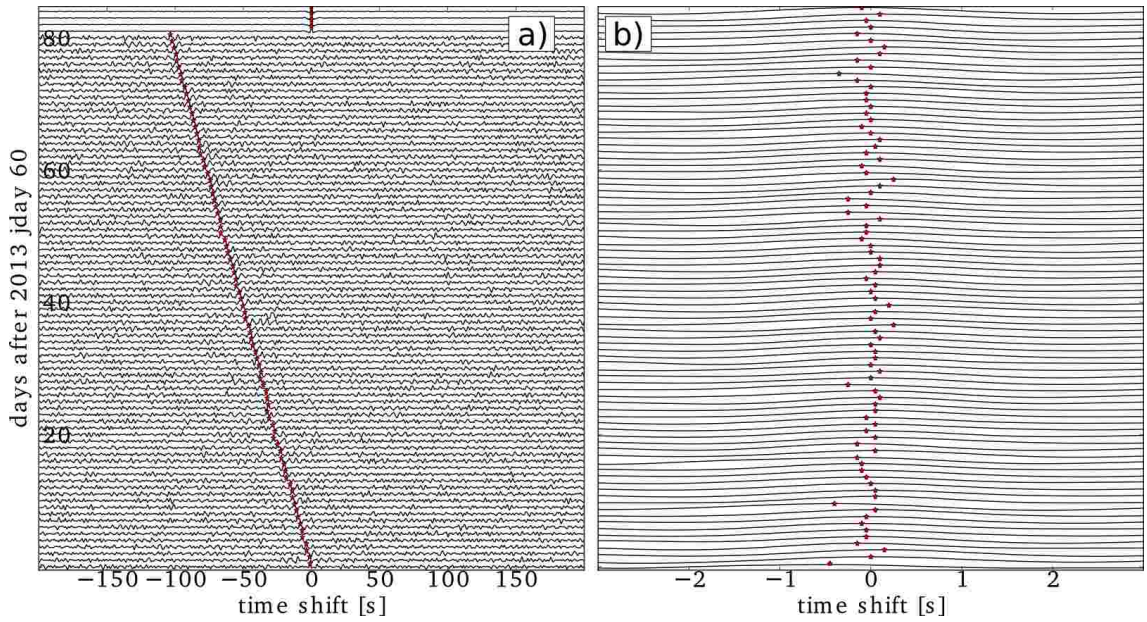

Figure A4: Cross-correlation against a reference stack for the east-west component of the cross-correlated KID2 and KSN2 stations for the time after the complete energy shut-down. For each day, the trace of the cross-correlation function is plotted in black. Red stars indicate the absolute maxima of the traces. **a)** Prior to the timing correction (the GPS antenna was re-installed at day 97). **b)** The same cross-correlation function calculated with the corrected data. Note the different x-axes of the two plots, the y-axes have the same scale.

between these two earthquakes recorded at adjacent stations (see Tab. A3) showed that the internal KID2 time was shifted over 15 hours. However, comparing the arrival times of two earthquakes in May and one in June 2013, showed that the internal timing of KID2 seemed to be nevertheless quite robust.

- Subsequently, the offset function was again constrained by noise cross-correlation. However, the clock drift of the station KID2 was relatively large, but clearly linear (Figs. A4a and A5a). Thus, I first determined a linear correlation function and corrected for this time shift by re-sampling the data of the KID2 station accordingly. In a second step, the corrected KID2 data was cross-correlated and corrected again using the neighboring stations in the same manner as the FRK2 and KSN2 stations before (Figures A5b). Figures A4b and A5c show the cross-correlation functions derived from the finally used data, which prove that the time shift was removed sufficiently well.

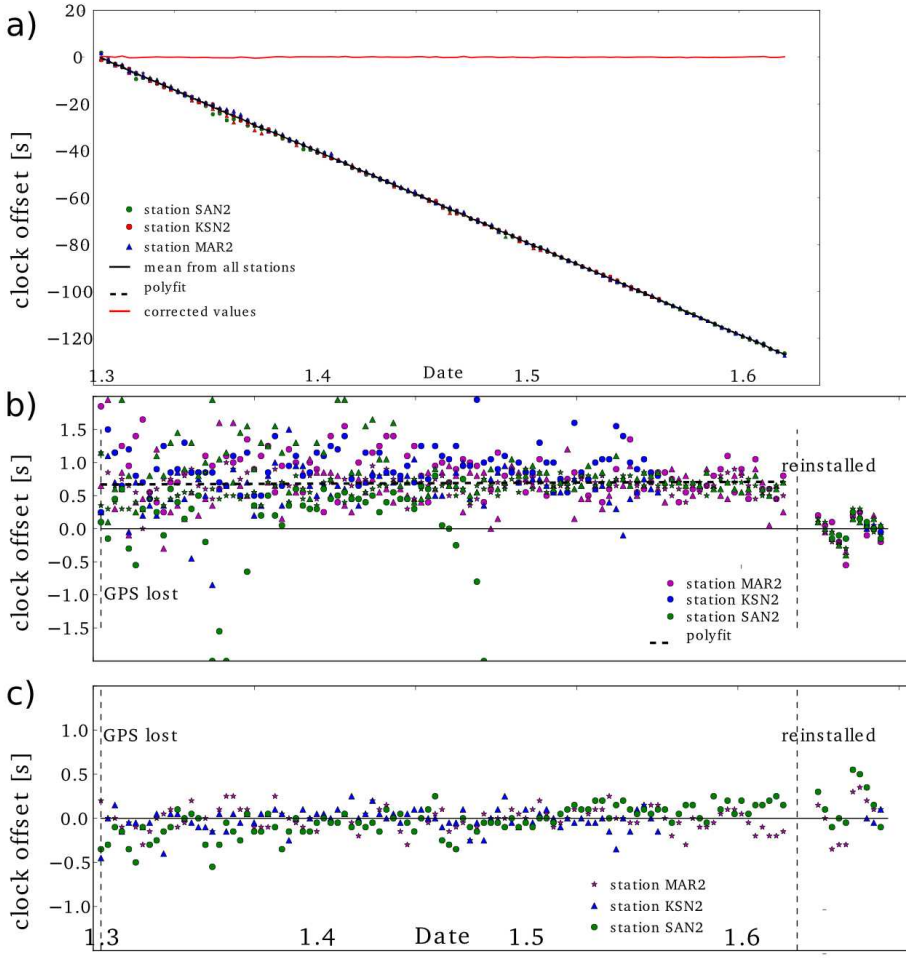

Figure A5: Maxima obtained from the cross-correlation against a reference stack (e.g. stars in Fig. A4) and derived correction function for all station-component pairs used at the KID2 station after the total energy outage. The color of the symbols indicates the different stations, the symbol the different component-combinations. **a)** First rough correction. **b)** Second correction of the corrected data. **c)** Cross-correlation with the finally used data (the same as plotted in Fig. A4b)

B Supplementary for Chapter 4

Complete velocity model from teleseismic tomography

In addition to the features discussed in the main article, the final teleseismic velocity model covers larger parts of Central Asia, i.e. the southern Tian Shan, Tajik and Fergana basins. Map view sections of the complete model are shown in Supplementary Figure B4. The velocity model resolves a clear velocity contrast across the Talas Fergana Fault in the upper mantle down to 150 km depth with low velocities under the Tian Shan and an elongated NW-SE striking high velocity anomaly under the margin of the Fergana basin (anomalies TS and TFF in Supplementary Fig. B4). Two other east trending high velocity zones can be seen in the shallow mantle below the southern rim of the Fergana basin (FB), and the northern edge of the Tajik basin (TB). Deeper in the mantle, the anomalies beneath the Pamir and Hindu Kush are the only remaining structures.

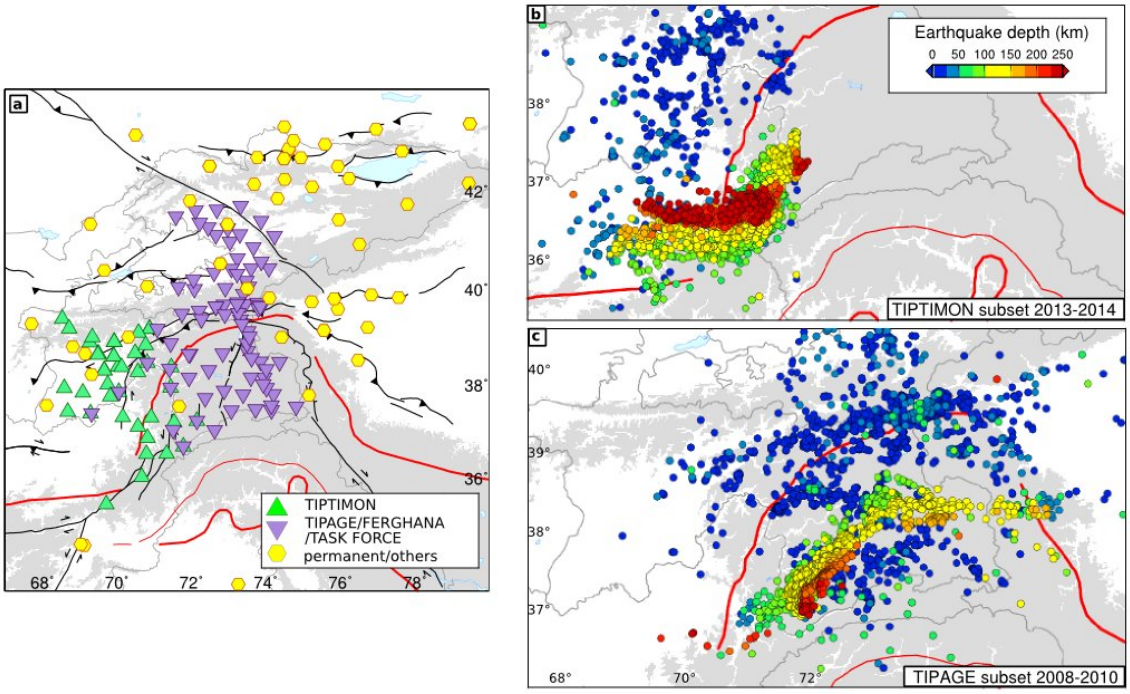

Figure B1: Summary of seismic stations used in this study and components of the updated earthquake catalog. **a)** Location map of these stations. **b)** Earthquakes located in this study using primarily the stations of the TIPTIMON network. **c)** Subset of the earthquake catalog of Sippl et al. (2013b) based on TIPTIMON and FERGHANA networks, excluding events with a backazimuthal gap larger than 120° in the Hindu Kush. Main tectonic features as in Figure 4.2.

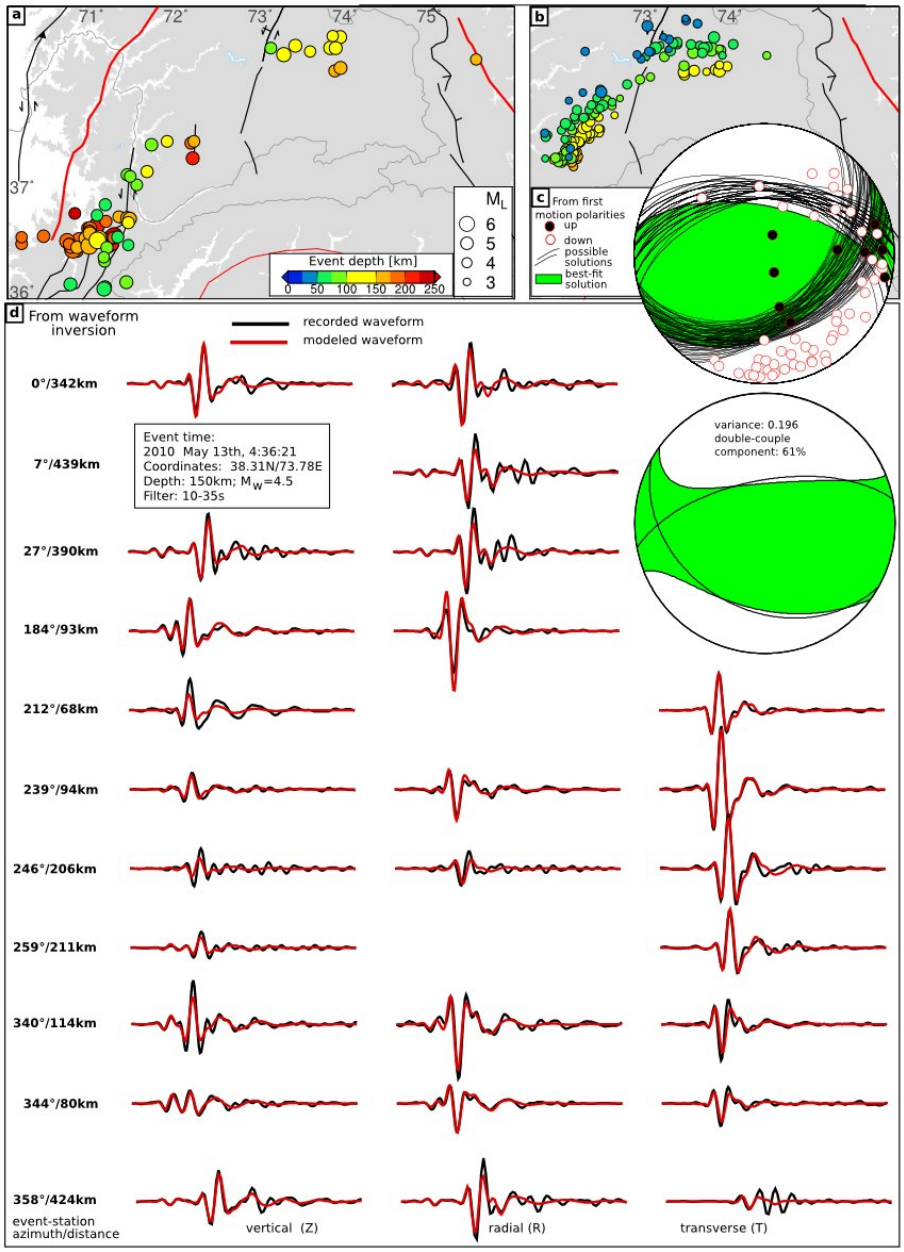

Figure B2: Earthquakes used for focal mechanism determination and example focal mechanism. a) 72 earthquakes with mechanism determined by waveform inversion. **b)** 166 earthquakes with mechanism determined from first motion polarities. Colors correspond to earthquake depth, size to the local magnitude M_L (Sippl et al., 2013b). **c)** Example focal mechanism for one earthquake determined from first-motion polarities (circles). Possible nodal planes are shown as black lines. The best fit solution is colored green. **d)** Moment tensor plotted as beachball for the same event determined by waveform inversion as well as sample traces of the modeled (red) and observed (black) waveforms.

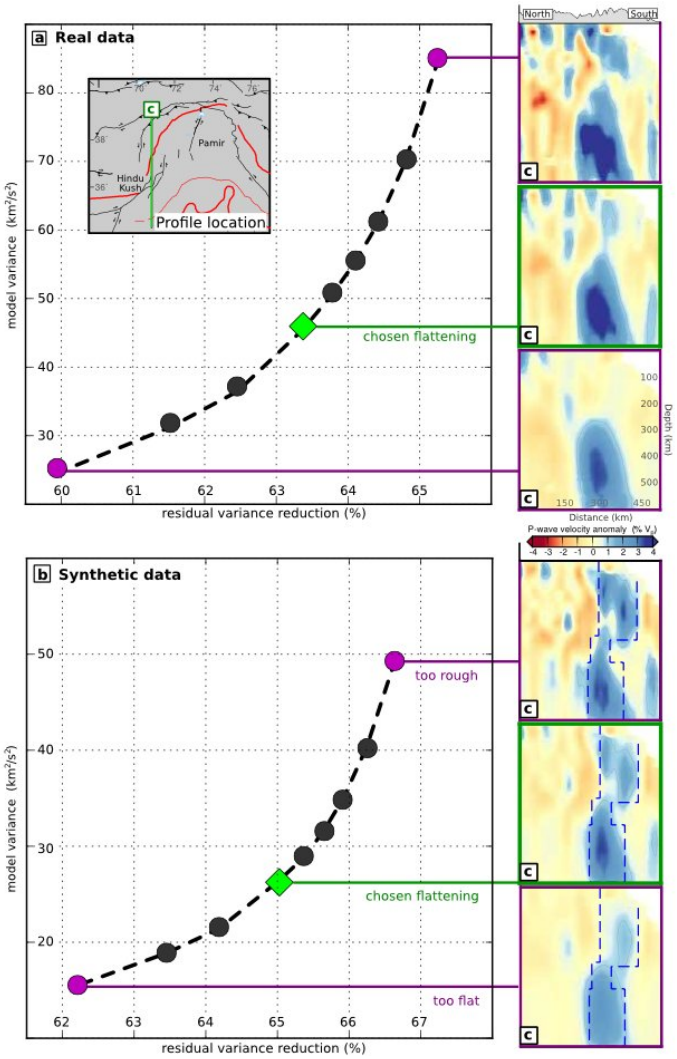

Figure B3: Trade-off curves for optimum flattening parameter. a) Model variance vs. residual reduction for different flattening values using real data. The chosen value constitutes an optimum between residual reduction and model roughness. **b)** Same test using synthetic data. The trade-off-curve yields the same optimum flattening parameter. **c)** Insets show the velocity model for different flattening parameters along the north-south profile of Figure 4.6c. Dashed lines in the profiles show the synthetic input anomaly ($dV_p = +2.5\%$).

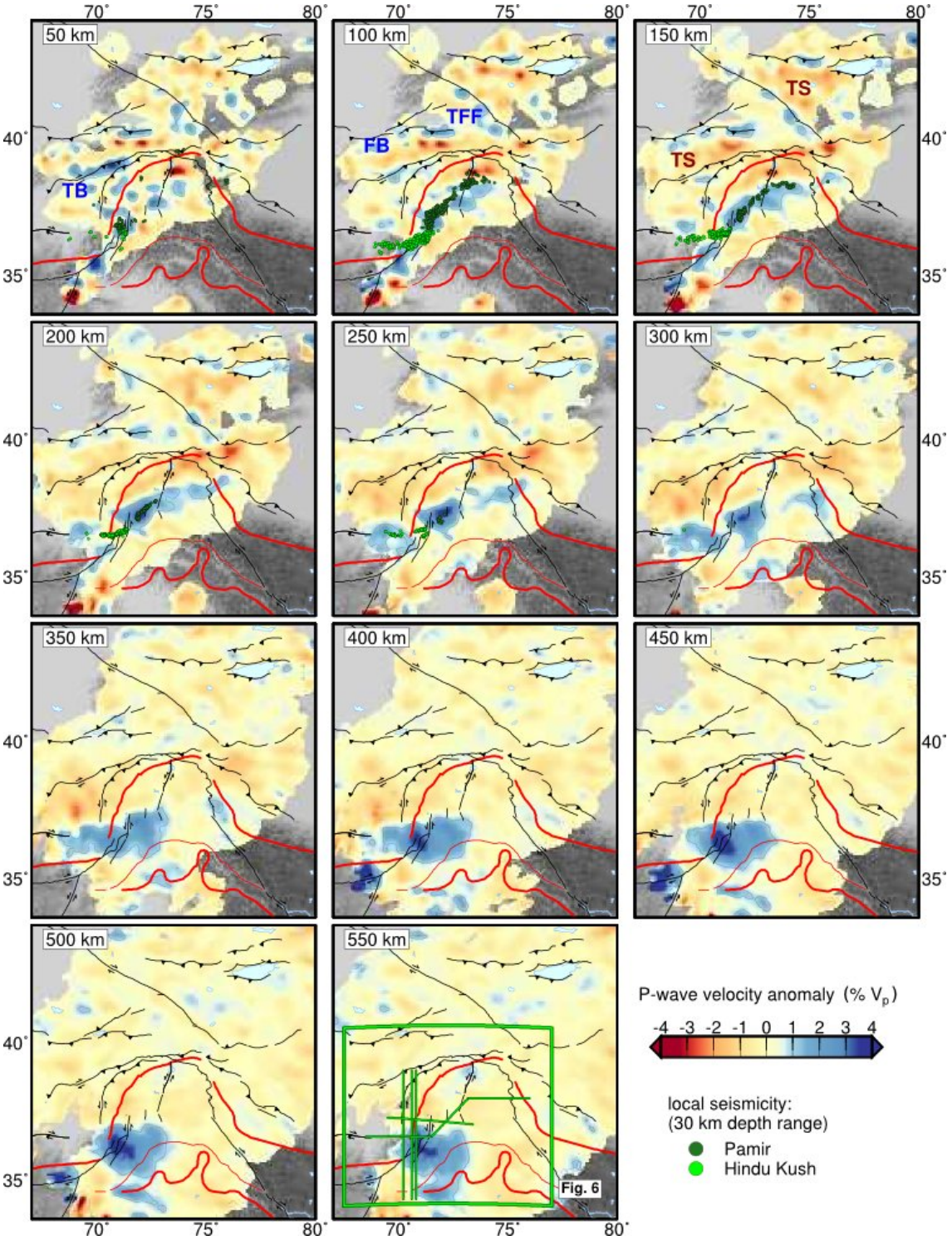

Figure B4: Depth sections of the complete tomographic P-velocity model. Anomalies mentioned in the Supplementary Material Section B: TS - Tian Shan, TB - Tajik basin, TFF - Talas-Fergana Fault, FB - Fergana basin. Earthquakes, tectonic features and color coding of the velocity model as in Figure 4.6. The locations of the cross sections and maps shown in Figure 4.6 are plotted in the 550 km depth slice.

C Supplementary for Chapter 5

Minimum 1D velocity model for the TIPTIMON network

We inverted a handpicked subset of the TIPTIMON catalog (155 earthquakes: 2507 P and 1900 S picks; Fig. C1a, b), which represents the overall seismogenic structures of the Tajik basin and Hindu Kush region, for a minimum 1D velocity model and station corrections using the software *velest* (Kissling et al., 1994). Initially, we tested a wide range of fine layered input models, including different Moho depths (light gray shaded area in Fig. 5.3) and subsequently removed depth layers that had little velocity contrast to its surroundings. The starting v_p/v_s ratio was constrained from a Wadati-diagram and set to 1.72. Despite the wide variability of input models, all these models converge around similar velocities (dark gray shaded in Fig. 5.3). The final minimum 1D model (Fig. 5.3, Tab. C1) was identified due to the smallest root mean square (RMS) residual after inversion. However, its close affinity to all other output models after inversion proves that it represents an absolute minimum.
Relocating the reference dataset, with hypocenters initially constrained from the Sippl et al. (2013a) minimum velocity model with the new velocity model decreases the RMS from 0.71 to 0.44 s (Fig. C1e). Final station corrections show relatively large variations (Fig. C1c, d; maximal/minimal values of 0.24/-1.17 s and 1.94/-1.6 s for P- and S-picks, respectively) and correlate with tectonic units (e.g. similar sign and magnitude in Pamir or Tajik basin). Thus, although the minimum velocity model represents a local minimum, it averages over a 3D heterogeneous subsurface and is therefore not necessarily geologically meaningful.

v_p (km/s)	Depth (km)
5.46	-5.00
5.64	0.00
5.86	10.00
6.28	20.00
7.76	55.00
8.05	65.00
8.29	80.00
8.36	100.00
8.36	350.00

Table C1: Minimum 1D P-wave velocity model derived from the TIPTIMON data, focusing on the Tajik-Afghan basin (for input see Figs. C1 and 5.3). *Depth* is downward positive and refers to the upper interface of a specific velocity layer. The deepest layer is a homogeneous half-space.

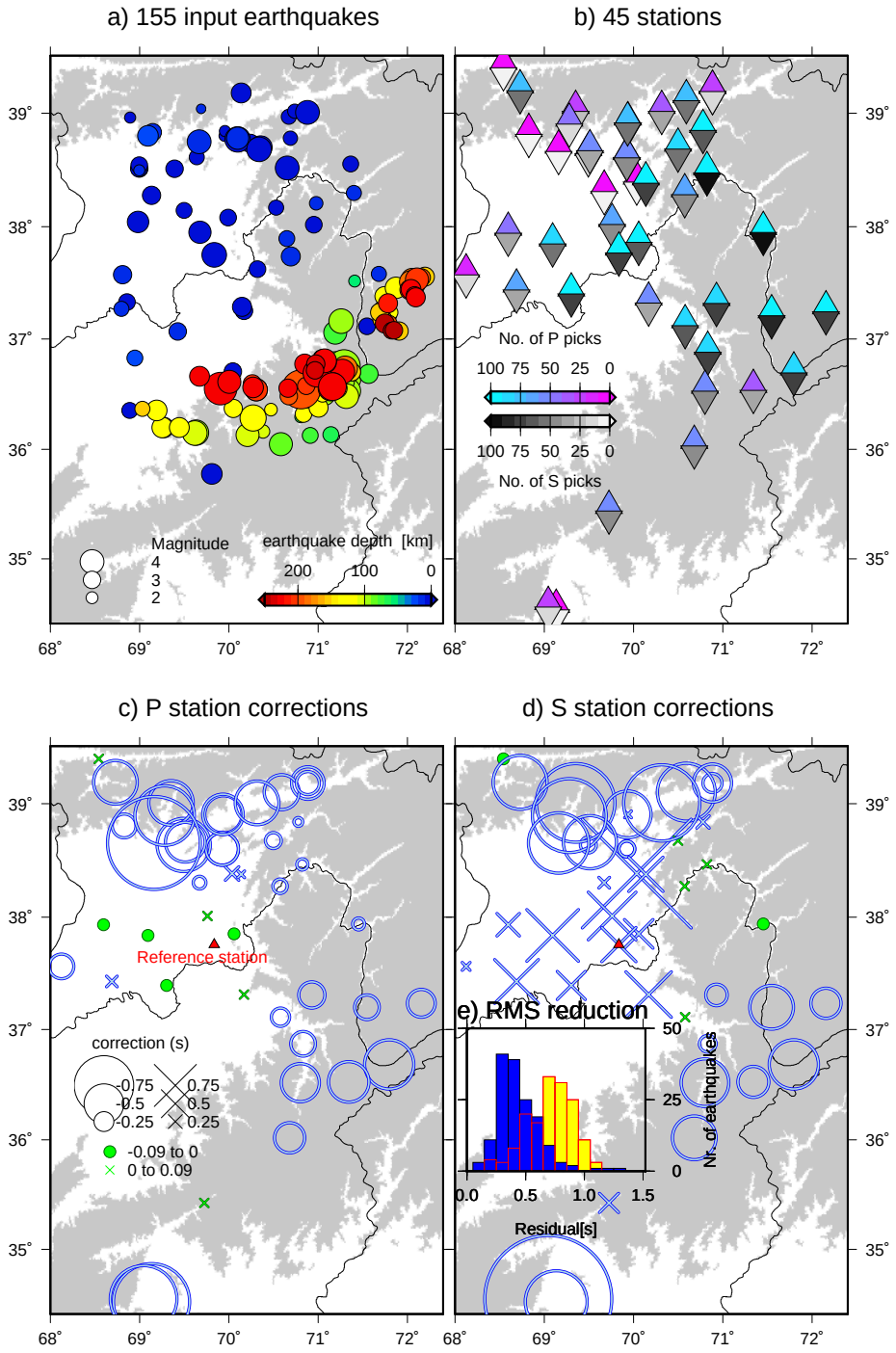

Figure C1: a/b) Input earthquakes and picks for the calculation of the minimum 1D velocity model (Fig. 5.3 and Tab. C1). **c/d)** Final station corrections, relative to the reference station CDA2 (37.76°N/69.83°E). Topography higher than 2500 m in gray. **e)** RMS residuals of earthquakes located in the velocity model of Sippl et al. (2013a) in yellow and the new minimum 1D velocity model (blue).

D Supplementary for Chapter 6

Shallow TIPAGE earthquake catalog subset

The events of the crustal TIPAGE earthquake catalog (Fig. D1a), which were additionally included in our analysis (Fig. D1b), contained a subset of the shallow (<50 km) seismicity from Sippl et al. (2013b). We disregard all events with an azimuthal gap larger than 120° west of 71.8°E to give preference to the better located TIPTIMON events and excluded the bulk of aftershocks of the Nura earthquake (all events from 3.10.2008 to 28.3.2009 in the range between 73.-74.25°E and 39.3-39.9°N). The Nura earthquake happened near the Chinese border in 2008 and was described in detail by Sippl et al. (2014). After applying these restrictions, the TIPAGE subset was relocated in the same 3D velocity model as the TIPTIMON data and the combined catalog was jointly double difference relocated (see Fig. D1d for the combined dataset).

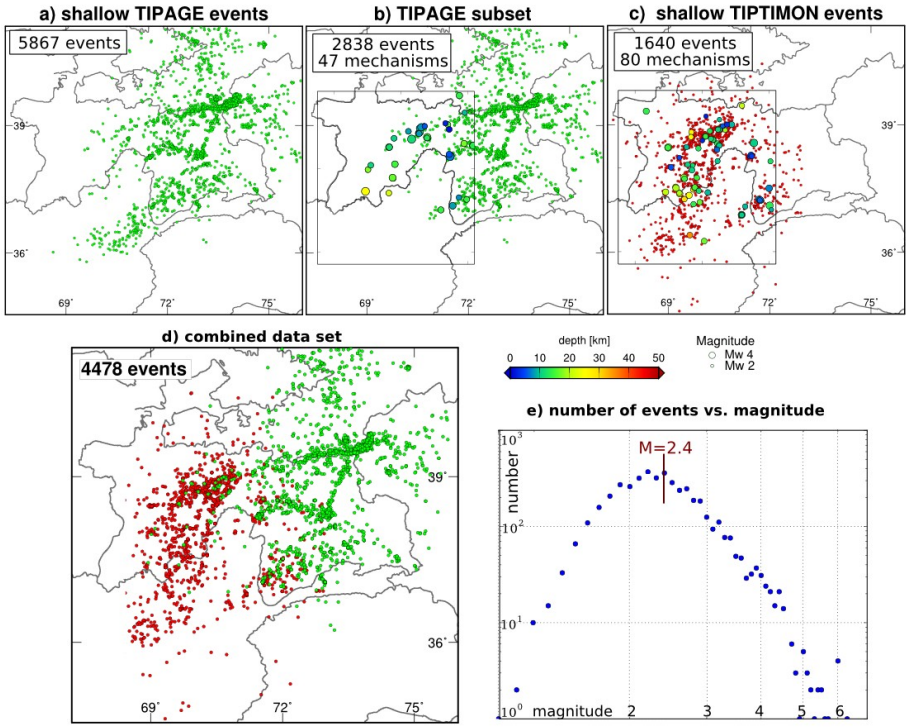

Figure D1: Components of the joint crustal event catalog from different networks: **a)** All shallow (<50 km) events located during the TIPAGE deployment (2008-2010; Sippl et al., 2013b). **b)** TIPAGE subset used here: earthquakes are plotted in green. Locations of TIPAGE focal mechanisms are plotted as larger circles, scaled by magnitude and depth (from Sippl, 2013). **c)** All shallow events located during the TIPTIMON deployment (2012-2014). Events with moment tensor solution are highlighted as in sub-figure b). **d)** Combined and relocated event catalog. **e)** Gutenberg-Richter plot for the combined catalog. The events are bundled according to their local magnitude in bins with the width of 0.1.

E Supplementary for Chapter 7

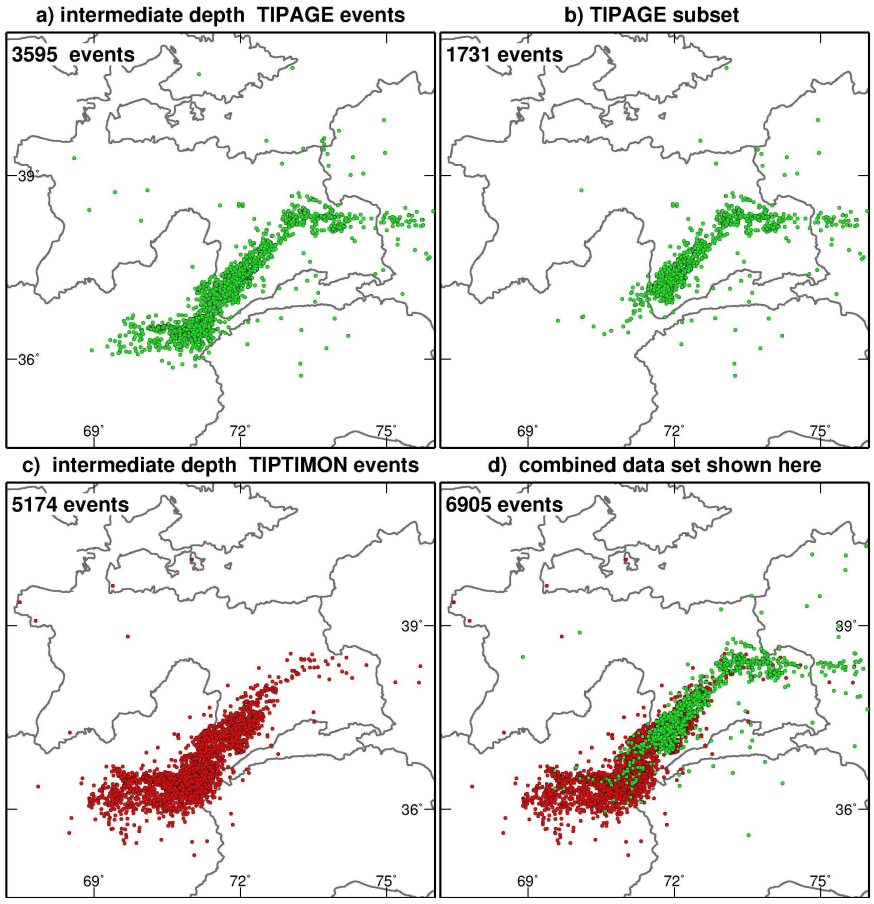

Figure E1: Components of the joint intermediate depth event catalog from different networks: in accordance with Chapters 4 and 6, we excluded all intermediate depth earthquakes with an azimuthal gap greater than 120° west of 71.8°E from the TIPAGE catalog. We expected to have smaller location errors for the Hindu Kush seismicity using only TIPTIMON events, due to the superior event-station geometry of the TIPTIMON stations. **a)** All intermediate depth (>50 km) events located during the TIPAGE deployment (2008-2010; Sippl et al., 2013b). **b)** TIPAGE subset used here. **c)** All intermediate depth events registered during the time of the TIPTIMON deployment (2012-2014). **d)** Combined and relocated catalog.

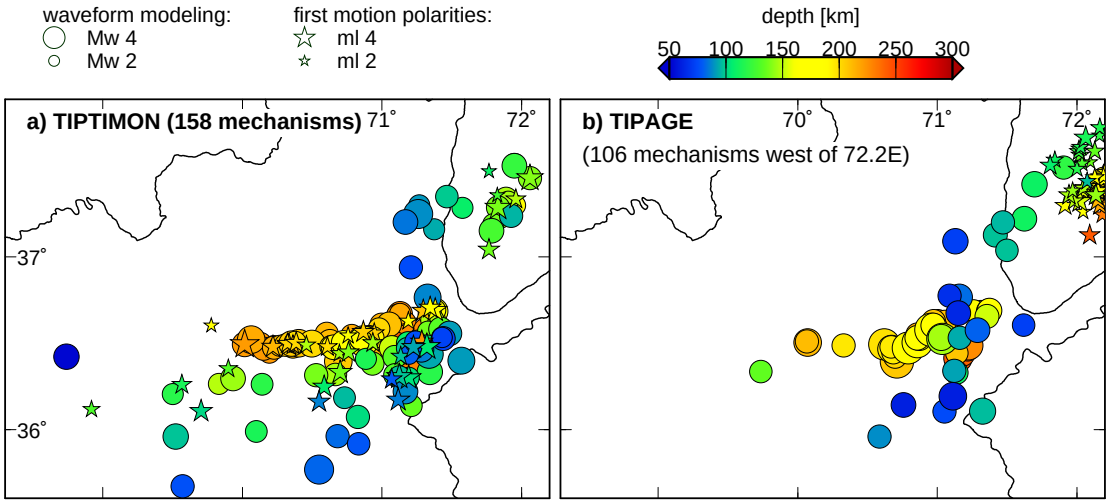

Figure E2: Composition of the focal mechanisms plotted in Figure 7.6: stars indicate earthquakes for which the mechanisms were derived from first motion polarities, circles earthquakes for which the mechanisms were derived from waveform modeling. Color corresponds to depth, size to the local magnitude (m_l) and to the moment magnitude (M_w) for the events derived from first motion polarities and waveform modeling, respectively. **a)** Events from the TIPTIMON recording period (2012-2014). **b)** Events from the TIPAGE recording period (2008-2010). The TIPAGE mechanisms are the same as used in Chapter 4.

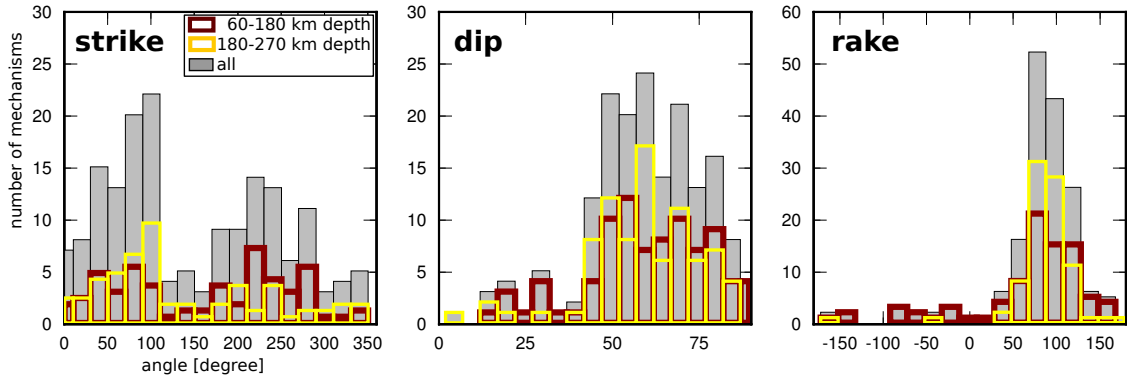

Figure E3: Histograms for strike, dip and rake of the source mechanisms from sub-crustal earthquakes (the events plotted in Fig. E2). P-axes and the double couple representations of these mechanisms are plotted in Figure 7.6.

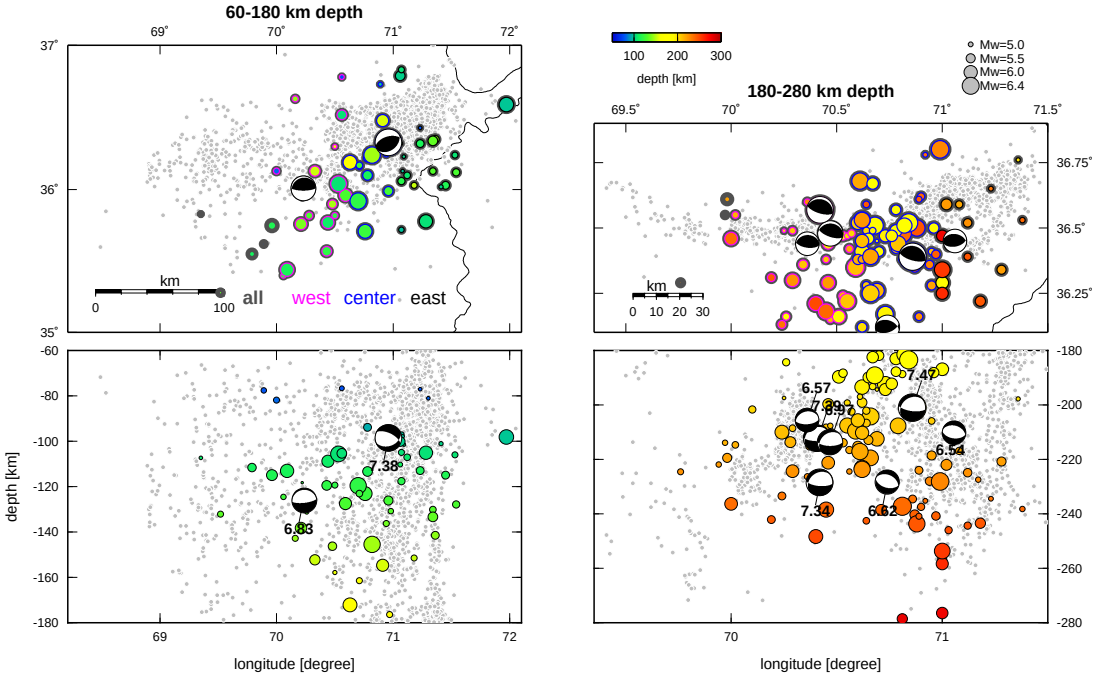

Figure E4: Earthquakes from the GCMT catalog (Dziewoński et al., 1981; Ekström et al., 2012) used for strain rate calculation. Events from the GCMT catalog are color coded by depth and scaled by their size. For earthquakes with $M_w > 6.5$ focal mechanisms are plotted. The numbers next to the mechanisms refer to their moment magnitudes. The colors surrounding the events in map view refer to the associated sub-region of the events in Table 7.3. Small gray circles are the earthquakes from the local earthquake catalog that has been used to constrain the geometry of the seismogenic volumes for strain rate calculation.

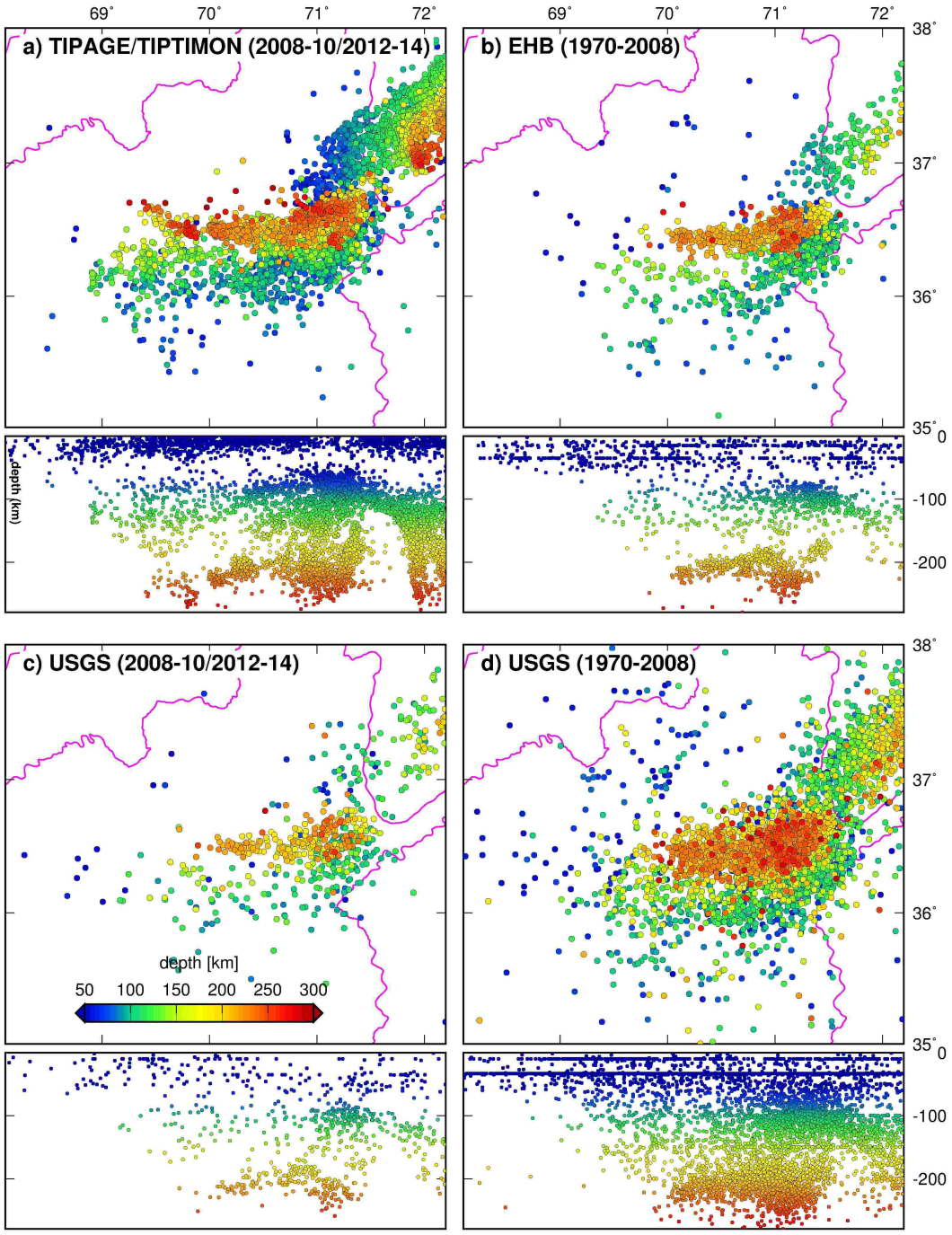

Figure E5: Comparison between different earthquake catalogs (*top* - map view, political boundaries plotted in pink; *bottom* - a west-east striking cross section). **a)** This study. **b)** All events listed in the global EHB bulletin (Engdahl et al., 1998). **c/d)** Events listed in the USGS catalog (USGS, 2016) during the time of the temporary deployments used here and during the same time period as the EHB catalog. The horizontal event clusters in the global catalogs indicate that the depth of these events could not be accurately constrained, thus it was set to a standard value.

Date	Location (lon/lat/depth)			M_w
(yyyy/mm/dd)	Local cat.	GEOFON	ISC	
2009/10/22	70.956/36.579/174.59	71.041/36.488/184.57	71.012/36.519/188.63	6.1
2009/10/29	70.711/36.396/206.84	70.760/36.340/212.59	70.768/36.382/213.93	6.2
2012/07/12	70.854/36.522/188.79	70.819/36.546/179.20	70.860/36.498/188.00	5.6
2012/07/12	70.863/36.514/189.34	70.928/36.503/191.99	70.872/36.511/197.20	4.6
2012/07/12	71.068/36.474/152.75	71.151/36.506/142.80	71.107/36.468/154.19	4.6
2012/09/12	71.376/36.685/185.79	71.458/36.733/169.96	71.391/36.688/186.70	4.9
2012/09/22	70.127/36.498/222.52	70.187/36.555/204.67	70.118/36.494/218.66	4.2
2013/02/05	70.627/36.510/211.08	70.700/36.539/198.85	70.704/36.474/212.00	4.6
2013/04/04	71.157/36.414/234.39	71.120/36.414/237.24	71.171/36.468/234.00	5.2
2013/05/20	70.351/36.500/206.22	70.540/36.536/192.45	70.440/36.491/207.40	4.7
2013/07/03	70.404/36.501/207.92	70.548/36.524/199.05	70.487/36.526/204.00	5.0
2013/07/29	70.498/36.499/200.71	70.735/36.514/185.63	70.544/36.501/206.90	4.9
2013/09/08	70.063/36.523/216.44	70.233/36.545/205.43	70.208/36.524/217.00	5.1
2013/10/13	70.688/36.397/205.90	70.762/36.444/199.75	not used	5.1
2013/11/02	71.052/36.611/209.34	71.127/36.666/195.39	71.119/36.642/211.00	4.6

Table E1: Hypocentral locations of the master events recorded during the time of the TIPTIMON/TIPAGE deployments used to deduce the station terms (*lon* and *lat* are longitude and latitude in degree, *depth* the event depth in km; the events are plotted in Fig. 7.3). The magnitude (M_w) was derived from waveform modeling in this study (*Local cat.*).

Time (yyyy-mm-dd (hh:mm:ss.ss)	Catalog location lon/lat depth	M_w	Relocated location	RMS (s)	No. phases	Gap (deg)	Difference lon/lat depth	Error lon/lat/depth/(no.) lon/lat/depth
2004-04-05 21:24:00.96	71.003/36.558 168.54	6.47	71.031/36.562 175.60	1.008	462	35	-0.028/-0.004/-7.06	0.009/0.021/0.98
2002-03-03 12:08:06.65	70.450/36.472 194.70	6.20	70.458/36.469 198.29	0.855	289	19	-0.008/0.003/-3.59	0.007/0.011/3.52
2002-03-03 12:08:18.00	70.517/36.496 208.90	7.34	70.430/36.516 212.77	1.071	93	33	0.087/-0.02/-3.87	0.02/0.022/1.815/(4) 0.013/0.018/3.715
1993-08-09 12:42:47.88	70.874/36.355 211.70	6.97	70.989/36.521 202.60	1.334	181	68	-0.115/-0.166/9.1	0.014/0.057/1.71/(2) 0.09/0.083/1.565
1985-07-29 07:54:44.52	70.901/36.208 101.90	7.38	70.835/36.213 111.04	1.137	105	49	0.066/-0.005/-9.14	0.011/0.049/1.514/(2) 0.041/0.073/34.43
1983-12-30 23:52:39.49	70.749/36.425 208.60	7.39	70.728/36.467 186.16	0.821	93	73	0.022/-0.042/22.44	0.024/0.053/1.709/(2) 0.024/0.059/3.13

Table E2: Relocated ISC events: *Catalog locations* are the event hypocenters as listed in the ISC catalog. *RMS* is the root mean square residual after event relocation, *No. phases* the number of phase picks used for the relocation, *Gap* the maximal azimuthal gap between these stations. Errors were estimated by relocating the *master events* of the local catalog using a similar station geometry as has been available for the aftershocks (*lon/lat/depth/(no.)*) and/or by varying the quality criteria for the station terms (*lon/lat/depth*). If the location errors were determined from the two different methods, the results are listed separately. For the first method, the number in brackets specifies the number of master events for which this procedure had been possible. In this case the error is the average difference between the hypocenter position of the relocated master event and its position in the local event catalog (see section 7.3.3 for further description). The big uncertainty of the 1985-earthquake in one test occurs because too few stations were left for relocation after restricting the quality criteria for the station terms.

Date time yyyy-mm-dd hh:mm	Catalog location lon/lat/depth	Mag.	Relocated location	RMS (s)	No. ph.	Gap (deg)	Difference lon/lat/depth	Error lon/lat/depth/(no.)
2015-11-08 15:37	70.412/36.577/179.44	3.76	70.421/36.484/197.51	0.630	25	76	-0.009/0.093/-18.07	0.016/0.010/1.97/(3)
2015-11-01 15:49	70.413/36.595/182.02	3.95	70.385/36.499/202.99	0.489	20	100	0.028/0.096/-20.97	0.046/0.021/0.85/(3)
2015-11-01 12:50	70.562/36.489/201.89	4.50	70.521/36.459/207.68	0.528	95	53	0.041/0.030/-05.79	-
2015-11-01 03:26	70.567/36.578/176.82	4.23	70.551/36.474/195.16	0.448	28	86	0.016/0.104/-18.35	0.038/0.010/1.66/(5)
2015-10-31 20:52	70.400/36.567/172.67	4.20	70.383/36.501/180.69	0.612	19	88	0.017/0.066/-08.02	0.015/0.020/1.96/(8)
2015-10-28 23:26	70.433/36.550/182.63	3.89	70.394/36.464/199.08	0.603	34	89	0.039/0.086/-16.45	0.042/0.011/2.44/(5)
2015-10-28 15:29	70.313/36.648/167.18	3.56	70.339/36.511/190.08	0.465	15	124	-0.026/0.138/-22.90	0.033/0.020/3.61/(7)
2015-10-28 10:04	70.431/36.595/179.20	4.08	70.409/36.494/199.08	0.649	22	91	0.022/0.102/-19.88	0.032/0.023/3.48/(5)
2015-10-28 00:04	70.401/36.550/192.13	3.44	70.325/36.521/204.16	0.526	18	72	0.076/0.030/-12.03	0.026/0.019/2.47/(6)
2015-10-27 17:55	70.450/36.573/179.70	3.97	70.409/36.479/197.51	0.481	33	76	0.041/0.094/-17.81	0.030/0.010/3.10/(2)
2015-10-27 13:14	70.633/36.543/192.22	4.59	70.530/36.491/201.03	0.506	81	52	0.103/0.052/-08.82	-
2015-10-27 01:17	70.387/36.553/188.33	4.42	70.327/36.506/195.56	0.341	16	115	0.059/0.048/-07.22	0.021/0.017/1.65/(8)
2015-10-26 23:35	70.492/36.617/161.58	3.68	70.433/36.499/192.03	0.543	18	122	0.059/0.119/-30.45	0.025/0.018/2.78/(6)
2015-10-26 19:35	70.417/36.536/190.52	3.85	70.317/36.506/198.69	0.516	11	93	0.100/0.030/-08.17	0.004/0.026/3.08/(7)
2015-10-26 16:47	70.422/36.546/187.56	3.28	70.435/36.545/183.03	0.444	10	122	-0.012/0.001/ 04.53	0.019/0.026/3.09/(8)
2015-10-26 15:47	70.428/36.530/205.68	3.75	70.337/36.506/198.69	0.336	12	124	0.091/0.024/ 07.00	0.020/0.022/4.40/(9)
2015-10-26 15:39	70.392/36.598/172.79	3.68	70.383/36.540/186.95	0.434	12	119	0.009/0.057/-14.16	0.032/0.033/1.28/(3)
2015-10-26 11:16	70.484/36.568/180.92	4.49	70.408/36.501/194.77	0.623	43	70	0.076/0.067/-13.85	0.046/0.012/3.23/(5)
2015-10-26 11:14	70.423/36.542/202.03	3.41	70.400/36.496/190.86	0.520	10	193	0.022/0.046/ 11.17	0.021/0.006/5.25/(6)
2015-10-26 09:49	70.575/36.522/190.19	4.76	70.443/36.499/193.60	0.723	87	64	0.132/0.024/-03.41	0.038/0.029/1.71/(1)
2015-10-26 09:48	70.506/36.577/177.11	4.72	70.511/36.503/192.03	0.817	32	85	-0.005/0.074/-14.93	0.031/0.011/4.01/(5)
2015-10-26 09:09	70.819/36.371/209.53	**7.46**	70.717/36.419/203.97	0.512	394	32	0.101/-0.048/ 05.57	0.008/0.011/0.20
2004-04-05 21:24	71.033/36.530/181.81	6.61	71.017/36.513/174.82	0.443	102	36	0.016/0.017/ 07.00	0.008/0.017/2.74

Table E3: Relocated GEOFON events. *Catalog location* refers to the hypocenter coordinates from the manually revisited *quakeML* files as received from GEOFON. *Time* refers to the event time listed in the global catalog. Magnitudes are M_w for the two large events and m_b for the aftershocks. All other headings as in Table E2. For two events (-) none of the master events could be used to assess the location uncertainty (see Section 7.3.3 for a detailed description regarding the error estimates).

Bibliography

Abdrakhmatov, K. Y., Aldazhanov, S., Hager, B., Hamburger, M., Herring, T., Kalabaev, K., Makarov, V., Molnar, P., Panasyuk, S., Prilepin, M., et al. (1996). Relatively recent construction of the Tien Shan inferred from GPS measurements of present-day crustal deformation rates. *Nature*, 384:450–453.

Aitchison, J. C., Ali, J. R., and Davis, A. M. (2007). When and where did India and Asia collide? *Journal of Geophysical Research: Solid Earth*, 112(B5):1–19.

Aki, K., Christoffersson, A., and Husebye, E. S. (1977). Determination of the three-dimensional seismic structure of the lithosphere. *Journal of Geophysical Research*, 82(2):277–296.

Aki, K. and Richards, P. G. (1980). *Quantitative Seismology: Theory and Methods*. W. H. Freeman, New York, 932 pp.

Ali, J. R. and Aitchison, J. C. (2005). Greater India. *Earth-Science Reviews*, 72(3):169–188.

Allegre, C. J., Courtillot, V., Tapponnier, P., Hirn, A., Mattauer, M., Coulon, C., Jaeger, J. J., Achache, J., Schärer, U., Marcoux, J., et al. (1984). Structure and evolution of the Himalaya–Tibet orogenic belt. *Nature*, 307:17–22.

Allen, M., Windley, B., and Zhang, C. (1993). Palaeozoic collisional tectonics and magmatism of the Chinese Tien Shan, central Asia. *Tectonophysics*, 220(1):89–115.

Ambraseys, N. and Bilham, R. (2003). Earthquakes in Afghanistan. *Seismological Research Letters*, 74(2):107–123.

Argand, E. (1924). La tectonique de l'Asie. In *Proceedings of the 13th International Geological Congess*, pages 171–372.

Arzhannikova, A., Arzhannikov, S., Jolivet, M., Vassallo, R., and Chauvet, A. (2011). Pliocene to Quaternary deformation in South East Sayan (Siberia): Initiation of the Tertiary compressive phase in the southern termination of the Baikal Rift System. *Journal of Asian Earth Sciences*, 40(2):581–594.

Auden, J. B. (1974). Afghanistan-West Pakistan. *Geological Society, London, Special Publications*, 4(1):235–253.

Austrheim, H. (1987). Eclogitization of lower crustal granulites by fluid migration through shear zones. *Earth and Planetary Science Letters*, 81(2):221–232.

Austrheim, H., Erambert, M., and Boundy, T. M. (1996). Garnets recording deep crustal earthquakes. *Earth and Planetary Science Letters*, 139(1):223–238.

Avouac, J.-P. and Tapponnier, P. (1993). Kinematic model of active deformation in central Asia. *Geophysical Research Letters*, 20(10):895–898.

Avouac, J.-P., Tapponnier, P., Bai, M., You, H., and Wang, G. (1993). Active thrusting and folding along the northern Tien Shan and late Cenozoic rotation of the Tarim relative to Dzungaria and Kazakhstan. *Journal of Geophysical Research: Solid Earth*, 98(B4):6755–6804.

Bai, L. and Zhang, T. (2015). Complex deformation pattern of the Pamir–Hindu Kush region inferred from multi-scale double-difference earthquake relocations. *Tectonophysics*, 638:177–184.

Bazhenov, M. and Burtman, V. S. (1990). Structural arcs of the alpine belt: Carpathians-Caucasus-Pamir. *Academy of Sciences Press, Moscow (in Russian)*.

Bazhenov, M. L., Perroud, H., Chauvin, A., Burtman, V. S., and Thomas, J.-C. (1994). Paleomagnetism of Cretaceous red beds from Tadzhikistan and Cenozoic deformation due to India-Eurasia collision. *Earth and Planetary Science Letters*, 124(1):1–18.

Bensen, G., Ritzwoller, M., Barmin, M., Levshin, A., Lin, F., Moschetti, M., Shapiro, N., and Yang, Y. (2007). Processing seismic ambient noise data to obtain reliable broad-band surface wave dispersion measurements. *Geophysical Journal International*, 169(3):1239–1260.

Beyreuther, M., Barsch, R., Krischer, L., Megies, T., Behr, Y., and Wassermann, J. (2010). ObsPy: A Python toolbox for seismology. *Seismological Research Letters*, 81(3):530–533.

Bezada, M., Faccenda, M., Toomey, D., and Humphreys, E. (2014). Why Ignoring Anisotropy When Imaging Subduction Zones Could be a Bad Idea. In *AGU Fall Meeting Abstracts*, number S41D-04.

Bianchi, M., Heit, B., Jakovlev, A., Yuan, X., Kay, S., Sandvol, E., Alonso, R., Coira, B., Brown, L., Kind, R., et al. (2013). Teleseismic tomography of the southern Puna plateau in Argentina and adjacent regions. *Tectonophysics*, 586:65–83.

Bijwaard, H., Spakman, W., and Engdahl, E. R. (1998). Closing the gap between regional and global travel time tomography. *Journal of Geophysical Research: Solid Earth*, 103(B12):30,055–30,078.

Billington, S., Isacks, B. L., and Barazangi, M. (1977). Spatial distribution and focal mechanisms of mantle earthquakes in the Hindu Kush–Pamir region: A contorted Benioff zone. *Geology*, 5(11):699–704.

Bird, P. (1979). Continental delamination and the Colorado Plateau. *Journal of Geophysical Research: Solid Earth*, 84(B13):7561–7571.

Boulin, J. (1981). Afghanistan structure, Greater India concept and eastern Tethys evolution. *Tectonophysics*, 72(3):261–287.

Boulin, J. (1988). Hercynian and Eocimmerian events in Afghanistan and adjoining regions. *Tectonophysics*, 148(3):253–278.

Boulin, J. (1991). Structures in Southwest Asia and evolution of the eastern Tethys. *Tectonophysics*, 196(3):211–268.

Boyd, O. S., Mueller, C. S., and Rukstales, K. S. (2007). Preliminary Earthquake Hazard Map of Afghanistan. *US Geological Survey Open-File Report*, 2007–1137(156).

Braeck, S. and Podladchikov, Y. (2007). Spontaneous thermal runaway as an ultimate failure mechanism of materials. *Physical Review Letters*, 98(9):095504.

Brookfield, M. E. and Hashmat, A. (2001). The geology and petroleum potential of the North Afghan platform and adjacent areas (northern Afghanistan, with parts of southern Turkmenistan, Uzbekistan and Tajikistan). *Earth-Science Reviews*, 55(1):41–71.

Brune, J. N. (1968). Seismic moment, seismicity, and rate of slip along major fault zones. *Journal of Geophysical Research*, 73(2):777–784.

Burov, E. and Yamato, P. (2008). Continental plate collision, P–T–t–z conditions and unstable vs. stable plate dynamics: insights from thermo-mechanical modelling. *Lithos*, 103(1):178–204.

Burtman, V. S. (1975). Structural geology of variscan Tien Shan, USSR. *American Journal of Science*, 275(A):157–186.

Burtman, V. S. and Molnar, P. H. (1993). Geological and geophysical evidence for deep subduction of continental crust beneath the Pamir. *GSA Special Papers*, 281:1–76.

Cai, F., Ding, L., and Yue, Y. (2011). Provenance analysis of upper Cretaceous strata in the Tethys Himalaya, southern Tibet: implications for timing of India–Asia collision. *Earth and Planetary Science Letters*, 305(1):195–206.

Cao, K., Bernet, M., Wang, G.-C., van der Beek, P., Wang, A., Zhang, K.-X., and Enkelmann, E. (2013). Focused Pliocene–Quaternary exhumation of the Eastern Pamir domes, western China. *Earth and Planetary Science Letters*, 363:16–26.

Capitanio, F. A. and Replumaz, A. (2013). Subduction and slab breakoff controls on Asian indentation tectonics and Himalayan western syntaxis formation. *Geochemistry, Geophysics, Geosystems*, 14(9):3515–3531.

Carrapa, B., DeCelles, P. G., Wang, X., Clementz, M. T., Mancin, N., Stoica, M., Kraatz, B., Meng, J., Abdulov, S., and Chen, F. (2015). Tectono-climatic implications of Eocene Paratethys regression in the Tajik basin of central Asia. *Earth and Planetary Science Letters*, 424:168–178.

Chang, C. and Zheng, S.-L. (1973). Tectonic features of the Mount Jolmo Lungma region in southern Tibet, China. *Scientia Geologica Sinica*, 1:1–12.

Chatelain, J.-L., Roecker, S., Hatzfeld, D., and Molnar, P. (1980). Microearthquake seismicity and fault plane solutions in the Hindu Kush region and their tectonic implications. *Journal of Geophysical Research: Solid Earth*, 85(B3):1365–1387.

Chemenda, A. I., Burg, J.-P., and Mattauer, M. (2000). Evolutionary model of the Himalaya–Tibet system: geopoem: based on new modelling, geological and geophysical data. *Earth and Planetary Science Letters*, 174(3):397–409.

Chen, W.-P. and Molnar, P. (1981). Constraints on the seismic wave velocity structure beneath the Tibetan Plateau and their tectonic implications. *Journal of Geophysical Research: Solid Earth*, 86(B7):5937–5962.

Chopin, C. (1984). Coesite and pure pyrope in high-grade blueschists of the Western Alps: a first record and some consequences. *Contributions to Mineralogy and Petrology*, 86(2):107–118.

Christensen, N. I. and Mooney, W. D. (1995). Seismic velocity structure and composition of the continental crust: A global view. *Journal of Geophysical Research: Solid Earth*, 100(B6):9761–9788.

Cloos, M. (1993). Lithospheric buoyancy and collisional orogenesis: Subduction of oceanic plateaus, continental margins, island arcs, spreading ridges, and seamounts. *Geological Society of America Bulletin*, 105(6):715–737.

Copley, A., Avouac, J.-P., and Royer, J.-Y. (2010). India-Asia collision and the Cenozoic slowdown of the Indian plate: Implications for the forces driving plate motions. *Journal of Geophysical Research: Solid Earth*, 115(B3).

Coutand, I., Strecker, M., Arrowsmith, J., Hilley, G., Thiede, R., Korjenkov, A., and Omuraliev, M. (2002). Late Cenozoic tectonic development of the intramontane Alai Valley, (Pamir-Tien Shan region, central Asia): An example of intracontinental deformation due to the Indo-Eurasia collision. *Tectonics*, 21(6).

Coward, M., Gillcrist, R., and Trudgill, B. (1991). Extensional structures and their tectonic inversion in the Western Alps. *Geological Society, London, Special Publications*, 56(1):93–112.

Cowgill, E. (2010). Cenozoic right-slip faulting along the eastern margin of the Pamir salient, northwestern China. *Geological Society of America Bulletin*, 122(1-2):145–161.

Cox, A. and Hart, R. B. (2009). *Plate tectonics: how it works*. Blackwell Scientific Publications, Oxford, 392 pp.

Cunningham, D. (2005). Active intracontinental transpressional mountain building in the Mongolian Altai: defining a new class of orogen. *Earth and Planetary Science Letters*, 240(2):436–444.

De Lapparent, A. (1972). L'Afghanistan et la dérive du continent indien. *Rev. Géogr. Phys. Géol. Dyn. (in French*, 14(4):449–455.

DeCelles, P. G., Robinson, D. M., and Zandt, G. (2002). Implications of shortening in the Himalayan fold-thrust belt for uplift of the Tibetan Plateau. *Tectonics*, 21(6):12–1–12–25.

DeMets, C., Gordon, R. G., and Argus, D. F. (2010). Geologically current plate motions. *Geophysical Journal International*, 181(1):1–80.

Docherty, C. and Banda, E. (1995). Evidence for the eastward migration of the Alboran Sea based on regional subsidence analysis: a case for basin formation by delamination of the subcrustal lithosphere? *Tectonics*, 14(4):804–818.

Duretz, T. and Gerya, T. V. (2013). Slab detachment during continental collision: Influence of crustal rheology and interaction with lithospheric delamination. *Tectonophysics*, 602:124–140.

Duretz, T., Gerya, T. V., and May, D. A. (2011). Numerical modelling of spontaneous slab breakoff and subsequent topographic response. *Tectonophysics*, 502(1):244–256.

Duretz, T., Schmalholz, S., and Gerya, T. V. (2012). Dynamics of slab detachment. *Geochemistry, Geophysics, Geosystems*, 13(3).

Dziewoński, A. M. and Anderson, D. L. (1981). Preliminary reference Earth model. *Physics of the Earth and Planetary Interiors*, 25(4):297–356.

Dziewoński, A. M., Chou, T.-A., and Woodhouse, J. (1981). Determination of earthquake source parameters from waveform data for studies of global and regional seismicity. *Journal of Geophysical Research: Solid Earth*, 86(B4):2,825–2,852.

Eberhart-Phillips, D. (1993). Local earthquake tomography: earthquake source regions. In *Seismic Tomography: Theory and Practice*. Edited by H. Iyer and K. Hirahara, Chapman and Hall, London, pp. 614–643.

Ekström, G., Nettles, M., and Dziewoński, A. M. (2012). The global CMT project 2004–2010: centroid-moment tensors for 13,017 earthquakes. *Physics of the Earth and Planetary Interiors*, 200:1–9.

Engdahl, E. R., van der Hilst, R., and Buland, R. (1998). Global teleseismic earthquake relocation with improved travel times and procedures for depth determination. *Bulletin of the Seismological Society of America*, 88(3):722–743.

Evans, J. R., Eberhart-Phillips, D., and Thurber, C. (1994). User's manual for simulps12 for imaging vp and vp/vs; a derivative of the "Thurber" tomographic inversion simul3 for local earthquakes and explosions. Technical report, Open File Report 94–431, US Geological Survey.

Faccenda, M., Gerya, T. V., Mancktelow, N. S., and Moresi, L. (2012). Fluid flow during slab unbending and dehydration: Implications for intermediate-depth seismicity, slab weakening and deep water recycling. *Geochemistry, Geophysics, Geosystems*, 13(1).

Fan, G., Ni, J. F., and Wallace, T. C. (1994). Active tectonics of the Pamirs and Karakorum. *Journal of Geophysical Research: Solid Earth*, 99(B4):7131–7160.

Faryad, S. W., Collett, S., Petterson, M., and Sergeev, S. A. (2013). Magmatism and metamorphism linked to the accretion of continental blocks south of the Hindu Kush, Afghanistan. *Lithos*, 175:302–314.

Feld, C., Haberland, C., Schurr, B., Sippl, C., Wetzel, H.-U., Roessner, S., Ickrath, M., Abdybachaev, U., and Orunbaev, S. (2015). Seismotectonic study of the Fergana Region (Southern Kyrgyzstan): distribution and kinematics of local seismicity. *Earth, Planets and Space*, 67(1):1–13.

Finlayson, D., Collins, C., and Prodehl, C. (1979). Explosion seismic profiles, and implications for crustal evolution, in southeastern Australia. *Austr. Government Publ. Service*, 4:243–252.

Frohlich, C. (2006). *Deep earthquakes*. Cambridge University Press, New York, 573 pp.

Gagala, L. (2014). *Structural geometry and kinematics of the Tajik Depression, Central Asia: Neogene basin inversion in front of the Pamir salient*. Doctoral thesis, TU Bergakademie Freiberg, Germany, 161pp.

Gaina, C., Hinsbergen, D. J., and Spakman, W. (2015). Tectonic interactions between India and Arabia since the Jurassic reconstructed from marine geophysics, ophiolite geology, and seismic tomography. *Tectonics*, 34(5):875–906.

Gaina, C., Müller, R. D., Brown, B., Ishihara, T., and Ivanov, S. (2007). Breakup and early seafloor spreading between India and Antarctica. *Geophysical Journal International*, 170(1):151–169.

Gansser, A. (1964). *Geology of the Himalayas*. Wiley, New York, 289 pp.

Garzanti, E., Le Fort, P., and Sciunnach, D. (1999). First report of Lower Permian basalts in South Tibet: tholeiitic magmatism during break-up and incipient opening of Neotethys. *Journal of Asian Earth Sciences*, 17(4):533–546.

GEOFON (2016). *On-line Bulletin*. GFZ German Research Centre for Geosciences, Potsdam, Germany. http://geofon.gfz-potsdam.de/.

Gerya, T. V., Yuen, D. A., and Maresch, W. V. (2004). Thermomechanical modelling of slab detachment. *Earth and Planetary Science Letters*, 226(1):101–116.

Girardeau, J., Marcoux, J., and Montenat, C. (1989). The Neo-Cimmerian ophiolite belt in Afghanistan and Tibet: comparison and evolution. In *Tectonic Evolution of the Tethyan Region*, pages 477–504. Springer.

Gordon, S., Luffi, P., Hacker, B., Valley, J., Spicuzza, M., Kozdon, R., Kelemen, P., Ratshbacher, L., and Minaev, V. (2012). The thermal structure of continental crust in active orogens: insight from Miocene eclogite and granulite xenoliths of the Pamir Mountains. *Journal of Metamorphic Geology*, 30(4):413–434.

Green, H. W. and Houston, H. (1995). The mechanics of deep earthquakes. *Annual Review of Earth and Planetary Sciences*, 23:169–214.

Gubin, I. (1960). Patterns of Seismic Events in the Territory of Tajikistan. *464, Akad. Nauk SSSR (in Russian)*.

Guillot, S., Garzanti, E., Baratoux, D., Marquer, D., Mahéo, G., and De Sigoyer, J. (2003). Reconstructing the total shortening history of the NW Himalaya. *Geochemistry, Geophysics, Geosystems*, 4(7).

Gung, Y., Panning, M., and Romanowicz, B. (2003). Global anisotropy and the thickness of continents. *Nature*, 422(6933):707–711.

Haberland, C., Rietbrock, A., Lange, D., Bataille, K., and Dahm, T. (2009). Structure of the seismogenic zone of the southcentral Chilean margin revealed by local earthquake traveltime tomography. *Journal of Geophysical Research: Solid Earth*, 114(B1).

Hacker, B., Kelemen, P. B., and Behn, M. D. (2011). Differentiation of the continental crust by relamination. *Earth and Planetary Science Letters*, 307(3):501–516.

Hacker, B., Luffi, P., Lutkov, V., Minaev, V., Ratschbacher, L., Plank, T., Ducea, M., Patiño-Douce, A., McWilliams, M., and Metcalf, J. (2005). Near-ultrahigh pressure processing of continental crust: Miocene crustal xenoliths from the Pamir. *Journal of Petrology*, 46(8):1661–1687.

Hacker, B., Peacock, S. M., Abers, G. A., and Holloway, S. D. (2003). Subduction factory 2. Are intermediate-depth earthquakes in subducting slabs linked to metamorphic dehydration reactions? *Journal of Geophysical Research: Solid Earth*, 108(B1).

Hamburger, M. W., Sarewitz, D. R., Pavlis, G. L., and Popandopulo, G. A. (1992). Structural and seismic evidence for intracontinental subduction in the Peter the First Range, central Asia. *Geological Society of America Bulletin*, 104(4):397–408.

Han, B.-F., He, G.-Q., Wang, X.-C., and Guo, Z.-J. (2011). Late Carboniferous collision between the Tarim and Kazakhstan–Yili terranes in the western segment of the South Tian Shan Orogen, Central Asia, and implications for the Northern Xinjiang, western China. *Earth-Science Reviews*, 109(3):74–93.

Hansen, S. M., Dueker, K., and Schmandt, B. (2015). Thermal classification of lithospheric discontinuities beneath USArray. *Earth and Planetary Science Letters*, 431:36–47.

Hardebeck, J. L. and Shearer, P. M. (2002). A new method for determining first-motion focal mechanisms. *Bulletin of the Seismological Society of America*, 92(6):2264–2276.

Hatzfeld, D. and Molnar, P. (2010). Comparisons of the kinematics and deep structures of the Zagros and Himalaya and of the Iranian and Tibetan plateaus and geodynamic implications. *Reviews of Geophysics*, 48(2).

Hendrix, M. S., Dumitru, T. A., and Graham, S. A. (1994). Late Oligocene-early Miocene unroofing in the Chinese Tian Shan: An early effect of the India-Asia collision. *Geology*, 22(6):487–490.

Hetényi, G., Cattin, R., Brunet, F., Bollinger, L., Vergne, J., Nábělek, J. L., and Diament, M. (2007). Density distribution of the India plate beneath the Tibetan plateau: geophysical and petrological constraints on the kinetics of lower-crustal eclogitization. *Earth and Planetary Science Letters*, 264(1):226–244.

Hildebrand, P., Noble, S., Searle, M. P., Waters, D., and Parrish, R. (2001). Old origin for an active mountain range: Geology and geochronology of the eastern Hindu Kush, Pakistan. *Geological Society of America Bulletin*, 113(5):625–639.

Hildebrand, P. R., Searle, M. P., Khan, Z., Van Heijst, H. J., et al. (2000). Geological evolution of the Hindu Kush, NW Frontier Pakistan: active margin to continent-continent collision zone. *Geological Society, London, Special Publications*, 170(1):277–293.

Hodges, K. V. (2000). Tectonics of the Himalaya and southern Tibet from two perspectives. *Geological Society of America Bulletin*, 112(3):324–350.

Holt, W. E. (1995). Flow fields within the Tonga slab determined from the moment tensors of deep earthquakes. *Geophysical Research Letters*, 22(8):989–992.

Holt, W. E. and Wallace, T. C. (1990). Crustal thickness and upper mantle velocities in the Tibetan Plateau region from the inversion of regional Pnl waveforms: Evidence for a thick upper mantle lid beneath southern Tibet. *Journal of Geophysical Research: Solid Earth*, 95(B8):12499–12525.

Hopper, E. and Fischer, K. M. (2015). The meaning of midlithospheric discontinuities: A case study in the northern US craton. *Geochemistry, Geophysics, Geosystems*, 16(12):4057–4083.

Houseman, G. A., McKenzie, D. P., and Molnar, P. (1981). Convective instability of a thickened boundary layer and its relevance for the thermal evolution of continental convergent belts. *Journal of Geophysical Research: Solid Earth*, 86(B7):6115–6132.

Hutton, L. and Boore, D. M. (1987). The ML scale in southern California. *Bulletin of the Seismological Society of America*, 77(6):2074–2094.

Isacks, B., Oliver, J., and Sykes, L. R. (1968). Seismology and the new global tectonics. *Journal of Geophysical Research*, 73(18):5855–5899.

ISC (2013). *On-line Bulletin*. Int. Seis. Cent., Thatcham, United Kingdom. http://www.isc.ac.uk.

Ischuk, A., Bendick, R., Rybin, A., Molnar, P., Khan, S. F., Kuzikov, S., Mohadjer, S., Saydullaev, U., Ilyasova, Z., Schelochkov, G., et al. (2013). Kinematics of the Pamir and Hindu Kush regions from GPS geodesy. *Journal of Geophysical Research: Solid Earth*, 118(5):2408–2416.

Ismail-Zadeh, A., Matenco, L., Radulian, M., Cloetingh, S., and Panza, G. (2012). Geodynamics and intermediate-depth seismicity in Vrancea (the south-eastern Carpathians): Current state-of-the art. *Tectonophysics*, 530:50–79.

Jaeger, J.-J., Courtillot, V., and Tapponnier, P. (1989). Paleontological view of the ages of the Deccan Traps, the Cretaceous/Tertiary boundary, and the India-Asia collision. *Geology*, 17(4):316–319.

Jakovlev, A. (2009). *The crustal and upper mantle isotropic and anisotropic velocity structure beneath the Rwenzori Mountains from travel-time tomograph*. Doctoral thesis, Goethe Universität, Frankfurt am Main, Germany, 101 pp.

John, T., Medvedev, S., Rüpke, L. H., Andersen, T. B., Podladchikov, Y. Y., and Austrheim, H. (2009). Generation of intermediate-depth earthquakes by self-localizing thermal runaway. *Nature Geoscience*, 2(2):137–140.

Karagianni, I., Papazachos, C., Scordilis, E., and Karakaisis, G. (2015). Reviewing the active stress field in Central Asia by using a modified stress tensor approach. *Journal of Seismology*, 19(2):541–565.

Käßner, A., Ratschbacher, L., Pfänder, J., Hacker, B., Sonntag, B.-L., Khan, J., Stanek, K., Zack, G., Gadoev, M., and Oimahmadoc, I. (2016). Proterozoic-Mesozoic history of the Central Asian Orogenic Belt in the Tajik-Kyrgyz Tian Shan: U-Pb, 40Ar-39Ar, fission-track geochronology, and geochemistry of granitoids. *Submitted to The Geological Society of America Bulletin*.

Kaz'min, V. G., Lobkovsky, L. I., and Tikhonova, N. F. (2010). Late Cretaceous-Paleogene Deepwater Basin of North Afghanistan and the Central Pamirs: Issue of Hindu Kush Earthquakes. *Geotectonics*, 44(2):127–138.

Kelemen, P. B. and Hirth, G. (2007). A periodic shear-heating mechanism for intermediate-depth earthquakes in the mantle. *Nature*, 446(7137):787–790.

Kennett, B., Engdahl, E., and Buland, R. (1995). Constraints on seismic velocities in the Earth from traveltimes. *Geophysical Journal International*, 122(1):108–124.

Khan, S. D., Walker, D. J., Hall, S. A., Burke, K. C., Shah, M. T., and Stockli, L. (2009). Did the Kohistan-Ladakh island arc collide first with India? *Geological Society of America Bulletin*, 121(3-4):366–384.

Kilb, D. and Hardebeck, J. L. (2006). Fault parameter constraints using relocated earthquakes: a validation of first-motion focal-mechanism data. *Bulletin of the Seismological Society of America*, 96(3):1140–1158.

Kind, R. and Yuan, X. (2010). Seismic images of the biggest crash on Earth. *Science*, 329(5998):1479–1480.

Kirby, S. H., Stein, S., Okal, E. A., and Rubie, D. C. (1996). Metastable mantle phase transformations and deep earthquakes in subducting oceanic lithosphere. *Reviews of Geophysics*, 34(2):261–306.

Kissling, E., Ellsworth, W., Eberhart-Phillips, D., and Kradolfer, U. (1994). Initial reference models in local earthquake tomography. *Journal of Geophysical Research*, 99(B10):19,635–19,646.

Klocke, M., Voigt, T., Kley, J., Pfeifer, S., Rocktäschel, T., Keil, S., and Gaupp, R. (2015). Cenozoic evolution of the Pamir and Tien Shan mountains reflected in syntectonic deposits of the Tajik Basin. *Geological Society, London, Special Publications*, 427:SP427–7.

Klootwijk, C. T., Gee, J. S., Peirce, J. W., Smith, G. M., and McFadden, P. L. (1992). An early India-Asia contact: paleomagnetic constraints from Ninetyeast ridge, ODP Leg 121. *Geology*, 20(5):395–398.

Kohn, M. J. and Parkinson, C. D. (2002). Petrologic case for Eocene slab breakoff during the Indo-Asian collision. *Geology*, 30(7):591–594.

Kostrov, V. (1974). Seismic moment and energy of earthquakes, and seismic flow of rock. *Physics of the Solid Earth*, 1:13–21.

Koulakov, I. (2009). LOTOS code for local earthquake tomographic inversion: Benchmarks for testing tomographic algorithms. *Bulletin of the Seismological Society of America*, 99(1):194–214.

Koulakov, I. (2011). High-frequency P and S velocity anomalies in the upper mantle beneath Asia from inversion of worldwide traveltime data. *Journal of Geophysical Research*, 116(B4):1–22.

Koulakov, I. and Sobolev, S. (2006). A tomographic image of Indian lithosphere break-off beneath the Pamir–Hindukush region. *Geophysical Journal International*, 164(2):425–440.

Krumsiek, K. (1976). Zur Bewegung der iranisch-afghanischen Platte. *Geologische Rundschau*, 65(1):909–929.

Krystopowicz, N. J. and Currie, C. A. (2013). Crustal eclogitization and lithosphere delamination in orogens. *Earth and Planetary Science Letters*, 361:195–207.

Kuchai, V. and Trifonov, V. (1977). Young left-lateral strike slip along the zone of the Darvaz-Karakul Fault. *Geotektonika*, 3:91–105.

Kufner, S.-K., Schurr, B., Sippl, C., Yuan, X., Ratschbacher, L., s/of Mohammad Akbar, A., Ischuk, A., Murodkulov, S., Schneider, F. M., Mechie, J., and Tilmann, F. (2016). Deep India meets deep Asia: Lithospheric indentation, delamination and break-off under Pamir and Hindu Kush (Central Asia). *Earth and Planetary Science Letters*, 435:171–184.

Kulikova, G. (2016). *Source parameters of the major historical earthquakes in the Tien-Shan region from the late 19th to the early 20th century.* Doctoral thesis, University of Potsdam, Germany, 164 pp.

Kulikova, G., Schurr, B., Krüger, F., Brzoska, E., and Heimann, S. (2016). Source parameters of the Sarez-Pamir earthquake of 1911 February 18. *Geophysical Journal International*, 205(2):1086–1098.

Kumar, P., Yuan, X., Kumar, M. R., Kind, R., Li, X., and Chadha, R. (2007). The rapid drift of the Indian tectonic plate. *Nature*, 449(7164):894–897.

Labrousse, L., Prouteau, G., and Ganzhorn, A.-C. (2011). Continental exhumation triggered by partial melting at ultrahigh pressure. *Geology*, 39(12):1171–1174.

Lacassin, R., Valli, F., Arnaud, N., Leloup, P. H., Paquette, J. L., Haibing, L., Tapponnier, P., Chevalier, M.-L., Guillot, S., Maheo, G., et al. (2004). Large-scale geometry, offset and kinematic evolution of the Karakorum fault, Tibet. *Earth and Planetary Science Letters*, 219(3):255–269.

Laske, G., Masters, G., Ma, Z., and Pasyanos, M. (2013). Update on CRUST1. 0-A 1-degree global model of Earth's crust. In *Geophys. Res. Abstracts*, volume 15, page 2658.

Lay, T. and Wallace, T. C. (1995). *Modern global seismology*. Academic Press., San Diego, CA, 521 pp.

Lee, W. H. and Lahr, J. C. (1975). Hypo71 (revised): a computer program for determining hypocenter, magnitude, and first motion pattern of local earthquakes. Technical report, Open File Report 75-311, 1–113, US Geological Survey.

Leech, M. L., Singh, S., Jain, A., Klemperer, S. L., and Manickavasagam, R. (2005). The onset of India–Asia continental collision: early, steep subduction required by the timing of UHP metamorphism in the western Himalaya. *Earth and Planetary Science Letters*, 234(1):83–97.

Leith, W. and Alvarez, W. (1985). Structure of the Vakhsh fold-and-thrust belt, Tadjik SSR: Geologic mapping on a Landsat image base. *Geological Society of America Bulletin*, 96(7):875–885.

Leith, W. and Simpson, D. W. (1986a). Earthquakes related to active salt doming near Kulyab, Tadjikistan, USSR. *Geophysical Research Letters*, 13(10):1019–1022.

Leith, W. and Simpson, D. W. (1986b). Seismic domains within the Gissar-Kokshal Seismic Zone, soviet central Asia. *Journal of Geophysical Research: Solid Earth*, 91(B1):689–699.

Leven, E. J. (1981). The age of the Upper Paleozoic volcanic formations of the North Pamir: Izvestyia. *Akad. Nauk SSSR , Geological Series*, (9):137–140.

Li, C., van der Hilst, R. D., Meltzer, A. S., and Engdahl, E. R. (2008). Subduction of the Indian lithosphere beneath the Tibetan Plateau and Burma. *Earth and Planetary Science Letters*, 274(1):157–168.

Lister, G., Kennett, B., Richards, S., and Forster, M. (2008). Boudinage of a stretching slablet implicated in earthquakes beneath the Hindu Kush. *Nature Geoscience*, 1(3):196–201.

Lomax, A. (2008). The nonlinloc software guide. *ALomax Scientific, Mouans-Sartoux, France, http://alomax. free. fr/nlloc*.

Lomax, A., Virieux, J., Volant, P., and Berge-Thierry, C. (2000). Probabilistic earthquake location in 3D and layered models. In *Advances in seismic event location*, edited by C. Thurber and N. Rabinowitz, Kluwer, Amsterdam, pp. 101–134.

Lorinczi, P. and Houseman, G. (2009). Lithospheric gravitational instability beneath the Southeast Carpathians. *Tectonophysics*, 474(1):322–336.

Lukk, A. A. (2011). A layer of an unstable seismotectonic strain as an analog of a waveguide at depths of 12–20 km in the Earth's crust of the Tajik Depression. *Izvestiya, Physics of the Solid Earth*, 47(4):299–316.

Lukk, A. A., Yunga, S. L., Shevchenko, V. I., and Hamburger, M. W. (1995). Earthquake focal mechanisms, deformation state, and seismotectonics of the Pamir-Tien Shan region, Central Asia. *Journal of Geophysical Research: Solid Earth*, 100(B10):20321–20343.

Magni, V., Van Hunen, J., Funiciello, F., and Faccenna, C. (2012). Numerical models of slab migration in continental collision zones. *Solid Earth*, 3(2):293.

Mahéo, G., Blichert-Toft, J., Pin, C., Guillot, S., and Pêcher, A. (2009). Partial melting of mantle and crustal sources beneath South Karakorum, Pakistan: implications for the Miocene geodynamic evolution of the India–Asia convergence zone. *Journal of Petrology*, 50(3):427–449.

Mattauer, M. (1986). Intracontinental subduction, crust-mantle décollement and crustal-stacking wedge in the Himalayas and other collision belts. *Geological Society, London, Special Publications*, 19(1):37–50.

McKenzie, D. P. (1969). Speculations on the consequences and causes of plate motions. *Geophysical Journal International*, 18(1):1–32.

Mechie, J., Yuan, X., Schurr, B., Schneider, F. M., Sippl, C., Ratschbacher, L., Minaev, V., Gadoev, M., Oimahmadov, I., Abdybachaev, U., et al. (2012). Crustal and uppermost mantle velocity structure along a profile across the Pamir and southern Tien Shan as derived from project TIPAGE wide-angle seismic data. *Geophysical Journal International*, 188(2):385–407.

Mellors, R., Pavlis, G. L., Hamburger, M., Al-Shukri, H., and Lukk, A. A. (1995). Evidence for a high-velocity slab associated with the Hindu Kush seismic zone. *Journal of Geophysical Research: Solid Earth*, 100(B3):4067–4078.

Menke, W. (1984). The resolving power of cross-borehole tomography. *Geophysical Research Letters*, 11(2):105–108.

Metcalfe, I. (2002). Permian tectonic framework and palaeogeography of SE Asia. *Journal of Asian Earth Sciences*, 20(6):551–566.

Michael, A. J. (1987). Use of focal mechanisms to determine stress: a control study. *Journal of Geophysical Research: Solid Earth*, 92(B1):357–368.

Michelini, A. and McEvilly, T. (1991). Seismological studies at Parkfield. I. Simultaneous inversion for velocity structure and hypocenters using cubic B-splines parameterization. *Bulletin of the Seismological Society of America*, 81(2):524–552.

Mishra, D., Kumar, M. R., and Arora, K. (2012). Long wavelength satellite gravity and geoid anomalies over Himalaya, and Tibet: lithospheric structures and seismotectonics of deep focus earthquakes of Hindu Kush–Pamir and Burmese arc. *Journal of Asian Earth Sciences*, 48:93–110.

Mistiaen, B., Brice, D., Hubert, B., and Pinte, E. (2015). Devonian palaeobiogeographic affinities of Afghanistan and surrounding areas (Iran, Pakistan). *Journal of Asian Earth Sciences*, 102:102–126.

Mitra, S., Priestley, K., Gaur, V., Rai, S., and Haines, J. (2006). Variation of Rayleigh wave group velocity dispersion and seismic heterogeneity of the Indian crust and uppermost mantle. *Geophysical Journal International*, 164(1):88–98.

Mohadjer, S., Bendick, R., Ischuk, A., Kuzikov, S., Kostuk, A., Saydullaev, U., Lodi, S., Kakar, D., Wasy, A., Khan, M., et al. (2010). Partitioning of India-Eurasia convergence in the Pamir-Hindu Kush from GPS measurements. *Geophysical Research Letters*, 37(4).

Mohan, G. and Rai, S. (1995). Large-scale three-dimensional seismic tomography of the Zagros and Pamir-Hindukush regions. *Tectonophysics*, 242(3):255–265.

Molnar, P. and Gray, D. (1979). Subduction of continental lithosphere: Some constraints and uncertainties. *Geology*, 7(1):58–62.

Molnar, P. and Stock, J. M. (2009). Slowing of India's convergence with Eurasia since 20 Ma and its implications for Tibetan mantle dynamics. *Tectonics*, 28(3).

Molnar, P. and Tapponnier, P. (1975). Cenozoic tectonics of Asia: effects of a continental collision. *Science*, 189(4201):419–426.

Mooney, W. D., Prodehl, C., and Pavlenkova, N. (2002). Seismic velocity structure of the continental lithosphere from controlled source data. *International Geophysics Series*, 81(A):887–910.

Moores, E. and Twiss, R. (1995). *Tectonics*. WH Freeman, New York, 415 pp.

Müller, R. D. (2007). Earth science: An Indian cheetah. *Nature*, 449(7164):795–796.

Nábělek, J., Hetényi, G., Vergne, J., Sapkota, S., Kafle, B., Jiang, M., Su, H., Chen, J., Huang, B.-S., et al. (2009). Underplating in the Himalaya-Tibet collision zone revealed by the Hi-CLIMB experiment. *Science*, 325(5946):1371–1374.

Nábělek, J. and Xia, G. (1995). Momenttensor analysis using regional data: Application to the 25 March, 1993, Scotts Mills, Oregon, Earthquake. *Geophysical Research Letters*, 22(1):13–16.

Negredo, A. M., Replumaz, A., Villaseñor, A., and Guillot, S. (2007). Modeling the evolution of continental subduction processes in the Pamir–Hindu Kush region. *Earth and Planetary Science Letters*, 259(1):212–225.

Nikolaev, V. (2002). Afghan-Tajik depression: Architecture of sedimentary cover and evolution. *Russian Journal of Earth Sciences*, 4(6):399–421.

Oncescu, M. C., Marza, V. I., Rizescu, M., and Popa, M. (1999). The Romanian earthquake catalogue between 984–1997. In *Vrancea earthquakes: tectonics, hazard and risk mitigation*, pages 43–47. Springer.

Paige, C. C. and Saunders, M. A. (1982). LSQR: An algorithm for sparse linear equations and sparse least squares. *ACM Transactions on Mathematical Software (TOMS)*, 8(1):43–71.

Pashkov, B. and Budanov, V. (1988). On the northern geological boundary of the crystalline rock mass in the southwest Pamir. *Akad. Nauk SSSR*, 302(2):400–403.

Pashkov, B. and Budanov, V. (1990). The tectonics of the zone of intersection between the southeastern and southwestern Pamir. *Geotectonics*, 24:246–253.

Pasyanos, M. E. (2010). Lithospheric thickness modeled from long-period surface wave dispersion. *Tectonophysics*, 481(1):38–50.

Patriat, P. and Achache, J. (1984). India–Eurasia collision chronology has implications for crustal shortening and driving mechanism of plates. *Nature*, 311:615–621.

Pavlis, G. L. and Booker, J. R. (1980). The mixed discrete-continuous inverse problem: Application to the simultaneous determination of earthquake hypocenters and velocity structure. *Journal of Geophysical Research: Solid Earth*, 85(B9):4801–4810.

Pavlis, G. L. and Das, S. (2000). The Pamir-Hindu Kush seismic zone as a strain marker for flow in the upper mantle. *Tectonics*, 19(1):103–115.

Pegler, G. and Das, S. (1998). An enhanced image of the Pamir–Hindu Kush seismic zone from relocated earthquake hypocentres. *Geophysical Journal International*, 134(2):573–595.

Petterson, M. G. (2010). A review of the geology and tectonics of the Kohistan island arc, north Pakistan. *Geological Society, London, Special Publications*, 338(1):287–327.

Peyrat, S., Campos, J., De Chabalier, J., Perez, A., Bonvalot, S., Bouin, M.-P., Legrand, D., Nercessian, A., Charade, O., Patau, G., et al. (2006). Tarapacá intermediate-depth earthquake (mw 7.7, 2005, northern chile): A slab-pull event with horizontal fault plane constrained from seismologic and geodetic observations. *Geophysical research letters*, 33(22).

Pinheiro, L., Wilson, R., Pena dos Reis, R., Whitmarsh, R., and Ribeiro, A. (1996). The western Iberia margin: a geophysical and geological overview. In *Proceedings-Ocean Drilling Program Scientific Results*, pages 3–26. National science foundation.

Podvin, P. and Lecomte, I. (1991). Finite difference computation of traveltimes in very contrasted velocity models: a massively parallel approach and its associated tools. *Geophysical Journal International*, 105(1):271–284.

Poli, P., Prieto, G., Rivera, E., and Ruiz, S. (2016). Earthquakes initiation and thermal shear instability in the Hindu-Kush intermediate-depth nest. *Geophysical Research Letters*, 308:131–190.

Pospelov, I. (1987). Formations and Tectonic Evolution of the Late Variscides in the South Tien Shan and the North Pamir. In *Early Eugeosynclinal Formations and Structures, Nauka, Moscow (in Russian)*, pages 149–178.

Pozzi, J.-P. and Feinberg, H. (1991). Paleomagnetism in the Tajikistan: Continental shortening of European margin in the Pamirs during Indian Eurasian collision. *Earth and Planetary Science Letters*, 103(1):365–378.

Prévost, J. H. (1980). Mechanics of continuous porous media. *International Journal of Engineering Science*, 18(6):787–800.

Rader, E., Emry, E., Schmerr, N., Frost, D., Cheng, C., Menard, J., Yu, C.-Q., and Geist, D. (2015). Characterization and Petrological Constraints of the Midlithospheric Discontinuity. *Geochemistry, Geophysics, Geosystems*, 16(10):3484–3504.

Raleigh, C. and Paterson, M. (1965). Experimental deformation of serpentinite and its tectonic implications. *Journal of Geophysical Research*, 70(16):3965–3985.

Rawlinson, N. and Sambridge, M. (2003). Seismic traveltime tomography of the crust and lithosphere. *Advances in Geophysics*, 46:81–199.

Reigber, C., Michel, G., Galas, R., Angermann, D., Klotz, J., Chen, J., Papschev, A., Arslanov, R., Tzurkov, V., and Ishanov, M. (2001). New space geodetic constraints on the distribution of deformation in Central Asia. *Earth and Planetary Science Letters*, 191(1):157–165.

Replumaz, A., Capitanio, F. A., Guillot, S., Negredo, A. M., and Villaseñor, A. (2014). The coupling of Indian subduction and Asian continental tectonics. *Gondwana Research*, 26(2):608–626.

Replumaz, A., Kárason, H., van der Hilst, R. D., Besse, J., and Tapponnier, P. (2004). 4-D evolution of SE Asia's mantle from geological reconstructions and seismic tomography. *Earth and Planetary Science Letters*, 221(1):103–115.

Replumaz, A., Negredo, A. M., Guillot, S., and Villaseñor, A. (2010). Multiple episodes of continental subduction during India/Asia convergence: Insight from seismic tomography and tectonic reconstruction. *Tectonophysics*, 483(1):125–134.

Replumaz, A. and Tapponnier, P. (2003). Reconstruction of the deformed collision zone between India and Asia by backward motion of lithospheric blocks. *Journal of Geophysical Research: Solid Earth*, 108(B6).

Robinson, A. C., Ducea, M., and Lapen, T. J. (2012). Detrital zircon and isotopic constraints on the crustal architecture and tectonic evolution of the northeastern Pamir. *Tectonics*, 31(2).

Robinson, A. C., Owen, L. A., Chen, J., Schoenbohm, L. M., Hedrick, K. A., Blisniuk, K., Sharp, W. D., Imrecke, D. B., Li, W., Yuan, Z., et al. (2015). No late Quaternary strike-slip motion along the northern Karakoram fault. *Earth and Planetary Science Letters*, 409:290–298.

Robinson, J., Beck, R., Gnos, E., and Vincent, R. K. (2000). New structural and stratigraphic insights for northwestern Pakistan from field and Landsat Thematic Mapper data. *Geological Society of America Bulletin*, 112(3):364–374.

Roecker, S. (1982). Velocity structure of the Pamir-Hindu Kush Region: Possible evidence of subducted crust. *Journal of Geophysical Research: Solid Earth*, 87(B2):945–959.

Rosenbaum, G. and Lister, G. S. (2005). The Western Alps from the Jurassic to Oligocene: spatio-temporal constraints and evolutionary reconstructions. *Earth-Science Reviews*, 69(3):281–306.

Rudnick, R. and Gao, S. (2003). Composition of the continental crust. *Treatise on Geochemistry*, 3:1–64.

Sánchez-Sesma, F. J. and Campillo, M. (2006). Retrieval of the Green's function from cross correlation: the canonical elastic problem. *Bulletin of the Seismological Society of America*, 96(3):1182–1191.

Schertl, H.-P. and O'Brien, P. J. (2013). Continental crust at mantle depths: key minerals and microstructures. *Elements*, 9(4):261–266.

Schmidt, J., Hacker, B., Ratschbacher, L., Stübner, K., Stearns, M. A., Kylander-Clark, A., Cottle, J. M., Alexander, A., Webb, G., Gehrels, G., et al. (2011). Cenozoic deep crust in the Pamir. *Earth and Planetary Science Letters*, 312(3):411–421.

Schneider, F. M. (2014). *Imaging an Intra-continental Subduction in Central Asia with Teleseismic Receiver Functions*. Doctoral thesis, Freie Universität Berlin, Germany, 151 pp.

Schneider, F. M., Yuan, X., Schurr, B., Mechie, J., Sippl, C., Haberland, C., Minaev, V., Oimahmadov, I., Gadoev, M., Radjabov, N., et al. (2013). Seismic imaging of subducting continental lower crust beneath the Pamir. *Earth and Planetary Science Letters*, 375:101–112.

Schurr, B. and Nábělek, J. (1999). New techniques for the analysis of earthquake sources from local array data with an application to the 1993 Scotts Mills, Oregon, aftershock sequence. *Geophysical Journal International*, 137(3):585–600.

Schurr, B., Ratschbacher, L., Sippl, C., Gloaguen, R., Yuan, X., and Mechie, J. (2014). Seismotectonics of the Pamir. *Tectonics*, 33(8):1501–1518.

Schurr, B., Yuan, X., Haberland, C., and Kufner, S.-K. (2012). TIPTIMON (Tien Shan-Pamir Monitoring Program) TAJIKISTAN (2012/2014). *Deutsches GeoForschungsZentrum GFZ*.

Schurr, B., Yuan, X., Haberland, C., and Kufner, S.-K. (2013). TIPTIMON (Tien Shan-Pamir Monitoring Program) AFGHANISTAN (2013/2014). *Deutsches GeoForschungsZentrum GFZ*.

Schwab, M., Ratschbacher, L., Siebel, W., McWilliams, M., Minaev, V., Lutkov, V., Chen, F., Stanek, K., Nelson, B., Frisch, W., et al. (2004). Assembly of the Pamirs: Age and origin of magmatic belts from the southern Tien Shan to the southern Pamirs and their relation to Tibet. *Tectonics*, 23(4).

Searle, M. P. (1991). *Geology and tectonics of the Karakoram Mountains*. John Wiley & Sons Inc, New York, 358 pp.

Searle, M. P. (1996). Geological evidence against large-scale pre-Holocene offsets along the Karakoram Fault: Implications for the limited extrusion of the Tibetan plateau. *Tectonics*, 15(1):171–186.

Şengör, A., Altıner, D., Cin, A., Ustaömer, T., and Hsü, K. (1988). Origin and assembly of the Tethyside orogenic collage at the expense of Gondwana Land. *Geological Society, London, Special Publications*, 37(1):119–181.

Şengör, A. and Natal'in, B. (1996). Paleotectonics of Asia: fragments of a synthesis. In *The Tectonics of Asia*, pages 486–640. Edited by A Yin and TM Harrison, Cambridge Univ. Press, New York.

Şengör, A., Natal'in, B., and Burtman, V. S. (1993). Evolution of the Altaid tectonic collage and Palaeozoic crustal growth in Eurasia. *Nature*, 364:299–307.

Şengör, A. C. (1984). The Cimmeride orogenic system and the tectonics of Eurasia. *Geological Society of America Special Papers*, 195:1–74.

Seno, T. and Rehman, H. U. (2011). When and why the continental crust is subducted: Examples of Hindu Kush and Burma. *Gondwana Research*, 19(1):327–333.

Sens-Schönfelder, C. (2008). Synchronizing seismic networks with ambient noise. *Geophysical Journal International*, 174(3):966–970.

Shareq, A. (1981). *Geological observations and geophysical investigations carried out in Afghanistan over the period of 1972–1979, Zagros Hindu Kush Himalaya, Geodynamic Evolution*. Geodyn. Ser., 3H. K. Gupta, F. Moplany, Washington, D.C., 75–86.

Shvolman, V. (1978). Relicts of the Mesotethys in the Pamirs. *Himalayan Geology*, 8:369–378.

Siehl, A. (2015). Structural setting and evolution of the Afghan orogenic segment–a review. *Geological Society, London, Special Publications*, 427:SP427–8.

Sippl, C. (2013). *Shallow and deep structure of the Pamir-Hindu Kush region from local seismic data*. Doctoral thesis, Freie Universität Berlin, Germany, 193 pp.

Sippl, C., Ratschbacher, L., Schurr, B., Krumbiegel, C., Rui, H., Pingren, L., and Abdybachaev, U. (2014). The 2008 Nura earthquake sequence at the Pamir-Tian Shan collision zone, southern Kyrgyzstan. *Tectonics*, 33(12):2382–2399.

Sippl, C., Schurr, B., Tympel, J., Angiboust, S., Mechie, J., Yuan, X., Schneider, F. M., Sobolev, S. V., Ratschbacher, L., and Haberland, C. (2013a). Deep burial of Asian continental crust beneath the Pamir imaged with local earthquake tomography. *Earth and Planetary Science Letters*, 384:165–177.

Sippl, C., Schurr, B., Yuan, X., Mechie, J., Schneider, F. M., Gadoev, M., Orunbaev, S., Oimahmadov, I., Haberland, C., Abdybachaev, U., et al. (2013b). Geometry of the Pamir-Hindu Kush intermediate-depth earthquake zone from local seismic data. *Journal of Geophysical Research: Solid Earth*, 118(4):1438–1457.

Smit, M. A., Ratschbacher, L., Kooijman, E., and Stearns, M. A. (2014). Early evolution of the Pamir deep crust from Lu-Hf and U-Pb geochronology and garnet thermometry. *Geology*, 42(12):1047–1050.

Smith, D. C. (1984). Coesite in clinopyroxene in the Caledonides and its implications for geodynamics. *Nature*, 310(1984):641–644.

Sobel, E. R., Chen, J., Schoenbohm, L. M., Thiede, R., Stockli, D. F., Sudo, M., and Strecker, M. R. (2013). Oceanic-style subduction controls late Cenozoic deformation of the Northern Pamir orogen. *Earth and Planetary Science Letters*, 363:204–218.

Sobel, E. R. and Dumitru, T. A. (1997). Thrusting and exhumation around the margins of the western Tarim basin during the India-Asia collision. *Journal of Geophysical Research: Solid Earth*, 102(B3):5043–5063.

Sobel, E. R., Oskin, M., Burbank, D., and Mikolaichuk, A. (2006). Exhumation of basement-cored uplifts: Example of the Kyrgyz Range quantified with apatite fission track thermochronology. *Tectonics*, 25(2).

Sobel, E. R., Schoenbohm, L. M., Chen, J., Thiede, R., Stockli, D. F., Sudo, M., and Strecker, M. R. (2011). Late Miocene–Pliocene deceleration of dextral slip between Pamir and Tarim: implications for Pamir orogenesis. *Earth and Planetary Science Letters*, 304(3):369–378.

Sobolev, N. and Shatsky, V. (1990). Diamond inclusions in garnets from metamorphic rocks: a new environment for diamond formation. *Nature*, 343(6260):742–746.

Sobolev, S. V. and Babeyko, A. Y. (1994). Modeling of mineralogical composition, density and elastic wave velocities in anhydrous magmatic rocks. *Surveys in Geophysics*, 15(5):515–544.

Sobolev, S. V., Zeyen, H., Granet, M., Achauer, U., Bauer, C., Werling, F., Altherr, R., and Fuchs, K. (1997). Upper mantle temperatures and lithosphere-asthenosphere system beneath the French Massif Central constrained by seismic, gravity, petrologic and thermal observations. *Tectonophysics*, 275(1):143–164.

Stearns, M. A., Hacker, B., Ratschbacher, L., Lee, J., Cottle, J. M., and Kylander-Clark, A. (2013). Synchronous Oligocene–Miocene metamorphism of the Pamir and the north Himalaya driven by plate-scale dynamics. *Geology*, 41(10):1071–1074.

Stearns, M. A., Hacker, B., Ratschbacher, L., Rutte, D., and Kylander-Clark, A. (2015). Titanite petrochronology of the Pamir gneiss domes: Implications for middle to deep crust exhumation and titanite closure to Pb and Zr diffusion. *Tectonics*, 34(4):784–802.

Stein, S. and Wysession, M. (2009). *An introduction to Seismology, Earthquakes, and Earth Structure*. John Wiley & Sons, Blackwell, Oxford.

Strecker, M. R., Frisch, W., Hamburger, M. W., Ratschbacher, L., Semiletkin, S., Zamoruyev, A., and Sturchio, N. (1995). Quaternary deformation in the Eastern Pamirs, Tadzhikistan and Kyrgyzstan. *Tectonics*, 14(5):1061–1079.

Stübner, K., Ratschbacher, L., Rutte, D., Stanek, K., Minaev, V., Wiesinger, M., and Gloaguen, R. (2013a). The giant Shakhdara migmatitic gneiss dome, Pamir, India-Asia collision zone: 1. Geometry and kinematics. *Tectonics*, 32(4):948–979.

Stübner, K., Ratschbacher, L., Weise, C., Chow, J., Hofmann, J., Khan, J., Rutte, D., Sperner, B., Pfänder, J. A., Hacker, B., et al. (2013b). The giant Shakhdara migmatitic gneiss dome, Pamir, India-Asia collision zone: 2. Timing of dome formation. *Tectonics*, 32(5):1404–1431.

Styron, R., Taylor, M., and Okoronkwo, K. (2010). Database of active structures from the Indo-Asian collision. *Eos, Transactions American Geophysical Union*, 91(20):181–182.

Sun, J., Zhang, L., Deng, C., and Zhu, R. (2008). Evidence for enhanced aridity in the Tarim Basin of China since 5.3 Ma. *Quaternary Science Reviews*, 27(9):1012–1023.

Tapponnier, P., Mattauer, M., Proust, F., and Cassaigneau, C. (1981). Mesozoic ophiolites, sutures, and arge-scale tectonic movements in Afghanistan. *Earth and Planetary Science Letters*, 52(2):355–371.

Tapponnier, P. and Molnar, P. (1979). Active faulting and Cenozoic tectonics of the Tien Shan, Mongolia, and Baykal regions. *Journal of Geophysical Research: Solid Earth*, 84(B7):3425–3459.

Tapponnier, P., Peltzer, G., Le Dain, A., Armijo, R., and Cobbold, P. (1982). Propagating extrusion tectonics in Asia: New insights from simple experiments with plasticine. *Geology*, 10(12):611–616.

Tapponnier, P., Zhiqin, X., Roger, F., Meyer, B., Arnaud, N., Wittlinger, G., and Jingsui, Y. (2001). Oblique stepwise rise and growth of the Tibet Plateau. *Science*, 294(5547):1671–1677.

Tarantola, A. and Valette, B. (1982). Generalized nonlinear inverse problems solved using the least squares criterion. *Reviews of Geophysics*, 20(2):219–232.

Thielmann, M., Rozel, A., Kaus, B., and Ricard, Y. (2015). Intermediate-depth earthquake generation and shear zone formation caused by grain size reduction and shear heating. *Geology*, 43(9):791–794.

Thomas, J.-C., Chauvin, A., Gapais, D., Bazhenov, M., Perroud, H., Cobbold, P., and Burtman, V. S. (1994). Paleomagnetic evidence for Cenozoic block rotations in the Tadjik depression (Central Asia). *Journal of Geophysical Research: Solid Earth*, 99(B8):15141–15160.

Thompson, J. A., Burbank, D. W., Li, T., Chen, J., and Bookhagen, B. (2015). Late Miocene northward propagation of the northeast Pamir thrust system, northwest China. *Tectonics*, 34(3):510–534.

Thurber, C. (1983). Earthquake locations and three-dimensional crustal structure in the Coyote Lake area, central California. *Journal of Geophysical Research*, 88(B10):8226–8236.

Thurber, C. (1993). Local earthquake tomography: velocities and Vp/Vs-theory. In *Seismic tomography: Theory and Practice*, pages 563–583. Chapman and Hall, London.

Toomey, D. and Foulger, G. (1989). Tomographic inversion of local earthquake data from the Hengill-Grensdalur central volcano complex, Iceland. *Journal of Geophysical Research: Solid Earth*, 94(B12):17497–17510.

Treloar, P. J. and Izatt, C. N. (1993). Tectonics of the Himalayan collision between the Indian plate and the Afghan block: A synthesis. *Geological Society, London, Special Publications*, 74(1):69–87.

Trifonov, V. G. (1978). Late Quaternary tectonic movements of western and central Asia. *Geological Society of America Bulletin*, 89(7):1059–1072.

Tryggvason, A. and Bergman, B. (2006). A traveltime reciprocity discrepancy in the Podvin & Lecomte time3d finite difference algorithm. *Geophysical Journal International*, 165(2):432–435.

Tsujimori, T., Sisson, V. B., Liou, J. G., Harlow, G. E., and Sorensen, S. S. (2006). Very-low-temperature record of the subduction process: A review of worldwide lawsonite eclogites. *Lithos*, 92(3):609–624.

Tympel, J. (2014). *Numerical modeling of the Cenozoic Pamir-Tien Shan orogeny*. Doctoral thesis, University of Potsdam, Germany, 160 pp.

Um, J. and Thurber, C. (1987). A fast algorithm for two-point seismic ray tracing. *Bulletin of the Seismological Society of America*, 77(3):972–986.

USGS (2016). USGS earthquake bulletins, On-line Bulletin. United States Geological Survey. *http://earthquake.usgs.gov/*.

Vacareanu, R., Radulian, M., Iancovici, M., Pavel, F., and Neagu, C. (2015). Fore-arc and back-arc ground motion prediction model for Vrancea intermediate depth seismic source. *Journal of Earthquake Engineering*, 19(3):535–562.

Van der Hilst, R., Widiyantoro, S., and Engdahl, E. (1997). Evidence for deep mantle circulation from global tomography. *Nature*, 386:578–584.

Van der Voo, R. (2005). *Paleomagnetism of the Atlantic, Tethys and Iapetus Oceans*. Cambridge University Press, 411 pp.

Van der Voo, R., Spakman, W., and Bijwaard, H. (1999). Tethyan subducted slabs under India. *Earth and Planetary Science Letters*, 171(1):7–20.

van Hinsbergen, D. J., Kapp, P., Dupont-Nivet, G., Lippert, P. C., DeCelles, P. G., and Torsvik, T. H. (2011a). Restoration of Cenozoic deformation in Asia and the size of Greater India. *Tectonics*, 30(5).

van Hinsbergen, D. J., Lippert, P. C., Dupont-Nivet, G., McQuarrie, N., Doubrovine, P. V., Spakman, W., and Torsvik, T. H. (2012). Greater India Basin hypothesis and a two-stage Cenozoic collision between India and Asia. *Proceedings of the National Academy of Sciences*, 109(20):7659–7664.

van Hinsbergen, D. J., Steinberger, B., Doubrovine, P. V., and Gassmöller, R. (2011b). Acceleration and deceleration of India-Asia convergence since the Cretaceous: Roles of mantle plumes and continental collision. *Journal of Geophysical Research: Solid Earth*, 116(B6).

van Hunen, J. and Allen, M. B. (2011). Continental collision and slab break-off: a comparison of 3-D numerical models with observations. *Earth and Planetary Science Letters*, 302(1):27–37.

Villaseñor, A., Spakman, W., and Engdahl, E. (2003). Influence of regional travel times in global tomographic models. In *EGS-AGU-EUG Joint Assembly*.

Vinnik, L. P., Lukk, A. A., and Nersesov, I. L. (1977). Nature of the intermediate seismic zone in the mantle of Pamirs–Hindu-Kush. *Tectonophysics*, 38(3):T9–T14.

Waldhauser, F. (2001). hypoDD–A program to compute double-difference hypocenter locations. Technical report, Open File Report 94–431, US Geological Survey, 01-113, 25 pp.

Waldhauser, F. and Ellsworth, W. L. (2000). A double-difference earthquake location algorithm: Method and application to the northern Hayward fault, California. *Bulletin of the Seismological Society of America*, 90(6):1353–1368.

Wassermann, J., Krischer, L., Megies, T., Barsch, R., and Beyreuther, M. (2013). Obspy: a Python toolbox for seismology. In *AGU Fall Meeting Abstracts*, number S51A-2322.

Windley, B. F., Alexeiev, D., Xiao, W., Kröner, A., and Badarch, G. (2007). Tectonic models for accretion of the Central Asian Orogenic Belt. *Journal of the Geological Society*, 164(1):31–47.

Wortel, M. and Spakman, W. (2000). Subduction and slab detachment in the Mediterranean-Carpathian region. *Science*, 290(5498):1910–1917.

Xiao, W., Wang, Y.-t., Jiang, S.-h., and Hou, W.-r. (2010). Explanatory Notes for the Simplified Geology and Mineral Resource Map and Typical Geographical and Topographic Features of Southern Mongolian and Its Neighboring Areas. *Acta Geoscientica Sinica*, 31(3):473–484.

Xu, Z., Dilek, Y., Cao, H., Yang, J., Robinson, P., Ma, C., Li, H., Jolivet, M., Roger, F., and Chen, X. (2015). Paleo-Tethyan evolution of Tibet as recorded in the East Cimmerides and West Cathaysides. *Journal of Asian Earth Sciences*, 105:320–337.

Yamasaki, T. and Seno, T. (2003). Double seismic zone and dehydration embrittlement of the subducting slab. *Journal of Geophysical Research: Solid Earth*, 108(B4).

Yang, Y. and Liu, M. (2002). Cenozoic deformation of the Tarim plate and the implications for mountain building in the Tibetan Plateau and the Tian Shan. *Tectonics*, 21(6).

Yin, A. (2010). Cenozoic tectonic evolution of Asia: A preliminary synthesis. *Tectonophysics*, 488(1):293–325.

Yin, A. and Harrison, T. M. (2000). Geologic evolution of the Himalayan-Tibetan orogen. *Annual Review of Earth and Planetary Sciences*, 28(1):211–280.

Yin, A., Harrison, T. M., Ryerson, F., Wenji, C., Kidd, W., and Copeland, P. (1994). Tertiary structural evolution of the Gangdese thrust system, southeastern Tibet. *Journal of Geophysical Research: Solid Earth*, 99(B9):18175–18201.

Yin, A. and Nie, S.-Y. (1996). A Phanerozoic palinspastic reconstruction of China and its neighboring regions. *World and Regional Geology*, 1(8):442–485.

Yuan, H. and Romanowicz, B. (2010). Lithospheric layering in the North American craton. *Nature*, 466(7310):1063–1068.

Zhang, Y., Feng, W., Chen, Y., Xu, L., Li, Z., and Forrest, D. (2012). The 2009 L'Aquila MW 6.3 earthquake: a new technique to locate the hypocentre in the joint inversion of earthquake rupture process. *Geophysical Journal International*, 191(3):1417–1426.

Zhang, Z., Deng, Y., Teng, J., Wang, C., Gao, R., Chen, Y., and Fan, W. (2011). An overview of the crustal structure of the Tibetan plateau after 35 years of deep seismic soundings. *Journal of Asian Earth Sciences*, 40(4):977–989.

Zubovich, A., Schöne, T., Metzger, S., Mosienko, O., Mukhamediev, S., Sharshebaev, A., and Zech, C. (2016). Tectonic interaction between the Pamir and Tien Shan observed by GPS. *Tectonics*.

Zubovich, A. V., Wang, X.-Q., Scherba, Y. G., Schelochkov, G. G., Reilinger, R., Reigber, C., Mosienko, O. I., Molnar, P., Michajljow, W., Makarov, V. I., et al. (2010). GPS velocity field for the Tien Shan and surrounding regions. *Tectonics*, 29(6).

List of Figures

List of Tables

Acknowledgments

Many thanks to Bernd Schurr, whose initiative made this whole work possible, who provided many thought-provoking impulses during these years but gave me any possible freedom to explore and follow my own ideas at the same time. Many thanks to Christian Sippl, not only for abundant helpful advice and comments on data processing and interpretative issues, but also for his role as a stable anchor during my whole time at GFZ. Many thanks to Frederik Tilmann for his advice and instant help at important points during my work. Many thanks to Lothar Ratschbacher for his strong interest in the geophysical work, for the enormous energy and time he put into our discussions and for his patience in reviewing and creating tectonic features in my maps. Many thanks to Onno Oncken for hosting me in his working group and for enriching this work due to his broad perspective on geodynamic processes.

I would like to acknowledge the co-authors of my EPSL paper, who very actively contributed to its creation process. Apart from the people already mentioned above, especially to Jim Mechie for his patience in carefully proofreading and sharp re-thinking. Further, I am extremely grateful to Bernd Schurr, Christian Sippl, Frederik Tilmann, Vasiliki Mouslopoulou, Ben Heit and Sabrina Metzger for proofreading different parts of this thesis.

Many thanks to the *TIPTIMON* and *TIPAGE* working groups, whose joint effort ultimately enabled this work. Especially, I would like to acknowledge Anatoly Ischuk, Shohruhk Murodkulov, Ilhomjon Oimahmadov and Mustafo Gadoev for their effort in joint fieldwork and their help in many organizational tasks. Further, I am grateful to the different Central Asian drivers and station-wards, whose effort and care ensured safe and successful field campaigns. Many thanks to Arib s/of Mohammad Akbar, who deployed the seismic stations in Afghanistan and to *Focus Humanitarian Assistance* who provided safe locations for these stations. At GFZ, I am happy to have had Walburga Korolevski as a helpful and positive *TIPTIMON*-PhD companion. I further would like to acknowledge Bernd Schurr, Xiaohui Yuan, Sabrina Metzger, Christian Sippl, and Ben Heit for their contributions in *TIPTIMON*-fieldwork and additionally Stephan Sobolev, Frederik Tilmann, Lothar Ratschbacher, Felix Schneider and Jim Mechie for their contributions to our discussions at group meetings and workshops. Many thanks to Matthias Rosenau for coordinating the *TIPTIMON* project.

Many thanks to the *Geophysical Instrument Pool Potsdam*, and especially to Christian Haberland, for providing the seismometers for the field deployments. Further, I would like to acknowledge the different Central Asian and global organizations who provided data that were used in this dissertation: First of all the *GEOFON* and *IRIS* data management centers for collecting and providing seismic data, as well as the *Central Asian Institute for Applied Geosciences*, the *Chinese Earthquake Network data center*, the *Institute of*

Seismology of the National Academy of Sciences of Kyrgyz Republic, the *Institute of Geophysical Research of Kazakhstan* and *PMP International*, who operate the *Tajik seismic network*. Further, *USGS* and the *EHB* and *ISC* bulletins.

Many thanks to different people that helped during specific processing or interpretation steps. Starting at the beginning, I would especially like to acknowledge: Marcelo Bianchi for advice on the teleseismic tomography. Sebastian Heimann for help in using the *Pyrocko* toolbox for handling and plotting seismic moment tensors. Sanaa Abdulhameed for providing the detailed fault map of the Tajik basin. Stephan Sobolev for his advice regarding the cross-plotting of the velocity models gained from local tomography. Christian Haberland for his comments on the local tomography and his help in creation of the synthetic tests as well as for several little and very helpful C-programs he provided for different tasks. Christoph Sens-Schönfelder for comments on the noise cross-correlation. Joachim Saul for providing and carefully reviewing the *GEOFON* data. Anthony Lomax for quick replies on questions regarding the *NonLinLoc* software. Yong Zhang and Rongjiang Wang for calculating the finite fault model of the M_w 7.5 October 2015 Hindu Kush earthquake.

I would like to thank all members of the *Dynamics of the Lithosphere* section at GFZ, who hosted me during the last years and how have created a pleasant environment for work. Especially many thanks to my office-mate Malte Ritter, for his company and numerous discussions as well as to and our extraordinary secretary Franziska Alberg. Many thanks to Maximiliano Bezada and Gene Humphreys for hosting me during two stays in the USA.

Apart from the software mentioned in the main part of this thesis, I would like to acknowledge *ObsPy* and *python*, which I used for many data processing steps as well as *GMT* and *Inkscape* for providing the possibility to create beautiful maps and sketches. Further, this whole thesis was written in *LaTeX*.

Finally, I would like to acknowledge different scientists whose work and personality influenced me during my PhD: Thibault Duretz for showing me *the dynamics of slab-detachment*, Douwe van Hinsbergen for *making the continents move*, Anne Replumaz for giving me a different perspective on geodynamics and Alexander Zubovich and Sagynbek Orunbaev, who I admire for the research they do in Central Asia.

Erklärung

Hiermit versichere ich, dass ich die vorliegende Dissertation ohne unzulässige Hilfe Dritter und ohne Benutzung anderer als der angegebenen Literatur angefertigt wurde. Die Stellen der Arbeit, die anderen Werken wörtlich oder inhaltlich entnommen sind, wurden durch entsprechende Angaben der Quellen kenntlich gemacht. Diese Arbeit hat in gleicher oder ähnlicher Form noch keiner Prüfungsbehörde vorgelegen.

Berlin, Mai 2016

Curriculum Vitae

Der Lebenslauf ist in der Online-Version aus Gründen des Datenschutzes nicht enthalten.